Master's thesis

NTNU
Norwegian University of Science and Technology
Faculty of Engineering
Department of Marine Technology

Linda Sieber

VIV fatigue of rigid spool for subsea template by a time domain model

Master's thesis in Maritime Engineering
Supervisor: Prof. Svein Sævik (NTNU), Prof. Jonas Ringsberg (Chalmers University of Technology) and Zhenhui Liu (Aker Solutions)
June 2020

NTNU
Norwegian University of Science and Technology

CHALMERS
UNIVERSITY OF TECHNOLOGY

Linda Sieber

VIV fatigue of rigid spool for subsea template by a time domain model

Master's thesis in Maritime Engineering
Supervisor: Prof. Svein Sævik (NTNU), Prof. Jonas Ringsberg (Chalmers University of Technology) and Zhenhui Liu (Aker Solutions)
June 2020

Norwegian University of Science and Technology
Faculty of Engineering
Department of Marine Technology

NTNU
Norwegian University of
Science and Technology

VIV fatigue of rigid spool for subsea template by a time domain model

Master's thesis

Submitted by	Linda Sieber
Submission	10th June 2020
Supervisors	Prof. Svein Sævik, Prof. Jonas Ringsberg
Industry contact	Zhenhui Liu (Aker Solutions)

Department of Marine Technology
Faculty of Engineering
Norwegian University of Science and Technology

Department of Mechanics and Maritime Sciences
Division of Marine Technology
Chalmers University of Technology

NTNU Trondheim
Norwegian University of Science and Technology *Faculty of Engineering*
Department of Marine Technology

MASTER THESIS WORK SPRING 2020

for

Stud. Tech. Linda Sieber

VIV fatigue of rigid spool for subsea template by a time domain model

Virvelindusert utmatting av stivt rørseksjon på undervannsramme etter en tidsplan modell

Vortex Induced Vibrations (VIV) can lead to fast accumulation of fatigue damage in offshore slender structures, such as rigid spools applied in the inboard piping of subsea templates for oil & gas production. A new empirical method for time domain (TD) calculation of VIV has been developed by NTNU. This method is capable of accounting for structural non-linearity and time-varying flow compared to the traditional frequency domain analyses. The objective of this study is to validate the TD VIV prediction tool for pipeline spool applications. The work is to be carried out as a continuation of the thesis work conducted during fall 2019 and is to include the following items:

1. Literature study on the fundamental theory of VIV and numerical prediction tools, relevant DnV GL rules and recommended practices related to spool design and VIV response analysis.
2. Learn the TD VIV prediction tool SIMLA.
3. Define a case scenario including mechanical properties, geometry and environmental conditions for an existing VIV model test
4. Perform eigenvalue analysis and explore the differences in terms of eigenvalues and mode shapes with respect to different modelling choices, i.e. with or without bend elements.
5. Perform TD VIV simulation for different load cases and compare the response to model test results and the results obtained from DNVGL-RP-F105. This is to include sensitivity analyses with respect to model parameters and fatigue estimates to explore differences.
6. Run eigenvalue analysis in Abaqus with and without bend elements and compare with eigenvalues from Simla.
7. Based on the above procedure, explore other relevant data published in literature and/or alternatively a realistic full-scale scenario to be agreed upon.
8. Conclusions and recommendations for further work

The work scope may prove to be larger than initially anticipated. Subject to approval from the supervisors, topics may be deleted from the list above or reduced in extent.

In the thesis report, the candidate shall present her personal contribution to the resolution of problems within the scope of the thesis work

Theories and conclusions should be based on mathematical derivations and/or logic reasoning identifying the various steps in the deduction.

The candidate should utilise the existing possibilities for obtaining relevant literature.

Thesis report format
The thesis report should be organised in a rational manner to give a clear exposition of results, assessments, and conclusions. The text should be brief and to the point, with a clear language. Telegraphic language should be avoided.

The report shall contain the following elements: A text defining the scope, preface, list of contents, summary, main body of thesis, conclusions with recommendations for further work, list of symbols and acronyms, references and (optional) appendices. All figures, tables and equations shall be numerated.

The supervisors may require that the candidate, in an early stage of the work, presents a written plan for the completion of the work.

The original contribution of the candidate and material taken from other sources shall be clearly defined. Work from other sources shall be properly referenced using an acknowledged referencing system.

The report shall be submitted in electronic format (.pdf):
- Signed by the candidate
- The text defining the scope shall be included (this document)
- Drawings and/or computer models that are not suited to be part of the report in terms of appendices shall be provided on separate (.zip) files.

Ownership
NTNU has according to the present rules the ownership of the thesis reports. Any use of the report has to be approved by NTNU (or external partner when this applies). The department has the right to use the report as if the work was carried out by a NTNU employee, if nothing else has been agreed in advance.

Thesis supervisors:

Prof. Svein Sævik, NTNU, Zhenhui Liu, Aker Solutions and Prof. Jonas Ringsberg, Chalmers University of Technology

Deadline: June 10th, 2020

Trondheim, January 10th, 2020

Svein Sævik

Jonas Ringsberg – date and signature: Jonas Ringsberg 19/2-2020

Candidate – date and signature: L. Sæv 09-03-2020

Abstract

Subsea spools and jumpers are commonly placed close to the seabed where they are exposed to low velocity currents. These currents lead to vortex induced vibrations (VIV) in in-line (IL) and cross-flow (CF) direction. VIV can lead to fast accumulation of fatigue damage and the prediction of VIV is therefore important in fatigue assessment of those structures.

In this thesis work, a typical 'M'-shaped jumper model was investigated. Due to the three-dimensional geometry, VIV predictions for spools and jumpers are more complicated compared to straight pipes, both from hydrodynamic and structural-dynamic perspective. The tri-axiality of flow makes it difficult to separate into IL and CF response, but it is crucial to understand which modes are active in VIV response. On a structural level, the stiffness is affected by bent pipe elements due to deformation of the cross-section and additional strains. The special considerations that must be made in analysis of spools and jumpers are pointed out in the literature study.

Further, two models were investigated, which differed only in the element type used to model the 90-degree pipe bends. One of these was a simple linear-elastic pipe element, while the other one was an elbow element, capable of accounting for deformation of the cross-section and additional strain terms due to bending. This allowed for evaluation of the importance of change in stiffness on modal analysis. Two software packages were used to verify the eigenvalue results and the use of elbow elements: Simla, developed at NTNU Trondheim, and Abaqus, developed by Dessault Systèmes®. It was shown that the reduced stiffness of the model including elbow elements improved the results of modal analysis, especially with regard to in-line bending, and caused a shift in the mode shape order.
Flexibility factors for a full-scale bend model including internal and external pressure were evaluated.

TD VIV simulations for different load cases were carried out in Simla. With this TD tool it was possible to account for large deflections and time-varying flow. A parameter study was conducted on the input parameters in Simla, especially for the TD VIV prediction tool. The results from VIV motion were compared to the empirical response model approach from DNVGL-RP-F105 (2019) and to experimental data. With varied parameters of the TD VIV tool it was possible to obtain results that are in good correlation with model test data. The DNV GL response model approach for many cases gave very conservative motion amplitudes, especially for CF VIV,

compared to experimental data.

Stresses and fatigue damage from VIV were calculated by two different methods, of which one used the moment signals obtained from the VIV tool in Simla directly and applied rainflow counting to find stress ranges. The other method followed the response model approach from the recommended practice DNVGL-RP-F105 (2019). For this latter method, modal analysis results were used together with response amplitudes obtained from the guidelines. For both methods the maximum principal stress criterion was used for equivalent stresses. Fatigue damage was calculated using the SN-data from DNVGL-RP-C203 (2005).
For most cases the fatigue damage calculated using the DNV GL response model procedure was higher than obtained from the TD tool, which was expected since motion amplitudes obtained from the guidelines were already very conservative. However, for several load cases with low-velocity currents up to 0.3 m/s the Simla tool gave higher fatigue estimates. These cases are due to IL VIV which occurs at low current velocities and is especially relevant for structures placed close to the seabed. It was also found that torsional stresses are relevant for observed flow directions and, thus, cannot be neglected. Sensitivity of fatigue damage to changes of the drag coefficient and model parameters of the VIV tool was discussed. Based on the findings of this thesis work, recommendations for future work were made.

Preface

This report is the result of my thesis work during the fourth semester in the study program Nordic Master in Maritime Engineering with study track Ocean Structures. It is a continuation of a project work conducted during fall 2019.

I would like to thank my supervisors, Prof. Svein Sævik, Prof. Jonas Ringsberg and Zhenhui Liu, for their continuous guidance and support throughout this semester. I really appreciate the time you have spent on helping me with this thesis.

Hannover, June 2020

Linda Sieber

List of Abbreviations

VIV - vortex induced vibration
FD - frequency domain
TD - time domain
IL - in-line
CF - cross-flow
KC - Keulegan-Carpenter number
CFD - computational fluid dynamics
SIF - stress intensification factors
FF - flexibility factors
FEM - finite element method
FEA - fine element analysis
DOF - degrees of freedom
FTT - Fast Fourier Transformation

List of Symbols

a	SN-curve parameter
A	motion amplitude
A/D	normalized VIV response amplitude
$(A_y/D)_j$	normalized IL VIV amplitude for the j-th mode in the DNVGL procedure
$(A_z/D)_j$	normalized CF VIV amplitude for the j-th mode in the DNVGL procedure
C_a	added mass coefficient
$C_{a,CF-RES}$	added mass coefficient due to CF response
C_D,C_{Drag}	Drag coefficient
C_L	Lift coefficient
C_M	Inertia coefficient
CV	CF lift force coefficient
$CVI1$	IL force coefficient for region one
D	hydrodynamic diameter (outer pipe diameter)
E	Young's modulus
F_d	damping force

$f_{CF-RES,j}$	response frequency for j-th CF VIV mode
$f_{cyc,IL}, f_{cyc,CF}$	cycle counting frequency for IL or CF stress cycles
$f_{n,j}$	natural still-water frequency for the j-th mode
$f_{IL,j}, f_{CF,j}$	natural frequency in IL or CF direction for the j-th mode
f_{ratio}	ratio of two consecutive CF modal frequencies
f_{vs}	vortex shedding frequency
$\hat{f}_{osc}$	non-dimensional oscillating frequency
$\hat{f}_{1I1}$	minimum non-dimensional oscillating frequency that gives energy input for IL region one
I_y, I_z	area moment of inertia with respect to y or z-axis
I_x	polar moment of inertia
k	stiffness
L	characteristic length, for a cylinder usually equal to D
m	SN-curve parameter, depending on context
m	mass, depending on context
m_a	added mass
μ	dynamic fluid viscosity
N_i	number of constant-amplitude cycles to failure
n_i	number of cycles for one block in stress histogram
Φ_v	instantaneous phase of the excitation force during VIV
Re	Reynolds number
ρ_w	fluid density
ΔS_i	stress range for one block in stress histogram
ΔS_{eq}	equivalent stress range for fatigue analysis
σ_1	principal stress
σ_{xx}	flexural stress for beam/pipe element
St	Strouhal number
t	wall-thickness
τ_{xy}	torsional stress for beam/pipe element
θ_1	time derivative of instantaneous force phase for IL region one
θ_2	time derivative of instantaneous force phase for IL region two

θ_{σ_1}	direction of principal stress
U,U_c	undisturbed flow velocity, here equal to current velocity
V_r,V_{red}	reduced velocity
ω	circular frequency

Contents

List of Figures

List of Tables

Chapter 1

Introduction

1.1 Background and motivation

In the offshore industry, rigid spools and jumpers are often placed close to the seabed in the environment of low-velocity currents. These currents can induce vortex induced vibration (VIV) of the structures as a result of oscillating forces from the fluid. VIV can lead to a fast accumulation of load cycles, which significantly decreases the life of the structures. For environmental and economical reasons, the prediction of VIV is therefore of high importance in fatigue life assessment.

Semi-empirical models in frequency domain (FD) have been widely used in industry applications to predict cross-flow (CF) VIV. A problem is that these models are not capable of accounting for structural non-linearity and time-varying flow. A time domain (TD) prediction tool for VIV has been developed at NTNU to overcome these drawbacks.

Furthermore, a response model approach, published in DNVGL-RP-F105 [7], is commonly used for the prediction of in-line (IL) VIV. The approach was developed for free spanning pipelines, thus, special considerations apply for non-straight pipes. For the latter one, it can be difficult to differentiate in damage contribution from IL VIV and CF VIV, since they no longer occur in each other's neutral plane. However, the response model approach can be used to compare and evaluate the results from the TD tool.

A new element type has been implemented into the TD prediction tool at NTNU that can account for reduced stiffness and cross-section deformation of bent pipe elements. The two main objectives of this project work are to show how this new element type affects the results in modal analysis and to demonstrate that the TD tool is applicable for pipeline spool and jumper applications with non-straight pipe parts.

1.2 Research questions

1. Is the TD VIV prediction tool - with adjustment of certain control parameters - applicable to non-straight pipes?

2. Which significance does the modeling choice between regular pipe elements and elbow elements have with respect to modal analysis and stresses for a jumper model?

1.3 Organization of thesis

The thesis consists of the following chapters.

Chapter 1 presents the motivation, objectives and research questions. It provides the outline of the thesis.

Chapter 2 provides a literature review on fundamental theory of VIV and numerical prediction tools, fatigue assessment and relevant DNV GL rules and recommended practices. This chapter was part of a previous study during fall semester 2019 and has been adopted with some modifications. Section 2.5 has been added.

Chapter 3 includes the methodology applied in this study. It gives detailed descriptions about element formulations and solvers of the utilized software, Simla and Abaqus. It explains the routines used for fatigue assessment. Further, the response models from DNVGL-RP-F105 are described in more detail.

Chapter 4 summarizes the input data for this study. This includes mechanical and geometrical model properties, environmental conditions, the choice of elements as well as input parameters for the VIV prediction tool in Simla and the DNV GL response models. It also includes a section about a single bend element with realistic full-scale dimensions and internal and external pressure to further explore the modeling choice between elbow elements and regular pipe elements.

Chapter 5 presents and discusses obtained results. It compares eigenfrequencies, mode shapes and modal stresses of the models with and without elbow elements in the bends from both Simla and Abaqus. It evaluates results from the TD VIV tool in Simla against experimental data and the DNV GL response models.
The response model approach and the TD tool in Simla are compared with respect to stresses and fatigue arising from VIV. Sensitivity of fatigue estimates is evaluated for the different modeling choices and VIV tool parameters.

As approved by the supervisors task seven from the initial description of the work scope was replaced due to the lack of other relevant publications. Instead, the effect of internal and external pressure on flexibility factors for elbow elements was observed for a realistic full-scale scenario.

Chapter 6 summarizes key results and main conclusions from chapter five. It also gives recommendations for future work.

Appendix A includes additional plots of modal stresses from Simla and Abaqus. Oscillating frequencies, motion amplitudes and identified modes from the VIV output in Simla can be found in **Appendix B**.
Appendix C contains calculation steps and intermediate results of the DNV GL response model approach.
The Matlab routine used to calculate stresses and fatigue from moment signals is presented in **Appendix D**. Due to the large amount of data, time signals obtained from Simla were submitted in a separate folder in addition to this report.

Chapter 2

Background and Literature review

2.1 Fundamental theory of VIV

This chapter provides the fundamental theory of occurrence and formation of VIV. The main parameters that are used in VIV analysis will be discussed here. The main objectives are to give a better understanding of the methodology to be used later and to summarize selected parts of the research that has been conducted previously.

2.1.1 Governing parameters

Reynolds number

The flow regime around a structure is governed by the Reynolds number. It is defined as the ratio between inertia forces and viscous forces as

$$Re = \frac{UL}{\mu} \tag{2.1}$$

where

U is the undisturbed flow velocity

L is the characteristic length, often also denoted as cylinder diameter D

μ is the dynamic viscosity of the fluid.

Generally, the flow regimes can be classified as laminar flow, turbulent flow, and the transition region. At low Reynolds's numbers ($Re < 200$), the viscous forces dominate and the streamlines in the wake field of the structure are attached. Velocity fluctuations are small and the flow is orderly. This is defined as laminar flow. At higher Reynolds numbers ($300 < Re$), when a critical velocity of the flow is exceeded and the inertia forces are large compared to the viscous forces, the flow becomes turbulent. Characteristics of a turbulent flow are high velocity fluctuations and chaotic motions [9]. The regime in between ($200 < Re < 300$) is denoted as

transition region. The flow regime also defines the vortex shedding pattern.

Formation of VIV occurs for any cylinder with a Reynolds number higher than 40, but in a laminar regime the vortex-street is two-dimensional. In a fully turbulent wake field ($300 < Re$) the vortex shedding becomes three-dimensional. The boundary layer of a circular cylinder changes with further increase of the Reynolds number.
In the sub-critical regime ($300 < Re < 3 \times 10^5$) the boundary layer remains laminar. In the critical regime ($3 \times 10^5 < Re < 3.5 \times 10^5$) the boundary layer becomes turbulent at the separation point of one side of the cross-section, but remains laminar at the separation point of the other side. This phenomenon causes an asymmetric flow and non-zero mean lift force [10]. For further increased Reynolds numbers the boundary layer becomes turbulent at both separation points, but not yet in between the stagnation point and the separation points. In the supercritical regime ($3.5 \times 10^5 < Re < 1.5 \times 10^6$), the transition from laminar to turbulent is shifted closer to the stagnation point. For higher Reynolds numbers ($1.5 \times 10^6 < Re < 4.5 \times 10^6$) the flow is asymmetric again, since first it becomes fully turbulent only on one side. This is denoted as upper-transitional regime. Beyond this, in the transcritical regime, the flow is turbulent everywhere [10].

The vortex shedding process as a function of the Reynolds number is also shown in Figure 2.1. To maintain kinematic similarity in experiments, is is important that the Reynolds number in model tests is the same as in full-scale. Experiments on the occurrence of VIV are often conducted in the sub-critical regime. Applying the results to full-scale cases, which are often in the critical and supercritical regime, is assumed to be conservative [11]. Another useful quantity in VIV analysis of cylinders with different dimensions and in flow of different velocities is the Strouhal number, which is related to the Reynolds number.

Strouhal number

The Strouhal number is a dimensionless parameter defined as

$$St = \frac{f_s L}{U} \tag{2.2}$$

where f_s is the vortex shedding frequency.

For Reynolds numbers in the sub-critical regime, the Strouhal number is almost constant $St \approx 0.2$ [1]. This means that the vortex shedding process remains almost unchanged in this regime. In VIV analysis, the Strouhal number is often set to this

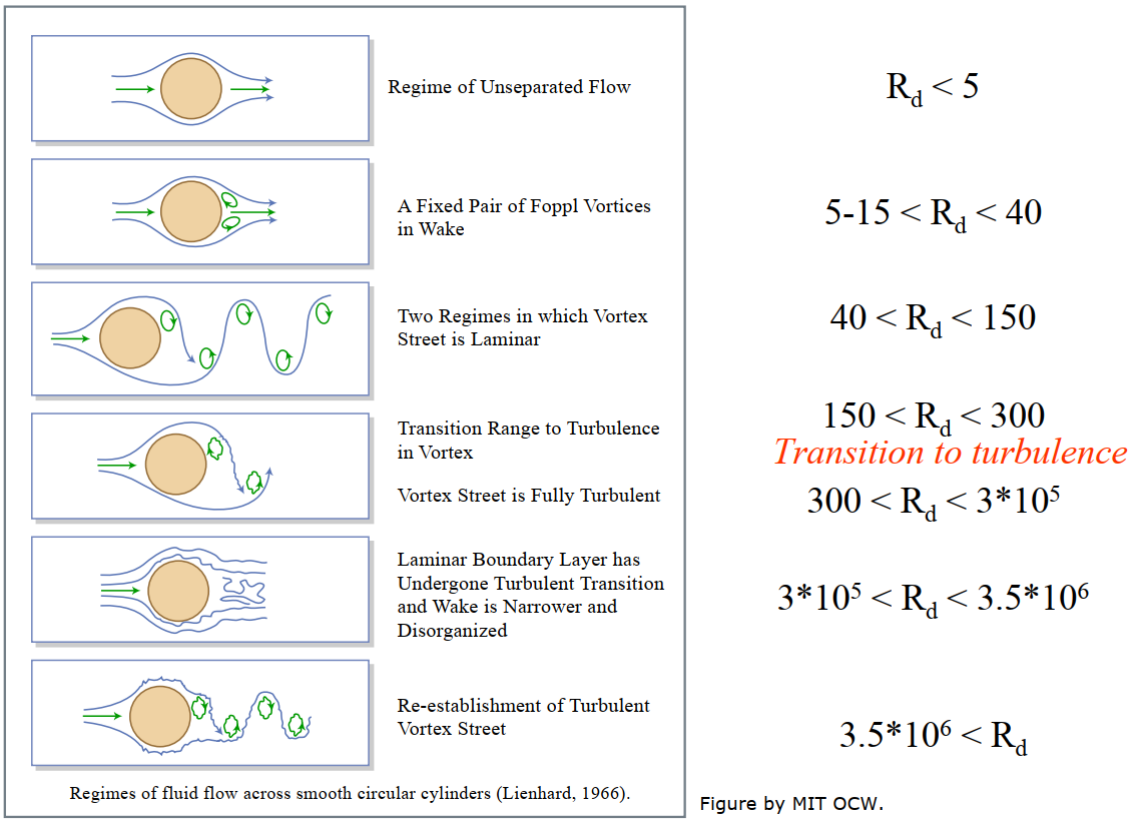

Figure 2.1: Reynolds number dependency of the vortex shedding process. Taken from Techet [1].

value. The relationship between Strouhal number and Reynolds number for cylinders with circular cross-section is shown in Figure 2.2.

Reduced velocity

In VIV analysis, the motion amplitude is usually plotted as non-dimensional vibration amplitude A/D against the reduced velocity [7]:

$$V_r = \frac{U_c + U_w}{f_{n,j} D} \tag{2.3}$$

where

$f_{n,j}$ is the natural still-water eigenfrequency for the j-th mode

U_c is the mean current velocity, normal to the pipe

U_w is the significant wave-induced flow velocity.

Keulegan-Carpenter number

When a cylinder is exposed to oscillating forces from the fluid, also the Keulegan-Carpenter (KC) number is an important dimensionless parameter to describe the

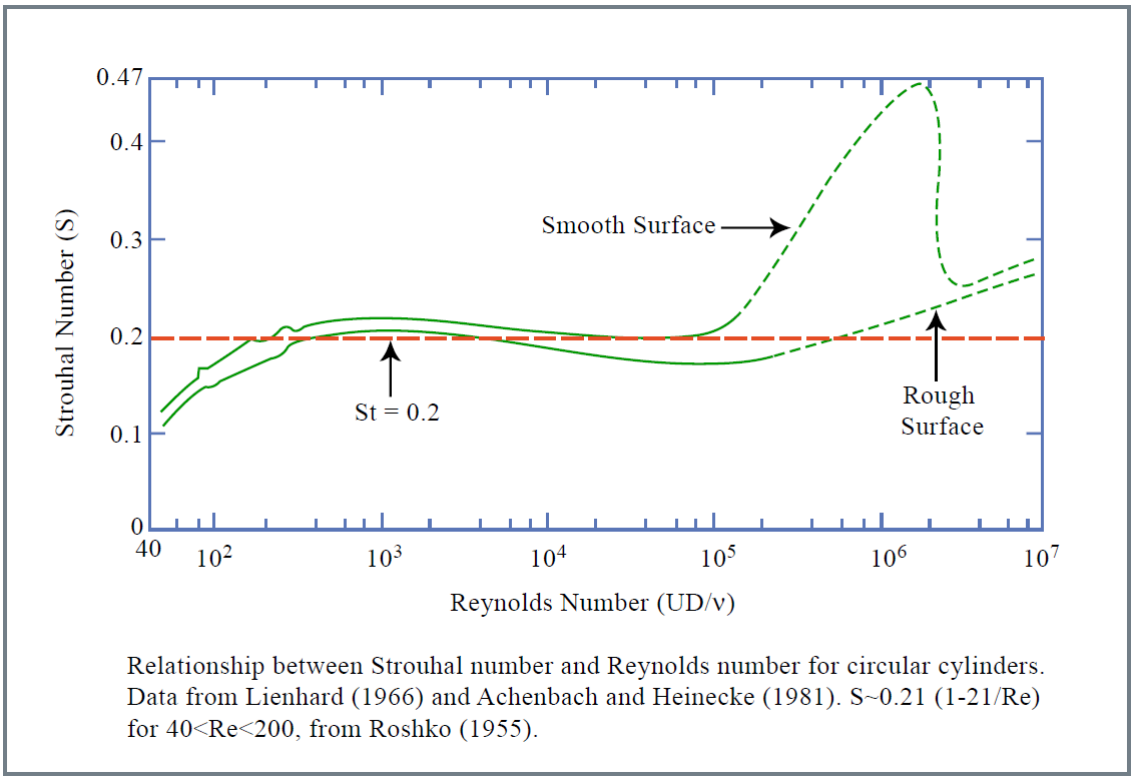

Figure 2.2: Relationship between Reynolds number and Strouhal number for a circular cylinder. Taken from Techet [1].

flow properties [7]:

$$KC = \frac{U_w}{f_w D} \tag{2.4}$$

Where

U_w is the Significant wave-induced flow velocity

f_w is the significant wave/oscillating frequency $f_w = 1/T_w$.

2.1.2 Formation of VIV

Sections 2.1.2 and 2.1.3 are based on the book by Sumer and Fredsoe [2].
When bluff bodies are exposed to motions of a fluid such as wave and current, a so-called Karman vortex street can arise on the downstream side of the body. In this section a smooth cylinder in stationary flow is assumed. As mentioned before, vortex shedding starts at a Reynolds number of 40, but vortices arise even earlier from Reynolds numbers of five. First, a fixed pair of small vortices arises simultaneously on both sides of the cross-section. The size of the vortices increases with the Reynolds number. For Reynolds numbers higher than 40, the vortex growth becomes unstable and the wake is sensitive to small perturbations. In addition, the pressure gradient of a circular cross-section changes sign when moving from the stagnation point towards the wake field. As a result, the boundary layer that has

formed over the cylinder surface starts to separate. These two phenomena lead to one vortex growing bigger than the other. This is visualized in Figure 2.3 and

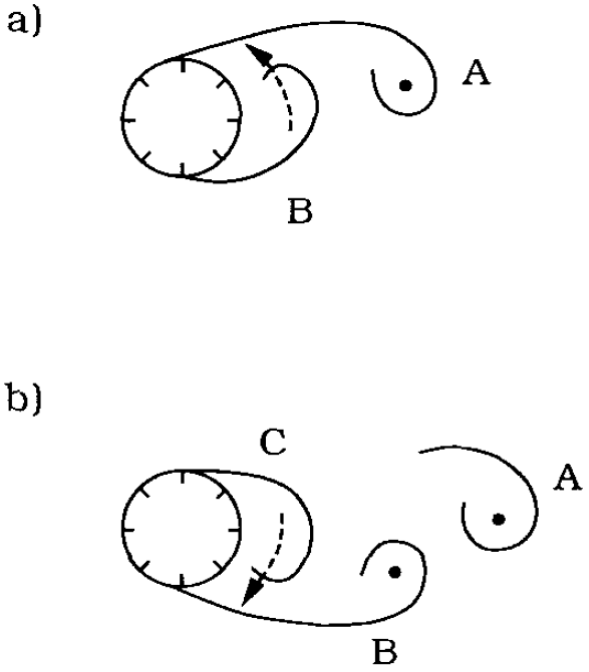

Figure 2.3: Vortex shedding process. Taken from Sumer and Fredsoe [2].

can be described as follows [2]. When vortex A, here rotating clockwise, becomes significantly larger than vortex B, vortex A will be able to draw vortex B across the wake. The counteracting rotation of vortex B will then cause the velocity supply of vortex A to stop. The same process repeats now with vortex B and C, where vortex B is growing bigger and becomes able to draw vortex C across the wake. Thus, the vortex shedding alters from one side to the other. These alternating vortices cause oscillatory forces, which can then induce structural vibrations [1]. The force component in the direction of the flow is called drag, while the one perpendicular to the flow direction is called lift. In dynamic analysis, the forces are commonly expressed as dimensionless coefficients.

$$C_D = \frac{F_x}{\frac{1}{2}\rho D U^2} \quad C_L = \frac{F_y}{\frac{1}{2}\rho D U^2} \tag{2.5}$$

Here,

C_D is the drag coefficient

C_L is the lift coefficient

F_x the in-line force per unit length

F_y the cross-flow force per unit length.

The terms cross-flow and in-line refer to the oscillation direction of the structure with respect to the flow angle. The lift force oscillates at the vortex shedding

frequency, while the drag force oscillates at a frequency twice as large. The frequency of structural vibration is a compromise between the vortex shedding frequency and the eigenfrequency of the relevant mode. When the frequency of structural vibration is equal to the vortex shedding frequency, the structure is said to be 'locked-in'. At this point the largest amplitudes of oscillation occur [1].

$$\text{Vortex shedding frequency} \quad \omega_{vs} = 2\pi f_{vs} = 2\pi \frac{StU}{D} \tag{2.6}$$

$$\text{Natural frequency} \quad \omega_n = \sqrt{\frac{k}{m + m_a}} \tag{2.7}$$

Here,

k is the stiffness

m is the mass and

m_a is the added mass.

Since the added mass depends on the non-dimensional oscillating frequency $\hat{f}_{osc} = f_{osc}D/U$ and the amplitude ratio A/D, the natural frequency of an oscillating body keeps changing [10]. This is important, because resonance can occur over a whole range of frequencies.

2.1.3 In-line vibrations of a circular cylinder

While research has focused on CF VIV for decades, IL VIV and a combination of the two phenomena have lately come more into focus. The vortex shedding frequency of IL VIV is approximately twice as high compared to CF VIV. Thus, IL VIV generally occurs at lower flow velocities. It also indicates that fatigue damage from IL VIV accumulates much faster than fatigue damage from CF VIV. Furthermore, long slender marine structures such as free-spanning pipelines are designed with the aim to avoid CF VIV. Accordingly, flexibly-mounted pipelines mainly experience oscillating drag force arising from IL vortex shedding as a cause for fatigue damage. IL vibrations can be classified into three categories, of which two occur for low-velocity current, while the third one is observed at higher velocities in connection with CF VIV.

First instability region

The so-called first instability region occurs for reduced velocities between one and 2.5. It is the result of two coupled processes. First, normal vortex shedding occurs, which induces two oscillations per shedding. Secondarily, the IL motion of the cylinder relative to the fluid leads to symmetric vortex shedding, as is shown in Figure 2.5. The formation of secondary, symmetric vortex shedding indicates that vibra-

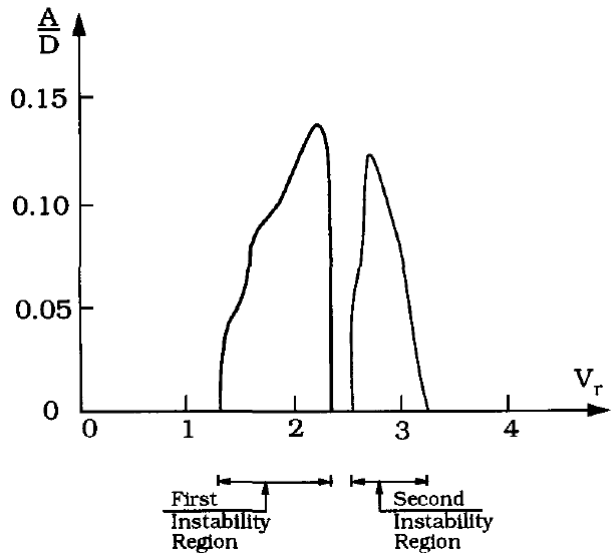

Figure 2.4: First and second instability region of IL VIV for a cylinder with $Re = 6 \times 10^4$. Taken from Sumer and Fredsoe [2].

tions from normal vortex shedding must already exist. In a flow without turbulence or perturbation, the secondary system will not be found. However, if excited, the IL force of the flow occurs to oscillate with a frequency that is approximately three times the Strouhal frequency [2]:

$$\frac{f_x D}{U} = 3St \tag{2.8}$$

where

f_x is the frequency of the oscillating IL force.

Large amplitudes arise if this frequency is close to a natural frequency, where the so-called first lock-in occurs. From Equation 2.8 and with $f_x = f_n$ it can be derived that this occurs at a reduced velocity of 1.7 [2]:

$$V_r = \frac{1}{3St} = \frac{1}{3 \times 0.2} \approx 1.7 \tag{2.9}$$

Second instability region

When the reduced velocity is further increased, the IL-force frequency becomes larger and so does the difference between f_x and f_n. Consequently, the symmetric vortex shedding stops. When only normal vortex shedding is active, the IL-force frequency is approximately twice the Strouhal frequency, which is a lower value than in the first instability region. For further increase of the reduced velocity of the flow, f_x approaches f_n again (second lock-in) which yields large amplitudes. The second instability region is specified for reduces velocities between 2.5 and four due to the

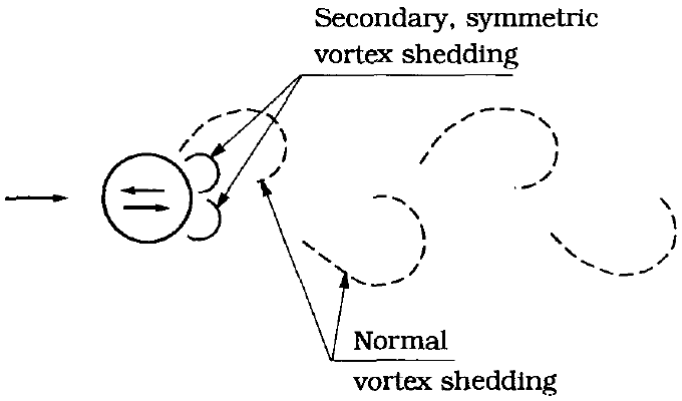

Figure 2.5: Combination of normal vortex shedding and secondary, symmetric vortex shedding, leading to the first instability region. Taken from Sumer and Fredsoe [2].

relation [2]:

$$V_r = \frac{1}{2St} = \frac{1}{2 \times 0.2} = 2.5 \tag{2.10}$$

It must be noted that until here, a constant Strouhal number of 0.2 was assumed, since this is the case for the sub-critical regime, see section 2.1.1. For larger Strouhal numbers, the first and second instability regions occur at lower reduced velocity values, and the graphs should be shifted to the left.
Generally, IL VIV amplitudes in these two regions are significantly smaller than CF VIV amplitudes. This is because IL VIV can be initiated from smaller forces and thus at smaller current velocities. Also, the drag coefficient C_D during IL VIV is smaller than the lift coefficient C_L during CF VIV [2].

Third kind of in-line vibrations

A third kind of IL VIV occurs in a reduced velocity region where CF VIV is usually initiated and far away from a lock-in point. However, much larger IL-motion and IL-force amplitudes compared to the first and second instability regions can be observed here. The IL-force frequency acting on the cylinder is still twice the Strouhal frequency. To initiate IL VIV in the higher reduced velocity region, the following phenomena must arise simultaneously. The cylinder experiences much higher velocities than in the IL region and larger vibration amplitudes in CF direction arise. Together with stronger and more orderly vortex shedding this leads to an increase in the drag force coefficient, which then causes IL VIV. A strong growth of the fluctuating drag coefficient for a cylinder oscillating in CF direction is observed for A/D-ratios greater than 0.2 to 0.3 [2].

2.2 Numerical prediction tools

Numerical prediction tools for VIV have been under development for many years, thus, a large amount of tools is available. They have been divided into the following categories by The Resistance Committee et al. [12].

2.2.1 Computational fluid dynamics

The term CFD covers different discretization methods to simulate the fluid flow, which are usually applied in combination with a finite element model to simulate the response of the structure. The working principle of these methods is to find the fluid forces acting on a body by integration of the fluid pressure and shear stresses, which are coupled with the velocity field formulation. CFD methods solve the Navier-Stokes equation by taking viscosity into account. However, not all available methods account for turbulence. Two popular methods for turbulence modeling are Large Eddy Simulation (LES), which solves a filtered Navier-Stokes equation, and Reynolds-averaged Navier-Stokes (RANS), which solves a time-averaged Navier-Stokes equation.
CFD methods are generally promising for VIV prediction when using 3D models, but they are very time-consuming. Several approaches using 2D models have been developed. They solve the 2D flow at many planes along the riser with the aim of saving computational time. However, 2D models are not commonly applied, since they give less accurate results than semi-empirical models [10].

2.2.2 Wake oscillator models

Models that describe the oscillating forces acting during IL VIV and CF VIV by using distributed Van der Pol wake oscillators are denoted as wake oscillator models [12]. Srinil et al [13] have succeeded in including the effect of initial curvature and time-varying lift and drag forces in a reduced-order model. From comparison with CFD, the results of wake oscillator models are in good agreement. A major problem is to find a set of parameters to solve for both free and forced vibration [12].

2.2.3 Semi-empirical models

Semi-empirical models are commonly applied to predict CF VIV. Two popular tools are VIVANA, developed by Sintef Ocean, and SHEAR7, developed by the MIT. They are based on Morison's equation and utilize databases to determine coefficients for hydrodynamic forces such as added mass, damping and lift forces [14]. The structure is typically modeled with finite element methods. Semi-empirical prediction tools operate in FD, assuming stationary flow and harmonic response

patterns. When using these tools, IL VIV must be treated separately from CF VIV. A commonly applied procedure is to utilize the response model approach from DNVGL-RP-F105 [7] for IL VIV and riser analysis methodology such as above mentioned tools for CF VIV assessment. However, this approach does not hold for flow-variations and structural non-linearity.

2.3 Time domain prediction tool

Since 2012 a TD prediction tool for VIV has been under development at NTNU. The main aim is to achieve precise predictions for non-linear structural-dynamic behavior and time-varying flow. In 2014, the tool was developed for CF VIV of cylindrical slender structures, for which it works with high accuracy in stationary flow [10]. In 2017 an extended version for IL VIV was published. This section is based on the doctoral thesis of Mats J. Thorsen [10], on the paper by Thorsen, Sævik and Larsen [15] and on the paper by Ulveseter, Sævik and Larsen [16].
The most important feature of the TD tool is the ability to synchronize forces with cylinder motion. Synchronization provides the possibility to transfer energy to the cylinder at specific frequencies and motion amplitudes [16]. This also allows the vortex-shedding frequency to lock on to the structure's frequency of oscillation.

Cross-flow model

In the pure CF model, the lift force acting on the cylinder is a function of the CF amplitude-over-diameter (A/D) ratio. A phase angle ($0 < \phi < 2\pi$) is introduced to account for fluctuations of the lift force. Furthermore, it is assumed that the time derivative of the lift force phase is a function of the phase difference between the lift force itself and the induced cylinder velocity [10]. The time derivative of the lift force phase is the lift force frequency.
A new hydrodynamic damping formulation for CF VIV was published by Thorsen, Sævik and Larsen [15]. The damping force is formulated as

$$F_{d,y} = -\frac{1}{2}\rho D C_{d,y} |\dot{y}| \dot{y} \tag{2.11}$$

where

$F_{d,y}$ is the CF damping force

ρ is the fluid density.

The coefficient $C_{d,y}$ is described with a linear function so that the energy loss per cycle is approximately the same as for the model proposed by Vikestad et al. [15].

The total CF fluid force is written as [15]

$$F_y = \frac{1}{2}\rho D U^2 C_v \cos\phi_{\text{exc},y} - \frac{1}{2}\rho D C_{d,y}|\dot{y}|\dot{y} - \rho\frac{\pi D^2}{4}\ddot{y} \tag{2.12}$$

where the first term represents the CF excitation force, the second term represents the damping force and the third term represents the added mass force. However, the total added mass is also partly represented in the first term. The dimensionless coefficient C_v determines the magnitude of the excitation force.

In-line model

In the pure IL model, it is assumed that vortex shedding gives rise to an IL fluctuating component and that the frequency is approximately twice the CF vortex shedding frequency. The vortex shedding frequency is described as a function of the phase difference between cylinder motion and the force itself. Non-zero mean drag due to low pressure in the wake region is not part of the excitation force model [16]. The damping term for IL VIV is formulated with respect to the x-axis where the coefficients C_1 and C_2 are determined so that the dissipated energy per oscillation cycle is approximately the same as for the model proposed by Venugopal [16].

$$F_{d,x}(t) = -\frac{1}{2}\rho D C_1 U\dot{x} - \frac{1}{2}\rho A_x C_2|\dot{x}|\dot{x} \tag{2.13}$$

here,

$F_{d,x}(t)$ is the IL damping force and

A_x is the motion amplitude in IL direction.

As discussed in section 2.1.3 two instability regions occur for pure IL VIV in low-velocity current. Within these two low-velocity regions, the excitation force oscillates with the same frequency as the cylinder velocity, but slightly out of phase with displacement and acceleration. The excitation force acting in the second instability region is given by the equation

$$F_{exc,2} = \frac{1}{2}\rho D U^2 C_{v2}\cos\left(\Phi_{v2}\right) \tag{2.14}$$

where

C_{v2} is a function of the in-line A/D-ratio and

Φ_{v2} is the instantaneous phase of the force [16].

The time derivative of the instantaneous force phase is a function of the instantaneous phase of the velocity minus the instantaneous phase of the force itself [16].

$$\frac{d\Phi_{v2}}{dt} = g_2(\theta_2) \tag{2.15}$$

$$\theta_2 = \Phi_{\dot{x}} - \Phi_{v2} \tag{2.16}$$

The frequency range of synchronization for the second instability region with a peak value of $\widehat{f} = 0.35$ is derived after Aronsen [17] who calculated the excitation force coefficient as a function of the non-dimensional frequency and A/D-ratio.

$$\widehat{f}\,(\theta_2) = \begin{cases} 0.35 + 0.055\sin(\theta_2) & \text{if } -\pi < \theta_2 < 0 \\ 0.35 + 0.035\sin(\theta_2) & \text{if } \pi > \theta_2 > 0 \end{cases} \tag{2.17}$$

Ulveseter et al. reformulated this as a sinusoidal function for the synchronization range, so that the instantaneous frequency of the force can vary with the difference of the instantaneous phase of the velocity and the instantaneous phase of the force itself [16]:

$$\frac{d\Phi_{v2}}{dt}(\theta_2) = \begin{cases} 2\pi\frac{U}{D}(0.35 + 0.055\sin(\theta_2)) & \text{if } -\pi < \theta_2 < 0 \\ 2\pi\frac{U}{D}(0.35 + 0.035\sin(\theta_2)) & \text{if } \pi > \theta_2 > 0 \end{cases} \tag{2.18}$$

The first instability region is described in a similar way to the second one [16]:

$$F_{exc,1} = \frac{1}{2}\rho D U^2 C_{v1}\cos(\Phi_{v1}) \tag{2.19}$$

$$\frac{d\Phi_{v1}}{dt} = g_1(\theta_1) \tag{2.20}$$

$$\theta_1 = \Phi_{\dot{x}} - \Phi_{v1} \tag{2.21}$$

The range of positive excitation is formulated for a peak value of $\widehat{f} = 0.45$ [16].

$$\frac{d\Phi_{v1}}{dt}(\theta_1) = \begin{cases} 2\pi\frac{U}{D}(0.45 + 0.055\sin(\theta_1)) & \text{if } -\pi < \theta_1 < 0 \\ 2\pi\frac{U}{D}(0.45 + 0.275\sin(\theta_1)) & \text{if } \pi > \theta_1 > 0 \end{cases} \tag{2.22}$$

The total pure in-line force for a single degree of freedom system can then be written as [16]:

$$F_x(t) = -\frac{1}{2}\rho D C_1 U\dot{x} - \frac{1}{2}\rho A_x C_2|\dot{x}|\dot{x} + \frac{1}{2}\rho D U^2 C_{v1}\cos\Phi_{v1} + \frac{1}{2}\rho D U^2 C_{v2}\cos\Phi_{v2} - \rho\frac{\pi D^2}{4}\ddot{x} \tag{2.23}$$

where the first two terms represent the linear and the quadratic damping term, the third and fourth term represent the excitation forces of the first and second instability region and the last term represent the force arising from hydrodynamic added

mass. The formulation for only one degree of freedom is applied for low velocity current. The magnitude of the excitation force is determined by the dimensionless coefficients C_{v1} and C_{v2}. Equations 2.12 and 2.23 can be combined with a simple FE model for the structure.

2.4 DNV GL rules and recommended practice

In DNVGL-RP-F105 (2019) [7], design criteria for VIV avoidance and fatigue are proposed together with a response model and a force modal approach for VIV. At present, the empirical response model approach is more detailed compared to the force model approach and therefore is the suggested choice. The recommended practice refers to free spanning pipelines. However, it can also be applied to subsea spools and jumpers under some special considerations.

Free spanning pipelines

For free spanning pipelines, assessment of IL VIV and CF VIV are conducted separately. Eigenvalues and mode shapes are generally obtained from FE-analysis. Modes are divided into dominating, weak and irrelevant modes by so-called mode competition. The dominating mode is the one with largest A/D-ratio or the one that leads to the largest stress, respectively, for CF VIV and IL VIV. Modes that contribute with ten to 100 percent of the magnitude of the dominating mode are identified as weak modes and must be taken into account in the analysis. Modes that contribute with less than ten percent of the magnitude of the dominating mode are identified as irrelevant modes and can be disregarded in the further procedure.

Jumpers, spools, flexible loops and subsea piping

Several exceptions apply when VIV fatigue is calculated for non-straight pipes by the DNVGL-RP-F105 procedure. They are described in Appendix A of DNVGL-RP-F105 (2019) [7]. Modes can no longer be strictly classified as IL or CF VIV modes. They can change their classifications depending on the incoming flow angle and the position of the non-straight parts. If a mode can be both IL and CF mode at the same time, the according flow velocity shall not be reduced with respect to the angle of attack. Mode reductions due to mode competition do not apply. Thus, each contributing mode is handled as the dominating mode and applied with the full stress range. Damage contribution from IL and CF VIV can act on the same hot spots. The damage contribution is thus added for both IL and CF rather than treated separately. Damage must either be calculated conservatively at one critical location, or be calculated for at least 16 points along the circumference of each girth weld.

2.4.1 Response models

The response models in DNVGL-RP-F105 are empirical models to determine the maximum steady-state VIV response. Input parameters are basic hydrodynamic and structural parameters. The models are valid for the following conditions [7]:
- IL VIV in steady current and current dominated conditions
- CF-induced IL motion, which is relevant in all regions where CF VIV occurs
- CF VIV in steady current and combined wave and current conditions
- CF VIV in wave-dominated Keulegan-Carpenter regimes.

The response models depend on the following hydrodynamic parameters [7]:
- reduced velocity, V_r
- Keulegan-Carpenter number, KC
- current flow velocity ratio, α
- turbulence intensity ratio, I_c
- flow angle, relative to the pipe, θ
- stability parameter, K_s.

The current flow velocity ratio is defined as [7]:

$$\alpha = \frac{U_c}{U_c + U_w} \tag{2.24}$$

If no other information is available, the turbulence intensity factor is set to 0.05 according to the guidelines. The stability parameter is calculated from the equation [7]

$$K_s = \frac{4\pi m_e \zeta_T}{\rho_w D^2} \tag{2.25}$$

where
ρ_w is the water density
ζ_T is the total modal damping ratio
m_e is the effective mass, defined as unit mass for the relevant mode.

2.5 Fatigue

If a structure is exposed to cyclic loading over time, it can experience fatigue damage. The load that causes fatigue failure is often far below the yield stress of the material [3]. This is because damage is accumulated cycle by cycle. For marine structures which are generally exposed to dynamic loading, fatigue failure is a common issue. Fatigue damage is categorized into two types [3]:
-high-cycle fatigue with 10^5 to 10^7 cycles where the stress is essentially elastic

-low-cycle fatigue with two to 10^5 cycles where plastic behavior occurs.
Fatigue data is obtained from empirical testing and usually presented in SN-diagrams, where the stress range is plotted over the number of cycles that would lead to failure if constant amplitude loading was applied alone. Such diagrams are available for different environments, geometries and load directions. Also, SN-diagrams are specified for different probabilities of failure. For engineering purposes it is common to use a mean-minus-two-standard-deviations curve. The SN curve is found from regression analysis of test data and lies two standard deviations below the mean regression line. The remaining probability of failure for this design curve is 2.3 percent.

High-cycle fatigue for marine applications

Marine structures are generally in the range of high-cycle fatigue. In this range, the SN-data tends to follow a log-linear relationship, which is described by

$$\log N = \log a - m \times \log S \tag{2.26}$$

where a and m are constants of the mean regression curve. When two standard deviations σ are included in the SN-curve this becomes [3]:

$$\log N = \log \bar{a} - m \times \log S \tag{2.27}$$

$$\log \bar{a} = \log a - 2\sigma_{logN} \tag{2.28}$$

SN-curves for seawater with cathodic protection as given in the guidelines mostly change slope at $1E+06$ cycles. This is because fatigue of welded joints, which are commonly applied in marine engineering, mainly is due to crack growth of initially small cracks. For cyclic loading with constant amplitude a threshold value exists for fatigue crack growth. For stress ranges below this threshold the crack will not grow. For environmental loads, some stress cycles are above this limit and some below, where the ones above the limit contribute to crack growth. As the fatigue limit is gradually lowered, more stress cycles will exceed the limit. The effect of crack-growth on the fatigue limit is represented by an extrapolation of the SN-curve with a slope of $(2m-1)^{-1}$, where m^{-1} is the initial slope of the curve, as shown in Figure 2.6. This model is valid for stationary load histories [3].

Palmgren-Miner hypothesis

To assess the cumulative damage over a certain time, the Palmgren-Miner approach

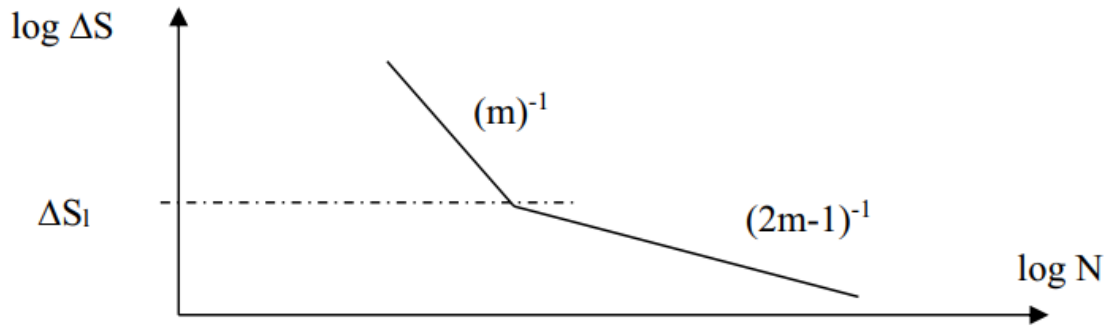

Figure 2.6: SN design curve with Haibach extrapolation beyond the fatigue limit to take into account small cycles. Taken from Ås and Berge [3].

is typically used. Damage D is calculated as the sum

$$D = \sum \frac{n_i}{N_i} \tag{2.29}$$

where n_i is the number of cycles of a given stress range experienced during a defined period and N_i is the number of constant-amplitude cycles which would cause failure for this stress range as found from the SN-curve. Summation is applied over all load cases i. Equation 2.29 is also known as 'Miner sum'. Failure is reached when D is equal to one.

Rainflow counting

In many engineering applications vibrations are assumed to have a time history of stress with Gaussian distribution and zero mean stress. A difference when considering real vibrations is that stress ranges of all magnitudes between zero and a fixed maximum can occur. For broad banded load histories, rainflow counting is a suitable method to calculate stress ranges. It is possible to identify small cycles within a group of larger cycles, independent of variations in the mean stress.
This method is implemented by counting the number of half-cycles in the stress diagram. This is done by identifying the first peak or valley as seen in Figure 2.7. When it reaches the edge, it drips down. The flow is terminated either when it merges with a previous flow or when the absolute value of a subsequent peak or valley is larger. Thus, small variations in the stress diagram are neglected. Finally, the difference between start and end point of each half cycle yields its magnitude. Half cycles of equal or similar magnitude, but opposite sign, are grouped to create a full cycle.

Uni-axial and multi-axial fatigue

Fatigue can be classified based on its stress state as uni-axial or multi-axial fatigue.

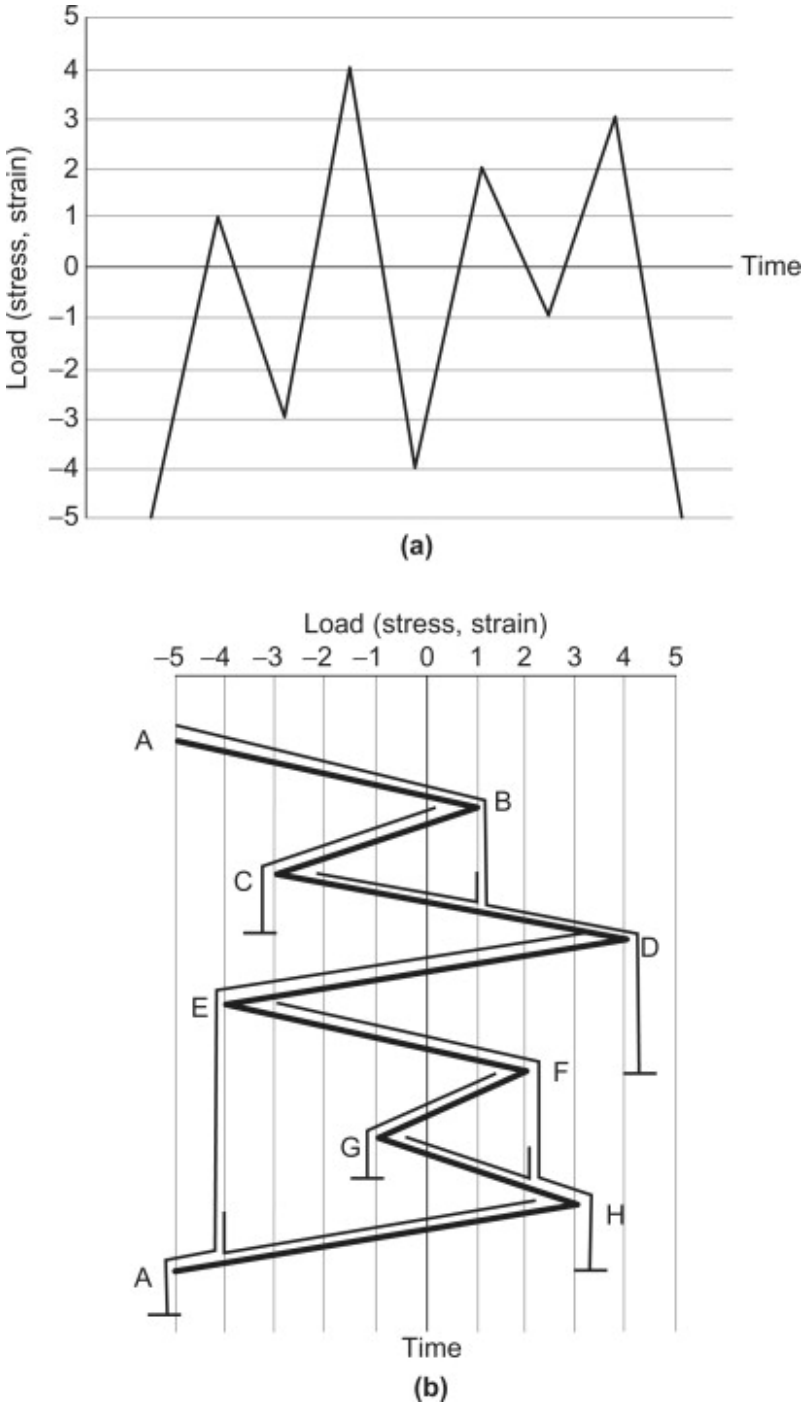

Figure 2.7: Principle of rainflow counting method. Taken from Lee, Barkey and Kang [4].

Stress can be described by six components. Three normal stress components act along the x, y or z-axis, while three shear stress components act in the yz, xz or xy-plane.

When cyclic stress acts in only one principal direction or plane, the stress state and the resulting fatigue damage are uni-axial.

On the contrary, when cyclic stress acts in more than one principal direction or

plane, the stress and its resulting fatigue damage are classified as multi-axial.

2.6 Special case of spools and jumpers

Modeling and investigation of spools and jumpers yields additional challenges compared to straight slender structures. Due to the three-dimensional geometry, the response under VIV is much more complicated to predict. The mode shapes are complex, including in-plane modes, out-of-plane modes and twist modes. For structures with complex geometry, each active mode can act as if it were dominating. This means all modes can apply their full stress range. With traditional methods, an accurate prediction of amplitudes may not be possible [18]. Also, semi-empirical methods that are often developed for risers or straight pipes may not be applicable to jumpers due to the complex flow around the structure.

2.6.1 Pipe bend elements

A typical jumper consists of several vertical and horizontal pipes that are connected by curved elements. Bends lead to decreased stiffness and hence increased stress compared to straight pipes. Unless the in-pipe pressure is very high, these parameters must be taken into account. This can be challenging when generally applying the straight beam theory. Shell models can be used, but the analysis costs can be very high.

For linear analysis, correction factors are commonly applied to estimate the flexibility and stress intensification. Such factors are more complicated to predict for non-linear problems. Another option to deal with the modified stiffness is to implement another pipe element type that allows for ovalization of the cross-section. A simple elbow element has been developed by Klaus-Jürgen Bathe [19], on whose article this section is based. Bathe's elbow elements hold for kinematic non-linearity and elastic-plastic material behaviour and are applicable in static and dynamic analysis. The elements are assumed to distort only in the cross-section plane when being bent, thus, warping is excluded. The ovalization displacement is described by the following equations [19]:

$$w_\xi(r,\phi) = \sum_{k=1}^{4} \left(\underbrace{\sum_{m=1}^{N_c} h_k c_m^k \sin 2m\phi}_{\text{in-plane bending}} + \underbrace{\sum_{m=1}^{N_d} h_k d_m^k \cos 2m\phi}_{\text{out-of-plane bending}} \right) \tag{2.30}$$

$$w_\zeta = -\frac{\mathrm{d}w_\xi}{\mathrm{d}\phi} \tag{2.31}$$

where

h_k are isoparametric interpolation functions

w_ζ and w_ξ are the pipe-skin displacements in the ζ and ξ direction, respectively, and c and d are the unknown generalized ovalization displacements.

Strain terms are applied to the initial configuration of the pipe elements to countenance ovalization. The following strain terms represent the common beam normal and shear strains and the additional ovalization strains [19].

$$\epsilon_{\eta\eta} = \frac{w_\xi \sin\phi + \frac{\mathrm{d}w_z}{\mathrm{d}\phi}\cos\phi}{R - a\cos\phi} - \left[\left(\frac{1}{R - a\cos\phi}\right)^2 \frac{\mathrm{d}^2 w_\zeta}{\mathrm{d}\theta^2}\right]\zeta \tag{2.32}$$

$$\epsilon_{\xi\xi} = -\frac{1}{a^2}\left[w_\zeta + \frac{\mathrm{d}^2 w_\zeta}{\mathrm{d}\phi^2}\right]\zeta \tag{2.33}$$

$$\gamma_{\eta\xi} = \left(\frac{1}{R - a\cos\phi}\right)\frac{\mathrm{d}w_\xi}{\mathrm{d}\theta} \tag{2.34}$$

These formulations are used to determine the strain-displacement matrix. To cover all ovalization modes of these elements 24 integration points are required, while for pure in-plane bending twelve points are suggested. For integration through the thickness of the pipe-skin, three points are usually considered appropriate. Total Lagrangian formulation is applied to make the analysis efficient for large displacements.

From comparison to curved shell elements it is evaluated that the predicted stiffness of elbow elements is slightly larger. However, the results are still in good accordance. The results for longitudinal stresses are similar, but circumference stresses show larger deviations [19]. Based on this element type, a new pipe element was implemented in Simla at NTNU to modify the flexibility of bends for the M-shaped jumper.

2.7 Previous work

Model tests with an M-shaped jumper model were carried out by ExxonMobil with the aim to assess validity of potential VIV prediction approaches [18]. Uniform bottom currents were simulated to achieve reduced velocities that excite the vibration modes of interest. With a scale ratio of 4.525 the model had a total arch length of 13.96m. The lengths of each segment and the model properties are listed in Table 4.1 and 4.2, respectively. In the first phase of the experiment the main question was if VIV occurs as expected at very low velocities under realistic flow conditions.

Tests with a straight cylinder section of one meter were also performed to measure drag forces and evaluate the sensitivity to changes in the Reynolds number. In the second phase static pull tests were performed to excite and identify the first modes. Thirteen tri-axial accelerometers and three strain gauges were installed along the jumper model. The test setting is shown in Figure 2.8. For flow angles of ten and 45 degrees current velocities between 0.05 and 0.98 m/s were tested. For a flow angle of 90 degrees data was measured for current velocities up to 0.79 m/s due to the capacity of the end dynamometers.

The following observations were made when the model was towed with an orientation of 10 degrees to the model plane [18]:

A typical cross-flow VIV response occurred at a towing speed of 0.412m/s, where out-of-plane vibration was observed at a frequency close to the model's out-of-plane natural frequency. This refers to the first mode. In-plane vibration (second mode) occurred at a towing speed of 0.206m/s and close to the model's in-line natural frequency. Out-of-plane twist vibration (third mode) was observed at a towing speed of 0.527m/s and at a frequency close to the jumper's out-of-plane twist vibration natural frequency.

For these three cases the response amplitudes were given for all accelerometers. Further information about VIV responses for a wider range of reduced velocities were available in plots for accelerometers three, five and seven.

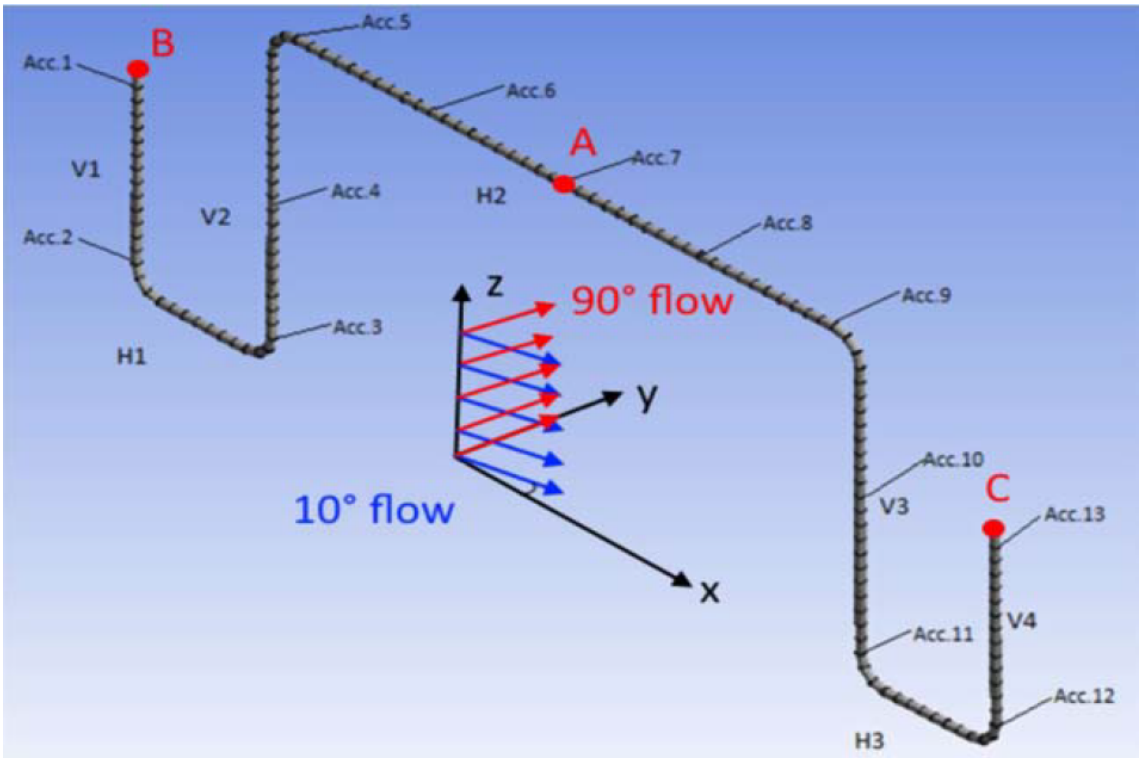

Figure 2.8: Jumper model with locations of accelerometers, strain gauges and pipe segments and the current directions. Taken from Liu et al. [5].

Chapter 3

Methodology

3.1 Simla analysis

Simla is a finite element method (FEM) based program for non-linear static and dynamic analysis developed at NTNU. It is specialized in simulations of pipe and cable structures and operations. Step-by-step time integration is used to describe load histories and analysis sequences. This section is based on the Simla Theory Manual [6].

Static analysis

Static analysis is performed based on the Newton-Raphson method. Equilibrium is found at each load step. More generally, the Newton-Raphson algorithm solves x for the problem f(x)=0 with the equation

$$x_{n+1} = x_n - \frac{f(x_n)}{f'(x_n)} \tag{3.1}$$

where $f'(x_n)$ is the first derivative of f(x) with respect to x at $x = x_n$. This algorithm can be used to find the relation between stress and strain increments. The iterative equation to find the incremental stress-strain relationship can be written as [6]

$$\Delta \mathbf{r}^{\mathbf{i}}_{\mathbf{n+1}} = \mathbf{K}^{-\mathbf{1i}}_{\mathbf{T,n+1}} \Delta \mathbf{R}^{\mathbf{i}}_{\mathbf{n+1}} \tag{3.2}$$

$$\Delta \mathbf{r}_{\mathbf{n+1}} = \mathbf{r}_{\mathbf{n+1}} - \mathbf{r}_{\mathbf{n}} \tag{3.3}$$

$$\Delta \mathbf{R}^{\mathbf{i}}_{\mathbf{n+1}} = \mathbf{R} - \mathbf{R}_{\text{int}} \tag{3.4}$$

where

$\Delta \mathbf{r}$ is the incremental displacement vector

$\mathbf{r}$ is the displacement vector

$\Delta\mathbf{R}$ is the incremental load vector

$\mathbf{R}$ is the total load vector

$\mathbf{R}_{\text{int}}$ is the internal load vector

$\mathbf{K_T^{-1}}$ is the inverse of the tangential stiffness matrix.

Subscript n+1 refers to the next load step and subscript n to the current one. Superscript i denotes the iteration step.

The load increment is given from equilibrium at step one to equilibrium at step two and results in a displacement increment. Stiffness matrix and internal load vector must be updated and iterations repeated until the convergence requirement is met.

Dynamic analysis

Nonlinear problems in dynamic analysis cannot be solved by using modal superposition. Instead, direct time-integration of the equation of motion is applied. This can be done by using either explicit or implicit methods. Explicit methods solve for the displacement at the next time step based on information from the current and previous steps. Implicit methods depend on quantities at the next time step together with information from the current step. Since they solve for the displacement at the next step by using information at this allocated step, implicit methods have higher numerical stability. The dynamic solution in Simla is found using the implicit HHT-α method in a time integration scheme. It solves the following modified equilibrium equation [6]:

$$\mathbf{M\ddot{r}_{k+1}} + (\mathbf{1}+\alpha)\mathbf{C\dot{r}_{k+1}} - \alpha\mathbf{C\dot{r}_k} + (\mathbf{1}+\alpha)\mathbf{R^I_{k+1}} - \alpha\mathbf{R^I_k} = (\mathbf{1}+\alpha)\mathbf{R^E_{k+1}} - \alpha\mathbf{R^E_k} \quad (3.5)$$

$\mathbf{M}$ is the mass matrix

$\mathbf{C}$ is the damping matrix

$\mathbf{R^I}$ is the internal load vector

$\mathbf{R^E}$ is the external load vector

$\mathbf{r}, \dot{\mathbf{r}}, \ddot{\mathbf{r}}$ are the displacement vector, the velocity vector and the acceleration vector, respectively. Subscript k+1 refers to the next time step and k to the current one. The velocity and acceleration at the next time step are found by using the same equations as for the Newmark-β method:

$$\Delta\ddot{\mathbf{r}}_{k+1} = \ddot{\mathbf{r}}_{k+1} - \ddot{\mathbf{r}}_k = \frac{1}{\Delta t^2\beta}\Delta\mathbf{r_{k+1}} - \frac{1}{\Delta t\beta}\dot{\mathbf{r}}_k - \frac{1}{2\beta}\ddot{\mathbf{r}}_k \quad (3.6)$$

$$\Delta\dot{\mathbf{r}}_{k+1} = \dot{\mathbf{r}}_{k+1} - \dot{\mathbf{r}}_k = \frac{\gamma}{\Delta t\beta}\Delta\mathbf{r}_{k+1} - \frac{\gamma}{\beta}\dot{\mathbf{r}}_k - \Delta t\left(\frac{\gamma}{2\beta} - 1\right)\ddot{\mathbf{r}}_k \quad (3.7)$$

Δt is the increase in time and α, β and γ are parameters of the HHT-α method. If α is set equal to zero, the method coincides with the Newmark-β family.

Since time integration does not generally lead to fulfillment of the equilibrium equation (Equation 3.5), iterations are necessary before the next time step. The iteration procedure can be formulated by a Newton-Raphson scheme [6] as:

$$\hat{\mathbf{K}}_k^i \delta \mathbf{r}_{\mathbf{k+1}}^{\mathbf{i+1}} = (\mathbf{1}+\alpha)\left[\mathbf{R}_{\mathbf{k+1}}^{\mathbf{E}} - \mathbf{R}_{\mathbf{k+1}}^{\mathbf{I,i}} - \mathbf{C}\dot{\mathbf{r}}_{\mathbf{k+1}}^{\mathbf{i}}\right] - \mathbf{M}\ddot{\mathbf{r}}_{\mathbf{k+1}}^{\mathbf{i}} - \alpha\left(\mathbf{R}_{\mathbf{k}}^{\mathbf{E}} - \mathbf{R}_{\mathbf{k}}^{\mathbf{I}} - \mathbf{C}\dot{\mathbf{r}}_{\mathbf{k}}^{\mathbf{i}}\right) \quad (3.8)$$

$\hat{\mathbf{K}}$ is the effective stiffness matrix, calculated from below equation.

$$\hat{\mathbf{K}}_k = a_0\mathbf{M} + \mathbf{c}_0\mathbf{C} + \mathbf{b}_0\mathbf{K}_{\mathbf{T,k}} \quad (3.9)$$

$\mathbf{K_T}$ is the tangential stiffness matrix that should be updated at each iteration cycle to improve the convergence rate. The parameters a_0, b_0 and c_0 are determined as follows [6]:

$$\begin{aligned} a_0 &= \frac{1}{\Delta t^2\beta} + (1+\alpha)\frac{\alpha_1\gamma}{\Delta t\beta} \\ c_0 &= (1+\alpha)\frac{\gamma}{\Delta t\beta} \\ b_0 &= (1+\alpha)\frac{\alpha_2\gamma}{\Delta t\beta} \end{aligned} \quad (3.10)$$

The right-hand side of Equation 3.8 represents the unbalance in inertia, damping and internal forces and vanishes when equilibrium is obtained.
In dynamic analysis, high-frequency modes are not usually of interest, while lower modes are described with high accuracy. An advantage of the HHT-α method is that it damps out high frequencies without losing second order accuracy [6].

Element loads, mass and damping

Mass matrices can be lumped or consistent in Simla. Both lumped damping and Raleigh damping are applied on element level. Hydrodynamic loads are established by the following form of the Morison equation [6]:

$$\rho\frac{\pi}{4}D^2C_{m,t}\ddot{u}_y = \frac{1}{2}\rho C_{d,t}\sqrt{(\dot{w}_x-\dot{u}_x)^2}\,(\dot{w}_x-\dot{u}_x) \quad (3.11)$$

$$\rho\frac{\pi}{4}D^2\left(C_{m,n}-1\right)\ddot{u}_y = \rho\frac{\pi}{4}D^2\ddot{w}_y + \frac{1}{2}\rho C_{d,n}\sqrt{(\dot{w}_y-\dot{u}_y)^2+(\dot{w}_z-\dot{u}_z)^2}\,(\dot{w}_y-\dot{u}_y) \quad (3.12)$$

$$\rho\frac{\pi}{4}D^2\left(C_{m,n}-1\right)\ddot{u}_z = \rho\frac{\pi}{4}D^2\ddot{w}_z + \frac{1}{2}\rho C_{d,n}\sqrt{(\dot{w}_y-\dot{u}_y)^2+(\dot{w}_z-\dot{u}_z)^2}\,(\dot{w}_z-\dot{u}_z) \quad (3.13)$$

where

$C_{m,t}$ is the tangential added mass coefficient

$C_{m,n}$ is the normal added mass coefficient

$C_{d,t}$ is the tangential drag coefficient

$C_{d,n}$ is the normal drag coefficient

$u_x - u_z$ describe the body displacements

$w_x - w_z$ describe the fluid particle displacement in the respective degree of freedom.

3.1.1 Pipe formulation

This section is based on the Simla Theory Manual [6] and the paper about elbow-elements by Bathe [19]. Pipe elements in Simla are formulated as two-node beam elements with twelve regular degrees of freedom (DOF). The orientation and motion is referred to a global coordinate system. For torsion rotation and axial displacement linear interpolation is applied, while cubic interpolation is used for transverse directions. The same interpolations are used to establish the mass matrix.

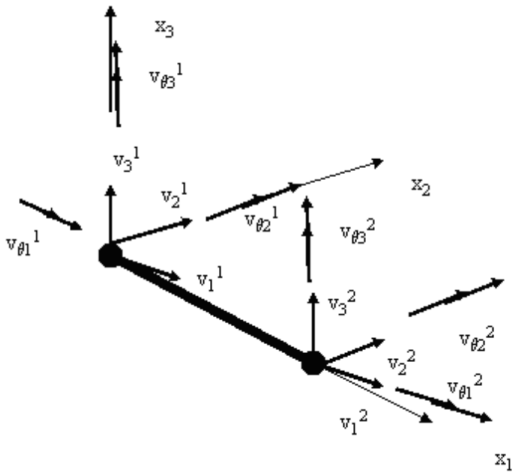

Figure 3.1: Dof of pipe element. Taken from Sævik [6].

Pipe31 is an elastic pipe element, for which plane stress is assumed. All DOF are uncoupled from hoop stresses and hoop strains, since they are known from shell theory.

Pipe34 is a bend element type implemented with reference to Bathe [19] and as described in section 2.6.1. It is able to account for deformation of the cross-section and kinematic non-linearity. For the jumper model, deformation of the cross-section is a result from bending an initially straight pipe during manufacturing. In contrast to Bathe's bend elements, Pipe34 is only linear-elastic. The ovalization of an initially circular cross-section is included in the strain terms in Equations 2.32 to 2.34. Six

ovalization DOF are introduced in addition to the twelve regular DOF. For thin-walled pipes, 48 additional integration points are used around the circumference, while no additional integration points through the thickness are required for D/t-ratios between 15 and 45. The model which includes Pipe34 elements is expected to have lower stiffness in the bend parts.

3.1.2 Eigenvalue analysis

Eigenvalues and their associated frequencies are found from solving the general eigenvalue problem [20]

$$\left(\mathbf{M}_0 - \omega_i^2 \mathbf{K}_0\right) \Phi_i = 0 \tag{3.14}$$

where Φ_i is the eigenvector of mode i and ω_i is the associated circular frequency. The mass matrix M_0 includes added mass, for which the added mass coefficient for still-water conditions is specified in the input file. The eigenvalue λ of mode i has the following relation to the circular frequency:

$$\lambda_i = \omega_i^2 \tag{3.15}$$

In Simla, the required number of eigenvalues, starting with the smallest one, is found from a Lanczos solver. The natural frequencies are obtained from the eigenvalue calculations with the following relation.

$$f_{n,i} = \frac{\sqrt{\lambda_i}}{2\pi} \tag{3.16}$$

The number of relevant modes for this study was based on the maximum oscillation frequency that occurred during VIV simulations.

3.1.3 Modal stresses

Information about axial strain, torsion and the curvature in both transverse directions could be extracted from the output file from eigenvalue analysis for each mode shape. Data was given for each element in its local coordinate system and scaled with respect to the maximum modal displacement equal to one. To obtain unit stresses, the information had to be multiplied with the outer diameter. According to the guidelines, total flexural stress was calculated at 16 points around the circumference with the equation

$$\sigma_{xx} = -\kappa_y ER\cos\theta_i + \kappa_z ER\sin\theta_i \tag{3.17}$$

where the curvature κ was scaled with the outer diameter before and E is the Young's modulus. In this and all following equations the radius R denotes the outer radius. The angle θ_i was specified for 16 points around the circumference. The local coordinate system is also shown in Figure 3.2. The maximum principal stress was then found with the equation:

$$\sigma_1 = \frac{\sigma_{xx}}{2} + \sqrt{\left(\frac{\sigma_{xx}}{2}\right)^2 + \tau_{xy}^2} \tag{3.18}$$

It is defined as the stress at a direction where only normal stress is acting and the shear stress is zero. The stress state of a 2D element is illustrated in Figure 3.3. The shear stress about the longitudinal pipe axis was calculated as

$$\tau_{xy} = \varphi_{,x} GR \tag{3.19}$$

where the torsion $\varphi_{,x}$ was given in radians per meter and scaled with the outer diameter before and G taken as the shear modulus.

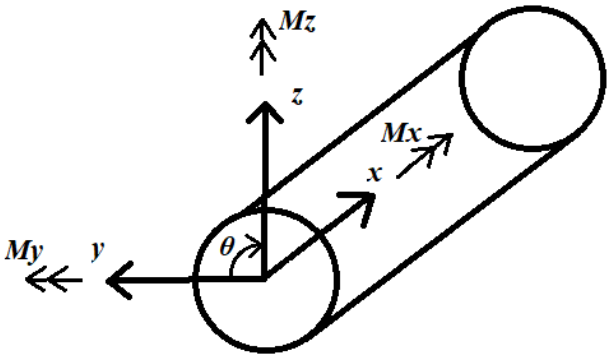

Figure 3.2: Local coordinate system and bending moment definition for pipe element

3.1.4 TD VIV simulation

Both CF VIV and IL VIV can be analyzed in the same tool in Simla. The program applies additional vortex-shedding terms to the Morison equation together with the synchronization model as was described in section 2.3.
For CF VIV hydrodynamic forces normal to the cylinder are calculated with Morison's equation and the additional vortex shedding term acts perpendicular to the normal component of the relative velocity [21].

$$\mathbf{F}_n = C_M \rho \frac{\pi D^2}{4} \dot{\mathbf{u}}_n - (C_M - 1)\, \rho \frac{\pi D^2}{4} \ddot{\mathbf{x}}_n + \frac{1}{2} \rho D C_D \left|\mathbf{v}_n\right| \mathbf{v}_n + \frac{1}{2} \rho D C_{vc} \left|\mathbf{v}_n\right| \left(\mathbf{j}_3 \times \mathbf{v}_n\right) \cos \phi_{\text{exc}} \tag{3.20}$$

C_M is the inertia coefficient from the Morison equation

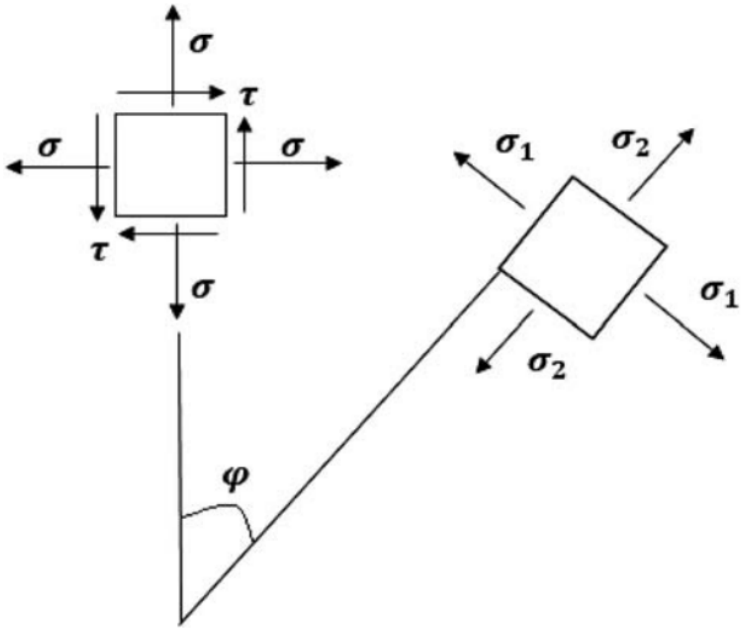

Figure 3.3: Stress state of a 2D element. Taken from Liu et al. [5].

C_D is the drag coefficient from the Morison equation

C_{vc} is a coefficient representing the magnitude of the CF vortex shedding force

$\dot{\mathbf{u}}_n$ is the fluid particle acceleration normal to the cylinder

$\ddot{\mathbf{x}}_n$ is the cylinder acceleration normal to the cylinder

$\mathbf{v}_n$ is the relative flow velocity normal to the cylinder, found as $\mathbf{v} = \dot{\mathbf{u}} - \dot{\mathbf{x}}$.

The instantaneous phase ϕ_{exc} is linked to the dimensionless excitation frequency [21],

$$\frac{d\phi_{\text{exc}}}{dt} = 2\pi f_{\text{exc}} = \frac{2\pi \left|\mathbf{v}_n\right|}{D} \hat{f}_{\text{exc}} \tag{3.21}$$

where the synchronization model comes into place.

For pure IL VIV hydrodynamic forces are calculated from the Morison equation, including two potential vortex shedding force terms [21].

$$\begin{aligned} \mathbf{F}_n =& C_M \rho \frac{\pi D^2}{4} \dot{\mathbf{u}}_n - \left(C_M - 1\right) \rho \frac{\pi D^2}{4} \ddot{\mathbf{x}}_n + \frac{1}{2} \rho D C_D \left|\mathbf{v}_n\right| \mathbf{v}_n + \\ & \frac{1}{2} \rho D C_{vi1} \left|\mathbf{v}_n\right| \mathbf{v}_n \cos\phi_{\text{exi},1} + \frac{1}{2} \rho D C_{vi2} \left|\mathbf{v}_n\right| \mathbf{v}_n \cos\phi_{\text{exi},2} \end{aligned} \tag{3.22}$$

C_{vi1} is a dimensionless coefficient representing the magnitude of the IL vortex shedding force for the first instability region

C_{vi2} is a dimensionless coefficient representing the magnitude of the IL vortex shedding force for the second instability region

$\phi_{\text{exi},1}$ is the instantaneous phase of the first vortex shedding force (referred to as region one in literature)

$\phi_{\text{exi,2}}$ is the instantaneous phase of the second vortex shedding force (referred to as region two).

Other parameters have the same definition as in Equation 3.20. Synchronization works in a similar way to CF VIV. The first time derivative of the instantaneous phase is linked to the phase difference between structural velocity in relative IL direction and the force itself [21].

$$\frac{d\phi_{\text{exi,j}}}{dt} = 2\pi f_{\text{exi,j}} = \frac{2\pi \left|\mathbf{v}_n\right|}{D} \hat{f}_{\text{exi,j}} \tag{3.23}$$

The decision to switch between CF or IL forces is made based on comparison of the CF and IL amplitudes. A synchronization model for CF-induced IL VIV is also included. The applied synchronization model follows the equation [21]

$$\frac{d\phi_{\text{exi}}}{dt} = 2\frac{d\phi_{\text{exc}}}{dt}\left[1 + \alpha \sin\left(\phi_{\dot{x}_{\text{rel}}} - \phi_{\text{exi}}\right)\right] \tag{3.24}$$

where α is a CF-induced IL force synchronization parameter. The procedure is described in more detail in the Simla user manual.

Furthermore, several parameters can be manipulated to control which VIV models are activated for certain reduced velocity ranges.

To obtain the best fit with the model test data, a parameter study was conducted on the Pipe31 model. Several parameters that can influence the VIV tool were varied and the results plotted over reduced velocities. Later, the parameters that gave the best fit were also applied on the Pipe34 model. The main reason to use the Pipe31 model for the study was time-efficiency, since the Pipe34 element type required much more computational time. The parameters are described in the input section 4.2.1.

Mode identification

To compare results from the VIV prediction tool with experimental data, non-dimensional response amplitudes were plotted against reduced velocities. Reduced velocities were defined in Equation 2.3 and depend on the flow velocity, the outer diameter and the natural frequency of the active mode. To find the active mode for each load case, Fast Fourier Transformation (FTT) was applied to transfer the TD signal into FD. From the location of the peak value, the oscillating frequency was found. The active mode was then identified as the one with its natural frequency closest to the structure's oscillating frequency.

3.1.5 Stresses from VIV analysis

In the TD VIV prediction tool, forces and moments in all DOF can be obtained directly. This has the advantage that no mode identification and combination of modal stresses is needed and uncertainties are limited. Moments around the x, y and z-axis were output for each sea state. They are given in the local coordinate system for each element. To reduce computational time, the output was specified for elements at critical locations. These are the jumper ends, the center point of the top horizontal, and the bends. Since welds are not placed in the bends, but close to it, the elements next to the bend at the longer of two adjacent straight parts were chosen. As for modal stresses, the flexural stresses were evaluated at 16 points around the jumper circumference.

Especially for larger current velocities, the stresses were fluctuating around a non-zero mean. This was due to a constant displacement of certain jumper parts, usually in flow-direction. Since constant stresses are not considered in fatigue calculations and they were not induced by VIV, the stresses were scaled so that zero mean stresses were obtained for all load cases.

Flexural stress was found from the moments around the y and z-axis.

$$\sigma_{xx} = -\frac{M_{\mathrm{y}}}{I_{\mathrm{y}}} R \sin\theta_i + \frac{M_{\mathrm{z}}}{I_{\mathrm{z}}} R \cos\theta_i \tag{3.25}$$

The area moments of inertia, I_y and I_z, are calculated with the equation for thin-walled circular cross-sections.

$$I_{\mathrm{y}} = I_{\mathrm{z}} = \pi R^3 t \tag{3.26}$$

The shear stress is constant around the circumference of each pipe section and calculated with the equation

$$\tau_{xy} = \frac{M_{\mathrm{x}}}{I_{\mathrm{x}}} R \tag{3.27}$$

where the polar moment of inertia I_x equals $2\pi R^3 t$. From the two stress signals, the maximum principal stress was calculated with Equation 3.18 at each time step. To the best of knowledge, the first principal stress criterion gives conservative results, since the maximum stress is assumed to contribute to crack-opening regardless of the real stress direction. When calculated at each time step, shifts between flexural and torsional stress cycles should also be taken care of. The direction of principal stress is a measure for how much torsional stress contributes to the total stress state. According to the coordinate transformation shown in Figure 3.3, the principal stress

direction was found from the following equation.

$$\theta_{\sigma_1} = \frac{1}{2} \times \arctan\left(\frac{2\tau_{xy}}{\sigma_{xx}}\right) \tag{3.28}$$

However, both signals were also observed individually for fatigue assessment.

3.1.6 Fatigue damage

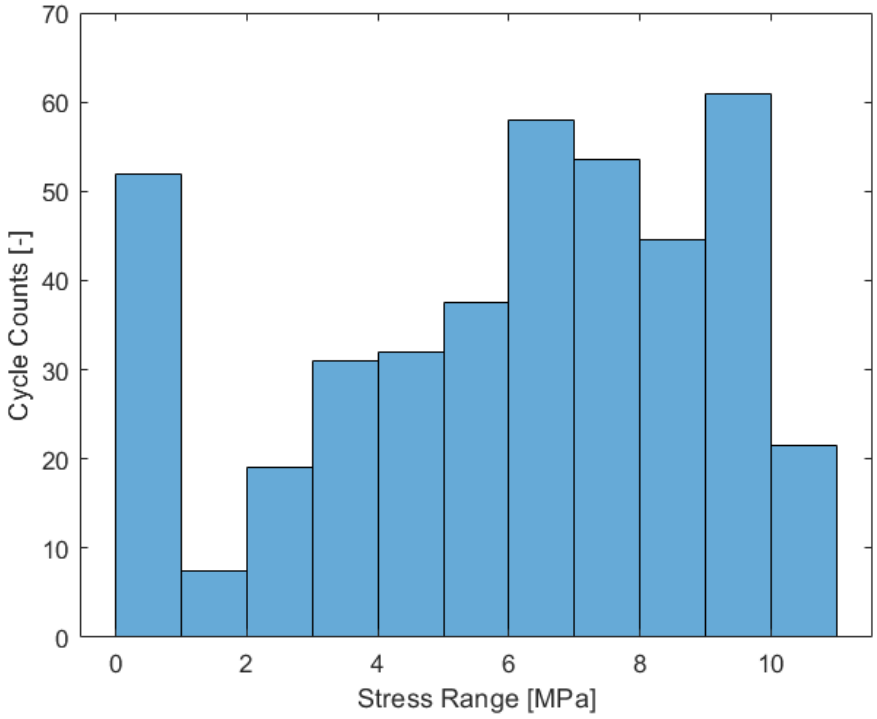

Figure 3.4: Example of a stress histogram obtained as output from rainflow counting.

To transform the signal of oscillating stresses into a set of stress reversals with constant amplitudes a rainflow counting algorithm was used. The basic principle was explained in section 2.5.
For each load case, a set of stress ranges ΔS_i with the corresponding number of cycles n_i during an observed time period were output. Obtained data can be illustrated in a stress histogram as shown in Figure 3.4. To enter the SN-curve and calculate damage from the Miner sum, an equivalent stress range was required. The concept is to find a constant amplitude stress range ΔS_{eq} that represents the combined effect of all stress ranges in a real load history. This was found by the direct summation method with the equation [3]

$$\Delta S_{\text{eq}} = \left[\frac{\Sigma_i n_i \left(\Delta S_i\right)^m}{\Sigma_i n_i}\right]^{\frac{1}{m}} \tag{3.29}$$

where

n_i is the number of cycles for one block in the histogram

ΔS_i is the stress range of the corresponding block

m is a constant of applied SN-curve.

Fatigue was calculated and compared for each load case under the assumption that it is present over one year with a probability of occurrence of 100 percent. Consequently, the number of cycles was adjusted. The SN-curve was entered with the equivalent stress range and the number of cycles that would lead to failure was obtained. By comparing this number with the amount of cycles per year obtained from rainflow counting, fatigue damage could be calculated with the Miner sum, as was explained in section 2.5. First, the procedure was applied on the flexural stress and the torsional stress signals separately to observe the significance of torsional stress. Later, the first principal stress was calculated at each time step and rainflow counting was applied to the new signal. It is assumed that phase shifts between torsional and flexural stress are taken care of in the rainflow algorithm, since they are represented in the combined stress signal.

3.2 Abaqus analysis

Abaqus/CAE is a set of finite element analysis (FEA) applications from SIMULIA™by Dessault Systèmes®. In this study, Abaqus/Standard was used, where several commands from Abaqus/Aqua were implemented in the input file. Abaqus/Standard can be used for linear and non-linear static and dynamic analysis. With Abaqus/Aqua sea loads, waves and winds can be added. This was used to include coefficients for added mass and drag in the eigenvalue analysis.

3.2.1 Element formulation

This section is based on the Abaqus documentation version 6.13 [22]. Pipe31 elements in Abaqus are linear two-node beam element with six DOF at each node. They are Timoshenko beams which allow for transverse shear deformation. Linear interpolation functions are used for displacements and rotations. Plane stress theory is applied for both pipe elements and elbow elements. Hoop stresses and hoop strains are not considered for standard pipe elements. They can, however, be considered when elbow elements are used.

The purpose of elbow elements is to obtain accurate results for initially circular pipes with distorted cross-section from bending during manufacture. They are applied for non-linear problems, when it is not sufficient to use flexibility factors to

correct results obtained from beam theory. Elbow elements in Abaqus appear like beam elements, but are actually shell type elements, which allows for complex deformation patterns. Because of the shell formulation, the number of possible DOF per element is large. Accordingly, the number of integration points through the thickness, the number of integration points around the pipe and the number of Fourier modes should be specified in the input file. For an Elbow31 element this means that linear interpolation is applied along its length, together with Fourier interpolation around the pipe and shell theory to model the behavior. Without a given number of Fourier modes, the elements become simple pipe elements with hoop stress and hoop strain included. In the Abaqus documentation 18 integration points around the pipe and six Fourier modes are suggested for thin-walled pipes [22]. Different elbow element types can be selected in Abaqus. For two-node elements, Elbow31 is the most complete one. In these elements, ovalization of the cross-section is continuous from one element to another and warping is included.
Elbow31B are simplified elements without warping and for which ovalization is discontinuous between elements. Since warping is excluded, they are most similar to Pipe34 elements in Simla.

3.2.2 Eigenvalue analysis

In this study, Abaqus was used to verify the results from modal analysis, in especially with respect to the bend element types. Thus, the analysis procedure was kept similar to that in Simla. Abaqus/Standard uses a set of implicit solvers for static problems. For eigenvalue analysis a Lanczos solver was chosen.

3.2.3 Modal stresses

Various stress components can be specified for the Abaqus output. Since they are commonly applied for fatigue analysis, maximum principal stresses were also output here. They were defined in Equation 3.18 in the section about Simla analysis. A more general form for first principal unit stress is

$$\sigma_1 = \frac{\sigma_{\text{flexural}} + \sigma_{\text{hoop}}}{2} + \sqrt{\left(\frac{\sigma_{\text{flexural}} - \sigma_{\text{hoop}}}{2}\right)^2 + \tau_{\text{shear}}^2} \tag{3.30}$$

where σ_{flexural} is bending stress and τ_{shear} is torsional stress. Hoop stresses, denoted as σ_{hoop} were neglected in this study. This also led to a zero-mean stress level.
To obtain unit stresses, the output stresses were multiplied with

$$\frac{D_{\text{out}}}{\max(\text{w}_i)} \tag{3.31}$$

where w_i is the displacement or rotation given for each of the six DOF.

3.3 DNV GL resonse model procedure

Empirical response models as proposed in DNVGL-RP-F105 (2019) [7] were used to assess the response amplitudes for IL VIV and CF VIV. Based on the response amplitude and the modal stresses obtained from FEA, combined stress ranges for CF VIV and IL VIV including CF-induced IL VIV could be calculated.
This section is based on the recommended practice DNVGL-RP-F105.

3.3.1 Response models

For each flow angle the amplitude response curves were developed by a set of parametric equations. They are plotted as non-dimensional response over reduced velocities. The basic generation principle for the CF and IL response curves are shown in Figure 3.5 and 3.6, respectively. It should be noted that the coordinate system is different from the one used in Simla. Especially, the guideline uses index y for IL direction and index z for CF direction.

CF VIV response

For CF VIV the amplitude response A_z/D was calculated as a function of the wave-current flow ratio α and the KC number. $\Psi_{\text{proxi,onset}}$ and $\Psi_{\text{trench,onset}}$ are reduction factors for onset CF due to seabed proximity and due to the effect of a trench, respectively. f_{ratio} is the minimum ratio between natural frequencies of two consecutive CF modes.

$$V_{R,\text{ onset}}^{CF} = \frac{3 \cdot \Psi_{\text{proxi,onset}} \cdot \Psi_{\text{trench,onset}}}{\gamma_{\text{on },CF}} \tag{3.32}$$

$$V_{R,1}^{CF} = 7 - \frac{\left(7 - v_{R,\text{ onset}}^{CF}\right)}{1.15} \cdot \left(1.3 - \frac{A_{z,1}}{D}\right) \tag{3.33}$$

$$V_{R,2}^{CF} = V_{R,\text{ end}}^{CF} - \left(\frac{7}{1.3}\right) \cdot \left(\frac{A_{z,1}}{D}\right) \tag{3.34}$$

$$V_{R,\text{ end}}^{CF} = 16 \tag{3.35}$$

$$\left(\frac{A_{Z,1}}{D}\right) = \begin{cases} 0.9 & \alpha > 0.8 & f_{\text{ratio}} < 1.5 \\ 0.9 + 0.5 \cdot (f_{\text{ratio}} - 1.5) & \alpha > 0.8 & 1.5 \leq f_{\text{ratio}} \leq 2.3 \\ 1.3 & \alpha > 0.8 & f_{\text{ratio}} < 2.3 \\ 0.9 & \alpha \leq 0.8 & 30 \leq KC \leq 40 \\ 0.7 + 0.01(KC - 10) & \alpha \leq 0.8 & 10 \leq KC \leq 30 \\ 0.7 & \alpha \leq 0.8 & KC < 10 \end{cases} \tag{3.36}$$

$$\left(\frac{A_{Z,2}}{D}\right) = \left(\frac{A_{Z,1}}{D}\right) \tag{3.37}$$

It should be pointed out that for pure current conditions the maximum amplitude of the CF response curve depends on the ratio of natural frequencies for the first three CF modes. These are taken from FEA.

IL VIV response

In current dominated conditions, IL VIV is associated with either alternating or symmetric vortex shedding. The IL response model includes contributions from the first and the second instability region. Parametric equations for the response curve are given below.

$$V_{R,\text{ onset}}^{IL} = \begin{cases} \frac{1}{\gamma_{\text{on,IL}}} & \text{for} \quad K_{sd} < 0.4 \\ \frac{0.6+K_{\text{sd}}}{\gamma_{\text{on,IL}}} & \text{for} \quad 0.4 \leq K_{sd} < 1.6 \\ \frac{2.2}{\gamma_{\text{on,IL}}} & \text{for} \quad K_{sd} \geq 1.6 \end{cases} \tag{3.38}$$

$$V_{R,1}^{IL} = 10 \cdot \frac{A_{y,1}}{D} + V_{R,\text{onset}}^{IL} \tag{3.39}$$

$$V_{R,2}^{IL} = V_{R,\text{end}}^{IL} - 2 \cdot \frac{A_{y,2}}{D} \tag{3.40}$$

$$V_{R,\text{end}}^{IL} = \begin{cases} 4.5 - 0.8K_{sd} & \text{for} \quad K_{sd} < 1.0 \\ 3.7 & \text{for} \quad K_{sd} \geq 1.0 \end{cases} \tag{3.41}$$

$$\frac{A_{y,1}}{D} = \max\left(0.18\left(1 - \frac{K_{sd}}{1.2}\right) \cdot R_{I\theta,1}; \frac{A_{y,2}}{D}\right) \tag{3.42}$$

$$\frac{A_{y,2}}{D} = 0.13\left(1 - \frac{K_{sd}}{1.8}\right) \cdot R_{I\theta,2} \tag{3.43}$$

Here, the amplitude response A_y/D is a function of the design stability parameter K_{sd} and of the reduction factors $R_{I\theta,1}$ and $R_{I\theta,2}$ that account for the effect of turbu-

lence intensity and for the angle of attack. The design stability parameter includes the stability parameter, as was defined in equation 2.25, and a safety factor. The reduction factors are calculated as

$$R_{I\theta,1} = 1 - \pi^2 \left(\frac{\pi}{2} - \sqrt{2} \cdot \theta_{rel} \right) (I_c - 0.03) \quad 0 \leq R_{I\theta,1} \leq 1 \tag{3.44}$$

$$R_{I\theta,2} = 1.0 - \frac{(I_c - 0.03)}{0.17} \quad 0 \leq R_{I\theta,2} \leq 1 \tag{3.45}$$

with the turbulence intensity factor I_c and the relative flow angle θ_{rel}.

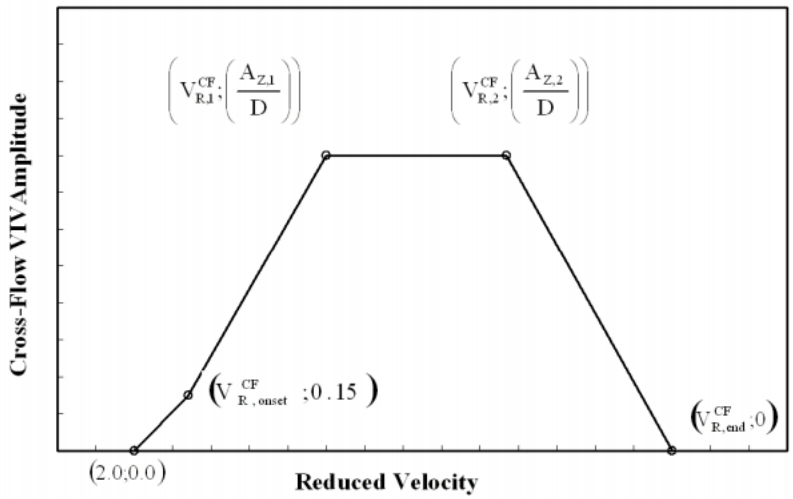

Figure 3.5: Generation principle for CF response curve. Taken from DNVGL-RP-F105 [7]

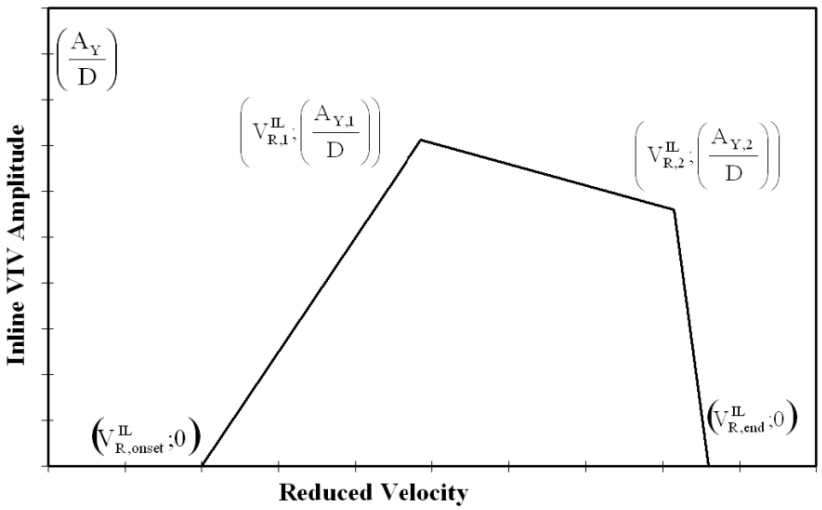

Figure 3.6: Generation principle for IL response curve. Taken from DNVGL-RP-F105 [7]

3.3.2 Stresses from VIV response models

In the DNV GL response model procedure, stresses arising from VIV are calculated from modal stresses, found from FEA, and the response model curves. Modal stresses were calculated for all relevant modes. Whether a mode is active and applies its stress range depends on the reduced velocity of each mode at a given current velocity and the associated response model curve. As mentioned above, all active modes are dominating modes for non-straight pipelines. Thus, only the procedure for dominating modes is covered in this section.

Stresses from CF VIV

The CF VIV-induced stress range is found from the equation

$$S_{CF,i}(x) = 2 \times A_{CF,i}(x) \times \left(\frac{A_z}{D}\right)_i \times R_k \times \gamma_s \tag{3.46}$$

where

$A_{CF,i}(x)$ is the unit diameter amplitude stress of CF-mode i at location x along the jumper

$\left(\frac{A_z}{D}\right)_i$ is the normalized response amplitude according to the CF response model

R_k is a reduction factor to cover the effect of damping

γ_s is the safety factor on stress amplitudes.

For a given sea state, the combined stress range from all active modes is calculated from the equation

$$S_{comb,CF}(x) = \sqrt{\sum_{j=1}^{m} \left(S_{CF,j}(x)\right)^2} \tag{3.47}$$

where m is the number of active CF modes.

To find the correct cycle-counting frequency for CF VIV, a correction of the added mass coefficient is required. This is due to variations of added mass when the structure oscillates. The corrected added mass coefficient $C_{a,CF-RES}$ is taken from Figure 3.7 from the guidelines and applied to correct the CF response frequency $f_{CF-RES,j}$ with the equation

$$f_{CF-RES,j} = f_{CF,j}\sqrt{\frac{s_g + C_a}{s_g + C_{a,CF-RES}}} \tag{3.48}$$

where

$f_{CF,j}$ is the CF response frequency without correction

s_g is the specific gravity of the pipe, calculated as $(q + b)/b$, where q is the submerged weight and b is the buoyancy

C_a is the still-water added mass coefficient and

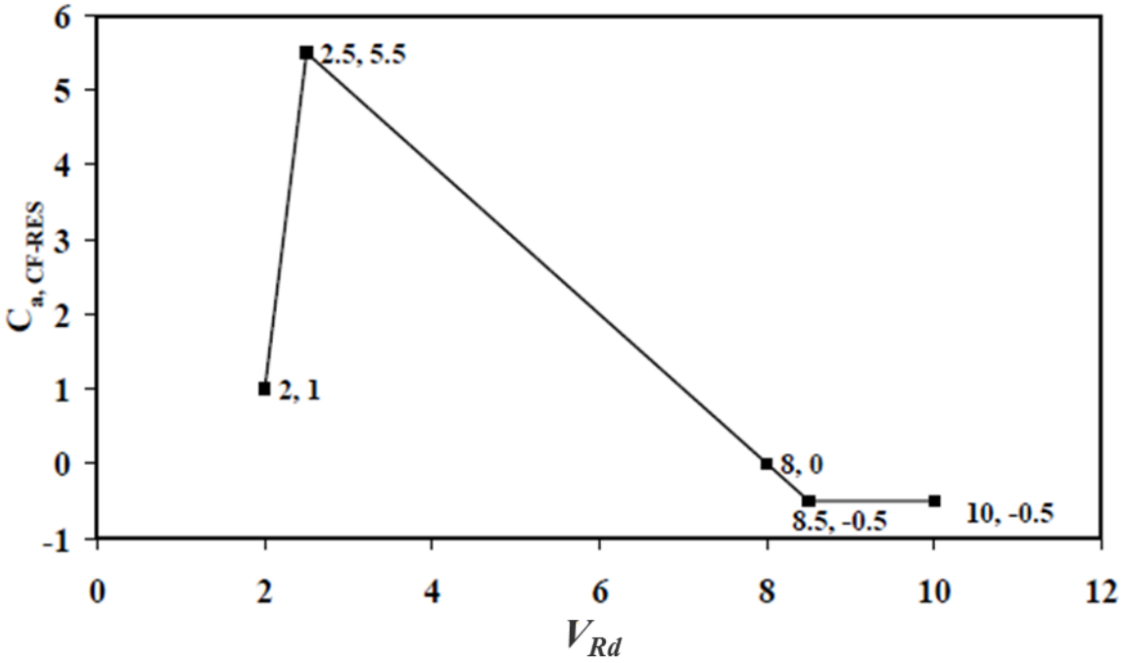

Figure 3.7: Correction of added mass coefficient to account for the difference of VIV added mass and still water added mass coefficient. Taken from DNVGL-RP-F105 [7].

$C_{a,CF-RES}$ is the added mass coefficient due to CF response.

It should be noted that the correction curve has the effect of still-water added mass already built into it.

The CF cycle-counting frequency is given by the following equation.

$$f_{cyc,CF}(x) = \sqrt{\sum_{j=1}^{m} \left(f_{CF-RES,j} \cdot \frac{S_{CF,j}(x)}{S_{comb,CF}(x)} \right)^2} \tag{3.49}$$

Stresses from IL VIV and CF-induced IL VIV

For IL VIV, a preliminary stress range for pure IL VIV is calculated using the following equation, before comparison with CF-induced IL VIV is applied.

$$S^P_{IL,j}(x) = 2 \times A_{IL,j}(x) \times \left(\frac{A_y}{D} \right)_j \times \psi_{\alpha,IL} \times \gamma_s \tag{3.50}$$

$A_{IL,j}(x)$ is the unit diameter amplitude stress of IL-mode j at location x along the jumper

$\left(\frac{A_y}{D}\right)_j$ is the normalized response amplitude according to the IL response model

$\psi_{\alpha,IL}$ is a correction factor for the current flow ratio α.

CF-induced IL VIV can arise from the dominating CF-mode. Accordingly, for non-straight pipelines all acting CF-modes must be considered. The candidate for CF-induced IL VIV is the IL mode with its eigenfrequency closest to twice the oscillating

frequency of the CF-mode with the largest response amplitude. This candidate is found from the minimum of the expression

$$|f_{IL,k}^{part} - 2 \cdot f_{CF-RES,i}| \tag{3.51}$$

where $f_{IL,k}^{part}$ is the natural frequency of the k-th participating IL-mode with $k \in \{1, 2, \ldots, n\}$. The stresses due to CF-induced IL VIV are calculated from the equation

$$S_{IL-CF}(x) = 0.8 \times A_{IL,k}(x) \times \left(\frac{A_z}{D}\right)_{max} \times R_k \times \gamma_s \tag{3.52}$$

where

$A_{IL,k}(x)$ is the unit diameter amplitude stress of the selected candidate

$\left(\frac{A_z}{D}\right)_{max}$ is the maximum normalized response amplitude from the CF response model

R_k is the reduction factor to cover the effect of damping as applied in Equation 3.46.

If the candidate mode for CF-induced IL VIV is an active IL mode, the stress from IL VIV is taken as the maximum of stresses due to CF-induced IL VIV and pure IL VIV. If the candidate is not among the active modes, it is added as a new active mode with its stress range. The combined IL stress range is then calculated as [7]

$$S_{comb,IL}(x) = \sqrt{\sum_{j=1}^{m_{aug}} (S_{IL,j}(x))^2} \tag{3.53}$$

where

$S_{IL,j}$ is the response stress range due to the j-th contributing IL mode

m_{aug} is equal to the number of contributing modes m if the CF-induced IL mode is among these. Otherwise, it is equal to $m + 1$.

The IL cycle-counting frequency is given by the equation [7]

$$f_{cyc,IL}(x) = \sqrt{\sum_{j=1}^{m_{aug}} \left(f_{IL,j} \cdot \frac{S_{IL,j}(x)}{S_{comb,IL}(x)}\right)^2} \tag{3.54}$$

where $f_{IL,j}$ is the natural frequency of the j-th contributing IL mode. For the CF-induced IL mode this is set to $2 \cdot f_{CF-RES,i}$.

3.3.3 Fatigue damage

From the DNV GL procedure two combined stress ranges, $S_{\text{comb,CF}}$ and $S_{\text{comb,IL}}$, were obtained that represent all stresses for a specific load case. The number of cycles per year was obtained from the corresponding cycle-counting frequency. With the

combined stress ranges the SN-curve could be entered and the number of cycles to failure was found. The damage from CF VIV and IL VIV could simply be added to a total damage.

3.4 Limitations

The work-flow of this thesis work is shown in the figure below. Simplifications were made when a case scenario was developed from a realistic full-scale scenario. Especially was the model initialized in a stress-free condition. Further, no internal pressure and only small external pressure from the hydrostatic condition one meter below surface were applied. Positive internal pressure would have a stiffening effect on the structure, while larger external pressure would soften it. These effects were not taken into account for the jumper model to be in agreement with the experimental setup. However, the stiffening and softening effects, also with respect to the modeling choice between elbow elements and regular pipe elements for the bends, were observed from a single bend model with realistic full-scale dimensions.
In modal analysis special focus was put on modeling flexibility of the bends correctly by utilizing the Pipe34 and Elbow31B element types. However, also regular pipe elements have different stiffness properties in Simla and Abaqus with respect to transverse shear. Thus, some deviation in results was accepted.
For VIV analysis and the resulting fatigue damage two procedures were applied. In Simla, VIV motion and moments were obtained directly as a time signal. For VIV motion, experimental data at two locations along the jumper could be used for comparison to ensure that the Simla results are in a conservative range. For stresses, no experimental data was available. To evaluate the fit of simulation results and adjust parameters in the VIV tool in Simla, the experimental data was considered precise. For the ten degree flow, information was given about active modes and shifts in vibration patterns. Such information was not made available for the other two flow directions.
Since both flexural and torsional stresses can have an important contribution to fatigue damage, the total damage was calculated from the first principal stress. This was calculated at each time step of the signal before rainflow counting was applied. It is assumed that the maximum principal stress is conservative for tensile crack-growth, since stresses contribute to crack-growth with their full range regardless of their direction. However, this method can be less precise than other criteria for multi-axial fatigue. Especially when torsional stresses are very large, the main driver for fatigue is shear crack growth, which behaves different from crack growth due to tensile load. In this study, the first principal stress approach is used, but limitations are discussed in the results.

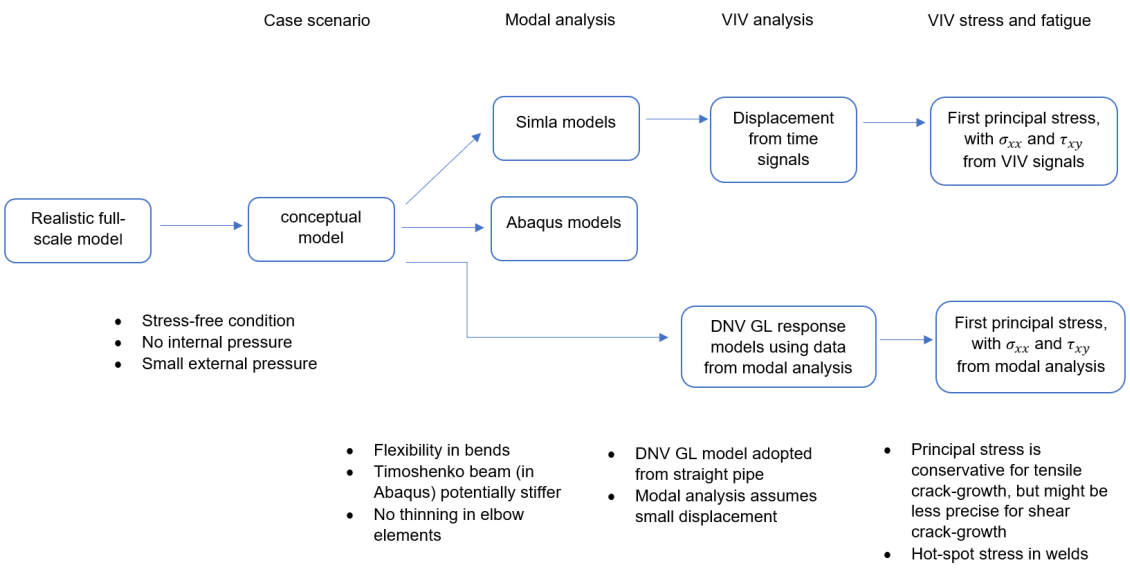

Figure 3.8: Flowchart of work steps.

The second procedure for VIV assessment is the DNV GL response model approach, which utilizes the maximum principal stress from modal analysis and scales it with response amplitudes from the guidelines itself. Modal analysis assumes small displacements, thus, limitations arise when it is applied for non-linear structural behavior. Further, the DNV GL procedure was adopted from the approach for straight pipes with several modifications. Thus, less precise, but conservative results must be expected here. Nonetheless, it was used to compare the Simla results for fatigue.

Chapter 4

Input for case-study

4.1 Case scenario

The case scenario was defined according to the experimental setup of the ExxonMobil model test to obtain comparable results. With a scale ratio of 4.525 an arch length of 13.96m is obtained. The jumper geometry was modeled using the dimensions given in Table 4.1 and Table 4.2. The model consisted of aluminum. As in the test, the highest point of the model was placed one meter below sea surface and the seawater density was 1000kg/m^3.

4.1.1 Jumper models and element types

The bends were modeled with a bending radius defined as three times the outer diameter of the pipe, which resulted in a bending radius of 0.1815 meters and an arch length of 0.2851 meters for each bend. The number of elements was chosen in such way that the element length in bent pipe parts did not exceed the outer diameter size. Five elements per bend were used in the simulation, which led to an element length of 0.057 meters. For the straight parts the element length was varied between once and twice the outer diameter. During modal analysis in Simla it was found that an element length of twice the outer diameter and accordingly twice the element length from the bent parts was sufficient.
In Simla, two models were used and compared, of which one consisted completely of Pipe31 elements, also referred to as 'Pipe31 model'. For the other model Pipe31 elements were used for the straight parts and Pipe34 elements for the pipe bends. This model will later be referred to as 'Pipe34 model'.
In Abaqus, two models were used to compare eigenvalue results from Simla and obtain modal principal stresses. One model consisted of Pipe31 elements, while the other one was modeled with Elbow31B elements for the bends. As mentioned in section 3.2.1, Elbow31B elements do not include warping and have most similar

properties compared to Pipe34 elements. As recommended in the Abaqus documentation, 18 additional integration points around the circumference and 6 Fourier modes were specified for ovalization.
Linear elastic material definition was applied for all models. The drag coefficient applied in the Morison equation was initially chosen according to Wang et al. [18], who had reported a normal drag coefficient of 1.1 from the model test. Since in Simla a value of 1.2 is recommended for the drag coefficient, simulations for VIV were later carried out for both values. The normal added mass coefficient was set to 1.0, since it is a typical value for structures with circular cross-section. Both the tangential drag and the tangential mass coefficients were set to zero.

Table 4.1: Segment lengths of the jumper model

Segment name	Length [m]
Vertical 1	1.495
Horizontal 1	1.000
Vertical 2	2.323
Horizontal 2	4.327
Vertical 3	2.326
Horizontal 3	1.000
Vertical 4	1.495

Table 4.2: Jumper model properties

Parameter	Value	Unit
Pipe density	2700	kg/m^3
Outer diameter	0.0605	m
Inner diameter	0.055	m
Wall thickness	2.77×10^{-3}	m
Elastic modulus (E)	6.90×10^{10}	N/m^2
Bending stiffness (EI)	1.44×10^{4}	N/m^2
Shear modulus (G)	2.61×10^{10}	N/m^2
Torsion stiffness (GJ)	1.08×10^{4}	N/m^2

4.1.2 Model setup

In Simla, the model was set up in a stress-free configuration by placing a straight pipe in a vertical position in the sea and applying initial curvature on the parts to form 90-degree bends. In a second step, gravity and external hydrostatic pressure were added. Fixed boundary conditions were added on both ends of the jumper.
In Abaqus, the geometry could be modeled as in its final state after bending during manufacture. Gravity was added and the model was placed in water to add the added mass coefficient and the drag coefficient.
In both tools the weight of the internal fluid was accounted for in the total unit mass. By this means, the dry mass consisted of two components, the structural weight and the weight of content. Both are considered constant along the pipe. No internal pressure or free-surface effects inside the pipe were considered.

4.2 VIV simulation in Simla

VIV simulations were run for at least 100 seconds per load case. During five seconds after initiation of the model setup the current velocity was smoothly increased from zero to the required value. This was done by ramping on the load in form of a half cosine function, starting at zero slope [21]. At the end of a simulation, the load was ramped off again during five seconds.
Simulations were run for flow angles of ten and 45 degrees with current velocities of 0.05 to 0.98 m/s, where the velocity was increased in steps of 0.05 m/s. For a flow angle of 90 degrees simulations were run up to a current velocity of 0.79 m/s, according to available model test data. Non-dimensional responses were plotted over reduced velocities. With these data the VIV response from Simla could be compared with model test results and with the DNV GL response models.

4.2.1 Parameter study

Table 4.3: Parameters for the parameter study on VIV prediction

Parameter	Default value	Observed values	Definition
C_{Drag}	1.2	1.1, 1.2	Drag coefficient
CV	1.0	1.0, 1.1, 1.2	CF lift force coefficient
$CVI1$	0.8	0.8, 0.9, 1.0, 1.1, 1.2	IL force coefficient for region one
$\hat{f}_{1I1}$	0.3	0.1, 0.13, 0.3	Minimum non-dimensional vibration frequency that gives energy input for IL region one

In a parameter study the influence on VIV prediction of the drag coefficient and several control parameters of the VIV tool were observed. In the first part of this study, the results were compared with the model test data for an incoming flow angle of ten degrees. After a first selection of parameters was decided on, these were tested for 45 and 90 degree flow angles and adjusted. The parameters are listed and explained in Table 4.2.1. They were observed with the goal to obtain parameters that give conservative results for all flow directions.
In the literature study Section 2.3 it was mentioned that another force coefficient can be defined for the second IL instability region. This coefficient was by default set to zero, since in the present model the first IL instability region can be excited over a wider range of reduced velocities.

4.3 DNV GL response model approach

The response models were calculated as described in section 3.3. For the purpose of comparability with the Simla results, all applied safety factors were here set to 1.0. Usually, the values are chosen according to the guidelines and as shown in Figure 4.1. They are defined as
γ_k - safety factor on stability parameter
γ_s - safety factor on stress amplitude
γ_{on} - safety factor on onset value for CF or IL reduced velocity
γ_f - safety factor on natural frequency.
Further, seabed proximity and the effect of a trench were neglected. The turbulence intensity factor I_c was set to 0.05 as recommended when no other information is available.
For pure current conditions, the flow ratio α is equal to one. The vortex-shedding frequency is steady and the KC-terms of the CF response model can be neglected.
For the calculation of the stability parameter, the effective mass per unit length was required, which consists of structural mass, added mass and mass of internal fluid. The mass components are listed in Table 4.4. Since the effect of added mass is taken into account with the added mass coefficient of 1.0 and the other two components are constant along the jumper length, the effective mass is constant, too. A correction for the deviation of the added mass during VIV and the still water added mass had to be applied on the CF response model, when the cycle-counting frequencies were calculated.

Table 2-2 General safety factors for fatigue

Safety factor	*Safety Class*		
	Low	*Medium*	*High*
η	1.0	0.5	0.25
γ_k	1.0	1.15	1.30
γ_s	1.3		
$\gamma_{on,IL}$	1.1		
$\gamma_{on,CF}$	1.2		

Table 2-3 Safety factors for natural frequencies, $\gamma_{f,IL}$ / $\gamma_{f,CF}$

Free span classifications	*Safety class*					
	Low		*Medium*		*High*	
	$\gamma_{f,IL}$	$\gamma_{f,CF}$	$\gamma_{f,IL}$	$\gamma_{f,CF}$	$\gamma_{f,IL}$	$\gamma_{f,CF}$
Very well defined	1.0	1.0	1.0	1.0	1.0	1.0
Well to very well defined	1.0	1.05	1.0	1.1	1.0	1.15
Well defined	1.05	1.05	1.1	1.1	1.15	1.15
Not well defined	1.1	1.1	1.2	1.2	1.3	1.3

Figure 4.1: Safety factors for the DNV GL response model procedure. Taken from DNVGL-RP-F105 [7].

Table 4.4: Unit mass components of the jumper model

Parameter	Value	Explanation
m_{pipe}	1.347 kg/m	
m_{content}	5.532 kg/m	
m_{dry}	6.879 kg/m	$m_{\text{pipe}}+m_{\text{content}}$
m_{added}	2.875 kg/m	with $C_a = 1.0$
m_{eff}	9.754 kg/m	$m_{\text{pipe}}+m_{\text{content}}+ m_{\text{added}}$

4.4 Fatigue life

The SN-curve was chosen according to the guideline DNVGL-RP-C203 (2005). For pipelines with single side or double side welds, curve D is recommended. SN-curves for structures in seawater with cathodic protection are shown in Figure 4.2 with associated parameters shown in Figure 4.3. Curve D changes slope at 1.00E+06 cycles, where the equivalent stress is approximately 83 mega-pascal. If the equivalent stress of a load case lies below this value, it is over-conservative to apply the parameters from the left side of the curve with a higher slope. Instead, the parameters from the right side of the curve should be chosen, which are still conservative for larger stresses, but not over-conservative for smaller equivalent stresses.
Thus, the parameters m and $\log \bar{a}$ were chosen with 5.0 and 15.606, respectively.
Correction with the thickness exponent was not applied, since the wall-thickness of the jumper model is smaller than the reference thickness and it is not allowed to take advantage from thickness correction. For fatigue of welds, more detailed analysis with respect to hot-spot stresses would be required. However, in this study the SN data is mainly used to compare fatigue results and no hot-spot correction was applied.

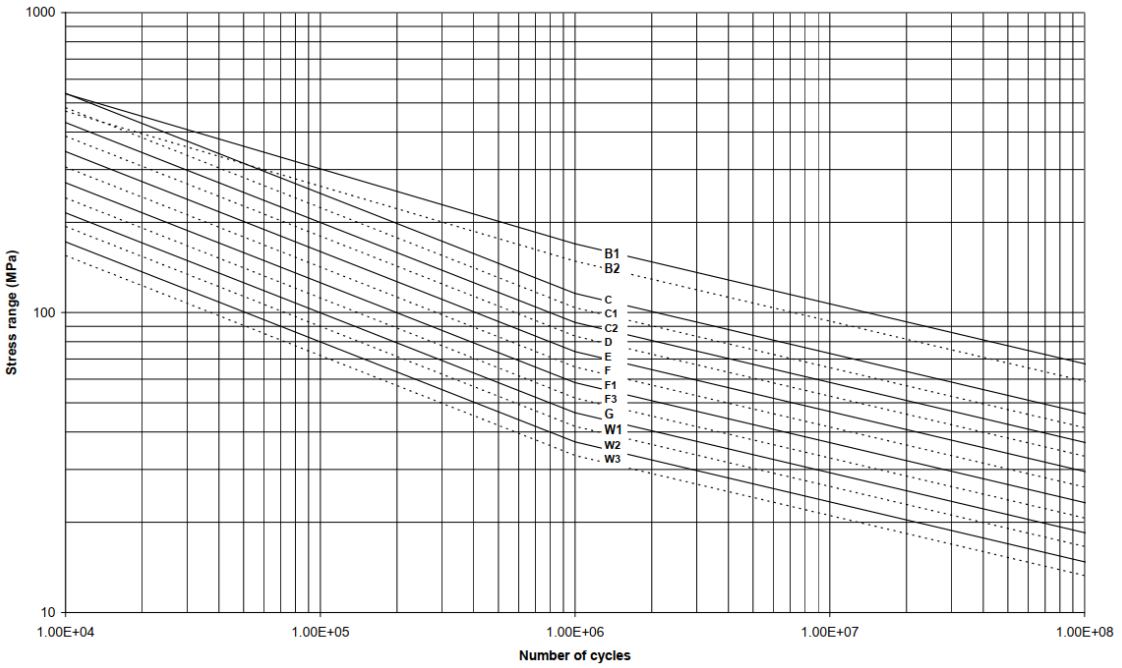

Figure 4.2: SN-curves in seawater with cathodic protection. Taken from DNVGL-RP-C203 [8].

Table 2-2 S-N curves in seawater with cathodic protection						
S-N curve	*N ≤ 10 ^{6} cycles*		*N > 10 ^{6} cycles* $\log\bar{a}_2$ m_2= 5.0	*Fatigue limit at 10 ^{7} cycles*)*	*Thickness exponent k*	*Stress concentration in the S-N detail as derived by the hot spot method*
	m_1	$\log\bar{a}_1$				
B1	4.0	14.917	17.146	106.97	0	
B2	4.0	14.685	16.856	93.59	0	
C	3.0	12.192	16.320	73.10	0.15	
C1	3.0	12.049	16.081	65.50	0.15	
C2	3.0	11.901	15.835	58.48	0.15	
D	3.0	11.764	15.606	52.63	0.20	1.00

Figure 4.3: Parameters of SN-curves in seawater with cathodic protection. Taken from DNVGL-RP-C203 [8].

4.5 Diameter-over-thickness study with internal and external pressure

It was assumed that the use of elbow elements in bends will have large effects for very thin-walled pipes, while the effect should vanish for relatively thick-walled pipes. A common definition is that pipes with a diameter-over-thickness (D/t) ratio of ten or larger are thin-walled, while with a ratio lower than ten they are thick-walled.
To further explore the effect of the modeling choice between regular pipe elements and elbow elements, a single bend section was modeled with constant outer diameter and varied wall-thickness, so that D/t-ratios between five and 45 were obtained.
A typical scenario with realistic pipe dimensions and steel material was used. The properties are given in Table 4.5 and the model is shown in Figure 4.4. Due to symmetry, only half of the 90-degree bend section was modeled with a radius of 2.25 meters and adjacent straight parts of 2.25 meters length. The element size was set equal to the outer diameter. On the left end translation in x-direction and rotation around the y-axis were restricted. The model was free to move in vertical direction and to deform its cross-section. On the right tip translation in both y and z-direction and rotation around the x- and z-axis were restricted, while translation in x-direction was possible. Here, a rotation of five degrees around the y-axis was applied which led to a constant bending moment.
Flexibility factors were measured at the intersection between bend and straight part using the following definition.

$$\mathrm{FF} = \frac{(M_y/\theta_y)_{\mathrm{Pipe31}}}{(M_y/\theta_y)_{\mathrm{elbow}}} \tag{4.1}$$

First, the behavior without internal or external pressure was observed. In a second and third step, internal and external pressure were included separately. The magnitudes are shown in Table 4.6 and were chosen corresponding to 80 percent of the pipe capacity with respect to elastic buckling pressure in hoop direction and yield stress. The simulations were carried out in both Simla and Abaqus.

Table 4.5: Properties of full-scale bend model

Pipe density	[kg/m^3]	7850
Outer diameter	[m]	0.45
Elastic modulus	[N/m^2]	2.1×10^{11}
Shear modulus	[N/m^2]	8.08×10^{10}

		D/t=15	D/t=30	D/t=45
Inner diameter	[m]	0.39	0.42	0.43
Wall thickness	[m]	0.03	0.015	0.01
Bending stiffness	[N/m^2]	1.83×10^8	1.02×10^8	7.02×10^7
Torsion stiffness	[N/m^2]	1.41×10^8	7.83×10^7	5.40×10^7

Table 4.6: Load cases for full-scale bend model

		D/t=15	D/t=30	D/t=45
Internal pressure	[N/m^2]	51.4×10^6	24.82×10^6	16.36×10^6
External pressure	[N/m^2]	39.2×10^6	10.55×10^6	2.65×10^6

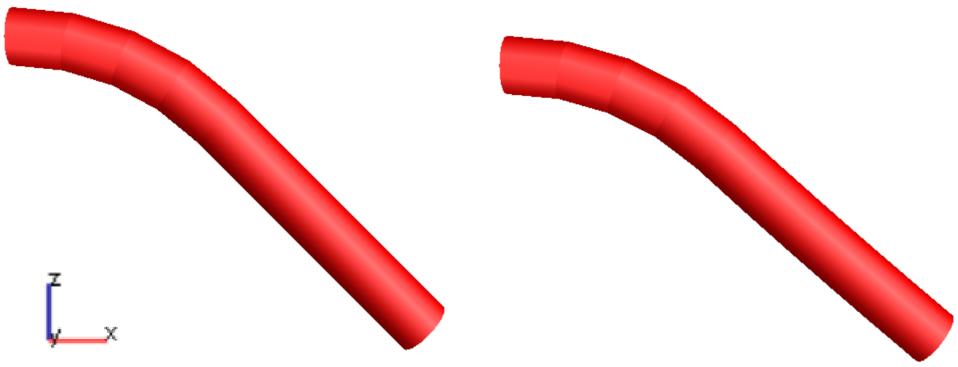

Figure 4.4: Half of the 90° bend model. Left hand side un-deformed, right hand side after rotation was applied on the right end.

Chapter 5

Results

5.1 Eigenvalue analysis

In a previous project work it was observed that the eigenfrequencies of the Pipe31 model in Simla are in very good correlation with the results from other numerical studies. The Pipe34 model in Simla, on the other hand, shows some differences, but is in better agreement with the mode shape order from the ExxonMobil model test reported by Wang et al. [18]. To verify the use of elbow elements and the observations from eigenvalue analysis in Simla, the two Simla models were compared to the two Abaqus models.

5.1.1 Pipe31 model in Simla and Abaqus

The eigenvalue results for the two models consisting completely of Pipe31 elements are in good correlation with each other, as shown in Figure 5.1. Relative errors of the eigenvalue results between the two Pipe31 models are plotted in Figure 5.2.
The maximum error occurs for mode one with about nine percent which is comparably high. For all other modes the error lies below 3.5 percent. The differences in results can be due to the fact that Pipe31 elements in Abaqus are Timoshenko beams which allow for transverse shear deformation. In Simla, on the contrary, the cross-section of Pipe31 elements remains plane and does not distort due to transverse shear. An overview of the first nine modes with mode shapes is also given in Table 5.1. Mode shapes are identical for the two Pipe31 models. Modes three, four, six and nine are in-plane bending modes, of which modes three and six have their largest displacement in x-direction and modes four and nine in z-direction. For these four modes the relative error is very small. Modes one, five, seven and eight are out-of-plane bending modes and mode two is an out-of-plane twist mode.
The eigenfrequencies of modes two and three are very close to each other. This gives a reason why they appear in switched order in the simulation results to how they

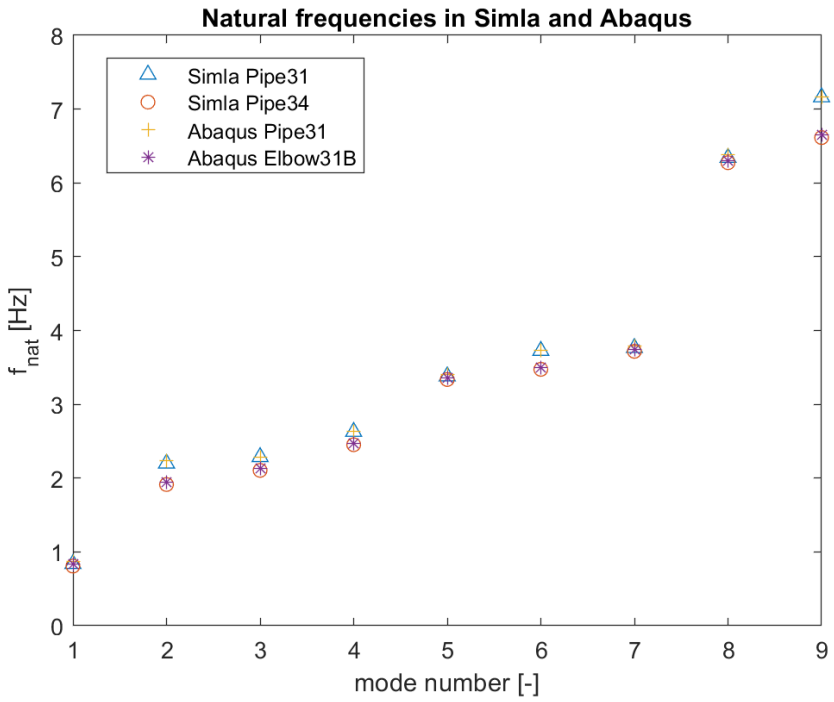

Figure 5.1: Comparison of natural frequencies in Simla and Abaqus

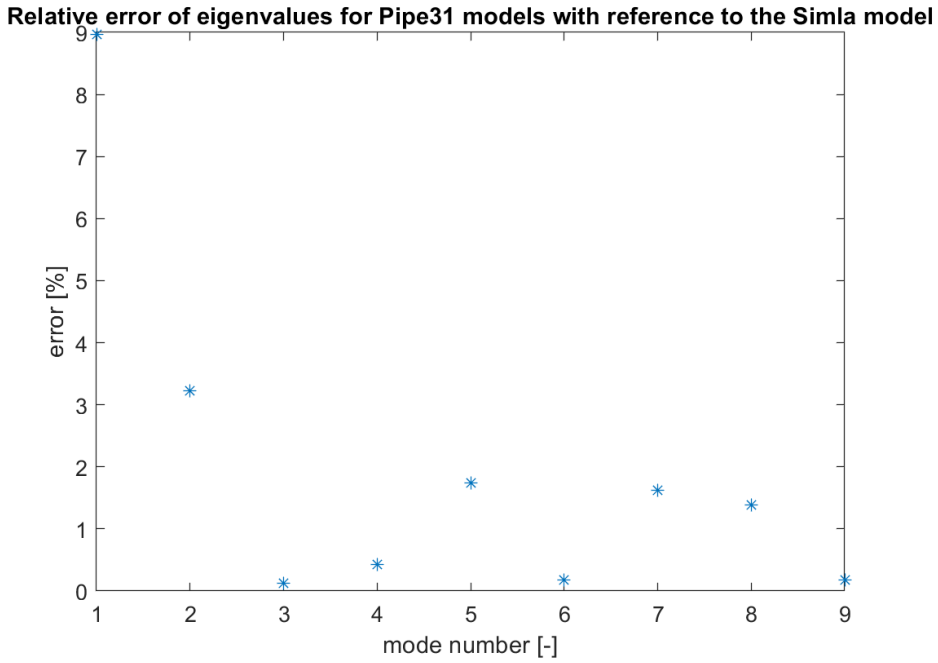

Figure 5.2: Relative error of natural frequencies obtained for the two Pipe31 models in Simla and in Abaqus

were reported from the ExxonMobil model test. Also, the eigenfrequencies of modes six and seven are very close to each other. However, information about the shapes reported from the model test were available only for the first three modes.

Table 5.1: Eigenfrequencies and mode shapes of Pipe31 models

Mode	f_n in Simla [Hz]	f_n in Abaqus [Hz]	Mode shape
1	0.8377	0.8744	out-of-plane bending in y-direction with largest displacement at top horizontal
2	2.1991	2.2343	out-of-plane twist around center point of top horizontal
3	2.2859	2.2844	in-plane bending in x-direction
4	2.6285	2.6341	in-plane bending in z-direction
5	3.3800	3.4094	symmetric out-of-plane bending in y-direction with largest displacement at the two bottom horizontals
6	3.7261	3.7294	diagonal distortion in both x and z-direction
7	3.7646	3.7949	asymmetric out-of-plane bending in y-direction with largest displacement at the two bottom horizontals
8	6.3413	6.3851	buckling of the top horizontal in y-direction
9	7.1614	7.1678	buckling of the top horizontal in z-direction

5.1.2 Pipe34 model in Simla and Elbow31B model in Abaqus

Eigenfrequencies for the Pipe34 model in Simla and the Elbow31B model in Abaqus are generally lower than the ones from the Pipe31 models, also shown in Figure 5.1. Moreover, mode two and three are switched in order for the elbow models as shown in Table 5.2, so that in-plane bending occurs at a lower frequency than out-of-plane twist. This is in correlation with the observations from the model test. Mode shapes of the two elbow element models are identical. The maximum relative error of eigenvalue results again occurs for mode one with 6.6 percent, as plotted in Figure 5.3. For the other modes, the error is below three percent which is a good correlation. Both Pipe34 and Elbow31B elements are beam elements for which shell theory is applied to model the deformation of the cross-section. The classical von Kármán approach is implemented to account for ovalization from pure bending. Since the two elements are very similar, the derogation of results, especially for the first mode, can also be attributed to the differences of Pipe31 elements to which the elbow elements are connected.

It should be pointed out that the shift in mode shapes could not be obtained with

models consisting only of Pipe31 elements, even with a refined mesh. This gives a relevant reason to use elbow elements in the analysis of subsea jumpers. When following the DNV GL response model procedure, FEA modal results are utilized for fatigue analysis, too. Thus, it is of great importance to obtain the correct order of mode shapes and correct modal frequencies. The mode shapes are also shown in Figures 5.4 to 5.8.

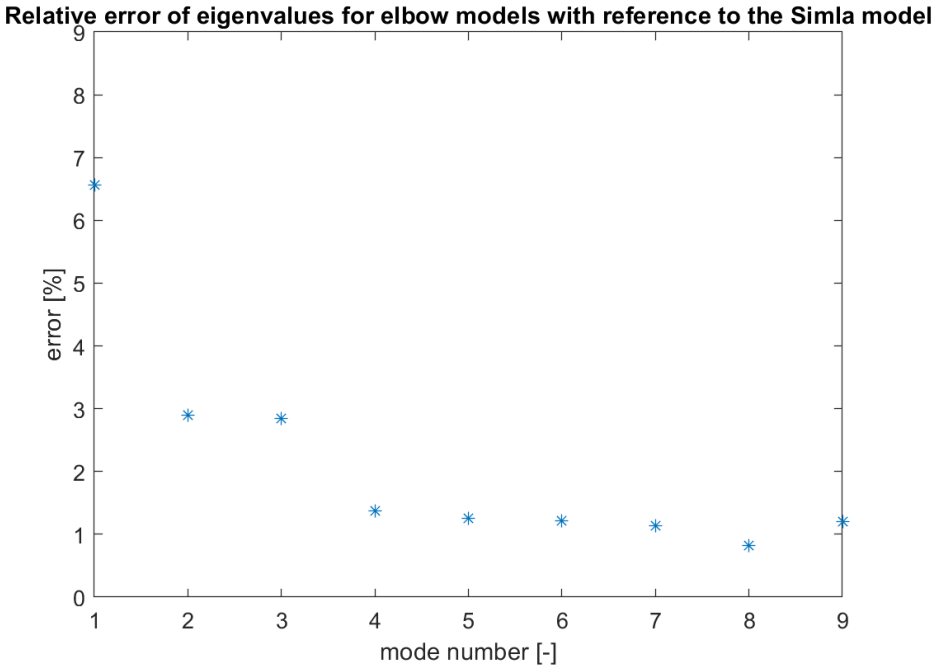

Figure 5.3: Relative error of eigenvalue results obtained for the two elbow element models in Simla and in Abaqus

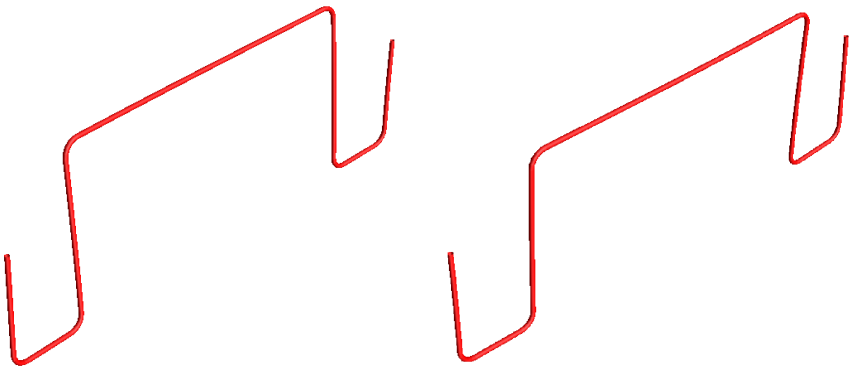

Figure 5.4: Mode one of the Pipe34 model. Out-of-plane bending of the top horizontal in y-direction.

Table 5.2: Eigenfrequencies and mode shapes of Pipe34 model (Simla) and Elbow31B model (Abaqus)

Mode	f_n in Simla [Hz]	f_n in Abaqus [Hz]	Mode shape
1	0.8076	0.8336	out-of-plane bending in y-direction with largest displacement at top horizontal
2	1.9131	1.9406	in-plane bending in x-direction
3	2.1047	2.1344	out-of-plane twist around center point of top horizontal
4	2.4522	2.4689	in-plane bending in z-direction
5	3.3357	3.3568	symmetric out-of-plane bending in y-direction with largest displacement at the two bottom horizontals
6	3.4739	3.4949	diagonal distortion in both x and z-direction
7	3.7181	3.7389	asymmetric out-of-plane bending in y-direction with largest displacement at the two bottom horizontals
8	6.2740	6.2998	buckling of the top horizontal in y-direction
9	6.6148	6.6539	buckling of the top horizontal in z-direction

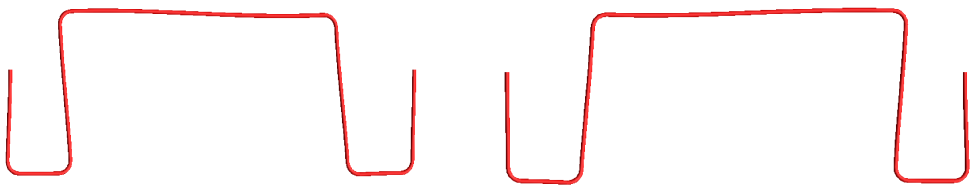

Figure 5.5: Mode two of the Pipe34 model. In-plane bending in x-direction.

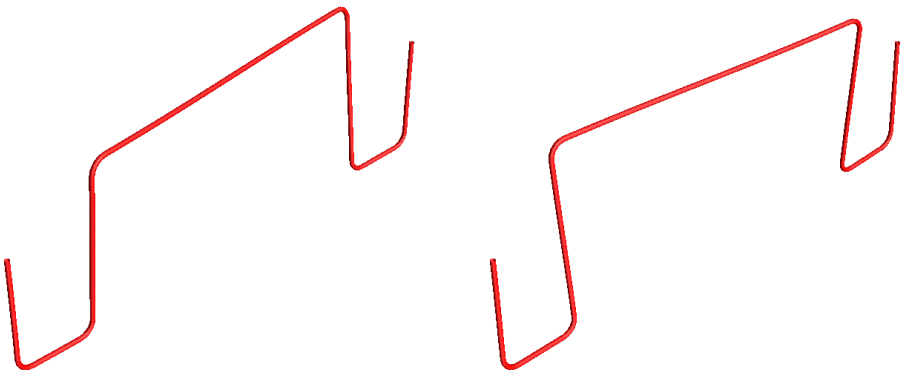

Figure 5.6: Mode three of the Pipe34 model. Out-of-plane twist.

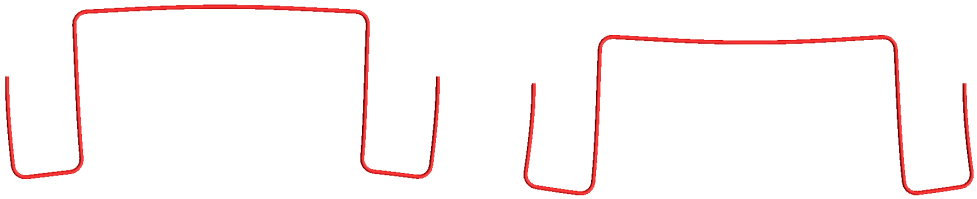

Figure 5.7: Mode four of the Pipe34 model. In-plane bending in z-direction.

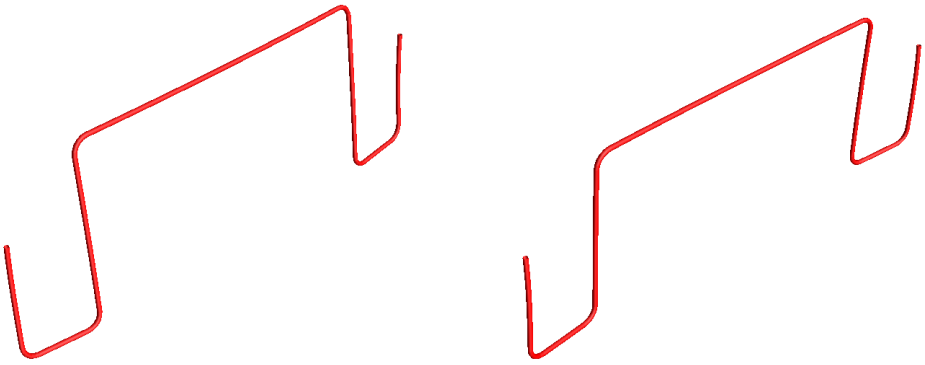

Figure 5.8: Mode five of the Pipe34 model. Symmetric out-of-plane bending of the two bottom segments in y-direction.

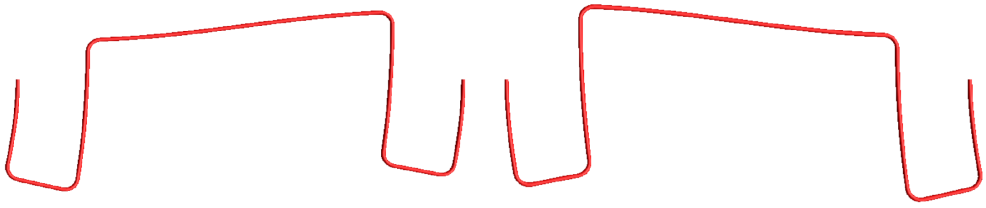

Figure 5.9: Mode six of the Pipe34 model. Diagonal distortion in both x and z-direction.

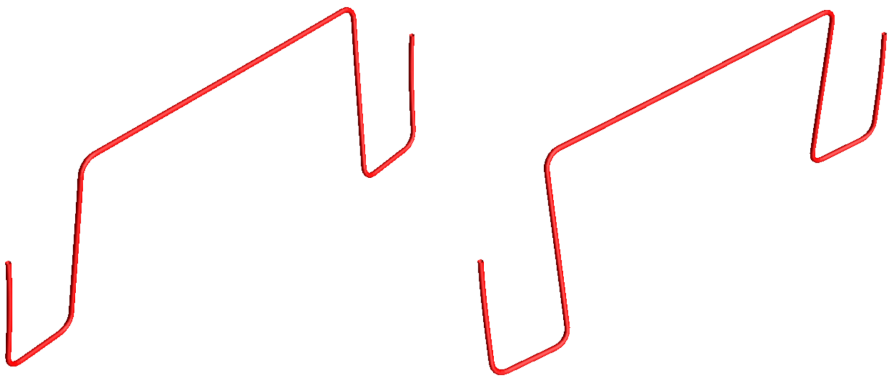

Figure 5.10: Mode seven of the Pipe34 model. Asymmetric out-of-plane bending of the two bottom segments in y-direction.

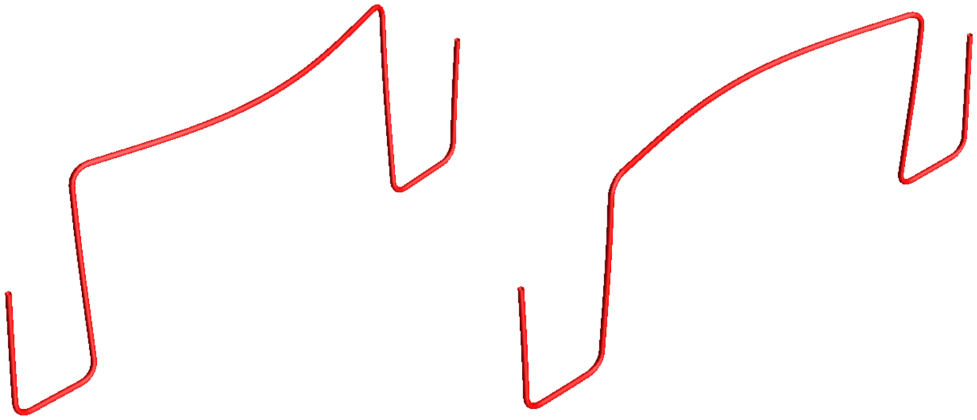

Figure 5.11: Mode eight of the Pipe34 model. Out-of-plane bending in y-direction. Largest displacement occurs as buckling of the top horizontal.

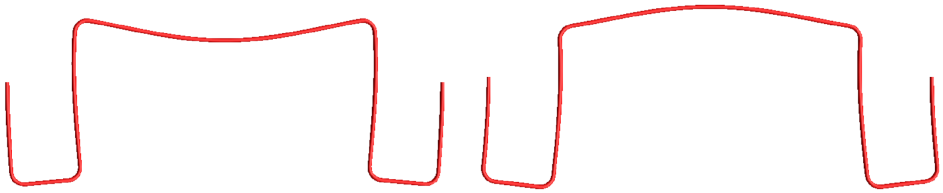

Figure 5.12: Mode nine of the Pipe34 model. In-plane bending in z-direction. Largest displacement occurs as buckling of the top horizontal.

5.2 Modal stresses

An overview of modal stresses for the first nine modes is given in Figures 5.13 to 5.18 where the maximum principal stress, the flexural stress and the shear stress is shown for the Pipe31 and Pipe34 models in Simla. For the Pipe34 model resulting stress in the bends is increased up to factor two compared with the Pipe31 model. In the adjacent straight parts, on the other hand, the stresses are decreased by up to 35 percent. The coupled effect of decreased stresses in straight parts and increased stresses in bends is most significant for the in-plane bending modes, which are shown in Figures 5.19, 5.20, 5.21 and 5.22. Generally, largest principal stresses occurred at the boundaries or in the midpoint of the top horizontal for the Pipe31 model, while they occurred in bends for the Pipe34 model. The difference is due to the flexural stress component. Torsional stresses have the same magnitude for both models.
The remaining plots that compare modal stresses, also with Abaqus results, can be found in Appendix A due to the amount of data. When comparing the results for the Pipe31 model in Simla and Abaqus as plotted in Figures 6 to 14 (Appendix A), minor differences are observed for the first four modes. They might be due to discontinuous curvature in Abaqus, while Pipe31 elements in Simla have continuous curvature. Although the relative difference for the first four modes is between 2.4 and 7.5 percent, the absolute difference is no more than 2.5 mega-pascal, since these modes generally have smaller stresses. For mode five and seven with large bending of the shorter segments, larger deviations are observed with a relative difference of about ten percent. The deviation for mode eight is most significant. Here, the long top horizontal bends outwards with large displacement in y-direction. The relative difference in results is 38.1 percent at the center point of the top horizontal. This might be attributed to higher stiffness of the Timoshenko beam elements in Abaqus. For all nine modes, Simla gives larger stresses than Abaqus. Thus, the Simla results are assumed to be conservative.
For the Pipe34 and Elbow31B model larger difference in peak stress occurs in the bends, as shown in Figures 15 to 23 (Appendix A). With deviations of 13 to 30 percent the derogation is quite large. An additional shell model should be used to review which of the models is more reliable. Even though elbow elements theoretically behave like shells, they are connected to straight pipe elements which in turn can cause imprecision. However, the Simla results are again larger than the Abaqus results, hence, they are used for further analysis without correction.

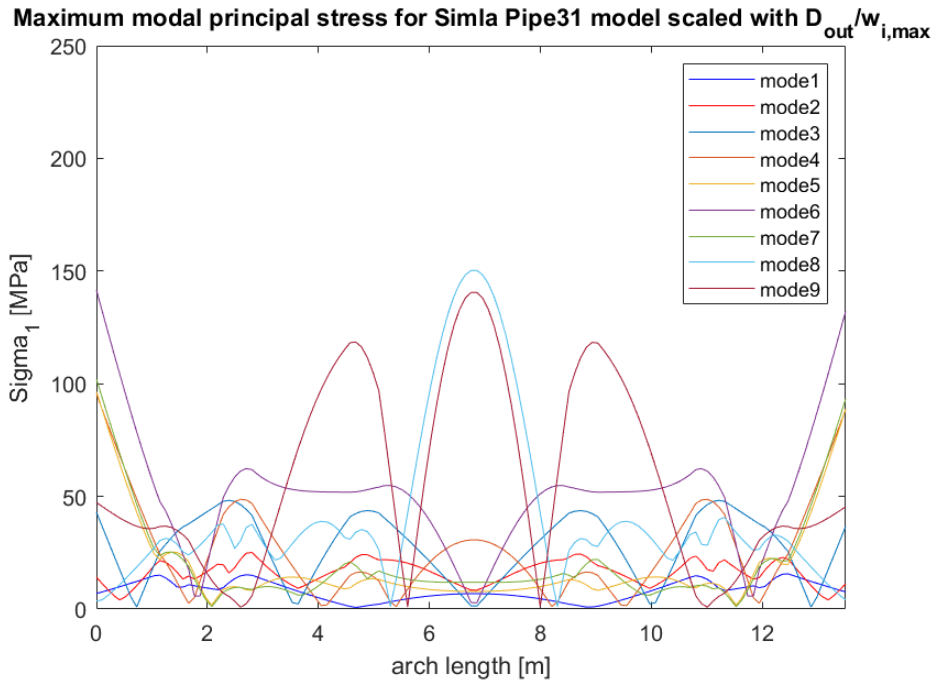

Figure 5.13: Maximum principal unit stress of the first nine modes obtained from the Simla Pipe31 model. Plotted over accumulated arch length and scaled with respect to the outer diameter and maximum modal displacement.

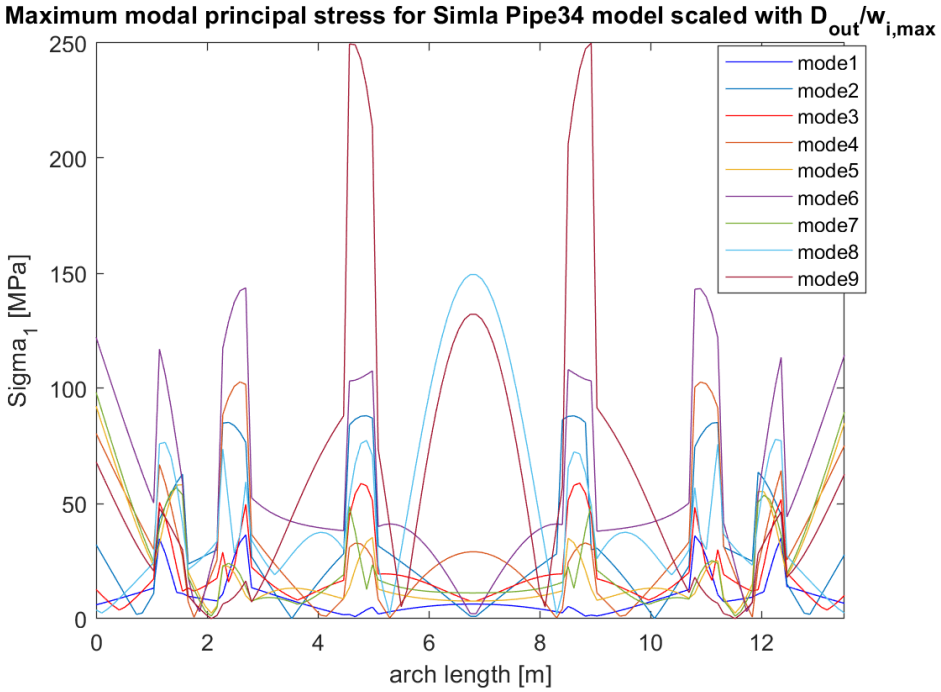

Figure 5.14: Maximum principal unit stress of the first nine modes obtained from the Simla Pipe34 model. Plotted over accumulated arch length and scaled with respect to the outer diameter and maximum modal displacement.

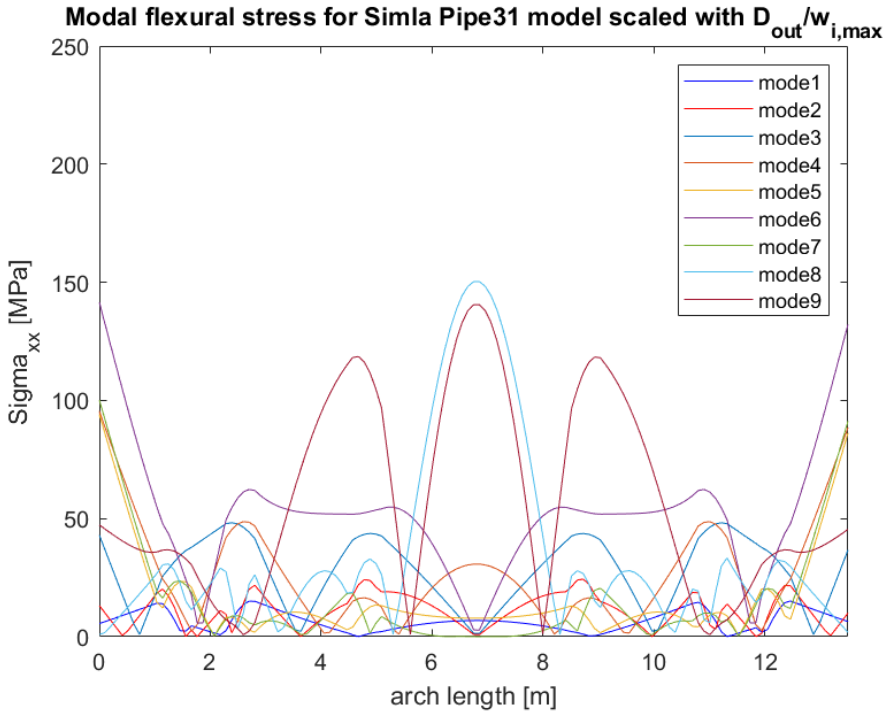

Figure 5.15: Flexural unit stress of the first nine modes obtained from the Simla Pipe31 model. Plotted over accumulated arch length and scaled with respect to the outer diameter and maximum modal displacement.

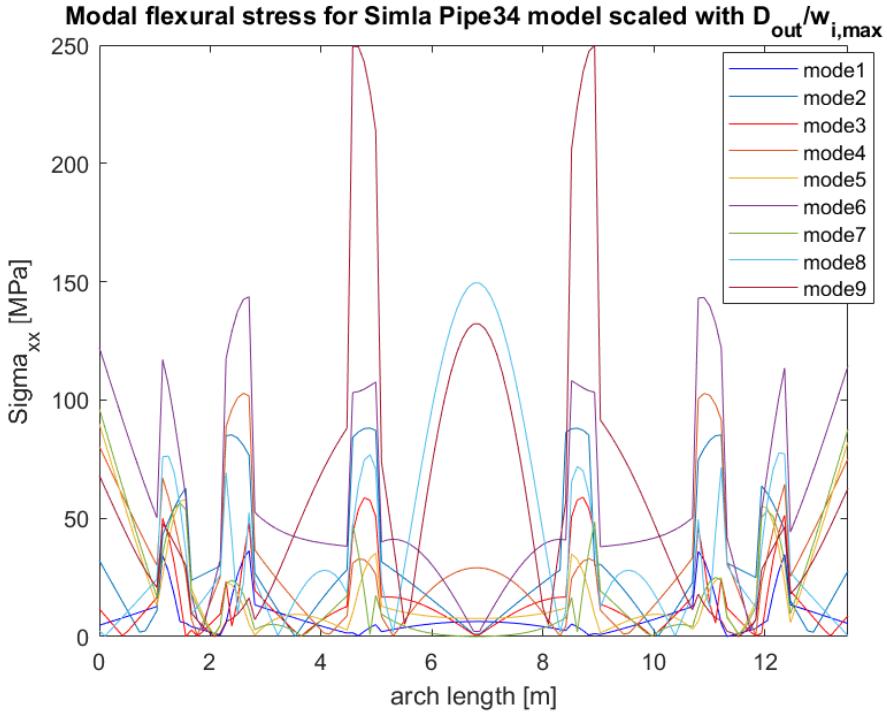

Figure 5.16: Flexural unit stress of the first nine modes obtained from the Simla Pipe34 model. Plotted over accumulated arch length and scaled with respect to the outer diameter and maximum modal displacement.

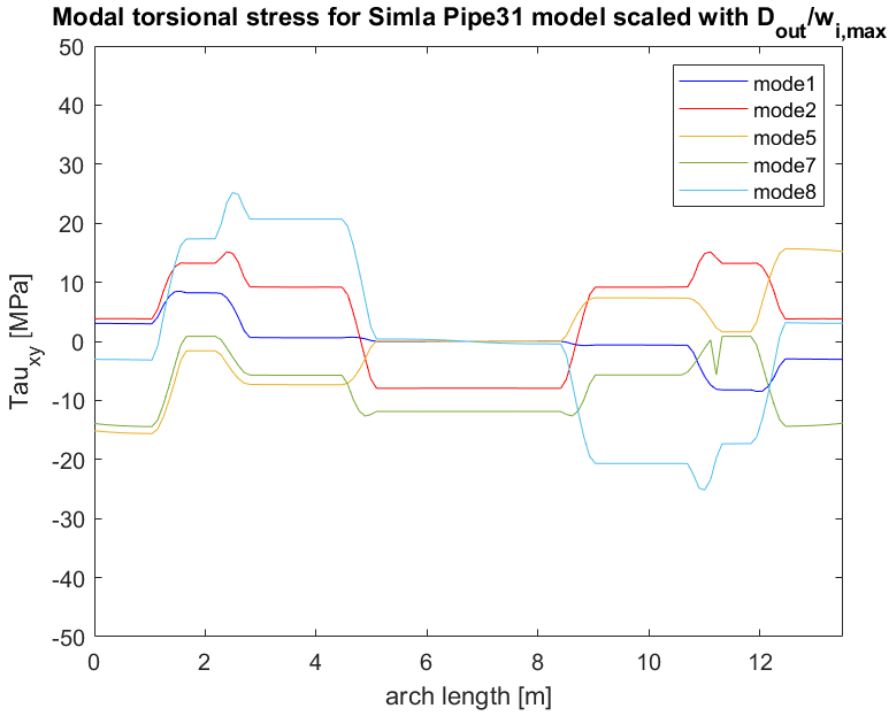

Figure 5.17: Torsional unit stress of out-of-plane twist or bending modes obtained from the Simla Pipe31 model. Plotted over accumulated arch length and scaled with respect to the outer diameter and maximum modal displacement.

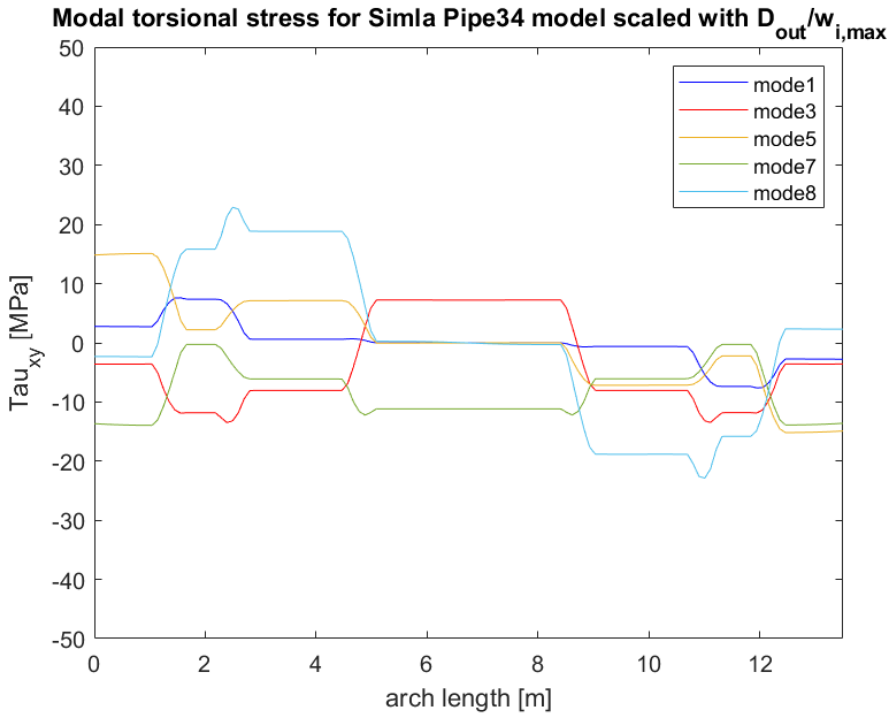

Figure 5.18: Torsional unit stress of out-of-plane twist or bending modes obtained from the Simla Pipe34 model. Plotted over accumulated arch length and scaled with respect to the outer diameter and maximum modal displacement.

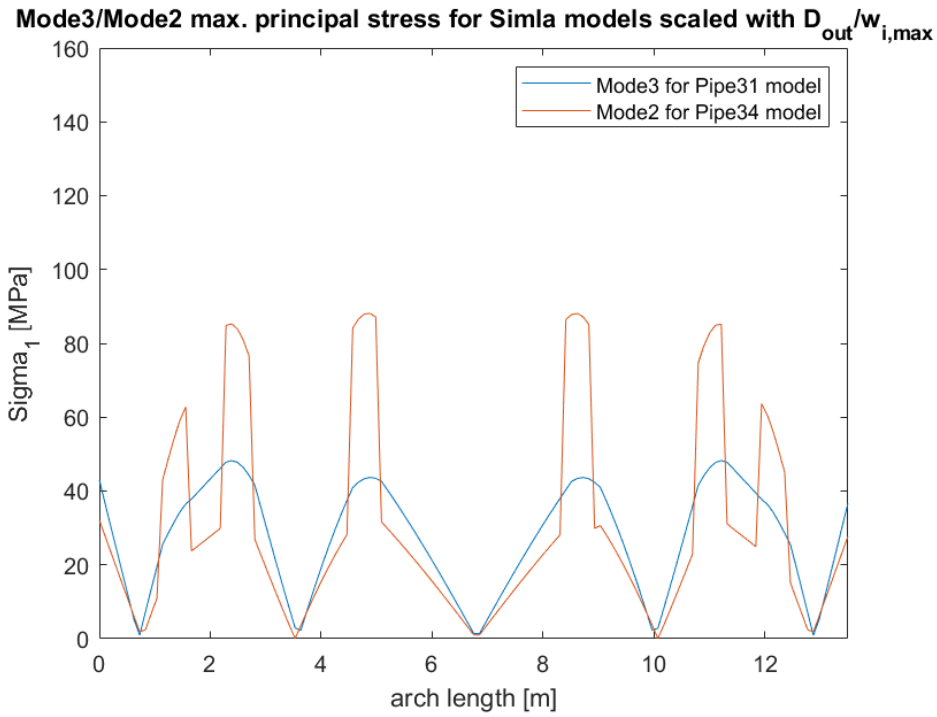

Figure 5.19: Maximum principal unit stress of mode three for the Pipe31 model and mode two for the Pipe34 model, which describe the same mode shape. Plotted over accumulated arch length and scaled with respect to the outer diameter and maximum modal displacement.

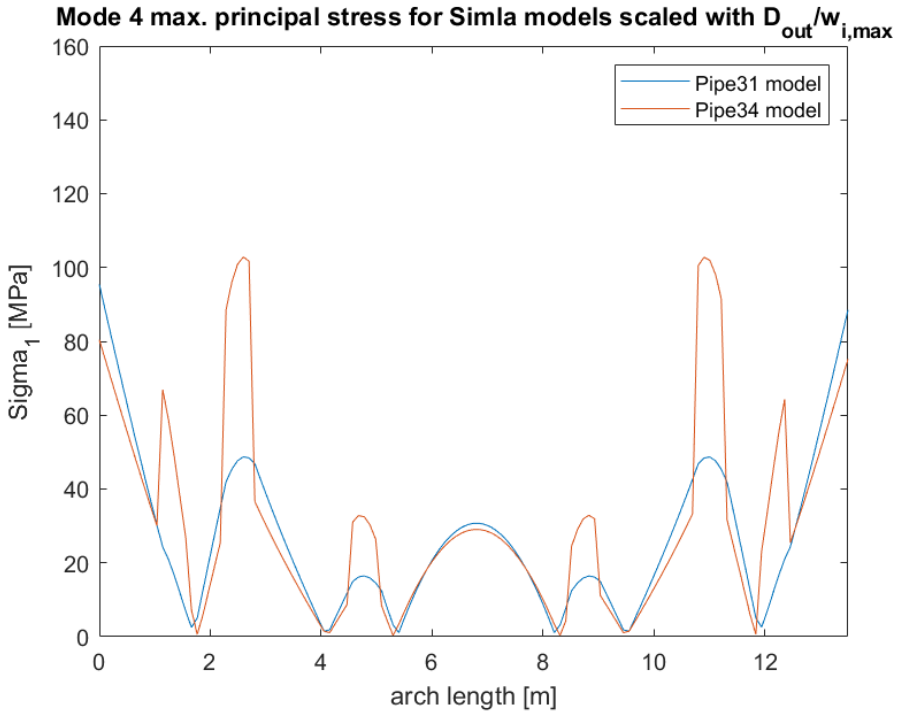

Figure 5.20: Maximum principal unit stress of mode four for the two Simla models. Plotted over accumulated arch length and scaled with respect to the outer diameter and maximum modal displacement.

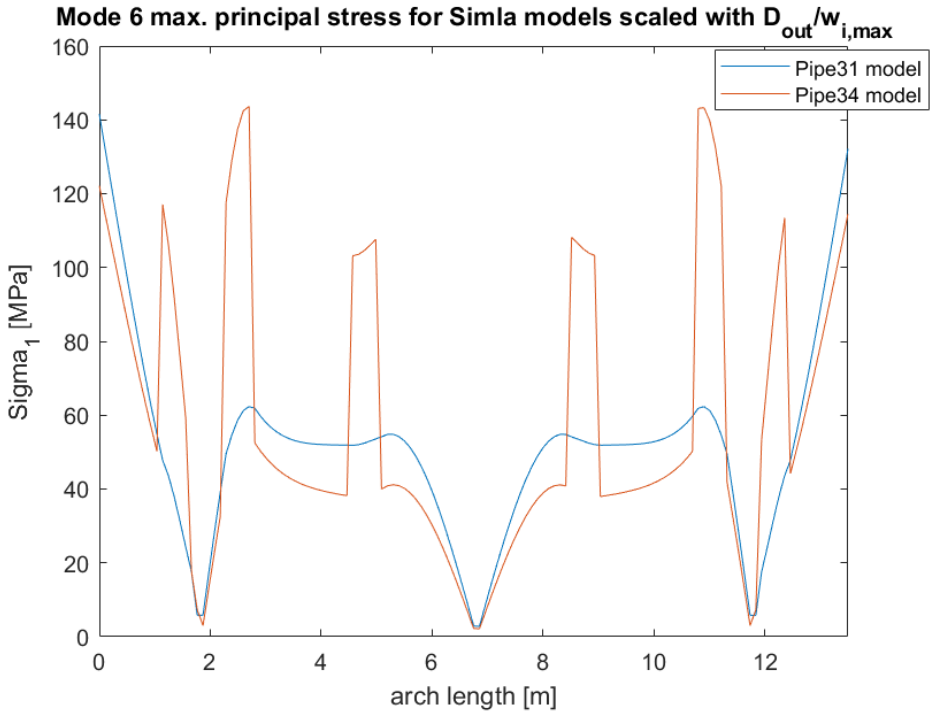

Figure 5.21: Maximum principal unit stress of mode six for the two Simla models. Plotted over accumulated arch length and scaled with respect to the outer diameter and maximum modal displacement.

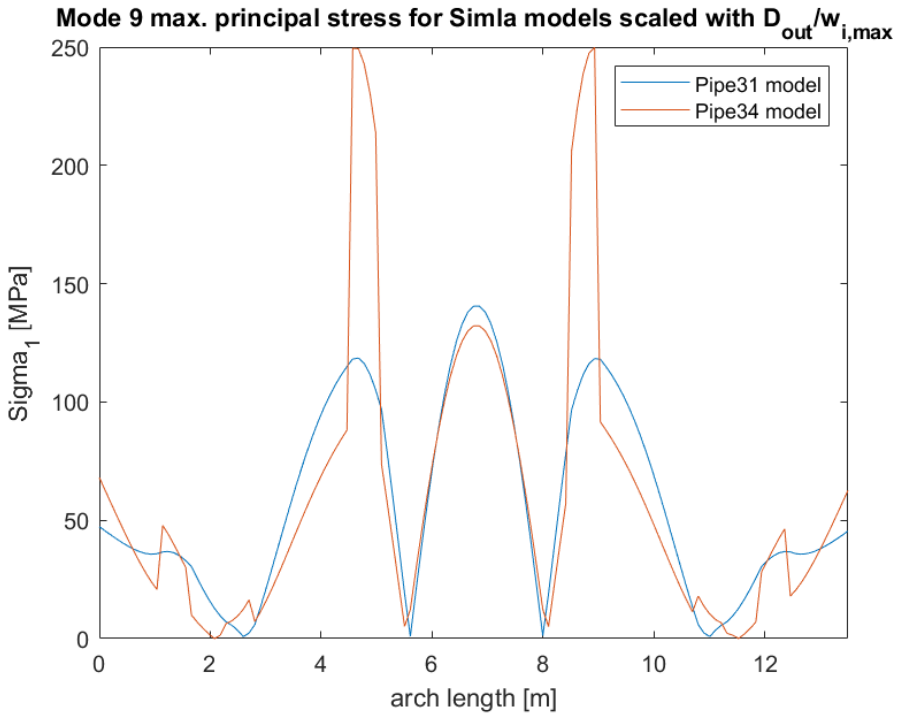

Figure 5.22: Maximum principal unit stress of mode nine for the two Simla models. Plotted over accumulated arch length and scaled with respect to the outer diameter and maximum modal displacement.

5.3 Diameter-over-thickness study with internal and external pressure

The effect of elbow elements in the bends was further explored for different D/t-ratios and including internal or external pressure. Flexibility factors (FF) at the intersection between bend and straight part from simulations with full-scale dimensions and steel material properties are shown in Figures 5.23 and 5.24.
The results from Simla and Abaqus are in good correlation with each other for the zero pressure case, but the Elbow31B elements in Abaqus are less affected by internal and external pressure. The curves for the different load cases are only slightly shifted for Elbow31B elements, while Pipe34 elements show increasing impact of pressure for thinner models as was expected.
The jumper model has a D/t-ratio of 21.8 which corresponds to a FF of 1.8 without pressure. This explains the stress amplification of modal stresses. With external pressure included the FF obtained from Pipe34 elements would raise up to 2.25 for the same D/t-ratio. With internal pressure the bends become stiffer and the FF for the jumper model would decrease to 1.45.
The chosen values for internal pressure are realistic scenarios for pipes in operating condition. The chosen external pressure values, on the other hand, will not be reached in a typical north-sea application due to comparably shallow water. Here, internal pressure is usually much higher than external pressure. With a FF of 1.45 the effect of bend elements is still relevant, but lower compared to the case scenario of the jumper model.

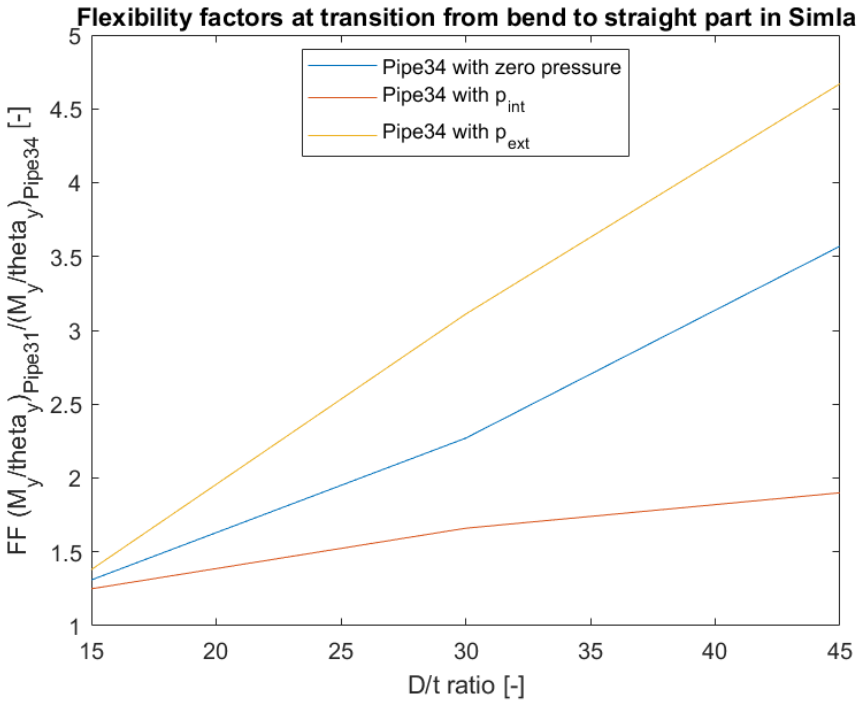

Figure 5.23: Flexibility factors obtained for Pipe34 elements in Simla with pressure from Table 4.6

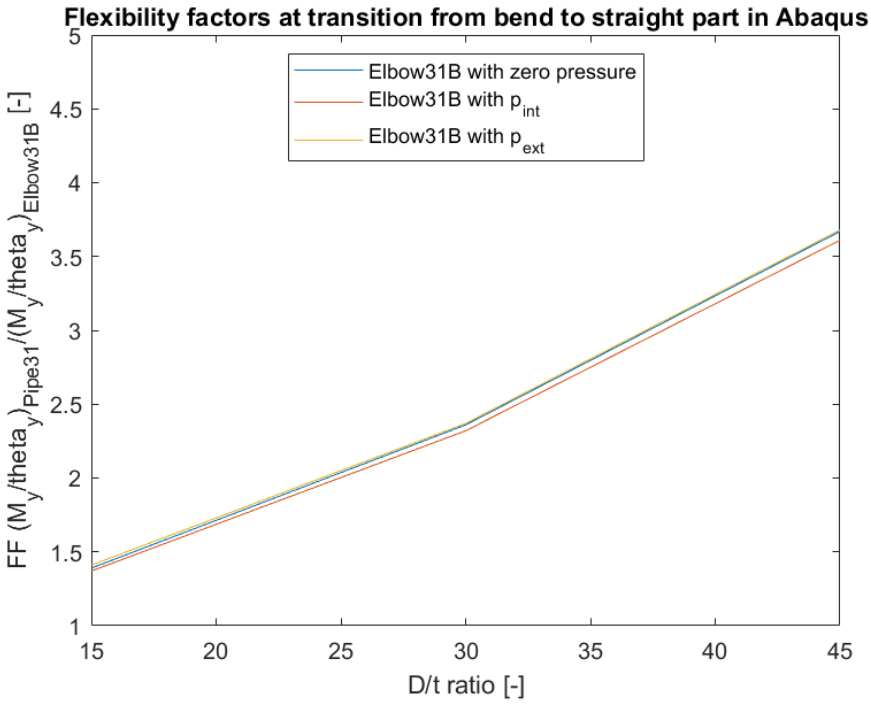

Figure 5.24: Flexibility factors obtained for Elbow31B elements in Abaqus with pressure from Table 4.6

5.4 VIV analysis

5.4.1 Parameter study in Simla

A parameter study was made by comparing the simulation results to the Exxon-Mobil model test results. In experimental data, peak values mainly occurred for a very narrow range, e.g. for reduced velocities between six and eight for the ten degree flow. In Simla, significant responses were usually spread over a wider range of reduced velocities. With the parameters of the TD tool, especially with the non-dimensional vibration frequencies that give energy input for specific regions, it is possible to narrow down the response to a certain reduced velocity range. However, this is problematic for complex geometries where the response is entirely different if the angle of attack is changed.
Accordingly, all three flow directions for which experimental results were available had to be observed in the parameter study. The parameters explained in section 4.2.1 were varied with the aim to apply the same values for each load case and obtain conservative results. Sensitivity of fatigue estimates to mentioned parameters is also discussed in Section 5.5.1.

CVI1

First, the IL force coefficient for IL region one, CVI1, was decided on. It mainly affects the non-dimensional response amplitude of IL VIV and to a smaller extent also the response amplitude in CF direction. The latter one might be due to coupling between IL and CF VIV.
The biggest effect was seen for the ten degree flow, since amplitudes in x-direction, which is associated with IL VIV here, are generally smaller than in y-direction for the model geometry. When this coefficient was changed from its default value 0.8 to 1.2, the response amplitude in x-direction was increased by up to 53.3 percent at its peak value. The response in y-direction was increased by up to 34.7 percent in the reduced velocity range where IL modes were dominating. In the higher reduced velocity range, where CF modes were dominating, the response amplitude in y-direction was increased by maximum 8.2 percent due to the change in CVI1.
The default value 0.8 of the IL force coefficient for region one in Simla was suggested for free spanning pipelines. It was observed that for the jumper model this value was not sufficient to capture the maximum IL response amplitudes for all flow directions. For the ten degree flow direction and a drag coefficient of 1.1, conservative results were obtained when CVI1 was set to 1.1 or 1.2. For a drag coefficient of 1.2 and the same flow direction, conservative results were obtained only for CVI1 equal to 1.2. Accordingly, it was set to 1.2 for all further analyses.

$\hat{f}_{1I1}$

The minimum non-dimensional vibration frequency that gives energy input for IL region one had to be modified in such way that IL VIV could be activated in a wider range of reduced velocity. Since it is a non-dimensional quantity, the reduced velocity range where IL VIV can be activated is approximately the inverse of $\hat{f}_{1I1}$. It is not exactly equal to this value, because reduced velocity was calculated with the natural frequency that was found closest to the vibration frequency and not with the vibration frequency itself. However, the default value in Simla referred to free spans. For the jumper model, IL VIV is not limited to the low velocity range.
From experimental data, it was observed that large displacement in IL direction could occur for reduced velocities of up to eight. This is in agreement with the paper by Wang, Ji, Chi and Wu [23] who investigated the coupling of IL and CF motion and reported that IL motion contributed to the path described by cylinder motion for $V_{\text{red}} = 8$, while at $V_{\text{red}} = 10$ the IL motion was negligible.
Therefore, $\hat{f}_{1I1}$ was set to 0.13. With this value conservative results were obtained for all flow directions when the drag coefficient was kept at 1.1.

C_{Drag}

The drag coefficient is represented in the excitation force in Simla. A strength of this TD prediction tool is that it operates in local systems and automatically obtains the drag amplification during VIV. The drag force oscillates with twice the vortex shedding frequency. However, it is crucial to choose an appropriate value for the still-water drag coefficient, since amplification is applied on this. A lower drag coefficient led to larger VIV response amplitudes for IL VIV and often also for CF VIV due to coupling. Therefore, the effect of changes in the drag coefficient is in the same range for all load cases. The value of 1.1 was chosen after Wang et al. [18] who had reported this from the model test. Further, conservative response amplitudes were obtained for all flow directions with this value. An increased drag coefficient can be obtained e.g. by strakes for VIV mitigation.

CV

The default value of the CF lift force coefficient was 1.0, referring to straight pipes. For the ten and 45 degree flow, conservative results were obtained with the default value. For the 90 degree flow, motion in x-direction is associated with CF VIV. Due to the jumper geometry it is easier to excite large amplitudes in y-direction than in x-direction. Since in experimental data large responses were reported for x-direction in the 90 degree flow, the CF lift force coefficient had to be increased to 1.2.

5.4.2 Comparison of VIV motion

Experimental data was available for accelerometer positions three and five for the ten degree flow and accelerometers three and seven for the 45 and 90 degree flow directions. Accelerometer five is located on the top horizontal H2 next to the bend, while number seven is located at the center of H2. Accelerometer three is placed at the lower part of the jumper, next to the bend at vertical part V2, as shown in Figure 2.8.

For structures with similar geometry to the jumper model the displacement close to bends typically is smaller compared with the straight parts. Thus, the positions of accelerometers three and five are predestined if significant out-of-plane bending displacements are expected rather than rotational deformations or in-plane distortions. The position of accelerometer seven, on the contrary, is predestined to capture all kinds of deformation including rotation and in-plane bending.

In this section test data is plotted together with results from the DNV GL response model procedure and from the TD VIV tool in Simla. The CF response model depends on modal frequencies, thus, it is plotted for both the Pipe31 and Pipe34 model. Also, Simla results are plotted for both models. Comparison is made using the following parameters for VIV analysis.

$CVI1 = 1.2$

$CV = 1.2$

$C_{\text{Drag}} = 1.1$

$\hat{f}_{1\text{I}1} = 0.13$

Sensitivity to an increased drag coefficient $C_{\text{Drag}} = 1.2$ is discussed. Relative difference in percent is always calculated with respect to the Pipe34 model.

10° flow

In Figures 5.25 and 5.26 the displacement during VIV in x, y and z-direction is shown for the Pipe31 and Pipe34 model, respectively. From left to right each block represents a period of constant current velocity, starting at 0.05 m/s and increased in steps of 0.05 m/s up to 0.98 m/s. For numerical stability, each load case started from zero current speed and was increased to the required speed. Current velocity was also reduced to zero before a new load case started. Since a steady state was of greatest interest, the blocks in these Figures each represent a period of stable vibrations.

At the position of accelerometer five, response in x-direction dominates for both the Pipe31 and Pipe34 model for low current velocities of 0.1 to 0.2 m/s. For this flow direction, this is linked with IL VIV. For current velocities 0.25 to 0.98 m/s the maximum response occurs in y-direction, which is associated with CF VIV. For

U_c=0.05 m/s no VIV was observed. From oscillating frequencies it was concluded that the in-plane bending mode (mode three for Pipe31 and mode two for Pipe34 model) is active for low current velocities up to 0.2 m/s. From 0.25 m/s the out-of-plane bending mode (mode one) is active. Transition to the twist mode (mode two for Pipe31 and mode three for Pipe34 model) occurs between 0.50 and 0.55 m/s for the Pipe34 model and between 0.6 and 0.65 m/s for the Pipe31 model. The earlier transition of the Pipe34 model is in better agreement with observations from the model test reported by Wang et al. [18]. This transition also causes a cut in the moment and stress diagrams for the ten degree flow, as will be shown later. This is due to the change of oscillating frequency, direction of maximum VIV motion and amplitude of vibrations.

Figures 5.27 to 5.29 show the ten degree amplitude response plotted over reduced velocities measured at accelerometer five. Both the Pipe31 and the Pipe34 model results are in very good agreement with experimental data.

In x-direction significant response from the simulations and test data is observed around $V_{\text{red}} = 1.7$, which is linked to the first IL instability region and first lock-in region. The largest results here come from the simulations at 0.15 and 0.2 m/s. No response was recorded in the second IL instability region, which would occur around $V_{\text{red}} = 2.5$. However, about twice as large IL response compared to the first instability region occurs at reduced velocities between six and eight, presumably due to CF-induced IL VIV. Larger amplitudes compared to the first and second instability region without lock-in are characteristic for the CF-induced IL region.

Peak values for pure CF VIV in y-direction are observed as in the model test at reduced velocities from six to eight. As mentioned previously, model test results show quite narrow peaks, while they are spread wider in Simla results. However, the Simla models are in a conservative range.

For motion in z-direction, the Simla models reach their maximum response at higher reduced velocities, between ten and twelve, while it occurs between six and eight in experimental data. However, the results in z-direction are very small for this flow direction. Generally, there is some uncertainty about reduced velocities, whether they are calculated from the modal frequency associated with motion in each direction individually or from the modal frequency found for the direction of maximum response.

For motion in x and z-direction, the Pipe34 model gives larger response than the Pipe31 model due to its decreased stiffness in the bends. The largest relative difference measures 17.4 percent and appears at $V_{\text{red}} = 6$ for the x-direction. Also, in z-direction the Pipe34 results are up to 17 percent larger around the same reduced velocity. In y-direction the Pipe31 model gives up to four percent larger responses when mode one is active. On the other hand, when the twist mode is dominant the

Pipe34 model shows larger response amplitudes in y-direction, too, with up to 10.5 percent difference.
When the drag coefficient is increased from 1.1 to 1.2, all VIV response amplitudes turn out smaller, but the Pipe31 results are more affected than the Pipe34 results. Since drag affects the IL force, the biggest difference for the Pipe31 model occurs for x and z-directions with an average decrease of seven and 6.3 percent, respectively. For the Pipe34 model the average difference in IL direction is only 0.7 percent.
Regarding the DNV GL response models, it is observed that they are very conservative for CF VIV. The maximum amplitude in particular is predicted over a very wide range of reduced velocities. For IL VIV the response model fits the maximum amplitudes for reduced velocities up to four. A drawback of the response model is that CF-induced IL VIV is only considered when stress ranges are calculated, but no amplitude response estimates are given for it. However, the formulation for stress ranges of CF-induced IL VIV is similar to the one for pure CF VIV, but scaled with factor 0.8 instead of factor two. With this knowledge it can be assumed that the response model also gives conservative results for CF-induced IL VIV over a wide span of reduced velocities.
Amplitude responses at accelerometer three are shown in Figures 5.30 to 5.32. Since this is located at the shorter part V2, smaller responses were expected compared to the ones from accelerometer five. In contrast to this, model test data showed significantly larger response in y-direction than for accelerometer five. Therefore, the data was considered less credible for comparison.
However, responses of the Simla models could be compared. Oscillating frequencies are in agreement with the active modes identified from the data at accelerometer position five. Also here, the Pipe34 model showed larger amplitudes in x and z-direction, while the Pipe31 model showed larger response in y-direction. For $C_{\mathrm{Drag}} = 1.2$ the results in all three directions are affected to a very similar extent. A decrease in results between 4.1 (for x-direction) and 4.9 (in y-direction) percent on the average is observed.
Altogether, the simulation results from Simla are in very good agreement with experimental data. Wang et al. [18] reported a strong IL VIV response at 0.206 m/s with an oscillating frequency close to the second modal frequency and an out-of-plane twist vibration at 0.527 m/s associated with the third modal frequency. Strong CF response with a frequency close to the first modal frequency was reported for 0.412 m/s. The Simla results show a promising correlation with test data.

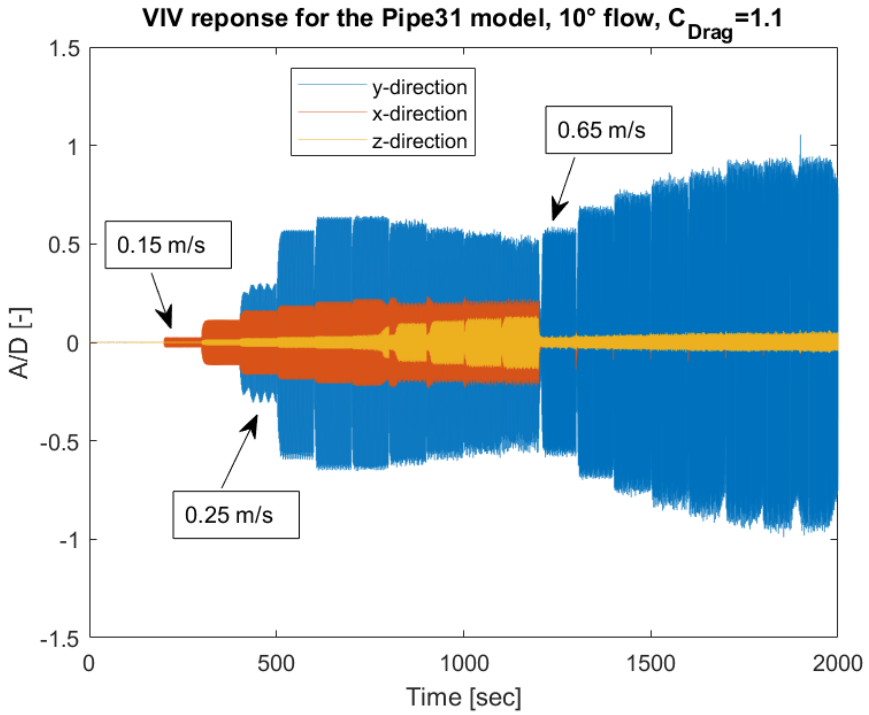

Figure 5.25: Displacement of Pipe31 model at accelerometer five for the 10° flow. Load cases from left to right are the current velocities from 0.05 to 0.98 m/s increased in steps of 0.05 m/s. For each load case, the current speed started at zero and was reduced to zero again after a time of stable vibrations.

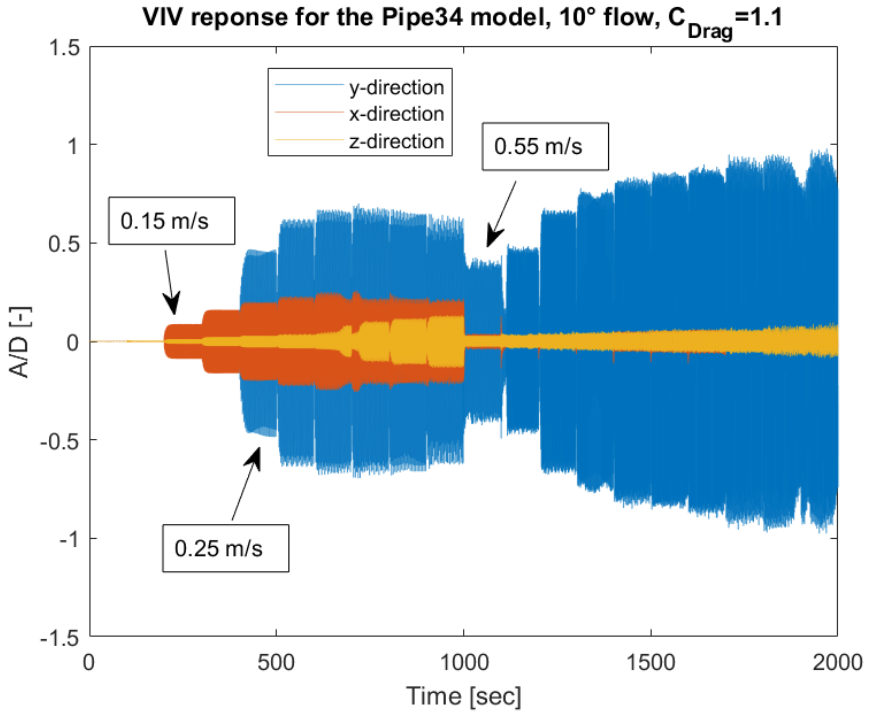

Figure 5.26: Displacement of Pipe34 model at accelerometer five for the 10° flow. Load cases from left to right are the current velocities from 0.05 to 0.98 m/s increased in steps of 0.05 m/s. For each load case, the current speed started at zero and was reduced to zero again after a time of stable vibrations.

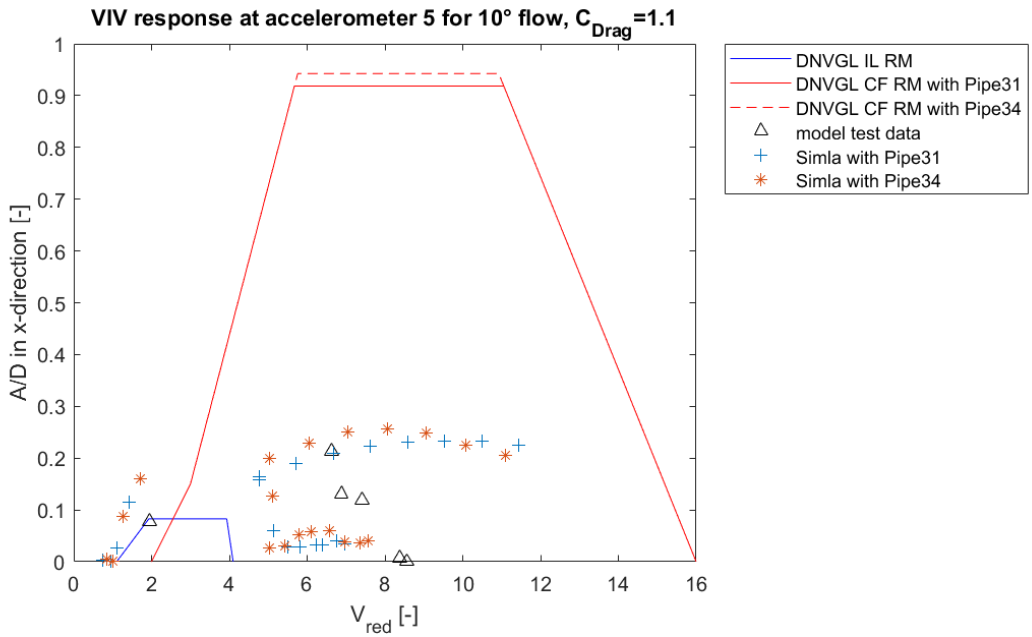

Figure 5.27: Comparison of VIV response in x-direction for 10° flow at accelerometer five.

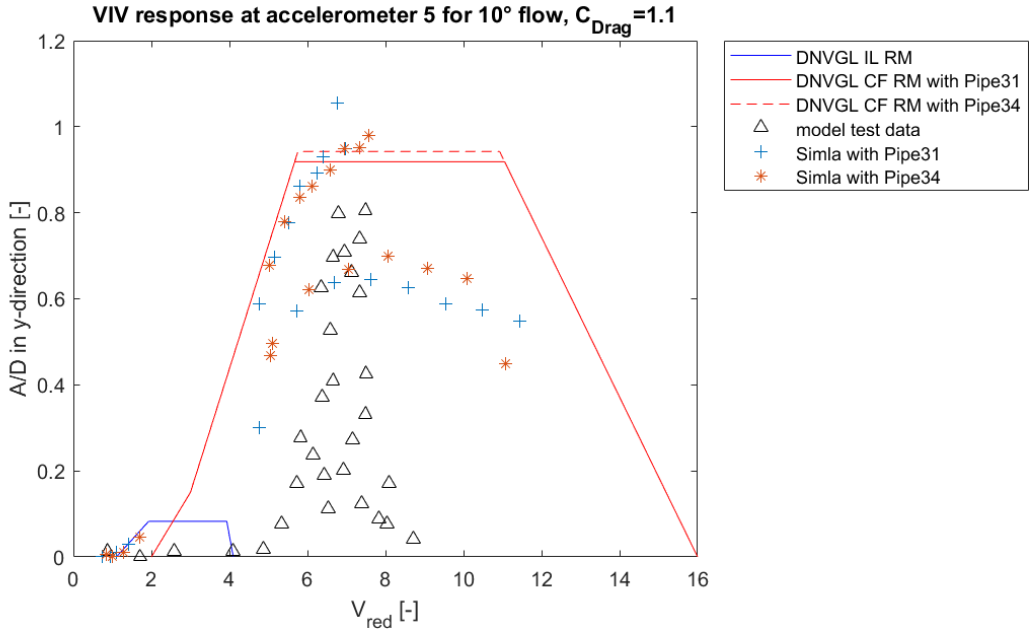

Figure 5.28: Comparison of VIV response in y-direction for 10° flow at accelerometer five.

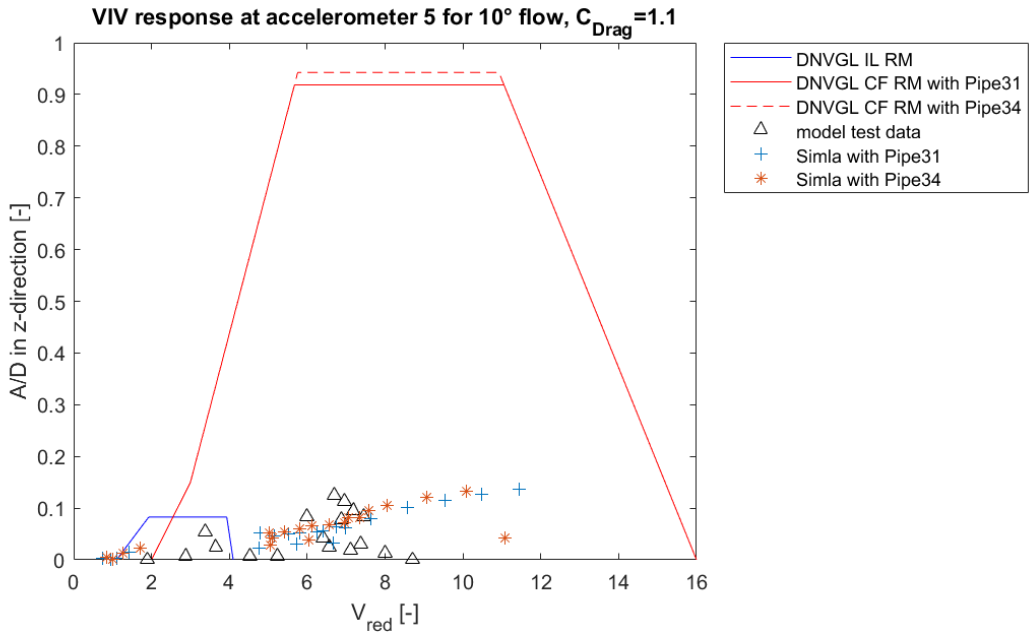

Figure 5.29: Comparison of VIV response in z-direction for 10° flow at accelerometer five.

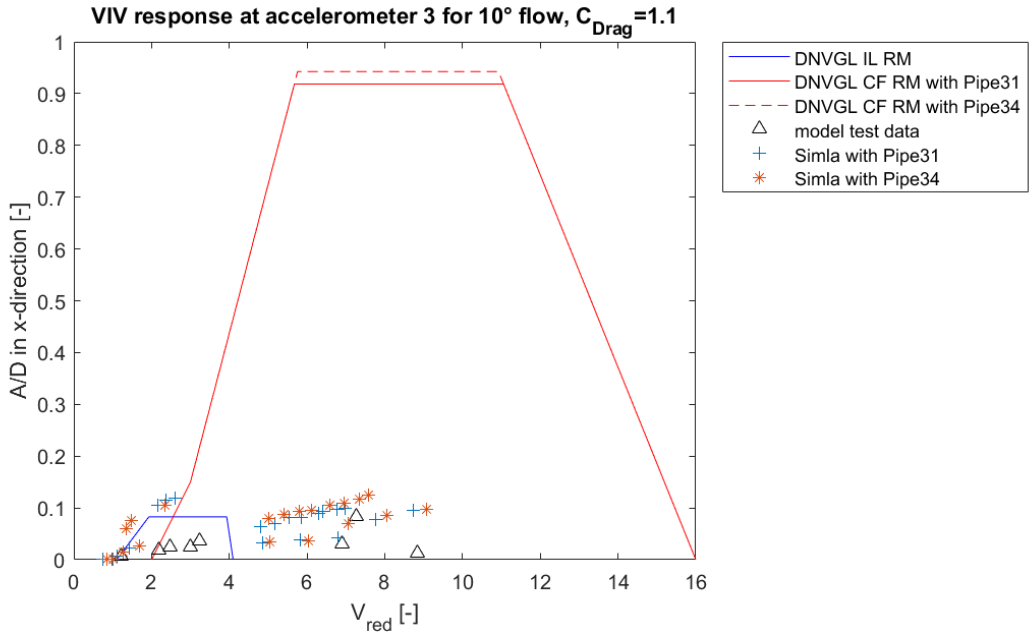

Figure 5.30: Comparison of VIV response in x-direction for 10° flow at accelerometer three.

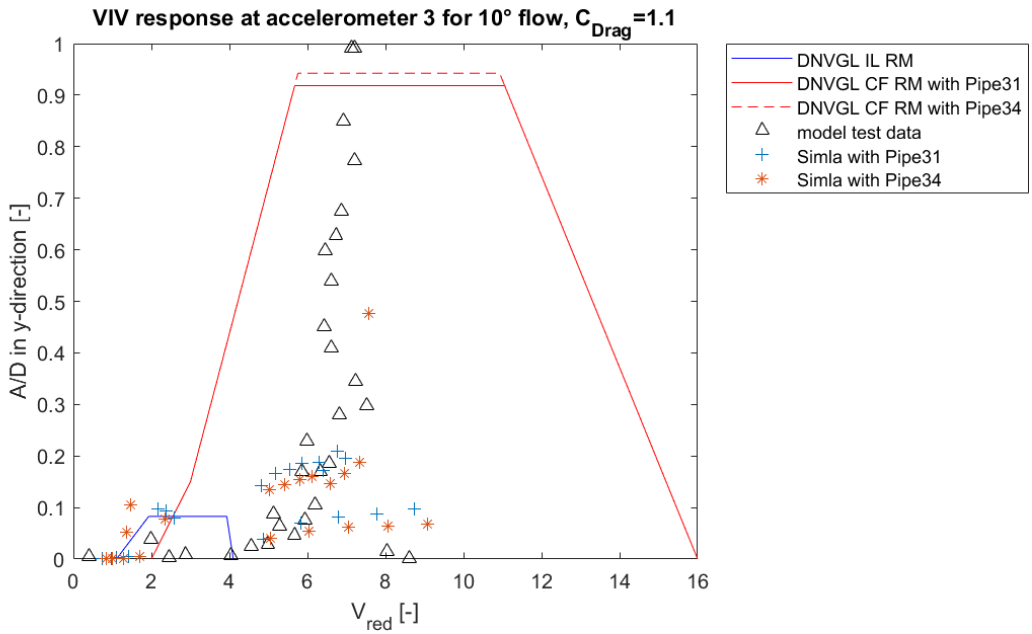

Figure 5.31: Comparison of VIV response in y-direction for 10° flow at accelerometer three.

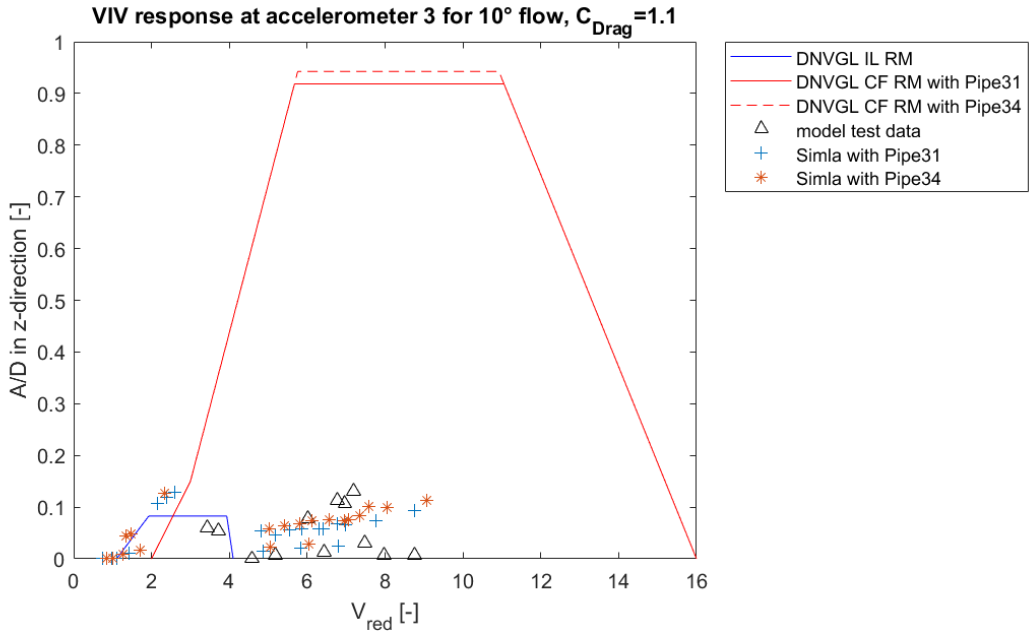

Figure 5.32: Comparison of VIV response in z-direction for 10° flow at accelerometer three.

90° flow

Figures 5.33 and 5.34 show the displacement in x, y and z-direction of respectively Pipe31 and Pipe34 model for 90 degree flow. For this flow angle, several current velocities show peaks in the beginning or end of the load case, where the current speed was increased or decreased. For current velocities between 0.7 and 0.79 m/s the response amplitudes in y-direction were not stable, even in the region where the current speed was constant. To find oscillating frequencies and response amplitudes, narrow peaks were excluded from the analysis. Nonetheless, for this flow direction it takes more time to reach a state of stable vibrations compared with the ten degree flow. What happens in y-direction for the highest current velocities could be observed during a longer simulation. As an example, the displacement in y-direction for 0.75 m/s is plotted from a simulation over 200 seconds in Figure 5.35. The displacement here is not scaled around a zero mean like it was done for the cases with stable vibrations. Unlike other load cases, the oscillating frequencies from rainflow counting and from FFT do not agree for this case. In the beginning, the oscillating frequency from rainflow counting is close to the natural frequency of mode nine, while from FFT it is close to mode one. This indicates that smaller and bigger cycles are present in the signal. After a period of irregular response, it approaches the same frequencies, but with smaller response amplitude. Finally, the signal approaches a frequency close to the first modal frequency, both when rainflow counting and FFT is applied, but amplitudes are very large. When the current velocity was not ramped out at this point, but the simulation prolonged, numerical problems occurred.

From the model test it was reported that end dynamometers had reached their load capacity and, thus, simulations were not continued beyond 0.79 m/s [18]. The correlation of results is interesting and shows that these load cases are critical. In Simla, quite a stable response was obtained for x and z-direction, also for the largest current velocities, which may be used for comparison.

For this flow angle the response in y-direction, which is associated with IL VIV, dominates for both models up to 0.3 m/s. The oscillating frequency is closest to the first modal frequency. For further increased current velocities, from 0.4 to 0.65 m/s the in-plane bending mode (mode three and two for Pipe31 and Pipe34, respectively) is active with largest non-dimensional amplitudes in x-direction. For the 90 degree flow, this is associated with CF VIV. Due to decreased stiffness, the Pipe34 model shows significantly larger responses in x-direction for above mentioned flow velocities. This is represented in Figure 5.36 for reduced velocities around five. Nonetheless, the peak values which occur at reduced velocities around six are in good agreement for both models and also in good correlation with experimental

results.
From 0.7 to 0.79 m/s the maximum response occurs in z-direction. For these load cases both models again show very similar response. The oscillating frequency is closest to the natural frequency of mode four, which is the up-and-down bending mode.
In Figures 5.36 to 5.38 the Simla results for both models at accelerometer seven are compared with model test data and the DNV GL response models, plotted over reduced velocities. Since the ratio of consecutive CF modes is similar for the Pipe31 and Pipe34 model for this flow direction, there is only one CF response model. For all three directions, the Simla results are in correlation with experimental data. For z-direction the Simla response might be over-conservative, but the plots for x and y-direction justify to keep both force coefficients in the VIV tool at 1.2.
When the drag coefficient is increased to 1.2, the Pipe31 results are more affected for higher current velocities than the Pipe34 results. For x and z-direction Pipe31 results are decreased by about 16 percent due to increased drag.
Regarding the DNV GL response models, the conclusion is similar as for the ten degree flow. The CF response model has a far wider range where large amplitudes are expected compared with the Simla and model test data .
At the position of accelerometer three stable vibrations were observed for all current velocities in Simla. The response in y-direction dominates up to $U_c = 0.6$ m/s. The oscillating frequency here is associated with the frequency of mode one for the lowest current velocities up to 0.2 m/s, and later with mode five whose mode shape shows symmetric out-of-plane bending of the two shorter horizontals. For all higher current velocities the oscillating frequency is closest to the fourth modal frequency for both models. This is in agreement with the findings from accelerometer position seven. In Figures 5.39 to 5.41 the simulation results are compared with experimental data and the DNV GL response models. The response in Simla is a bit offset from model test results with respect to reduced velocities. In especially occur peak values from the Simla results at lower reduced velocities than from experimental data. The maximum responses in x and z-direction come from the simulation at 0.7 to 0.79 m/s. It is not known which oscillating frequency was measured during the experiment for the 90 degree flow and, thus, from which modal frequency the reduced velocities were calculated. However, the large response in z-direction supports the assumption that the oscillating frequency was close to the fourth modal frequency. Further, the responses from the two Simla models overestimate amplitudes for x and z-direction at this location, while at the position of accelerometer seven they just met the experimental data. Thus, VIV motion from the TD tool gives conservative results also for this flow angle. When the drag coefficient was increased to 1.2, a small reduction in peak values was observed of 4.7 to 6.4 percent.

For the 90 degree flow, less detailed description was available from the model test. Especially, it was not reported for which flow velocities largest responses or mode shifts occurred. However, from A/D-comparison plotted over reduced velocities, the simulation results are in good correlation with experimental data.

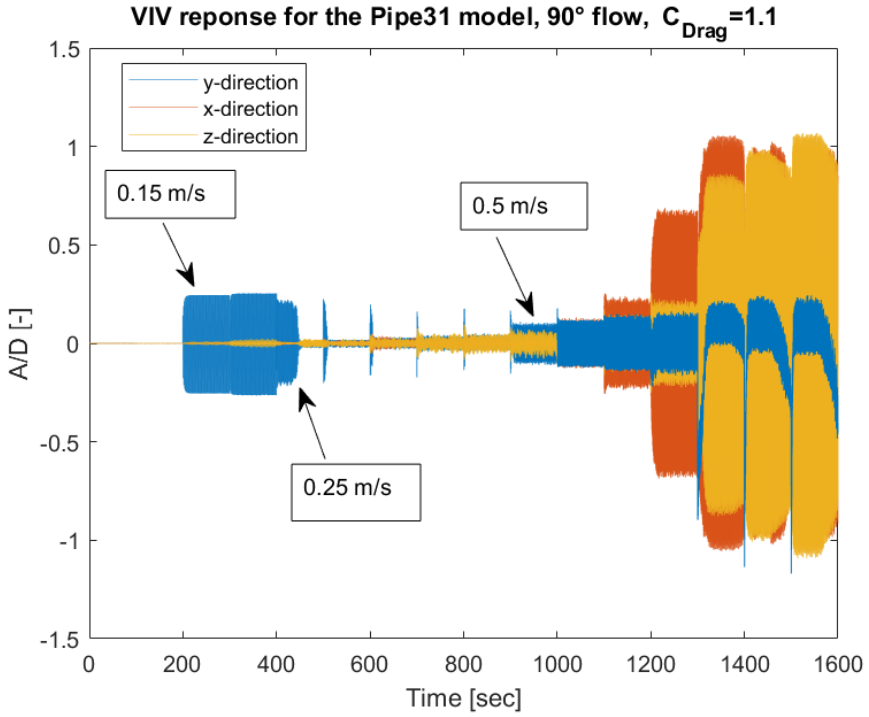

Figure 5.33: Displacement of Pipe31 model at accelerometer seven for the 90° flow. Load cases from left to right are the current velocities from 0.05 to 0.79 m/s increased in steps of 0.05 m/s. For each load case, the current speed started at zero and was reduced to zero again after a time of stable vibrations.

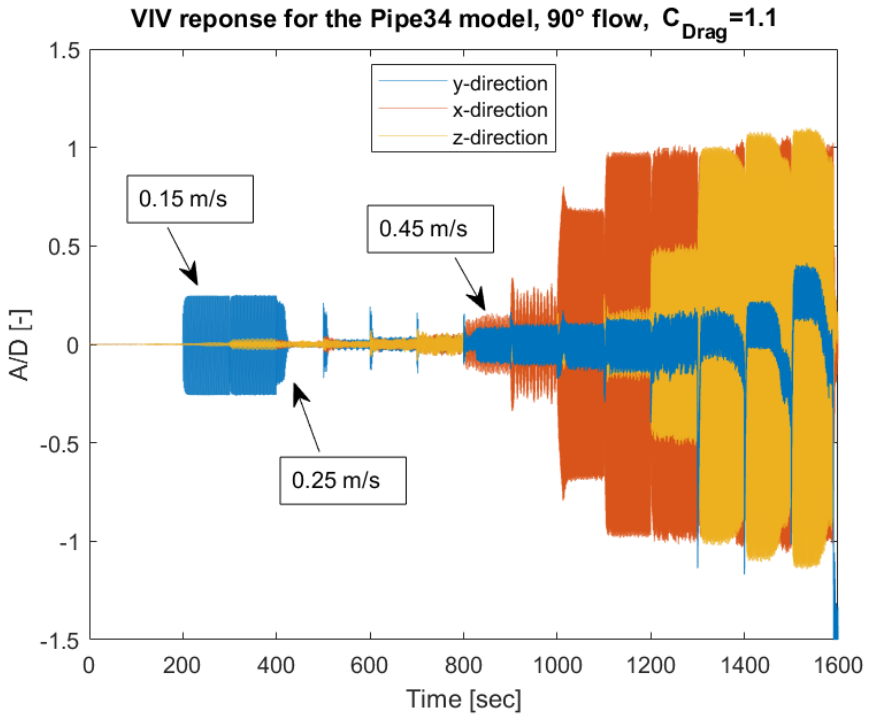

Figure 5.34: Displacement of Pipe34 model at accelerometer seven for the 90° flow. Load cases from left to right are the current velocities from 0.05 to 0.79 m/s increased in steps of 0.05 m/s. For each load case, the current speed started at zero and was reduced to zero again after a time of stable vibrations.

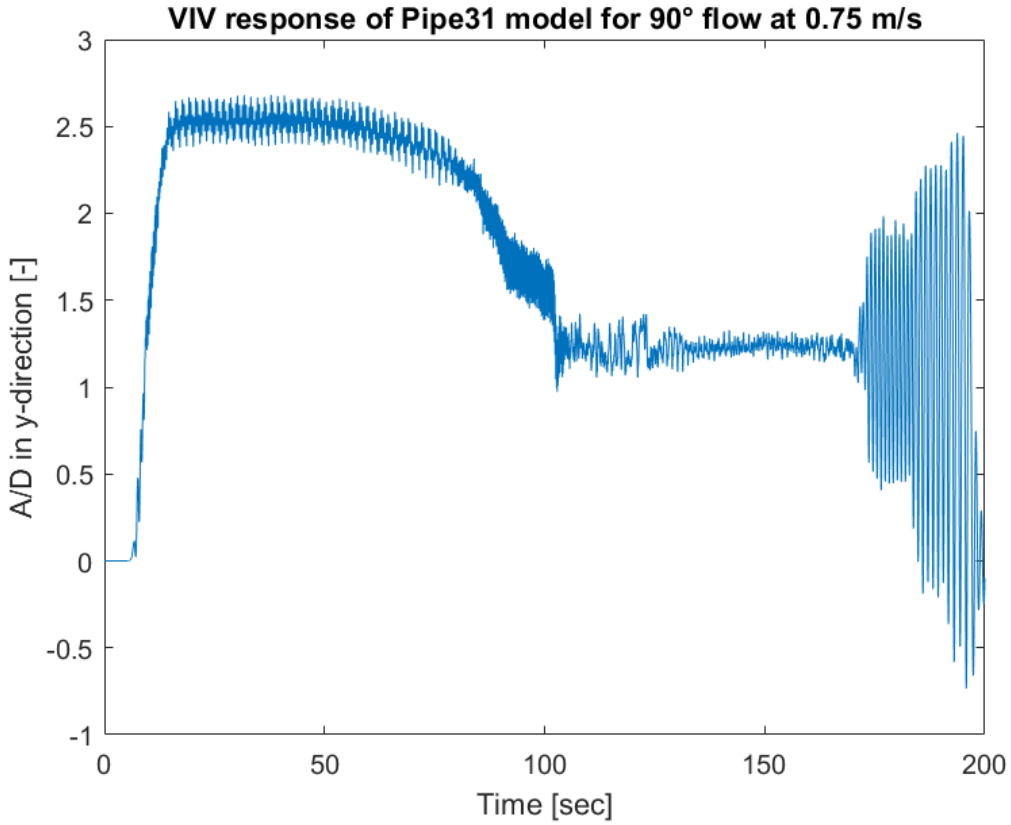

Figure 5.35: Displacement in y-direction for Pipe31 model at accelerometer seven for the 90° flow. Current velocity U_c=0.75 m/s.

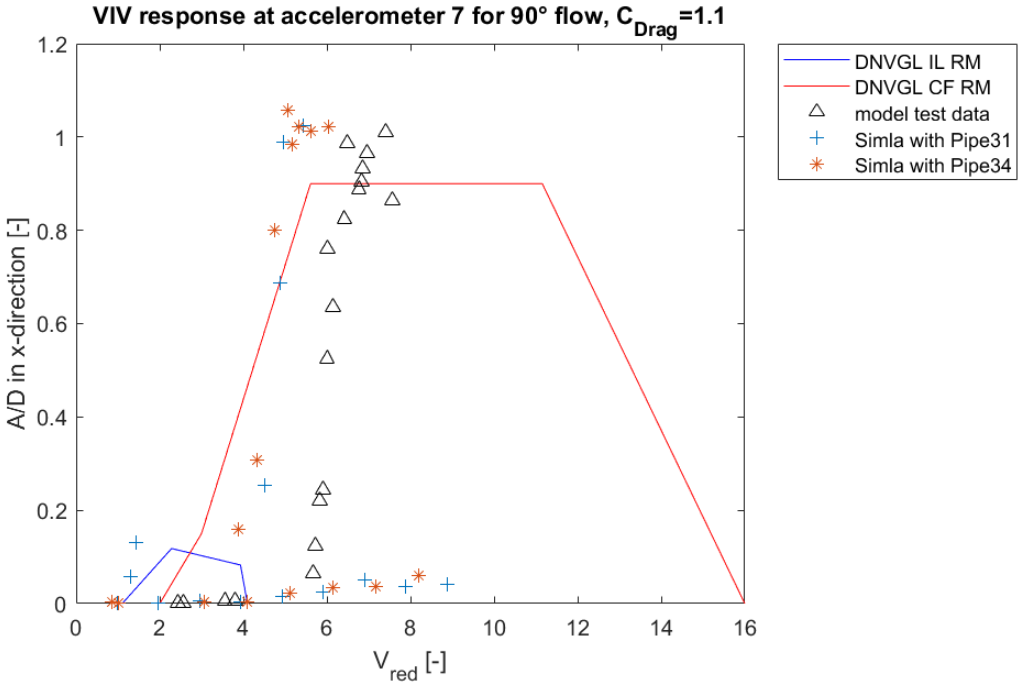

Figure 5.36: Comparison of VIV response in x-direction for 90° flow at accelerometer seven.

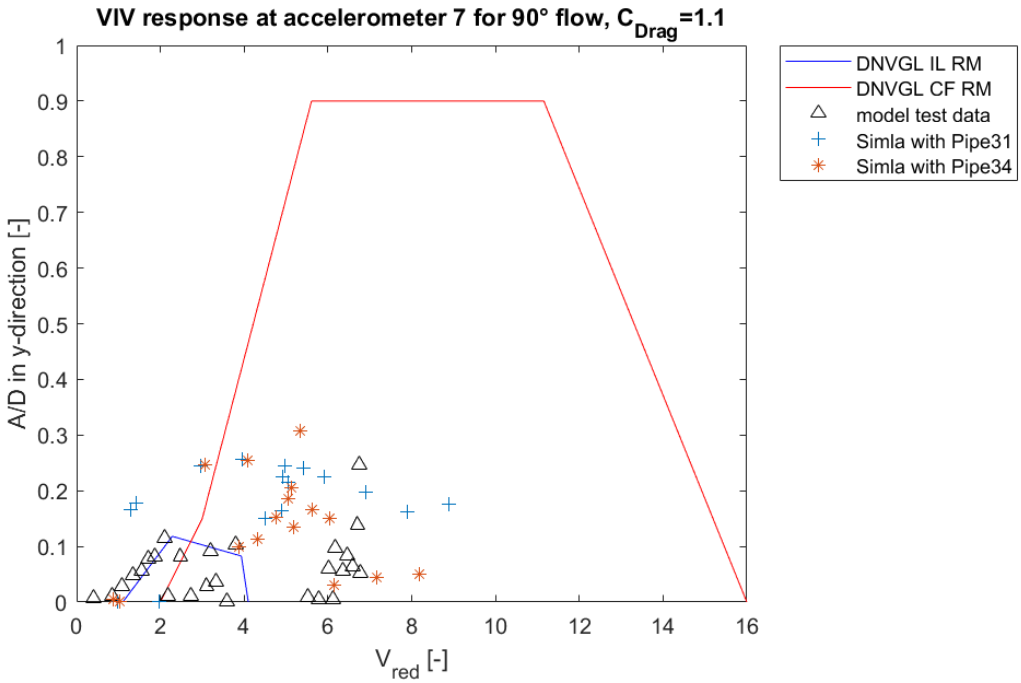

Figure 5.37: Comparison of VIV response in y-direction for 90° flow at accelerometer seven.

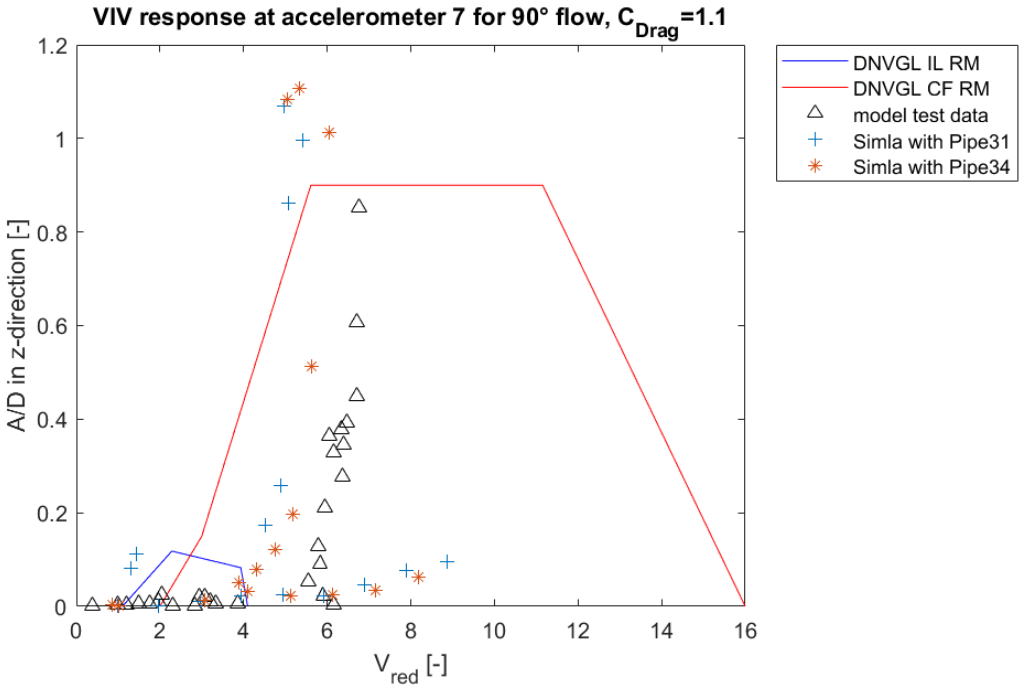

Figure 5.38: Comparison of VIV response in z-direction for 90° flow at accelerometer seven.

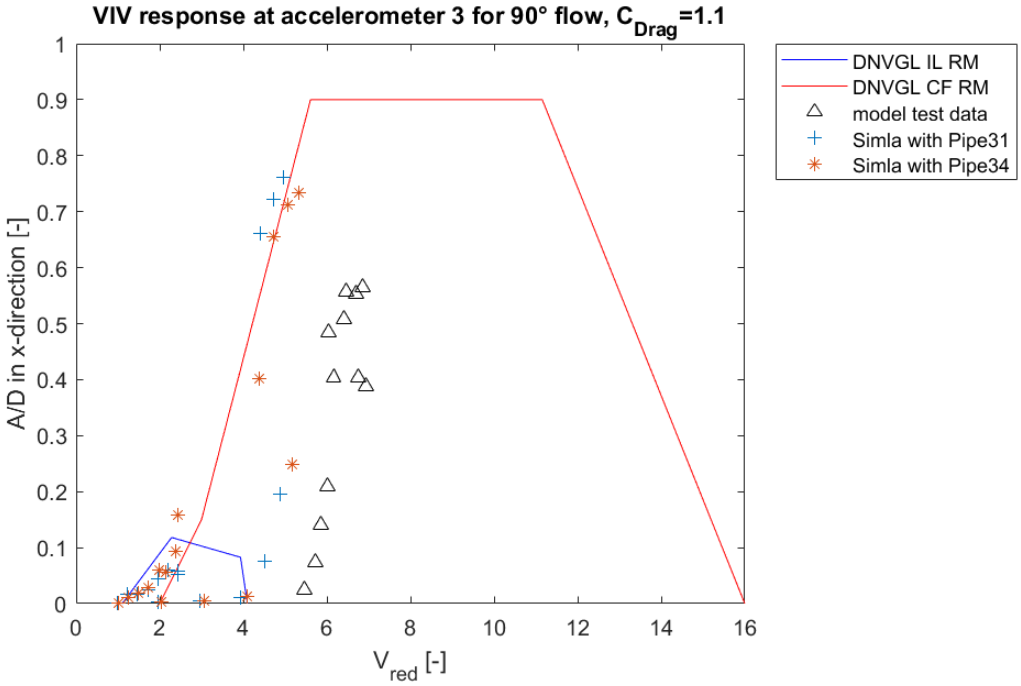

Figure 5.39: Comparison of VIV response in x-direction for 90° flow at accelerometer three.

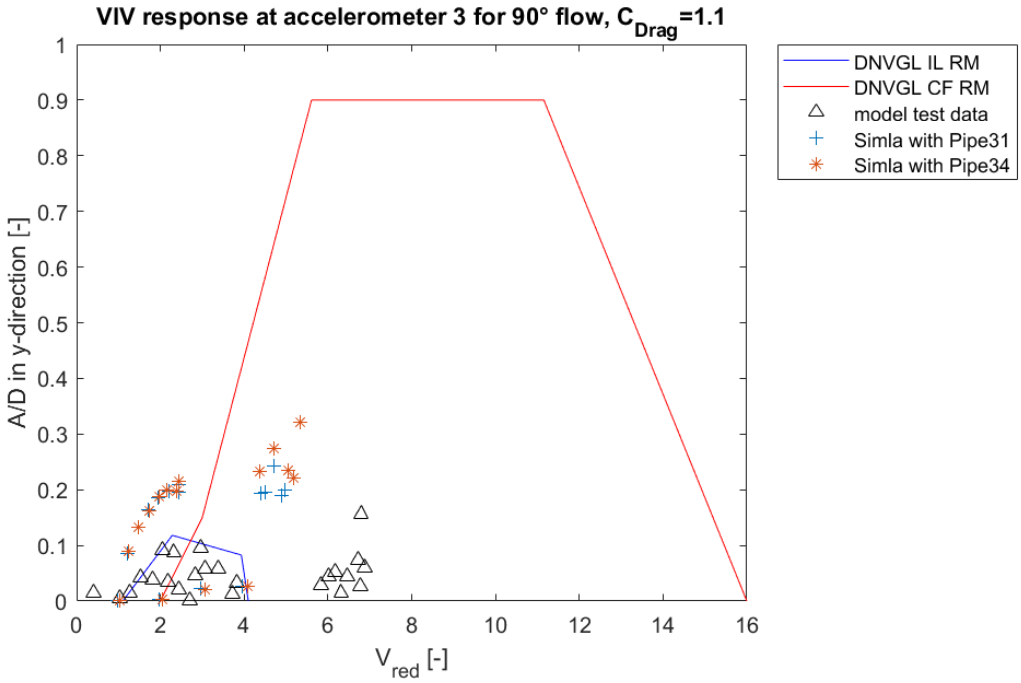

Figure 5.40: Comparison of VIV response in y-direction for 90° flow at accelerometer three.

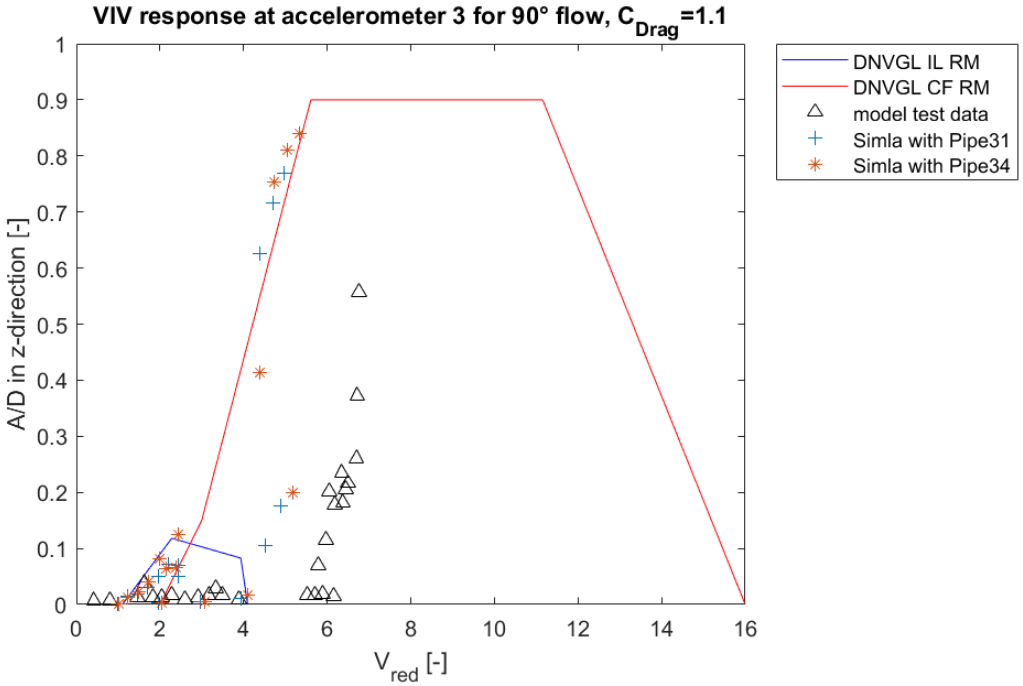

Figure 5.41: Comparison of VIV response in z-direction for 90° flow at accelerometer three.

45° flow

For the 45 degree flow direction it is more complex to identify IL and CF VIV. For the DNV GL response model approach it was considered that all modes with maximum deformation in x and y-direction could be both IL and CF modes, while the ones with maximum displacement in z-direction can solely be CF modes. In the Simla VIV tool it is not necessary to decide which direction is associated with which kind of VIV.

The time signals at location of accelerometer seven are plotted in Figures 5.42 and 5.43. For low velocity currents the response in y-direction shows maximum amplitudes and its oscillating frequency is associated with mode one. For the Pipe31 model the response in y-direction remains dominating up to 0.8 m/s, where the response in x-direction becomes larger for higher load cases. For the Pipe34 model, the response in x-direction is significant also for lower current velocities (0.25, 0.3 and 0.4 m/s) and is dominating for current velocities of 0.65 to 0.9 m/s. For these current velocities the mode with its frequency closest to the oscillating frequency is mode two for both models. Since both x and y-direction show large amplitudes for low velocity currents, it supports the theory that modes with main displacement in either of the directions must be considered for IL VIV, when the response model approach is used. The response in z-direction only becomes large for the highest current velocities and oscillates with a frequency close to the fourth modal frequency. For many current velocities the signal is not steady at this flow angle and amplitudes are decreased or increased during a period of steady flow. Especially for some lower current velocities the response starts with large amplitudes in y-direction, which are canceled out soon and are followed by VIV motions in x or z-direction. This indicates that different types of oscillations are overlaying or cancel out each other. It stands out that changes of vibration amplitudes during a single load case are more significant for the Pipe31 model than for the softer Pipe34 model, especially for low current velocities.

In the scope of this thesis it was not possible to explore all irregularities, e.g. transition between modal frequencies for each current velocities. However, these cases are very interesting, since rapid chances in structural dynamics also affect the flow and much energy is transferred.

It is also interesting that the Pipe31 signal is more volatile than the Pipe34 model. For the Pipe31 model, longer simulations were run to observe the development of VIV motion. Results over a region with stable vibrations were used for comparison, as shown in Figures 5.44 to 5.46. The Simla results are in a conservative range and describe the peak response at reduced velocities between six and eight where they occur also in test data. For both models very large response in z-direction was observed for the highest current velocities, which is represented at V_{red}=6. For the

other current velocities, on the other hand, the results are in good correlation.
Since the trend for all three flow directions is that responses at largest current velocities are over-conservative, it can be considered to decrease the TD VIV tool parameters CV and CVI1 for these cases in future work.
The guideline's response model approach is quite over-conservative for CF VIV and CF-induced IL VIV.

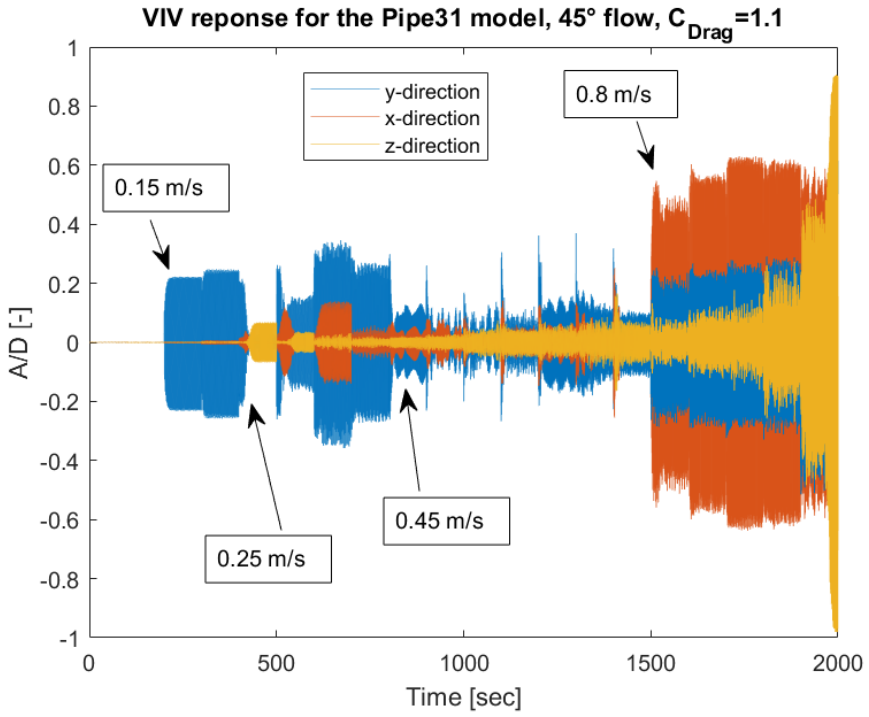

Figure 5.42: Displacement of Pipe31 model at accelerometer seven for the 45° flow. Load cases from left to right are the current velocities from 0.05 to 0.98 m/s increased in steps of 0.05 m/s. For each load case, the current speed started at zero and was reduced to zero again after a time of stable vibrations.

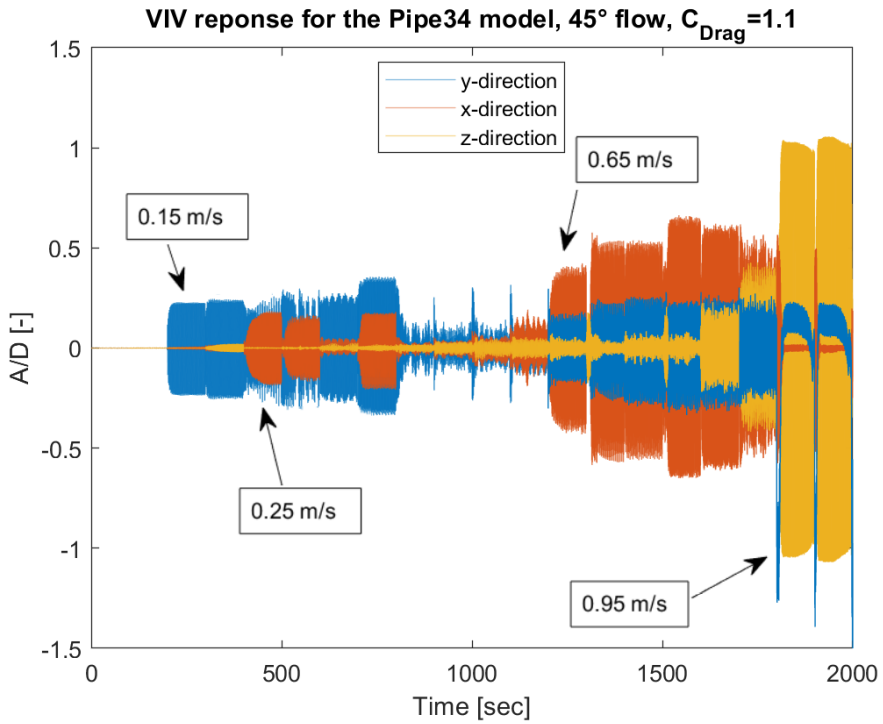

Figure 5.43: Displacement of Pipe34 model at accelerometer seven for the 45° flow. Load cases from left to right are the current velocities from 0.05 to 0.98 m/s increased in steps of 0.05 m/s. For each load case, the current speed started at zero and was reduced to zero again after a time of stable vibrations.

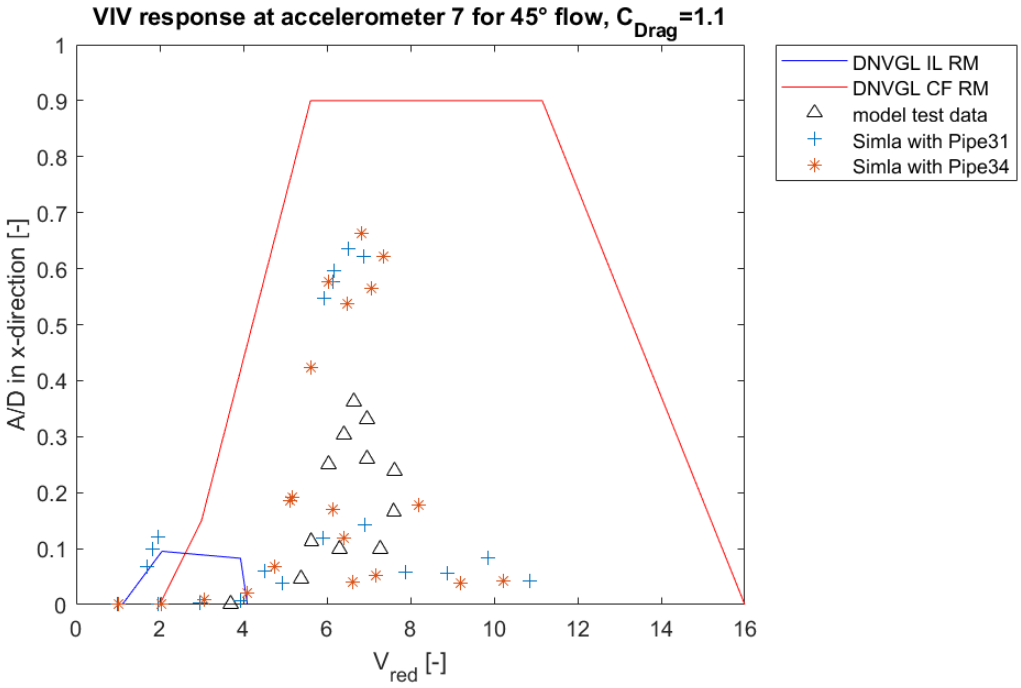

Figure 5.44: Comparison of VIV response in x-direction for 45° flow at accelerometer seven.

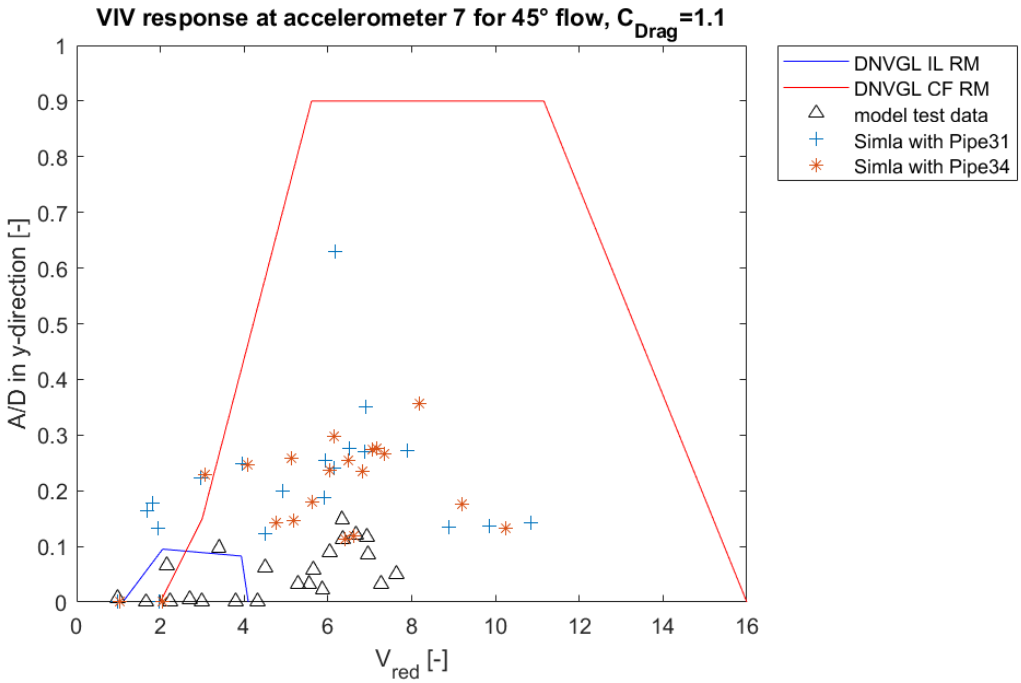

Figure 5.45: Comparison of VIV response in y-direction for 45° flow at accelerometer seven.

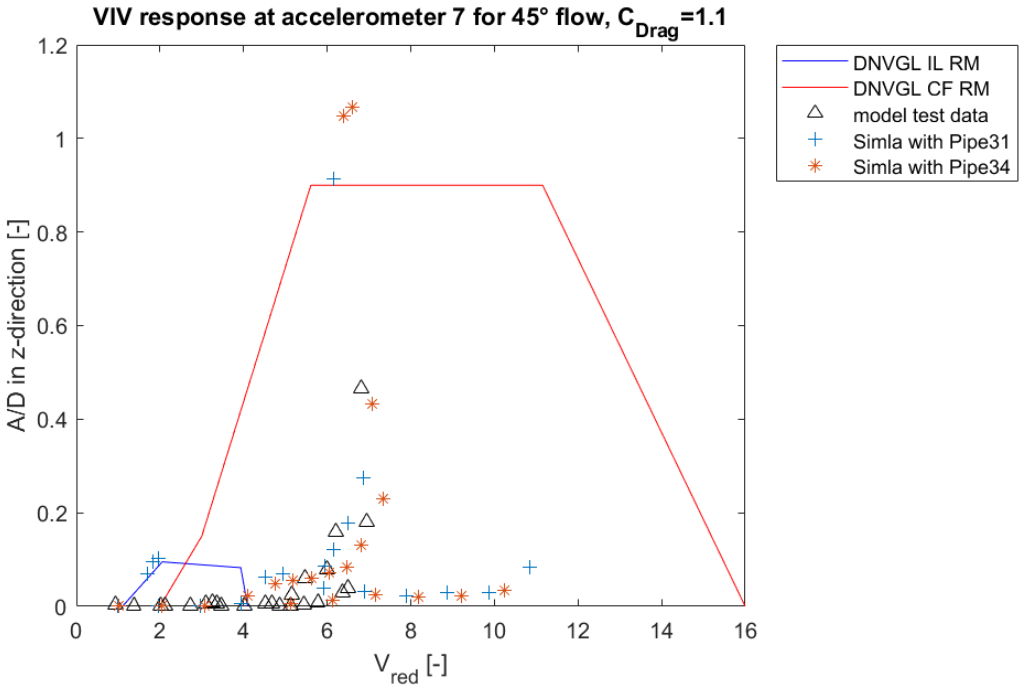

Figure 5.46: Comparison of VIV response in z-direction for 45° flow at accelerometer seven.

5.4.3 Summary of the section about VIV motion

- The dominating VIV response with respect to direction of motion and location along the jumper could be associated with one of the first four modes for all three flow directions. Thus, these four modes require highest standards of accuracy. In the direction where smaller VIV motion occurred and at the shorter jumper segments, also higher modal frequencies were identified.

- The Simla results are in a conservative range and in good correlation with test data. Thus, the VIV tool is promising for non-straight geometries in steady flow. The DNV GL response models are very conservative for the jumper model, especially for CF VIV. Both from experimental data and from the Simla VIV tool peak values occurred for reduced velocities of six to eight and in quite a narrow range for most load cases.

- For the ten degree flow, VIV histories have very stable amplitudes. For the 90 degree flow, irregularities are observed when the current velocity changes and for the highest load cases, while for the 45 degree flow irregularities are present for most load cases.
  Generally, the 45 degree flow is very interesting, since VIV motions in the different directions tend to cancel out each other and are followed by a different vibration pattern during a steady flow condition. These rapid chances in structural dynamics also affect the flow.

- The Pipe31 model tends to have more volatile VIV response than the Pipe34 model. This makes sense, since stiffer structures generally show higher-frequent response, while softer ones oscillate with lower frequencies. Presumably, the Pipe34 model is less sensitive to higher-frequent disturbances. This can be in favor to observe a steady state of vibrations.

- The shift from one oscillation pattern to another one (with respect to oscillating frequency and direction of largest amplitudes) for consecutive load cases happened at lower current velocities for the Pipe34 model than for the Pipe31 model.

- When the drag coefficient is increased, the IL VIV results of the Pipe31 are more affected than of the Pipe34 model. This indicates that the higher drag coefficient has a softening effect on the structure in flow direction.

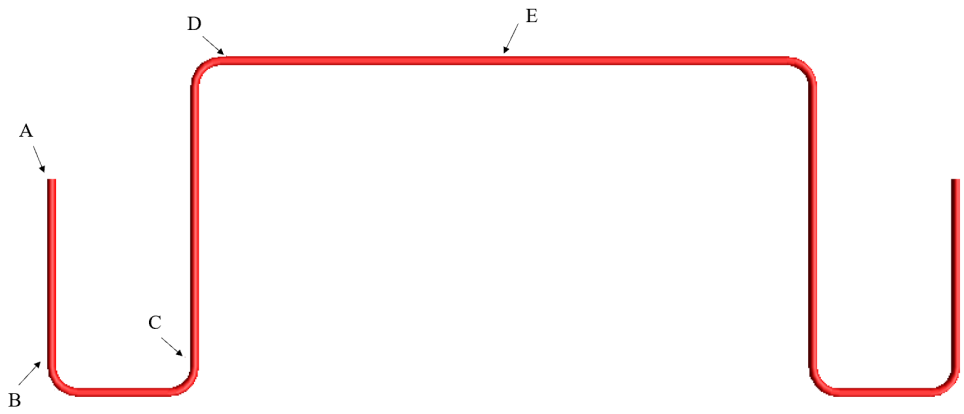

Figure 5.47: Critical locations for stress assessment along the jumper

5.5 Stresses and fatigue damage for VIV

The stress ranges for fatigue calculations were assessed by two different methods. One of them was to follow the procedure proposed in DNVGL-RP-F105 and using modal stresses obtained from Simla. The other one was to use the moment output from TD analysis in Simla directly and apply rainflow counting on obtained stress signals.

To get comparable results all safety factors in the DNV GL response model were set to one.

Stresses were compared at five locations (A to E) as shown in Figure 5.47, which are considered as critical locations. As discussed earlier, maximum modal stresses usually occurred in the ends for the Pipe31 models and in the bends for the Elbow element models. Accordingly, the jumper end was chosen as one of the critical locations. Since welds are usually placed next to the bend parts, but with a small offset, the elements next to the bends and at the longer of two adjacent straight parts were chosen as locations B to D. Location E is the center of the top horizontal, which is the part with longest unsupported length.

Moment signals were extracted from Simla and the observations fit into one of the the following three patterns:

(1) Steady oscillations over the observed time. When ramped on, the oscillating moments increased smoothly. When ramped off, they decreased smoothly.

(2) Steady oscillations at the beginning of the simulation, later transition to another steady pattern.

(3) Steady oscillations over most of the time. When current velocity was ramped out, large peaks occurred in the moment signal.

10° flow

For the ten degree flow, very stable oscillations were observed for the lower current velocities, while the signal for higher current velocities became more volatile. Large peaks were observed for U_c =0.98 m/s. At location A next to the support a transition from one oscillation pattern with smaller amplitudes to one with larger amplitudes was observed at 0.4 m/s. This is shown in Figure 5.48. During longer simulations for this case it was observed that before the transition the oscillation frequency is close to the third modal frequency, while after it the oscillation frequency is close to the seventh modal frequency. These events can be interesting for future model test series. Since both the equivalent stress range and frequency are larger after the transition and it remains stable, only the latter case was taken into account for fatigue calculation. Torsional moments are close to zero in the IL VIV region up to 0.2 m/s. For locations A and B, which are closer to the support, torsional moments are present for higher current velocities, but still comparatively small for this flow angle. Therefore, fatigue estimates from the first principal stress are dominated by flexural stresses. The fatigue damage obtained from Simla is shown in Figure 5.49 for location A. For the Pipe34 model, a change in the moment signal is also seen between U_c=0.5 m/s and 0.55 m/s, since the out-of-plane twist mode becomes active here.

For comparison the fatigue damage obtained from the DNV GL response model procedure is shown in Figure 5.50. Also here, the main contribution to the maximum principal stress comes from flexural stresses. The damage estimates for current velocities 0.5 to 0.6 m/s stand out from the other current velocities. The contribution from IL VIV and CF VIV can be observed separately in Figure 5.51. Here it is seen that the drop of fatigue estimates is due to jumps in IL VIV fatigue damage. This is because of small contribution from the pure IL response model for current velocities of 0.5 m/s and higher, while at 0.65 m/s the contribution from CF-induced IL VIV becomes larger. At 0.9 m/s also CF-induced IL VIV is smaller.

For both methods the overall fatigue damage has its maximum at location A. For current velocities 0.05 and 0.1 m/s Simla gives larger fatigue estimates, while for the higher current velocities, the DNV GL response model procedure calculates significantly higher fatigue damage.

At locations C, D and E torsional moments become more significant for larger current velocities. As an example the moment history from Simla at location E is shown in Figure 5.52 and associated fatigue damage in Figure 5.53. For current velocities of 0.6 m/s and higher, torsional stresses have a relevant contribution to fatigue damage. The DNV GL response model fatigue estimates at the same location are shown in Figure 5.54. Here, torsional stresses slowly increase within the plotted range starting at 0.3 m/s. For lower current velocities from 0.05 to 0.2 m/s the fatigue damage

obtained with Simla is larger than from the response model approach. For higher current velocities the damage from flexural stress and thus, from the first principal stress is estimated higher with the DNV GL procedure than with the Simla output. Damage from torsional stresses is similar from both methods. In the DNV GL procedure all active modes apply their full stress range, which can lead to over-estimation of fatigue damage. Torsional stresses do not occur for all modes, thus, this effect is less significant here. When excluding the load case with 0.55 m/s, the fatigue damage at location E differs by up to factor 20 and the largest difference occurs for the highest current velocities. However, the difference at location A is much larger. This indicates, that the jumper ends experience far less VIV stress in a TD simulation than obtained from the guidelines by scaling modal stresses.

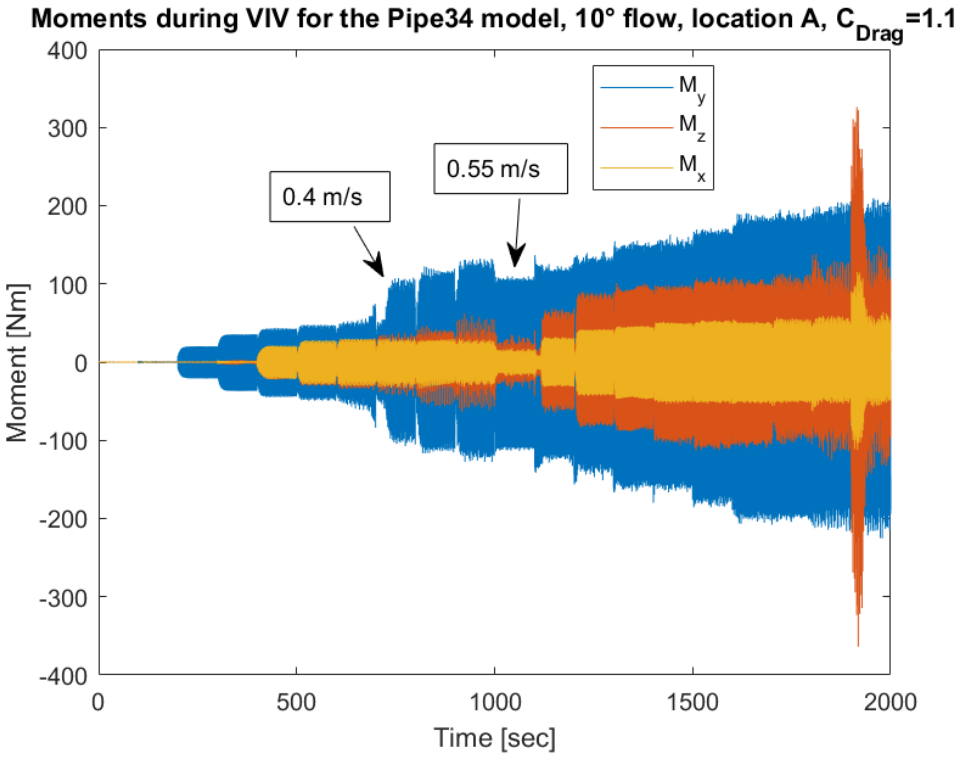

Figure 5.48: Moment signal during VIV for the Pipe34 model in 10° flow at location A

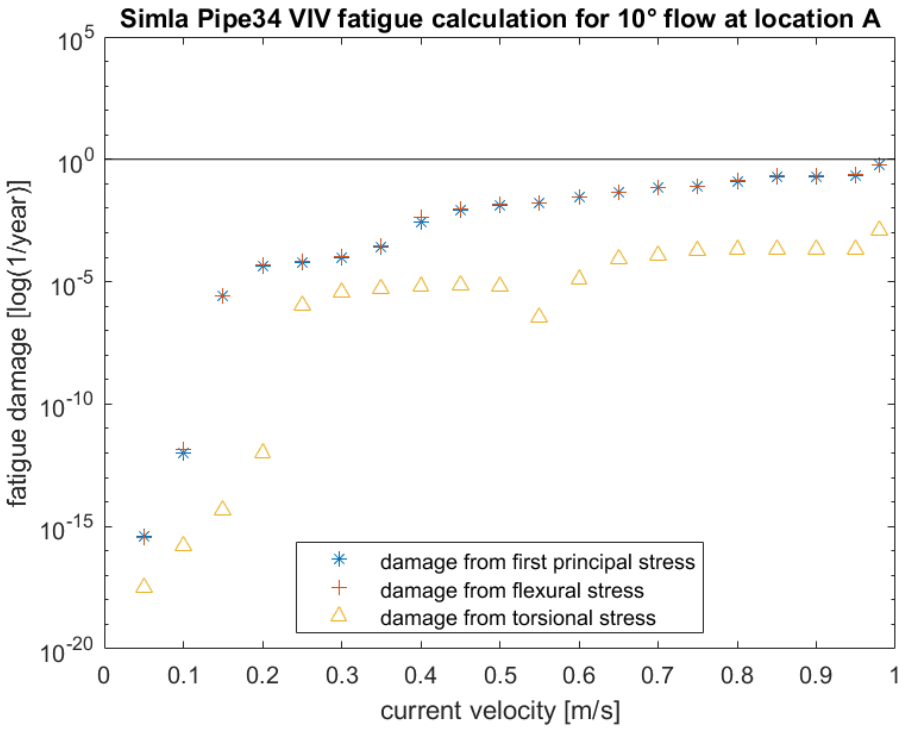

Figure 5.49: VIV fatigue damage per year for the Pipe34 model in 10° flow at location A

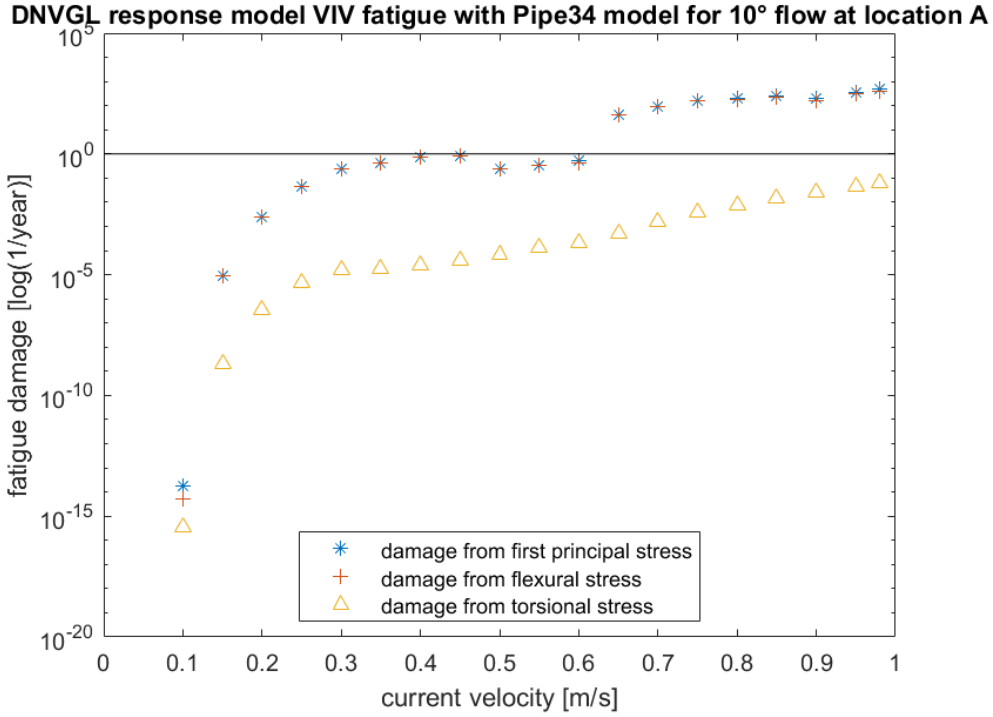

Figure 5.50: VIV fatigue for the 10° flow at location A calculated with the DNV GL response model procedure and modal stresses from the Simla Pipe34 model

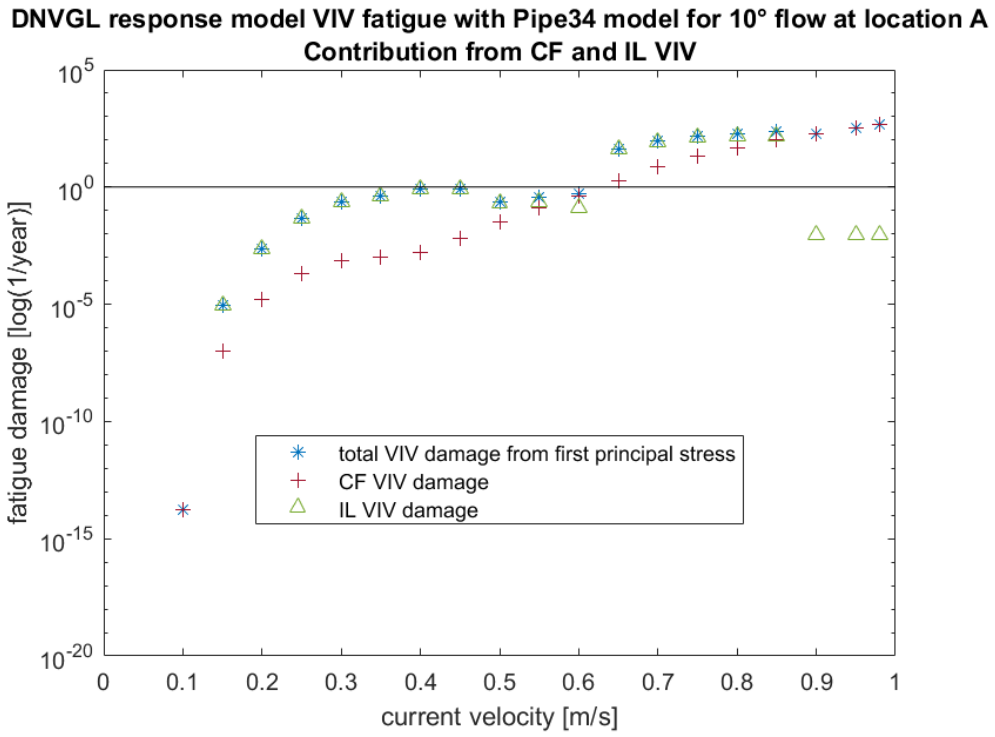

Figure 5.51: VIV fatigue for the 10° flow at location A calculated with the DNV GL response model procedure and modal stresses from the Simla Pipe34 model

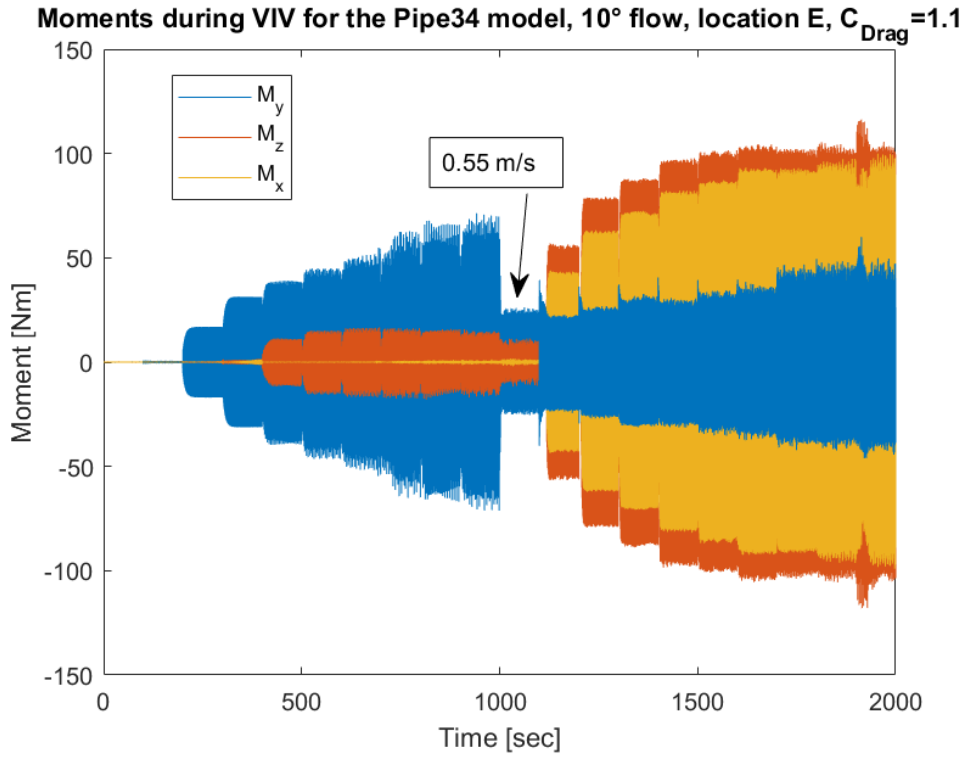

Figure 5.52: Moment signal during VIV for the Pipe34 model in 10° flow at location E

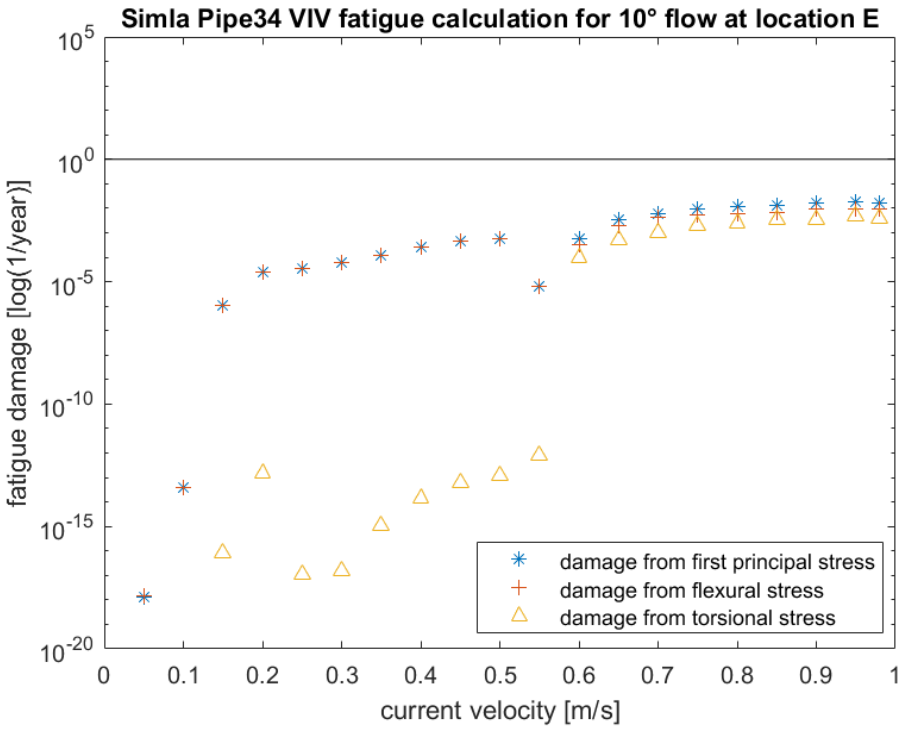

Figure 5.53: VIV fatigue damage per year for the Pipe34 model in 10° flow at location E

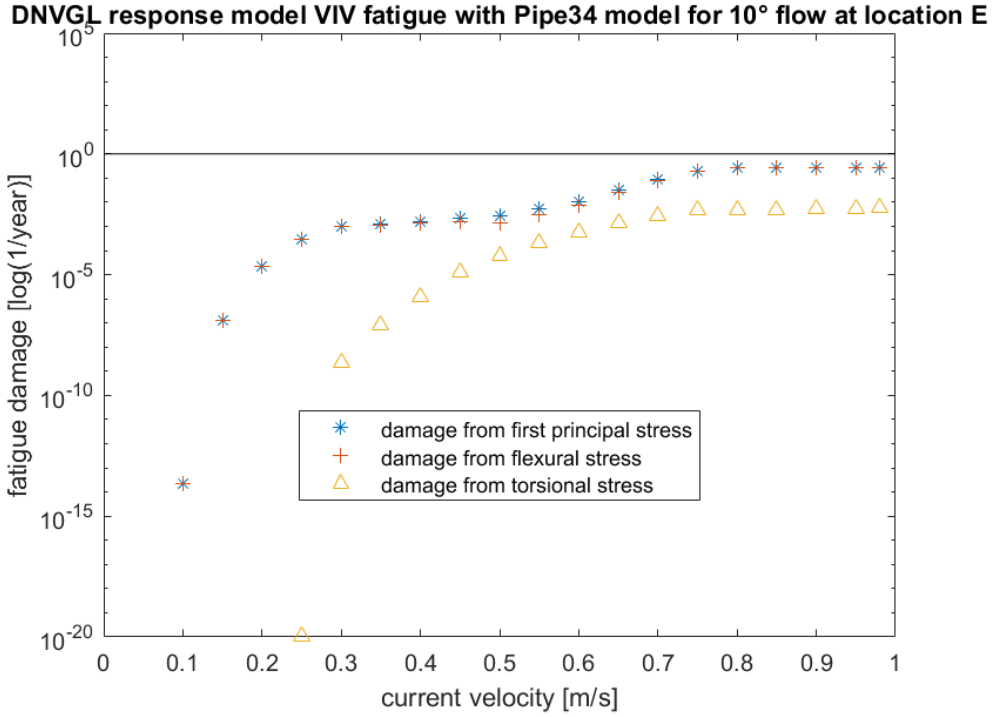

Figure 5.54: VIV fatigue for the 10° flow at location E calculated with the DNV GL response model procedure and modal stresses from the Simla Pipe34 model

90° flow

For the 90 degree flow the in-plane flexural moment M_y is small for lower current velocities up to 0.45 m/s. At locations B and C next to the bends at the lower part, there are several load cases for which the torsion moment is larger than the flexural moments. Further, the flexural moments are more unsteady in the same region. At location B this can be seen at 0.3 to 0.5 m/s in Figure 5.55. In Figure 5.56 corresponding fatigue estimates are shown. In the above mentioned region the fatigue damage calculated from torsional stresses becomes very large and at some load cases even exceeds the damage calculated from the first principal stress.

Here, the torsion stress has a lower number of cycles, but a higher equivalent stress range compared with the first principal stress. It seems that in these cases it is not suitable to calculate the principal stress at each time step and determine the stress ranges afterwards from rainflow counting how it was done in this method. This is because amplitudes can be decreased when two signals are combined. Details of the two stress components are shown in Figure 5.58. Stress ranges should rather be calculated for both signals and be combined within the rainflow algorithm. This can be done by defining a master and slave for each load case and find the stress ranges for the master. The stress ranges of the slave component should be found and the principal stress ranges be calculated based on the time where the master has its peaks and troughs. Since not all moment signals were steady, especially for described load cases, a major intervention in the algorithm would be necessary to capture the stress cycles correctly. These issues are also known from flexible pipe analyses.

It was not possible in the scope of this work to amend the rainflow algorithm, but it is recommended to investigate the possibilities further.

At locations A, D and E the torsion stress is much smaller and such irregularities as mentioned above are not present. The maximum fatigue damage occurs at the supports. Figures 5.59 and 5.60 show the fatigue estimates at location A from Simla and from the DNV GL procedure, respectively. For current velocities up to 0.3 m/s the Simla model gives larger fatigue damage, while for all higher load cases the DNV GL response model gives higher fatigue estimates. The largest difference occurs at 0.5 m/s, because in the response model the flexural stress contribution to fatigue damage is increased steadily, but in Simla strong flexural stress response only arises beyond that.

As was observed for the ten degree flow direction, the smallest difference in results between the two methods occurs at the center of the top horizontal, while the difference at locations A, B and C is larger. This is reasonable, since the DNV GL procedure is adopted from straight pipes and the response at location E is least influenced by deviations of the jumper compared to a straight pipe. Nevertheless,

deviations at location E are significant, too. It highlights the differences in the two approaches.

When fatigue damage is calculated, the SN-curve coefficient m is applied as an exponent on the stress range. For chosen SN-curve this means that the difference in stress levels is represented with the power of five in the fatigue estimates. Further, when following the recommended practice for non-straight pipes all modes that are active based on their reduced velocity apply their full stress range. Already from the VIV motion amplitudes it was seen that the DNV GL procedure gives higher response estimates for many reduced velocities compared to the Simla results and model test data. In Simla, several modes can be active at the same time, too, but obviously not all apply their full stress range. From the oscillating frequencies in Simla the dominating response could always be associated with one of the first four modes, which have lower unit stresses compared to the higher modes. At the shorter segments also higher modes were identified during VIV, but the response amplitudes are significantly lower than from the guidelines. Following the DNV GL procedure also higher modes were active, which contribute with higher unit stresses.

It is interesting that for some cases with low velocity currents Simla gives larger fatigue estimates, however, fatigue damage for these cases is small in general.

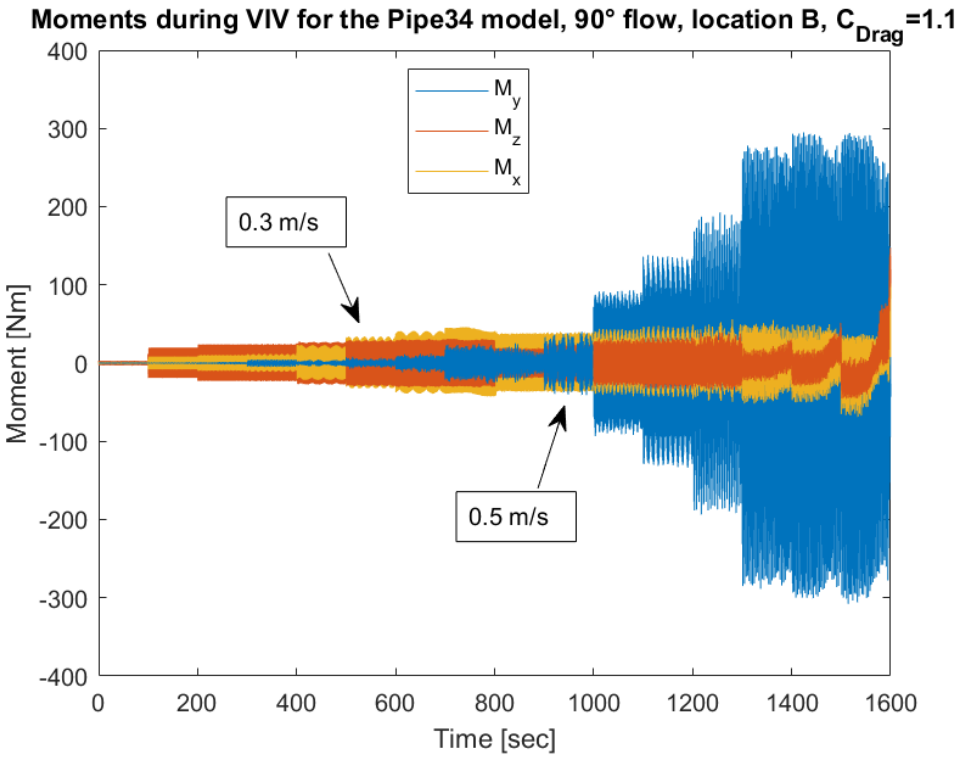

Figure 5.55: Moment signal during VIV for the Pipe34 model in 90° flow at location B

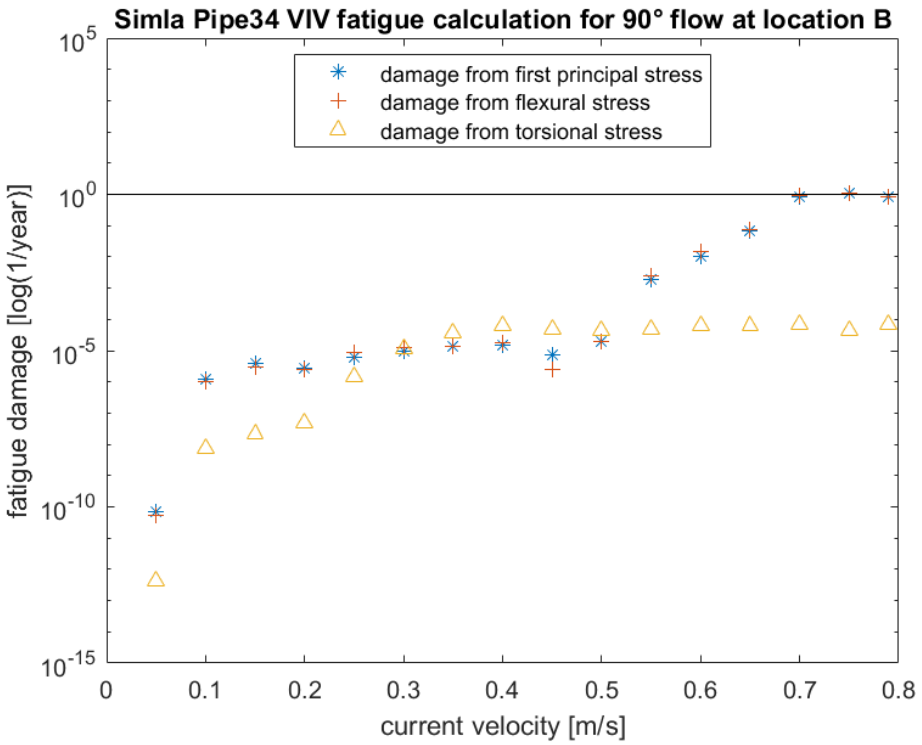

Figure 5.56: VIV fatigue damage per year for the Pipe34 model in 90° flow at location B

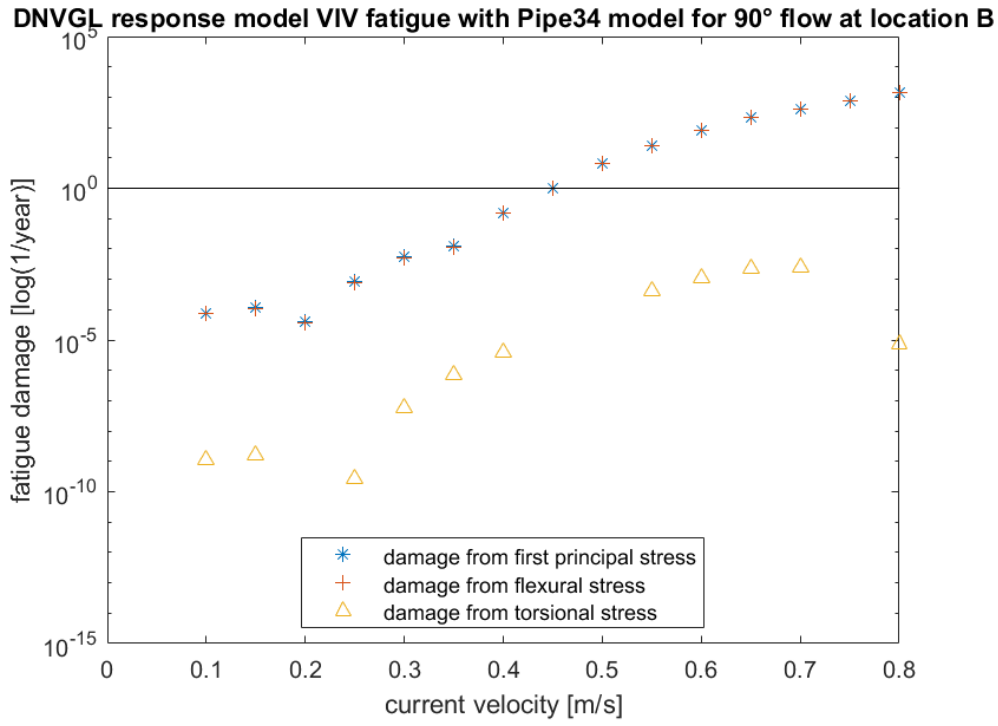

Figure 5.57: VIV fatigue for the 90° flow at location B calculated with the DNV GL response model procedure and modal stresses from the Simla Pipe34 model

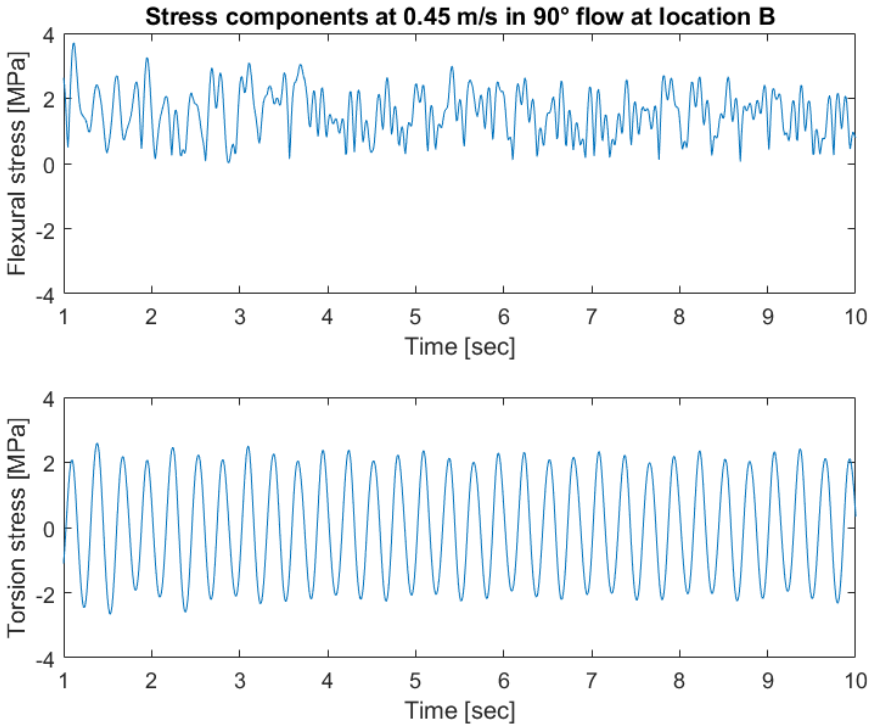

Figure 5.58: Stress details for $U_c = 0.45$ m/s over ten seconds in 90° flow at location B

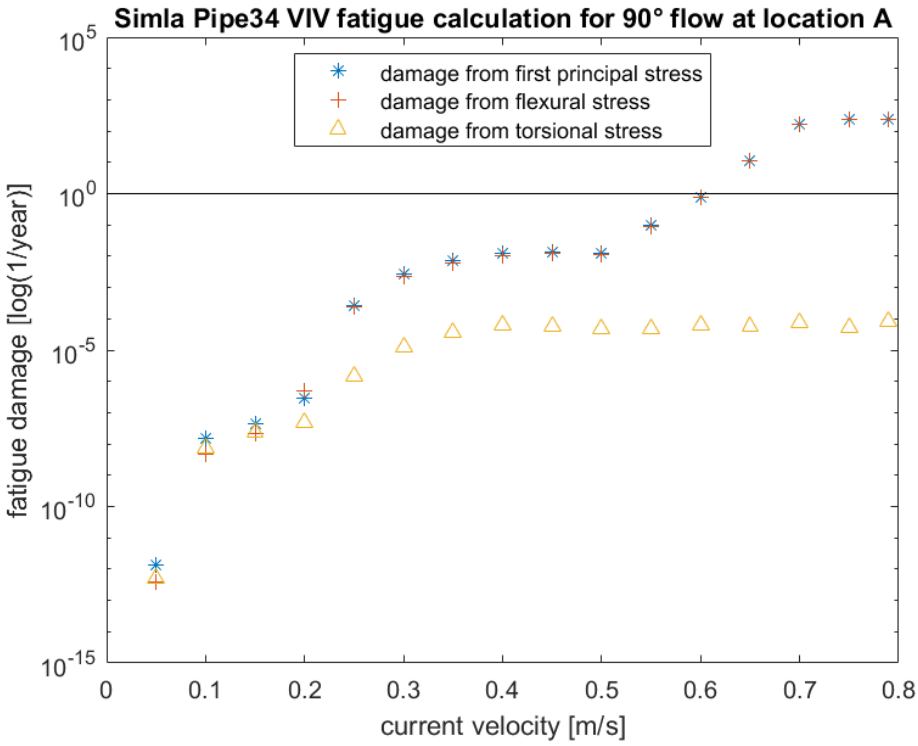

Figure 5.59: VIV fatigue damage per year for the Pipe34 model in 90° flow at location A

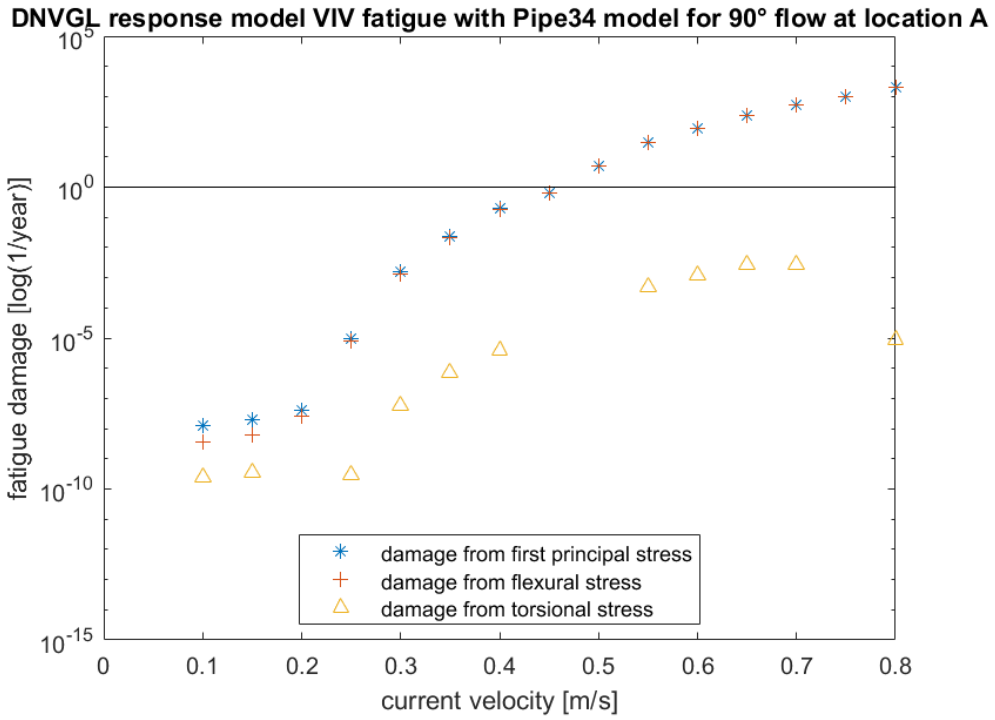

Figure 5.60: VIV fatigue for the 90° flow at location A calculated with the DNV GL response model procedure and modal stresses from the Simla Pipe34 model

45° flow

Also for the 45 degree flow several load cases have large torsion moments at locations B and C close to the bends in the lower part. The moment signal at location B is shown in Figure 5.61 and associated fatigue damage from Simla in Figure 5.62. The same conclusion as for the 90 degree flow is drawn here, that in regions with large torsion moments it is not sufficient to calculate the first principal stress from stress amplitudes of the two stress components and instead it should be calculated using stress ranges after specifying master and slave for each case. From the fatigue estimates it stands out that they do not increase as steadily and show more jumps than for the other flow directions. Also from VIV motion it was observed that the vibration patterns of consecutive load cases with respect to main direction and oscillation frequency differ much more for this flow angle. It can be concluded that the change in vibration patterns is also evident in fatigue damage calculations.

Next to the bends the DNV GL response model procedure gives much higher fatigue estimates which also steadily rise for increasing current velocities. For location B this is shown in Figure 5.63.

Largest fatigue damage occurs at the support as for the other flow directions. From VIV motion it was shown that large response arises in z-direction for 0.95 and 0.98 m/s. This causes an increase in fatigue damage at locations A, B and C. At locations D and E it has the opposite effect. Nonetheless, at location E the Simla results exceed the fatigue estimates from the response model approach for current velocities of 0.7 to 0.9 m/s. As mentioned before it can be considered to reduce the load parameters in the VIV tool for the highest load cases to avoid over-conservative results.

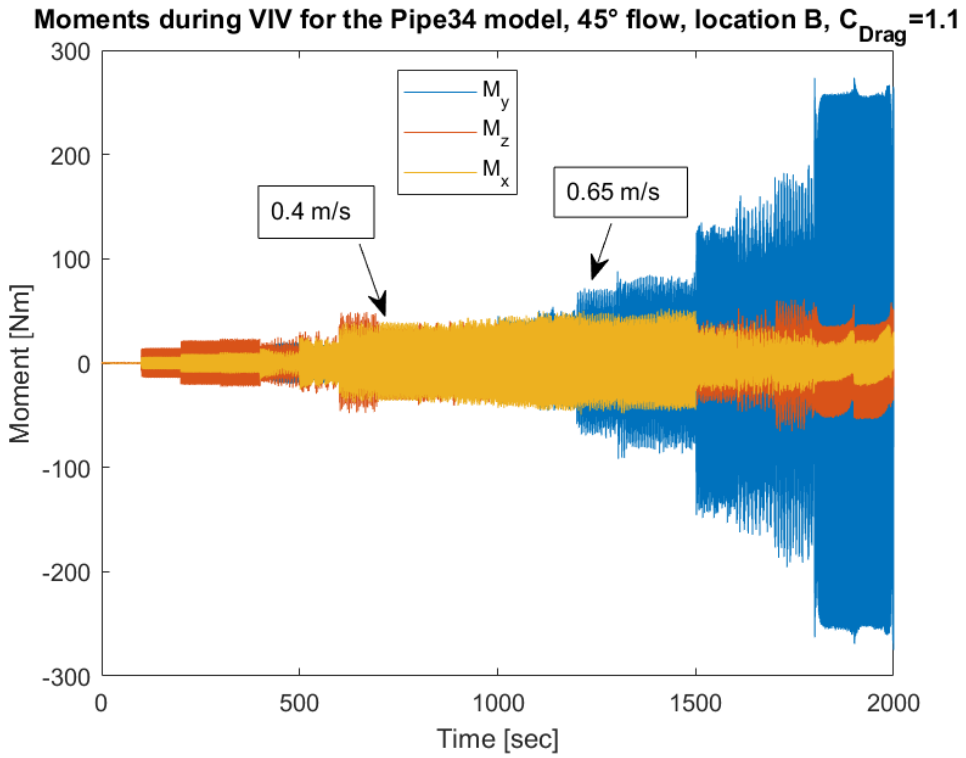

Figure 5.61: Moment signal during VIV for the Pipe34 model in 45° flow at location B

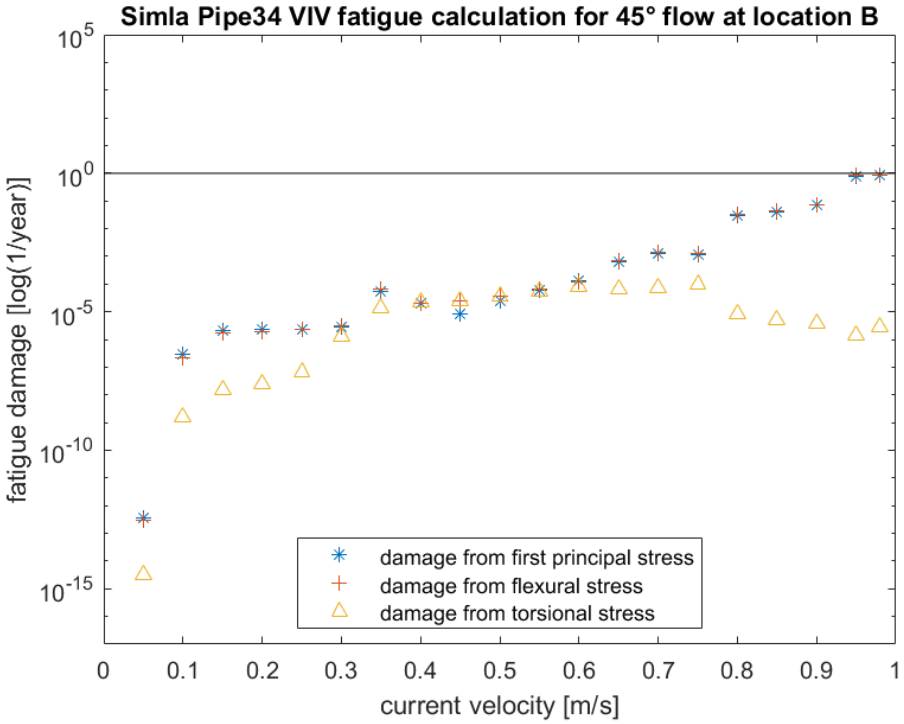

Figure 5.62: VIV fatigue damage per year for the Pipe34 model in 45° flow at location B

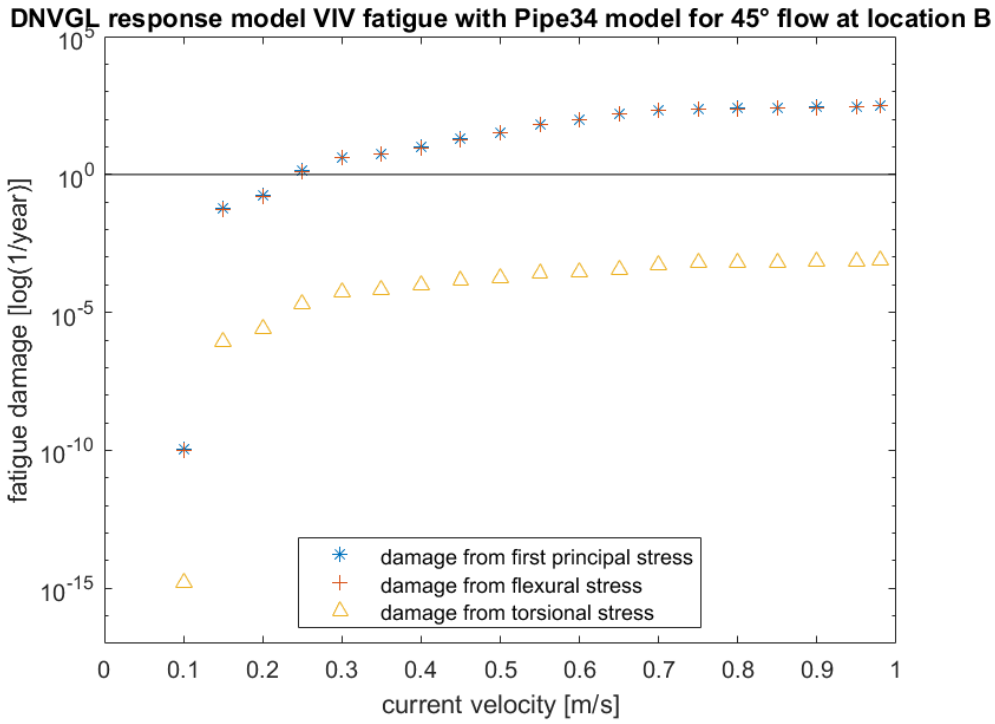

Figure 5.63: VIV fatigue for the 45° flow at location B calculated with the DNV GL response model procedure and modal stresses from the Simla Pipe34 model

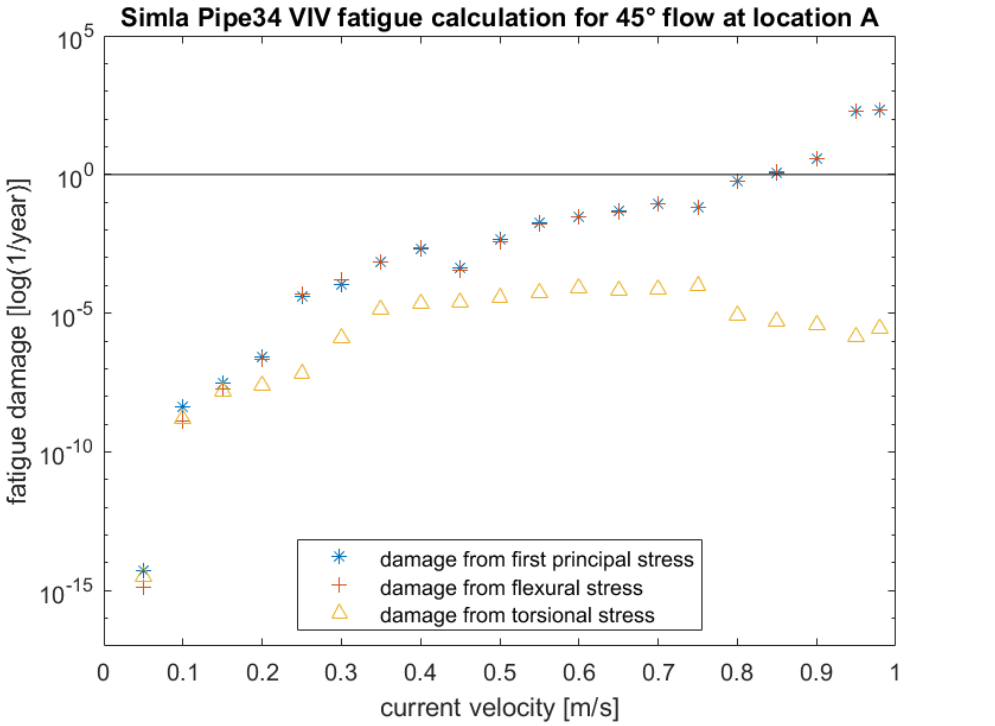

Figure 5.64: VIV fatigue damage per year for the Pipe34 model in 45° flow at location A

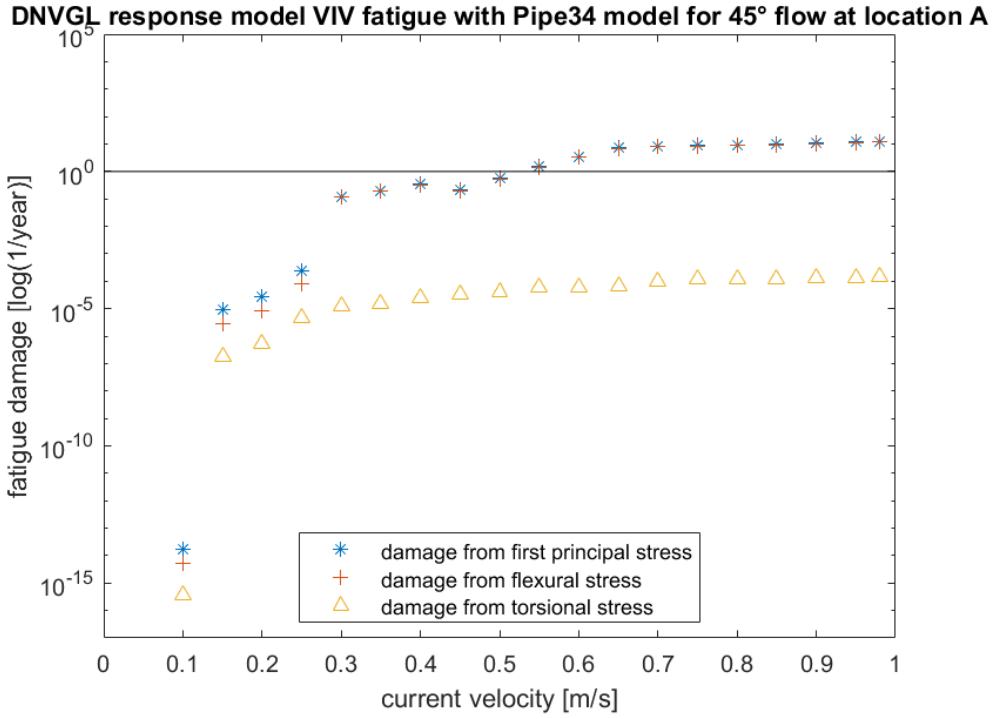

Figure 5.65: VIV fatigue for the 45° flow at location A calculated with the DNV GL response model procedure and modal stresses from the Simla Pipe34 model

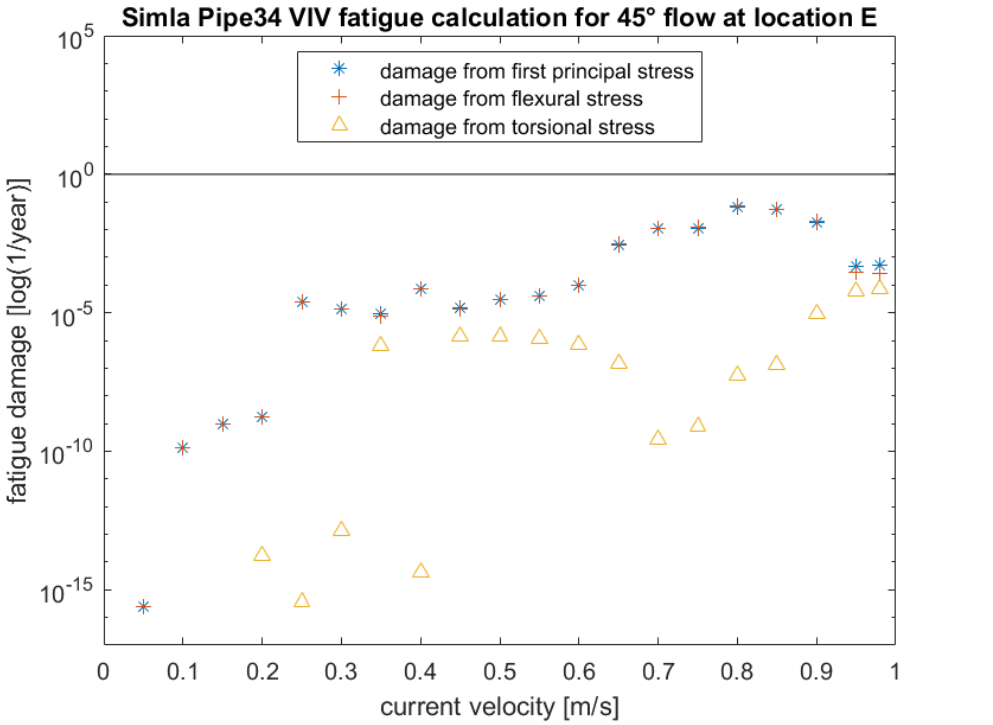

Figure 5.66: VIV fatigue damage per year for the Pipe34 model in 45° flow at location E

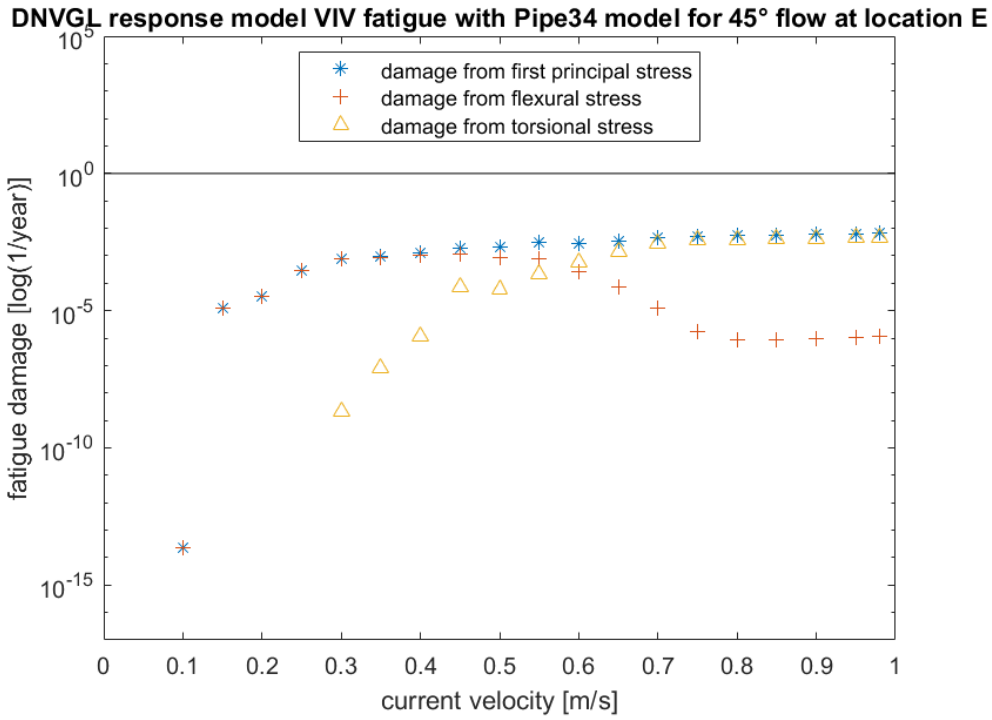

Figure 5.67: VIV fatigue for the 45° flow at location E calculated with the DNV GL response model procedure and modal stresses from the Simla Pipe34 model

5.5.1 Sensitivity to modeling choices and model parameters

In this section sensitivity of fatigue damage results to modeling choices, especially with or without bend elements, and to the model parameters of the TD VIV tool is discussed. The results were obtained from simulations in Simla, for which only one parameter was changed at a time. They are reported for the pure flow angles of ten and 90 degrees, since these cases are most suitable to draw conclusions.

Pipe31 and Pipe34 model

From modal analysis the main difference in fatigue damage between the two Simla models is expected to occur in the bends and at the transition to the straight parts. In the bends the Pipe34 model experiences higher stresses, whereas the Pipe31 model shows higher stresses right next to the bends and, thus, at possible weld locations. In correlation with that gives the Pipe31 model higher fatigue damage at locations B, C and D for the ten degree flow and current velocities higher than 0.2 m/s. For the lowest current velocities mainly IL VIV is active, which is associated with vibrations in x-direction at this flow angle. Thus, for these cases the Pipe34 model experiences higher fatigue damage. In Figures 5.68 and 5.69 the relative difference in fatigue damage is shown. At 0.55 m/s some results are not within the plotted range, but larger. This is because the twist mode becomes active and causes smaller vibration amplitudes for the Pipe34 model. From 0.7 m/s on the trend is that the Pipe31 model gives increasingly larger fatigue damage.
For the 90 degree flow, where motion in x-direction is associated with CF VIV, the Pipe31 model gives significantly lower fatigue damage for current velocities 0.5 to 0.65 m/s, not only close to the bends, but also at location E. Here, the maximum displacement due to VIV was in x-direction. For 0.7 to 0.79 m/s, where the largest displacement was in z-direction, the Pipe31 model again gives larger fatigue estimates.

C_{Drag}

When the drag coefficient is changed to 1.2 and all other parameters are kept the same, fatigue damage for the ten degree flow is decreased by 15 to 35 percent for almost all load cases. Larger deviations occur for the 0.05, 0.1 and 0.55 m/s load cases. The influence on fatigue damage is shown in Figures 5.70 and 5.71 for the ten and 90 degree flow, respectively. For the 90 degree flow angle the relative difference in fatigue damage per year is decreased between 25 to 45 percent for most load cases. Here, exemptions occur at current velocities 0.05 and 0.5 m/s.
For the lowest current velocities the results are less affected when the drag coefficient is changed, but damage here is generally low. Also at 0.55 and 0.5 m/s respectively

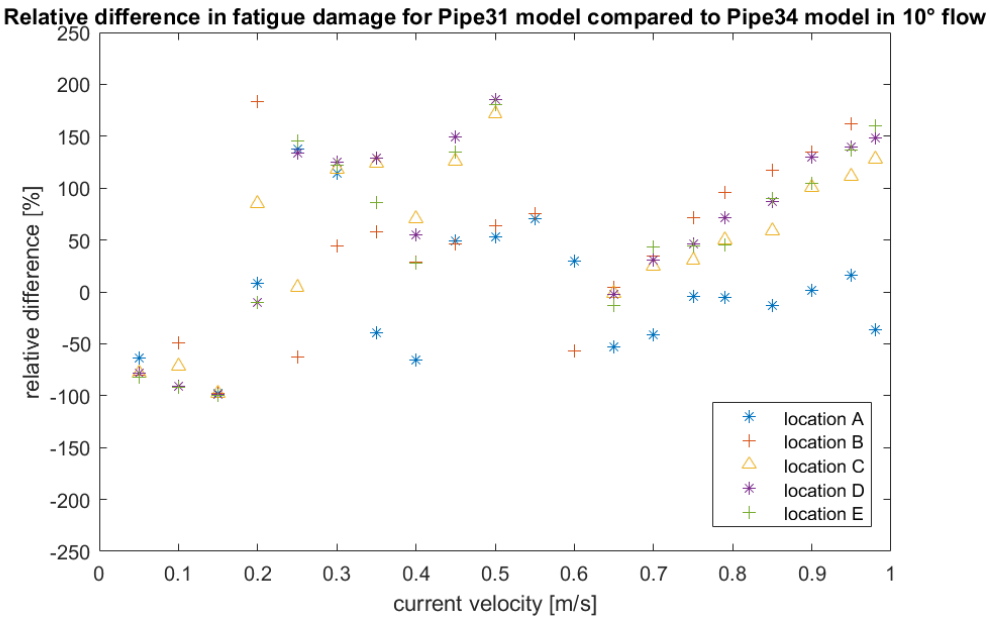

Figure 5.68: Sensitivity of fatigue damage with respect to modeling choices (with or without bend elements) for the 10° flow.

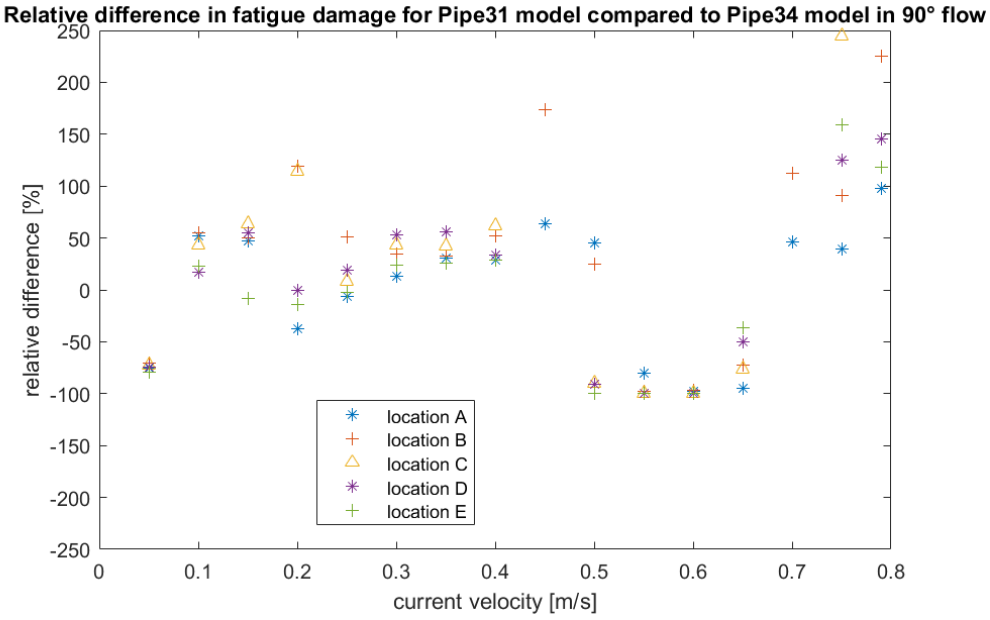

Figure 5.69: Sensitivity of fatigue damage with respect to modeling choices (with or without bend elements) for the 90° flow.

for the two flow angles, major changes in vibration patterns occurred, which led to smaller stress amplitudes. Besides that the change in drag coefficient has a similar effect at all locations along the jumper and all flow velocities. This is reasonable, since the drag coefficient is defined for still-water conditions and amplification during VIV is applied to this value.

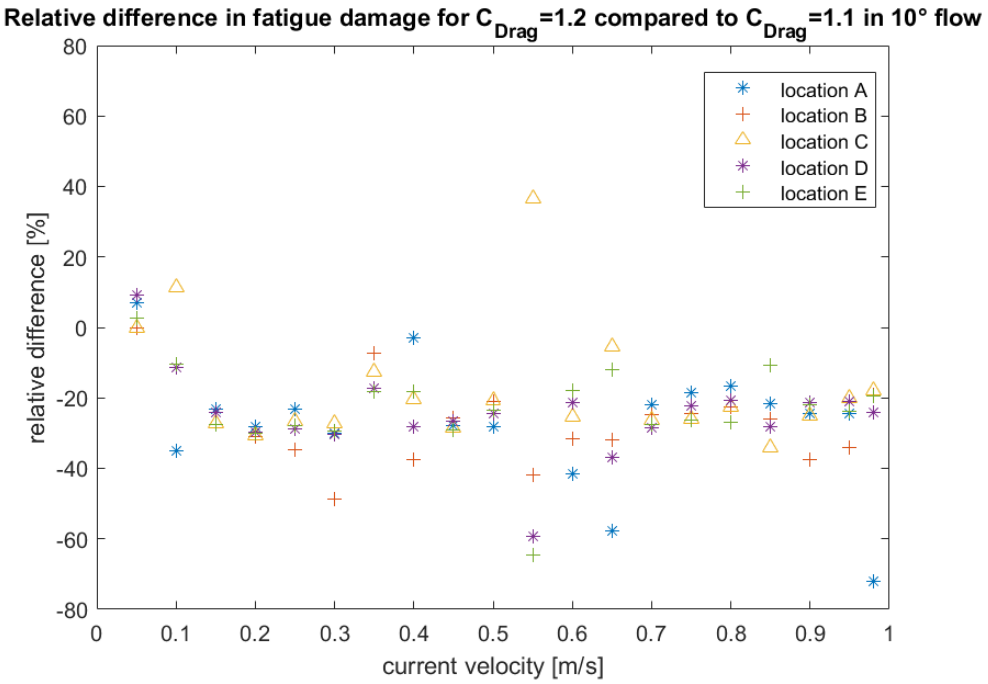

Figure 5.70: Sensitivity of fatigue damage with respect to the drag coefficient for the 10° flow.

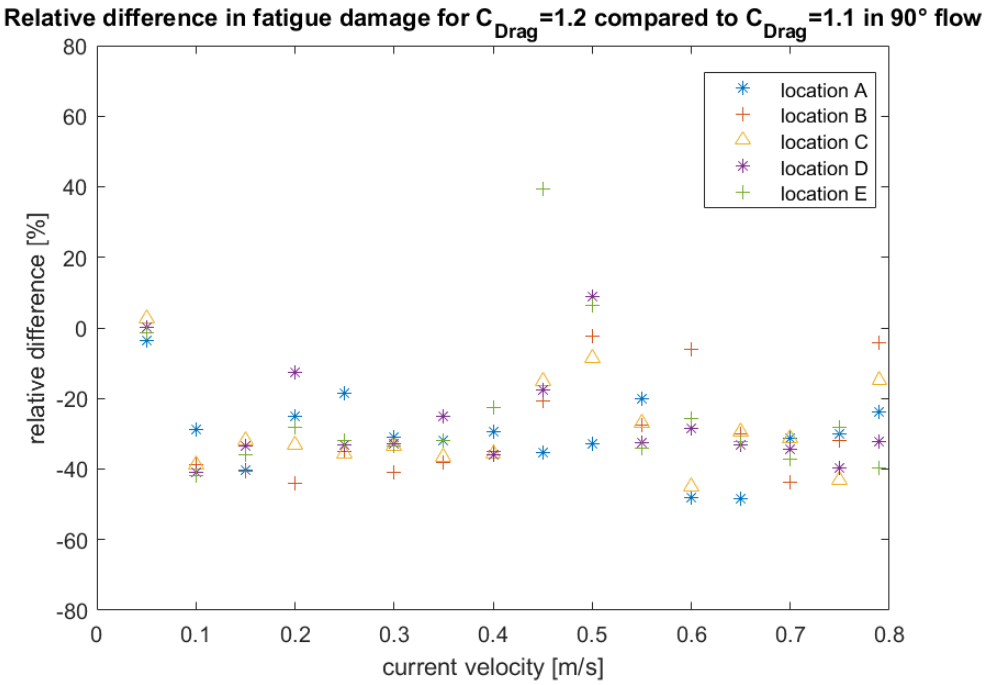

Figure 5.71: Sensitivity of fatigue damage with respect to the drag coefficient for the 90° flow.

CVC

When the CF lift force coefficient is changed back to its default value of 1.0, the impact varies more for the different locations at the jumper and different current velocities. This is shown in Figures 5.72 and 5.73. Generally, smaller VIV amplitudes

and, thus, lower fatigue damage is expected for the default value when CF VIV is active. For the ten degree flow, this can be seen for current velocities of 0.6 to 0.98 m/s and for the 90 degree flow for current velocities of 0.5 to 0.79 m/s. Location A at the support is an exception for the ten degree flow, since fatigue damage here is between 20 and 40 percent higher at most load cases for the lower CF force coefficient. Furthermore, in the ten degree flow an increase in fatigue damage is observed for small flow velocities up to 0.5 m/s, while for the 90 degree flow it had only small impact for the low current velocities.

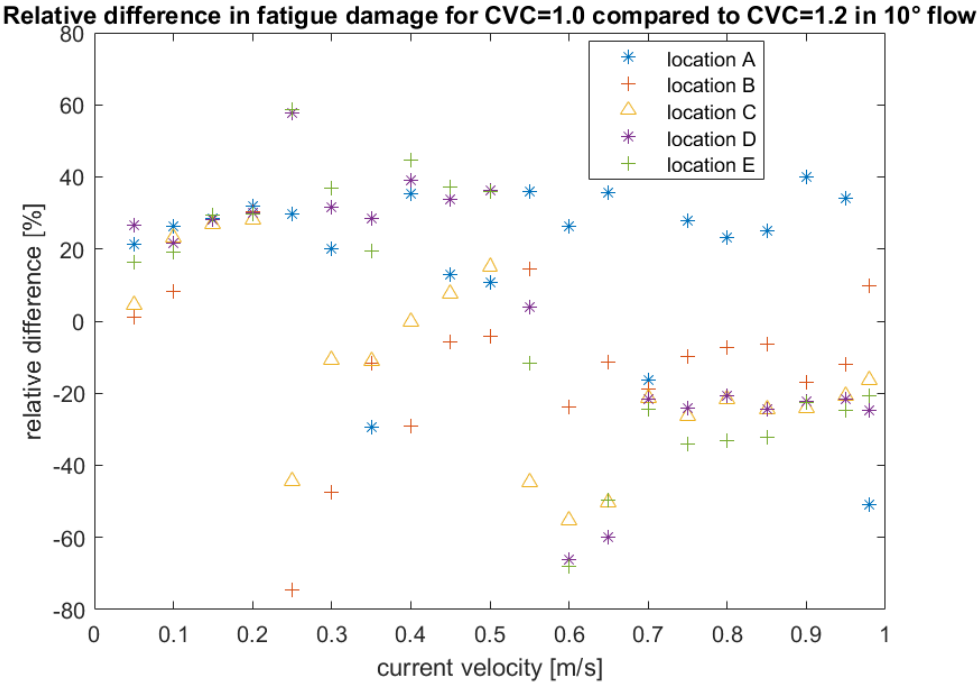

Figure 5.72: Sensitivity of fatigue damage with respect to the CF force coefficient for the 10° flow.

CVI1

Also for the IL force coefficient the effect on fatigue damage varies at the different locations. In contrary to the CF force coefficient, the biggest impact is expected for low-velocity currents, for which IL VIV dominates. The impact is clearer for the 90 degree flow compared to the ten degree flow as shown in Figures 5.74 and 5.75. For the 90 degree flow, fatigue damage for current velocities up to 0.35 m/s is decreased by 85 to 90 percent when the IL force coefficient of 0.8 is used. This is observed at all five locations. For the ten degree flow, the same effect is observed for U_c = 0.15 and 0.2 m/s. Besides that, the deviations are spread wider for this flow angle. For current velocities of 0.6 to 0.98 m/s fatigue damage at the top horizontal is even increased. This might be due to the coupling between IL and CF VIV. When IL VIV and therefore also CF-induced IL VIV are decreased more energy can be

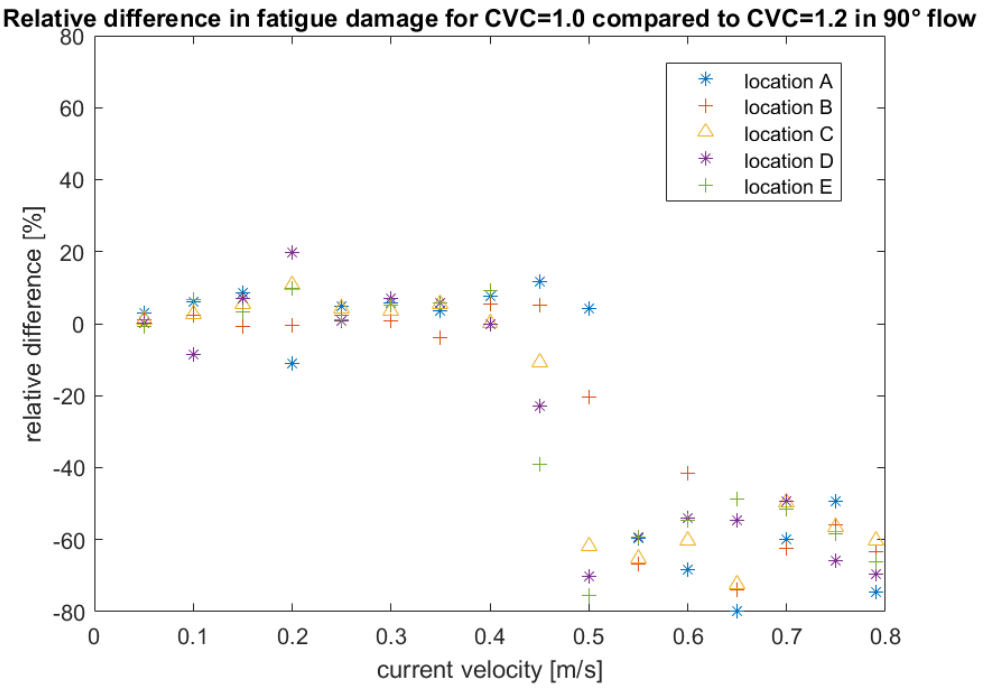

Figure 5.73: Sensitivity of fatigue damage with respect to the CF force coefficient for the 90° flow.

utilized for the pure CF response at higher reduced velocities. This may be a reason why fatigue damage is increased for the lower IL force coefficient in a region, where CF response is typically dominating.
The observations of the two force coefficients again show the complexity of the flow around such structure and of the structural-dynamic response.

$\hat{\mathbf{f}}_{1I1}$

With the default value of the minimum vibration frequency that gives energy input to IL region one of 0.3, IL VIV could only be activated over a smaller range of reduced velocity than with the chosen value of 0.13. However, even for low-velocity currents, where IL VIV was active for both values of $\hat{f}_{1I1}$, fatigue damage is significantly lower when using the default value. For the 90 degree flow, fatigue damage is lowered for almost all cases, whereas for the ten degree flow fatigue damage is increased for the higher current velocities, where CF VIV is dominating. As for the force coefficients, it is assumed that this is due to coupling between the two kinds of VIV.

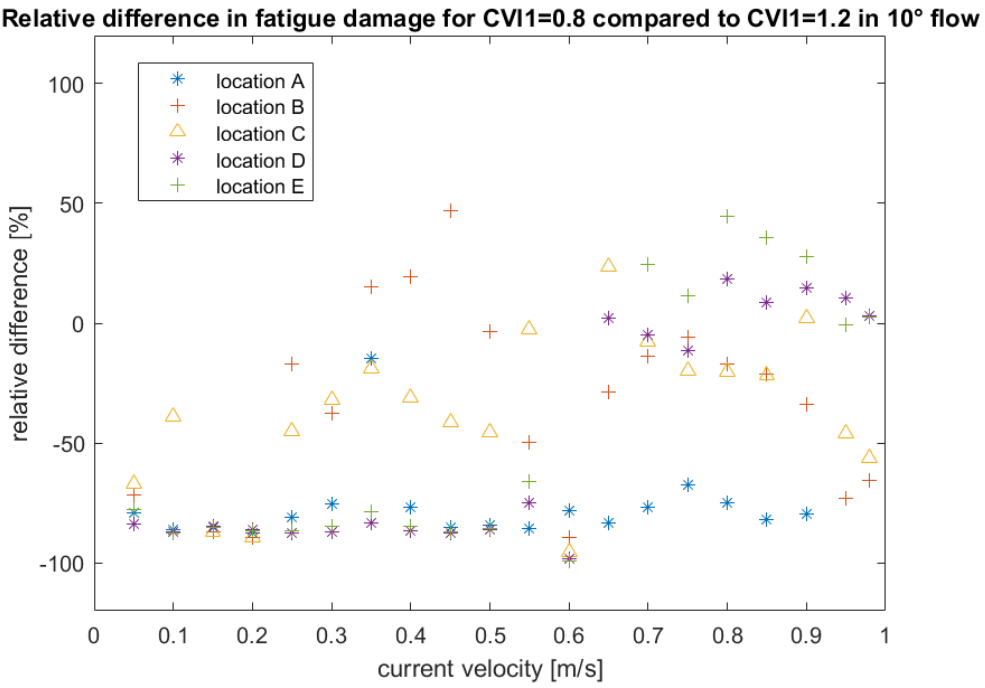

Figure 5.74: Sensitivity of fatigue damage with respect to the IL force coefficient for the 10° flow.

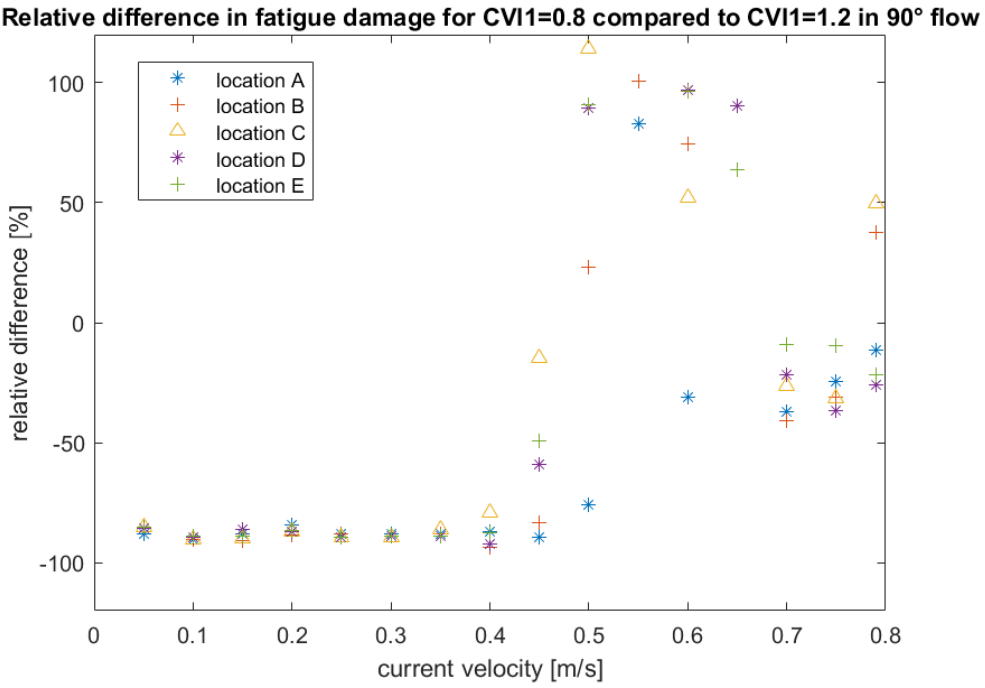

Figure 5.75: Sensitivity of fatigue damage with respect to the IL force coefficient for the 90° flow.

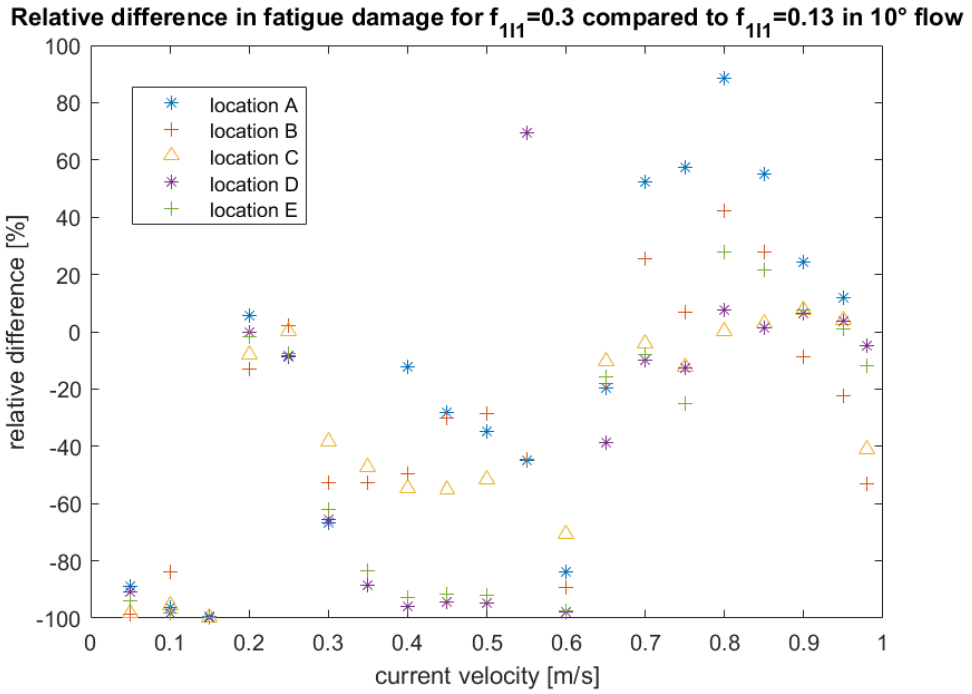

Figure 5.76: Sensitivity of fatigue damage with respect to the minimum vibration frequency that gives energy input for IL region one for the 10° flow.

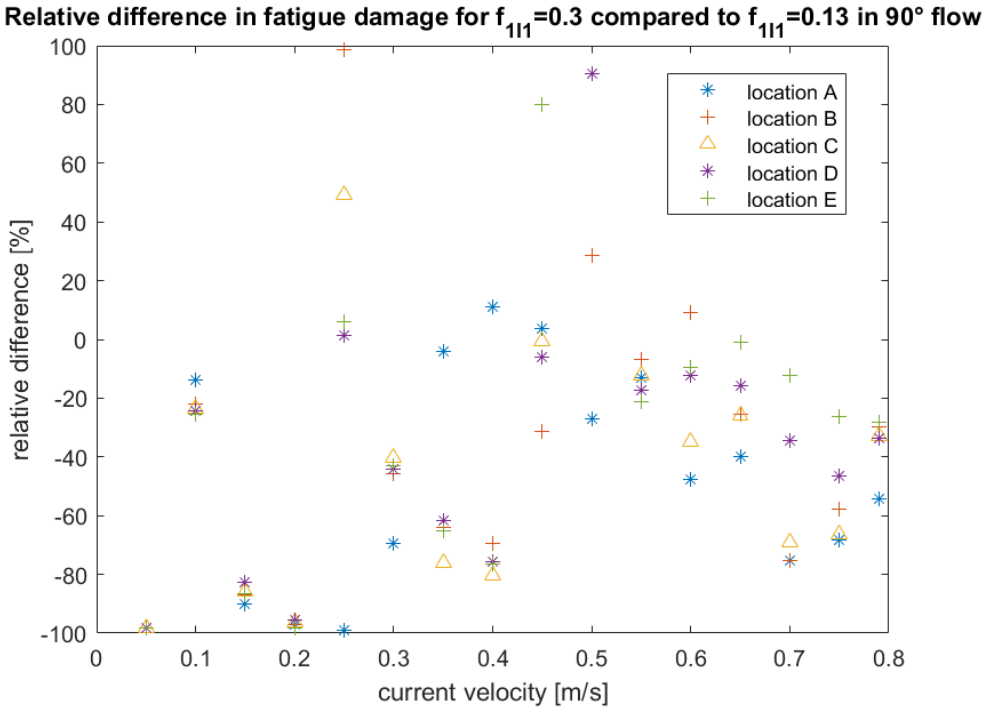

Figure 5.77: Sensitivity of fatigue damage with respect to the minimum vibration frequency that gives energy input for IL region one for the 90° flow.

5.5.2 Summary of the section about VIV stresses and fatigue damage

- Largest fatigue damage is observed at the jumper supports for all three flow directions. The largest deviations of fatigue estimates from the two methods also occur at this location. Except for the lowest current velocities, fatigue damage from the DNV GL response models is significantly higher than obtained from Simla. This is because the response model procedure assumes that all active modes contribute with their full stress range. In the TD tool several modes are active in the same load case, too, but they have the possibility to compete with each other and contribute with less than the full amount. The smallest difference between the two methods is observed at the center of the top horizontal. This is reasonable, since the DNV GL procedure is adopted from straight pipes and at this location the response is presumably least affected by the non-straight jumper geometry.

- Torsional stresses are relevant for all three flow directions. Especially for the 45 and 90 degree flow and at the lower jumper segment, the contribution to fatigue damage is significant. A weakness in the way that principal stresses were calculated here was discovered for these cases. When the first principal stress is calculated at each time step from the maximum flexural stress around the circumference and the torsional stress, resulting stress ranges can turn out smaller than when each component is considered separately. It is recommended to include a master and slave condition in the rainflow algorithm, and calculate the principal stress from stress ranges instead of stress amplitudes.

- Largest difference in fatigue estimates between the Pipe31 and Pipe34 model occurs next to the bends.
  When the value of the drag coefficient is changed, the impact on fatigue damage is very similar for all locations and load cases, whereas, when the parameters of the VIV tool are changed the affect on fatigue estimates is much more complex.
  For the lower default values of the load coefficients, the damage as expected is smaller in the corresponding velocity region, but apart from that coupling effects occur for other current velocities, too. For the higher default value of the minimum vibration frequency that gives energy input for IL region one, the impact on fatigue estimates at higher current velocities varies for the different flow angles and locations along the jumper, too. It highlights the complexity of VIV for non-straight pipes and emphasizes the importance of precise prediction tools.

Chapter 6

Conclusion and recommendations

6.1 Conclusion

Modal analysis has been carried out for two models in Simla and Abaqus. It was shown that the models using elbow elements in the bends are in better agreement with results from the ExxonMobil model test, since the first in-plane bending mode has a lower natural frequency compared to the out-of-plane twist mode for these models. The results from modal analyses have shown the relevance of accounting for additional strains and deformation of the cross-section due to bending during manufacture.

For the model with Pipe34 elements in the bends the modal stress in bends is increased by up to factor two compared with the Pipe31 model. At the transition to straight parts the stresses are decreased by up to 35 percent. These coupled effects are most significant for in-plane bending modes.

The parameters of the TD VIV tool in Simla have been adjusted, since default values referred to straight pipes. In this study the IL and CF force coefficients were increased from 0.8 to 1.2 and 1.0 to 1.2, respectively. The minimum non-dimensional vibration frequency that gives energy input to IL region one was changed from 0.3 to 0.13, so that IL VIV can be activated over a wider range of reduced velocities. With these parameters conservative results for VIV motion were obtained for all observed load cases. From comparison with experimental data, it was shown that Simla results are in very good correlation. The DNV GL response model over-predicted the response for many cases, especially for CF VIV.

With respect to fatigue damage, the relevance of torsional stresses was pointed out. Especially close to the bends in the lower jumper segment, torsional stresses became the largest stress components for several flow velocities in the 90 and 45 degree flow. Maximum fatigue damage occurred at the supports for all flow angles. At the same location, the results from the DNV GL procedure and from Simla differed most.

Smaller derogation between the two methods was observed at the center of the long top horizontal part, but also here the response model approach gave far higher fatigue estimates compared with the TD tool. When the DNV GL procedure is used for non-straight pipes, all active modes apply their full stress range, whereas in Simla, several modes can be active, too, but they can compete with each other. Sensitivity of fatigue estimates to the control parameters of the TD VIV tool was discussed. For the lower default values of the force coefficients fatigue damage as expected was smaller in the corresponding velocity region. Also for the higher default value of the minimum non-dimensional oscillating frequency that gives energy input to IL region one, fatigue damage was smaller for low current velocities. Apart from that, coupling effects occurred in the other velocity regions, too. It once more highlighted the complexity of VIV for non-straight pipes and the importance of accurate prediction tools.

6.2 Recommendations for further work

Some recommendations for future work are as follows:

- Based on the large difference in modal stresses between the two models with and without elbow elements, relevance of thinning in bends can be explored
- Include internal and external pressure in the analysis to observe stiffening and softening effects for the full jumper model
- Initialize the jumper model in a pre-stressed condition
- Observe VIV for the jumper model when placed horizontally and close to the seabed, like it is often done for shallow water
- Investigate multi-axial stress. Furthermore, principal stresses should be calculated from stress ranges of contributing components within the rainflow algorithm instead of stress amplitudes at each time step. Therefore a master-slave relationship should be implemented. Different stress criteria for bend segments and straight parts can be used.

Bibliography

[1] A.H. Techet. 13.42 lecture: Vortex induced vibrations. *Massachusetts Institute of Technology, Open Courseware*, 21, 2005.

[2] B. Mutlu Sumer et al. *Hydrodynamics around cylindrical strucures*, volume 26. World scientific, 2006.

[3] Sigmund Kyrre Ås and Stig Berge. Compendium fatigue and fracture design of marine structures, Revised as of 2017.

[4] Yung-Li Lee, Mark E Barkey, and Hong-Tae Kang. *Metal fatigue analysis handbook: practical problem-solving techniques for computer-aided engineering*. Elsevier, 2011.

[5] Zhenhui Liu, Laila Aarstad Igeh, Jie Wu, and Muk Chen Ong. Fatigue damage assessment to a rigid planar jumper on model scale. *Journal of Offshore Mechanics and Arctic Engineering*, 142(1), 2020.

[6] Svein Sævik. Simla-theory manual. Revised as of 2017.

[7] DNVGL-RP-F105. Recommended practice. free spanning pipelines. Revised as of 2019.

[8] DNVGL-RP-C203. Recommended practice. fatigue design of offshore steel structures. 2005.

[9] Scott Post. *Applied and computational fluid mechanics*. Jones & Bartlett Publishers, 2010.

[10] Mats Jørgen Thorsen. Time domain analysis of vortex-induced vibrations. 2016.

[11] Laila Aarstad Igeh. Viv fatigue investigation for subsea planar rigid spools and jumpers. Master's thesis, University of Stavanger, Norway, 2017.

[12] Resistance Committee et al. Final report and recommendations to the 26th ittc. In *Proceedings of 26th International Towing Tank Conference, Rio de Janeiro, Brazil*, volume 38, 2011.

[13] Narakorn Srinil, Marian Wiercigroch, and Patrick O Brien. Reduced-order modelling of vortex-induced vibration of catenary riser. *Ocean Engineering*, 36(17-18):1404–1414, 2009.

[14] Mats Jørgen Thorsen, Svein Sævik, and Carl Martin Larsen. A simplified method for time domain simulation of cross-flow vortex-induced vibrations. *Journal of Fluids and Structures*, 49:135–148, 2014.

[15] Mats Jørgen Thorsen, Svein Sævik, and Carl Martin Larsen. Time domain simulation of vortex-induced vibrations in stationary and oscillating flows. *Journal of Fluids and Structures*, 61:1–19, 2016.

[16] Jan Vidar Ulveseter, Svein Sævik, and Carl Martin Larsen. Time domain model for calculation of pure in-line vortex-induced vibrations. *Journal of Fluids and Structures*, 68:158–173, 2017.

[17] Kristoffer Høyem Aronsen. An experimental investigation of in-line and combined in-line and cross-flow vortex induced vibrations. 2007.

[18] Howard Wang, Jerry Huang, Sungho Lee, Paulo Gioielli, Wan Kan, Don Spencer, and Mohammed Islam. Viv response of a subsea jumper in uniform current. In *ASME 2013 32nd International Conference on Ocean, Offshore and Arctic Engineering*. American Society of Mechanical Engineers Digital Collection, 2013.

[19] Klaus-Jürgen Bathe, Carlos A Almeida, and Lee W Ho. A simple and effective pipe elbow element - some nonlinear capabilities. *Computers & Structures*, 17(5-6):659–667, 1983.

[20] Ivar Langen and Ragnar Sigbjörnsson. *Dynamisk analyse av konstruksjoner: Dynamic analysis of structures*. Tapir, 1979.

[21] Svein Sævik, Gro S Baarholm, Ole D Økland, and Janne KØ Gjøsteen. Simla version 3.16.0 user manual, 2019.

[22] AAUs Manual. Abaqus documentation version 6.13. *Dassault Systems SIMULIA Corp., Providence, RI, USA*, 2013.

[23] Kunpeng Wang, Chunyan Ji, Qinghai Chi, and Hairong Wu. Hydrodynamic force investigation of a rigid cylinder under the coupling cf and il motion. *Journal of Fluids and Structures*, 81:598–616, 2018.

Appendices

Appendix A: Modal stress output from Simla and Abaqus

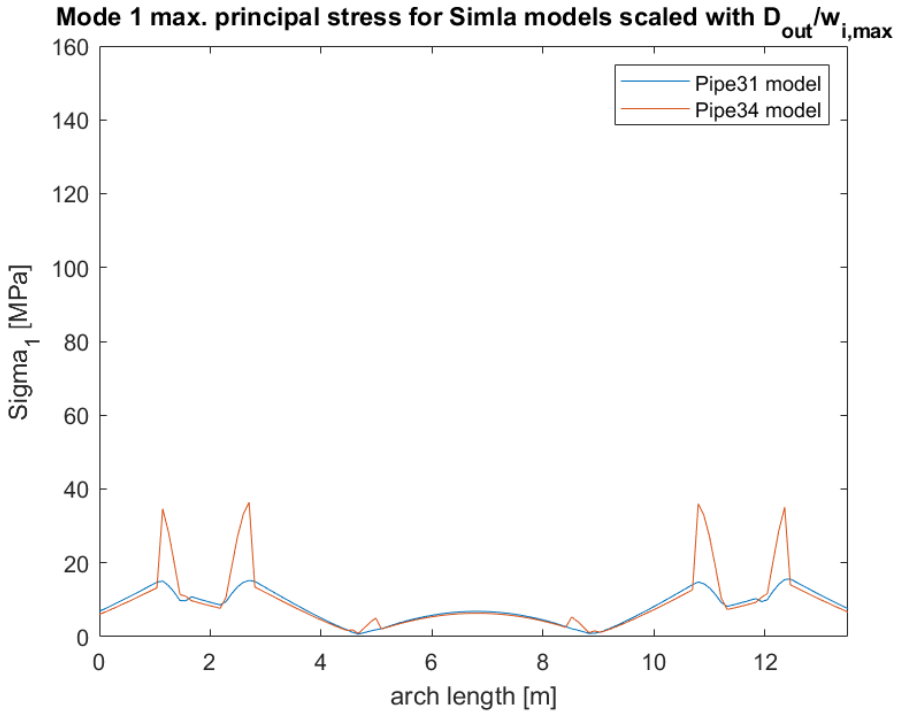

Figure 1: Maximum principal unit stress of mode one for the two Simla models. Plotted over accumulated arch length and scaled with respect to the outer diameter and maximum modal displacement.

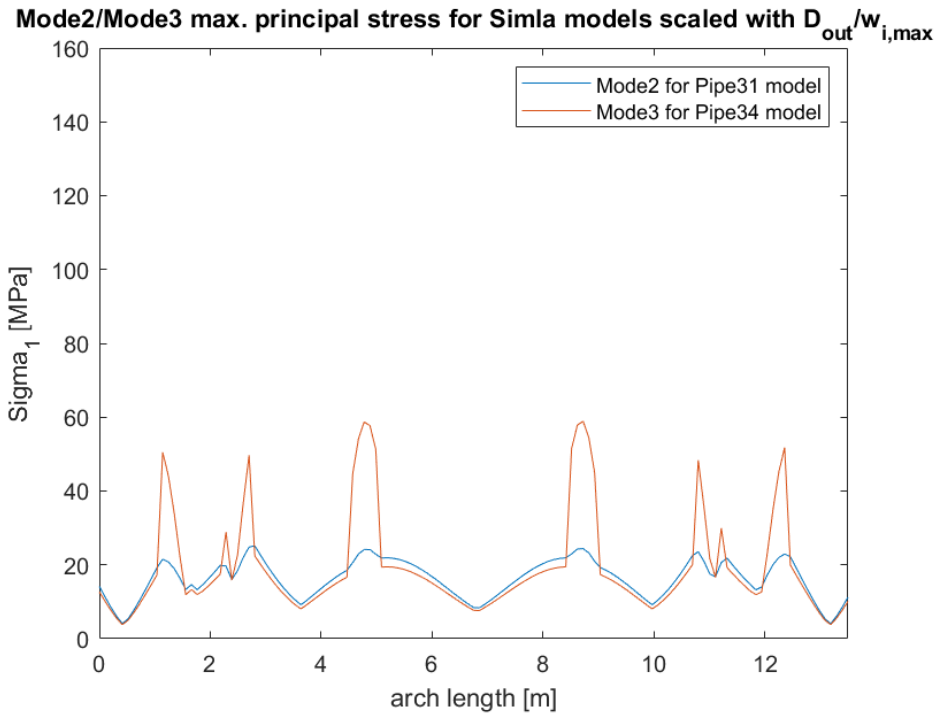

Figure 2: Maximum principal unit stress of mode two for the Pipe31 model and mode three for the Pipe34 model, which describe the same mode shape. Plotted over accumulated arch length and scaled with respect to the outer diameter and maximum modal displacement.

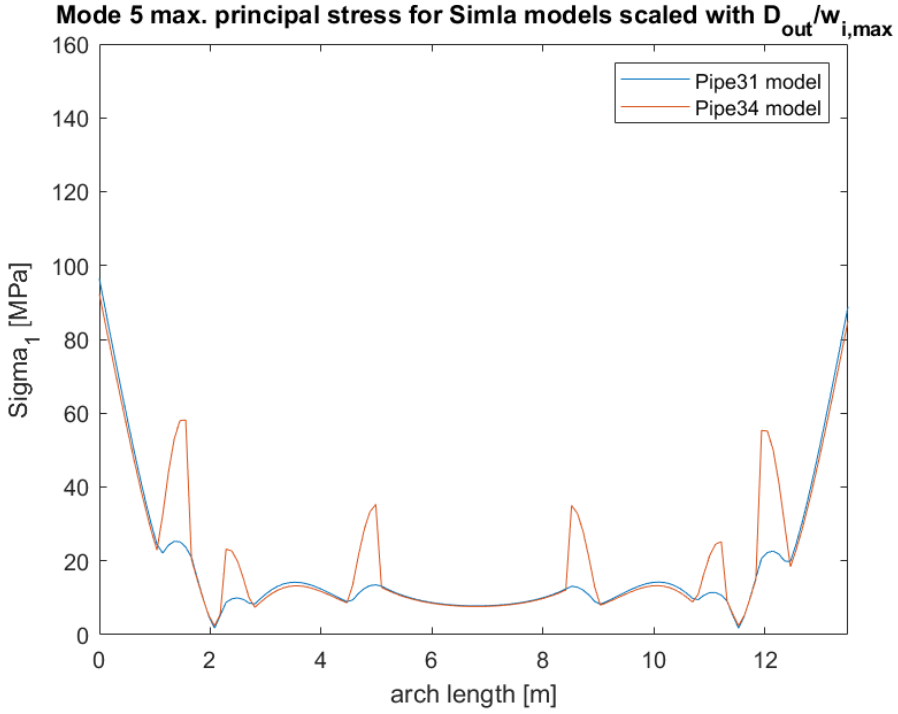

Figure 3: Maximum principal unit stress of mode five for the two Simla models. Plotted over accumulated arch length and scaled with respect to the outer diameter and maximum modal displacement.

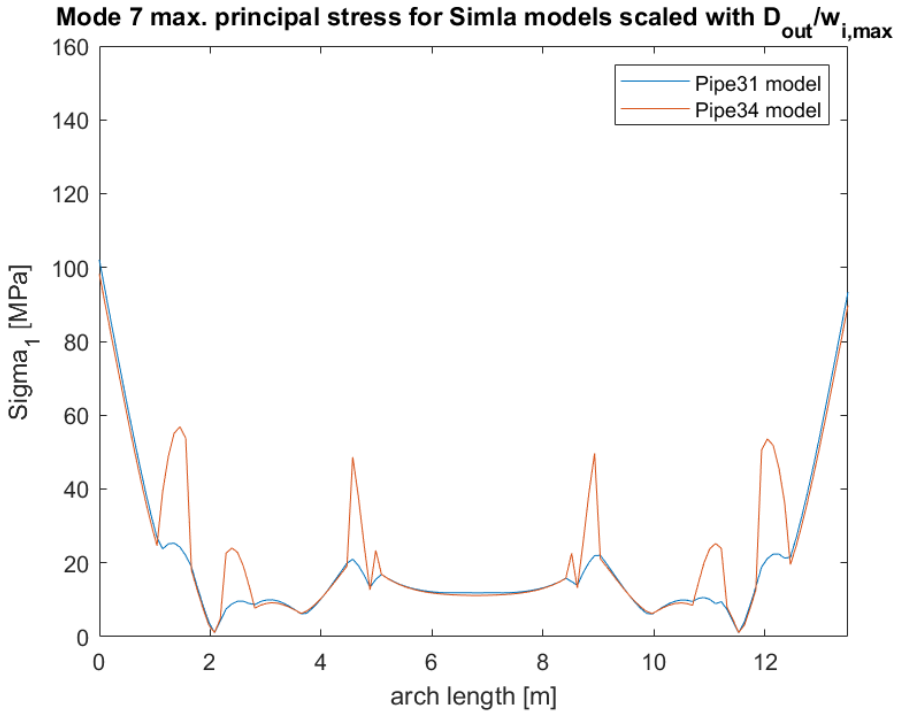

Figure 4: Maximum principal unit stress of mode seven for the two Simla models. Plotted over accumulated arch length and scaled with respect to the outer diameter and maximum modal displacement.

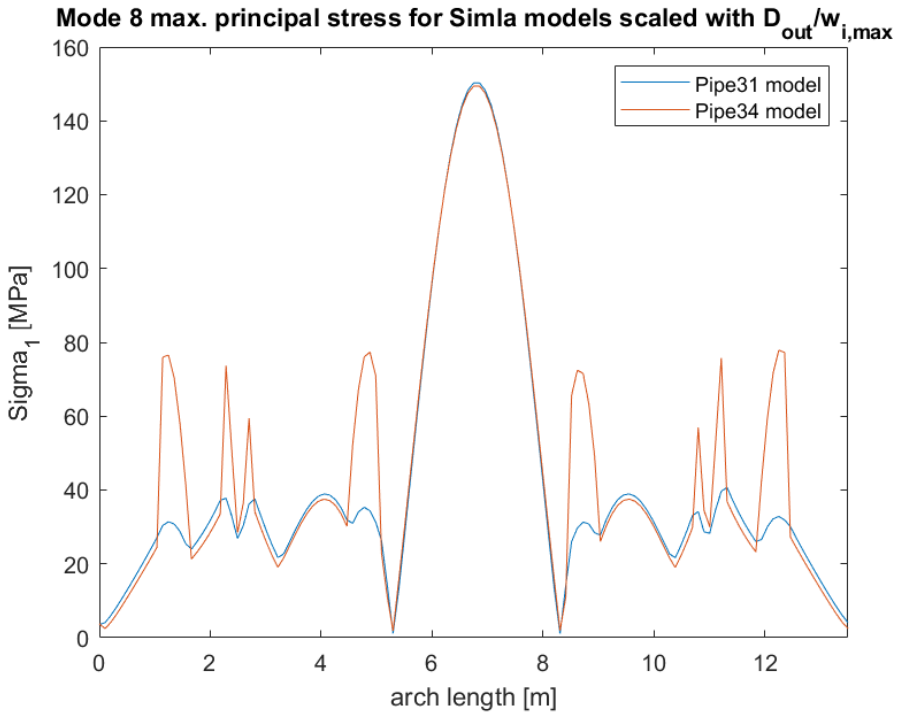

Figure 5: Maximum principal unit stress of mode eight for the two Simla models. Plotted over accumulated arch length and scaled with respect to the outer diameter and maximum modal displacement.

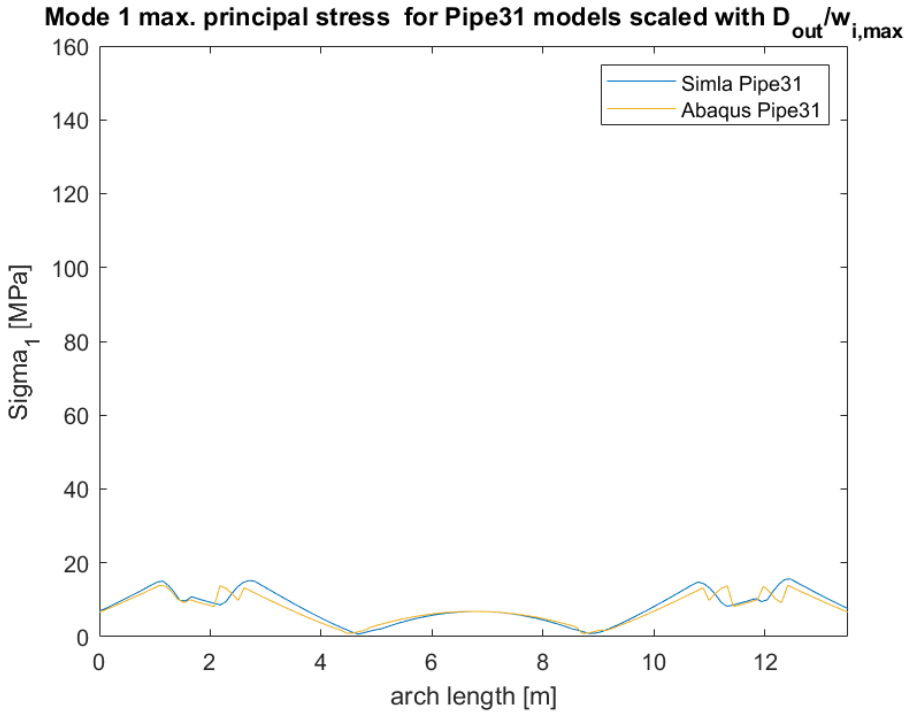

Figure 6: Maximum principal unit stress of mode one for the two Pipe31 models in Simla and Abaqus. Plotted over accumulated arch length and scaled with respect to the outer diameter and maximum modal displacement.

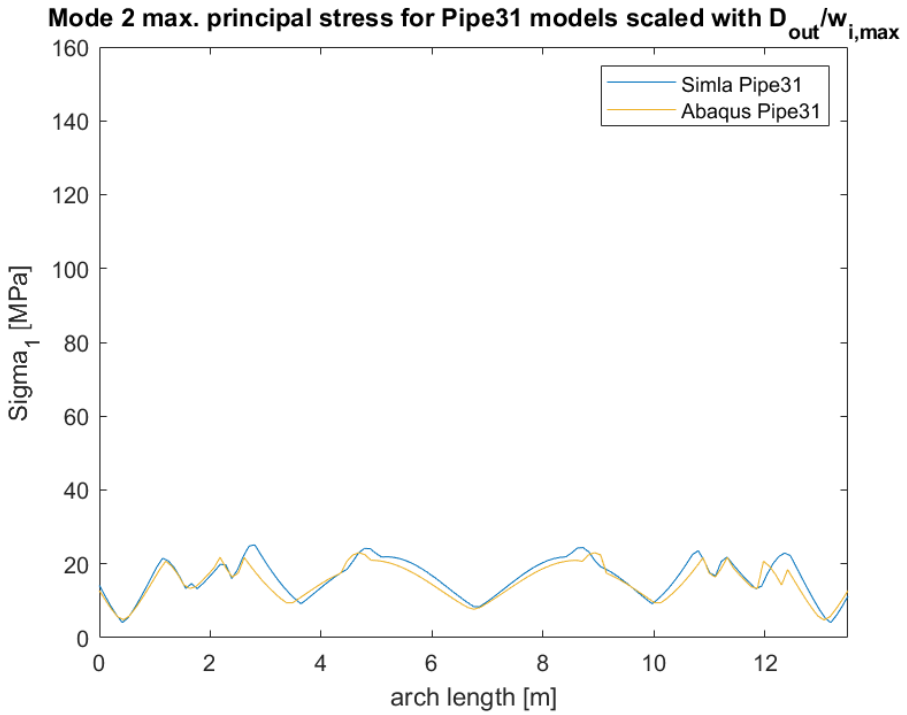

Figure 7: Maximum principal unit stress of mode two for the two Pipe31 models in Simla and Abaqus. Plotted over accumulated arch length and scaled with respect to the outer diameter and maximum modal displacement.

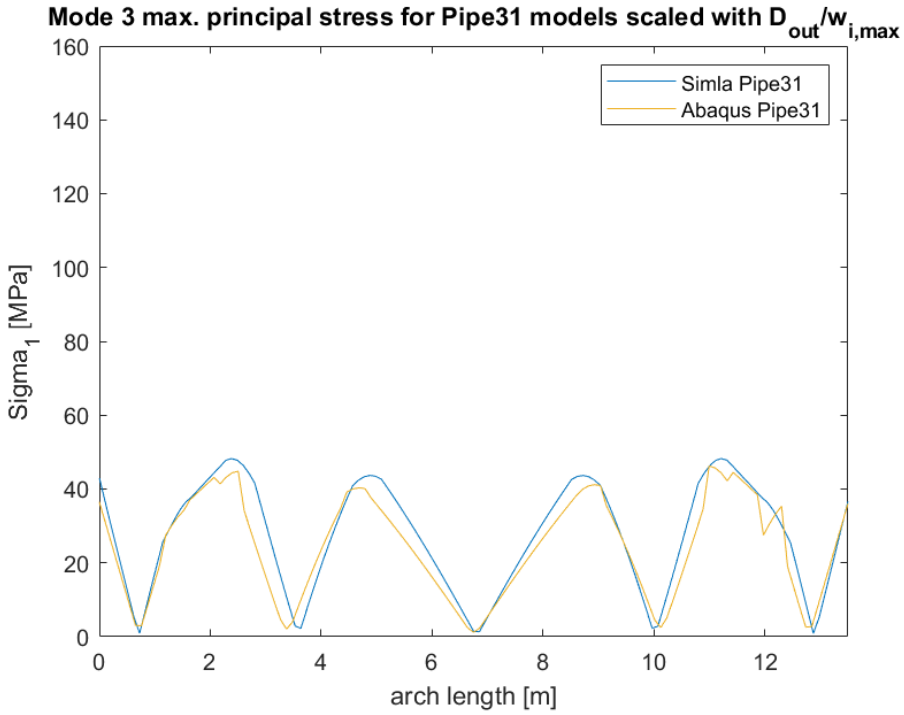

Figure 8: Maximum principal unit stress of mode three for the two Pipe31 models in Simla and Abaqus. Plotted over accumulated arch length and scaled with respect to the outer diameter and maximum modal displacement.

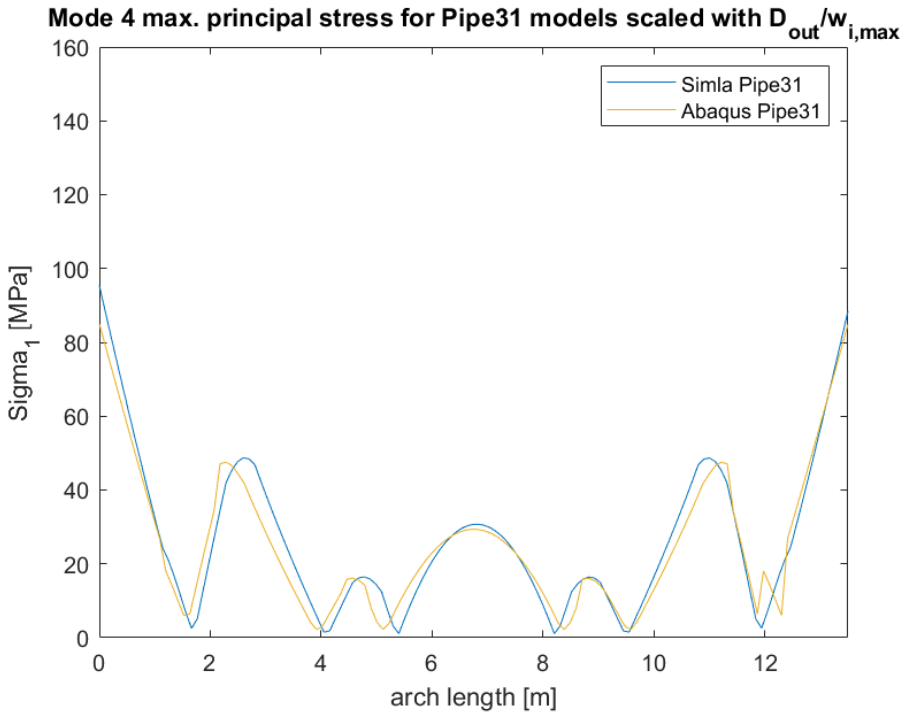

Figure 9: Maximum principal unit stress of mode four for the two Pipe31 models in Simla and Abaqus. Plotted over accumulated arch length and scaled with respect to the outer diameter and maximum modal displacement.

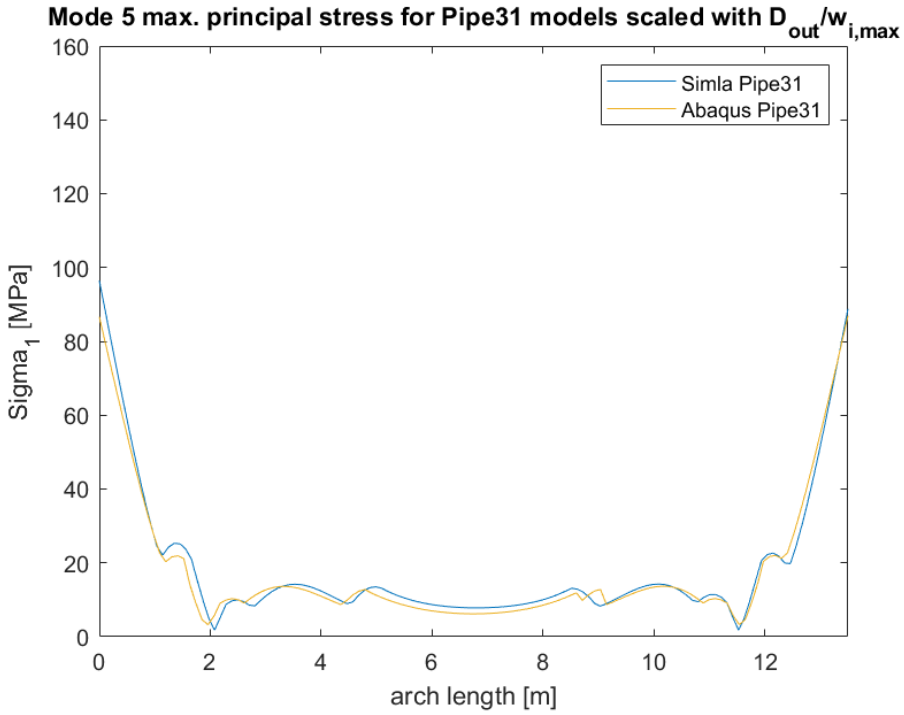

Figure 10: Maximum principal unit stress of mode five for the two Pipe31 models in Simla and Abaqus. Plotted over accumulated arch length and scaled with respect to the outer diameter and maximum modal displacement.

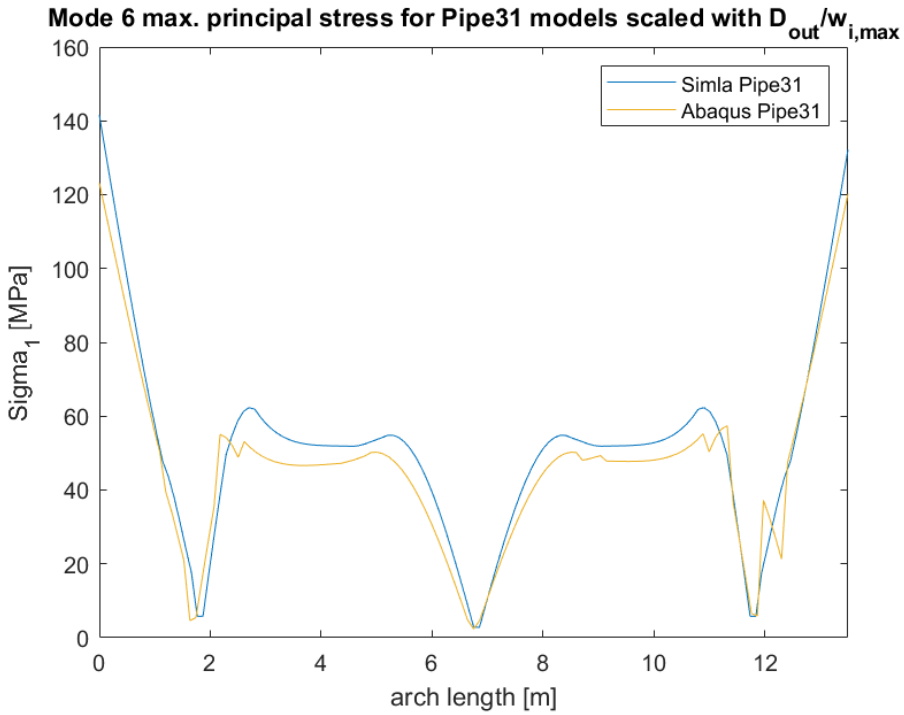

Figure 11: Maximum principal unit stress of mode six for the two Pipe31 models in Simla and Abaqus. Plotted over accumulated arch length and scaled with respect to the outer diameter and maximum modal displacement.

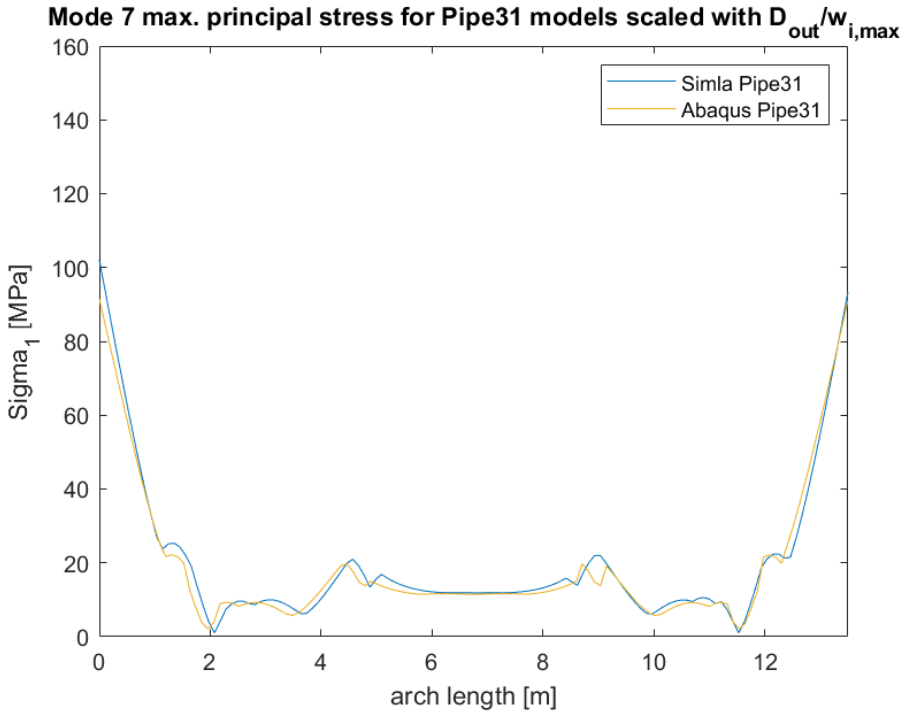

Figure 12: Maximum principal unit stress of mode seven for the two Pipe31 models in Simla and Abaqus. Plotted over accumulated arch length and scaled with respect to the outer diameter and maximum modal displacement.

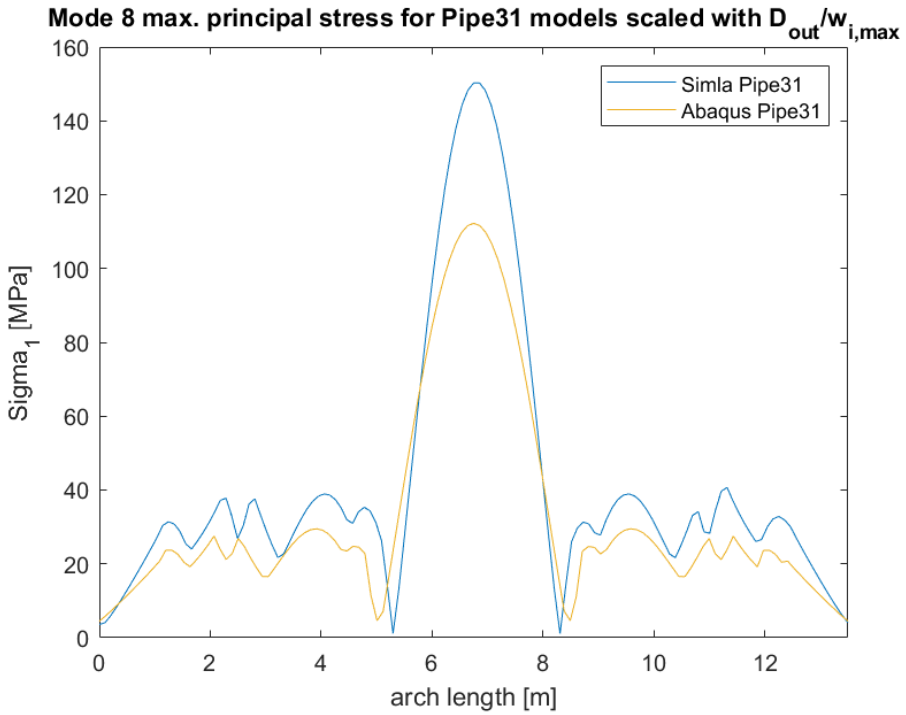

Figure 13: Maximum principal unit stress of mode eight for the two Pipe31 models in Simla and Abaqus. Plotted over accumulated arch length and scaled with respect to the outer diameter and maximum modal displacement.

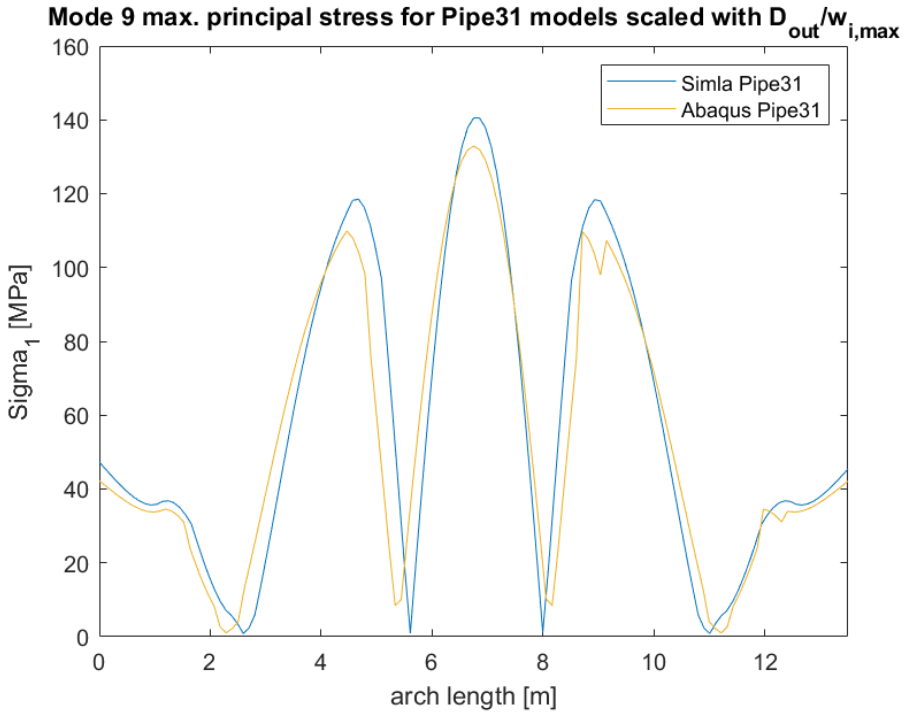

Figure 14: Maximum principal unit stress of mode nine for the two Pipe31 models in Simla and Abaqus. Plotted over accumulated arch length and scaled with respect to the outer diameter and maximum modal displacement.

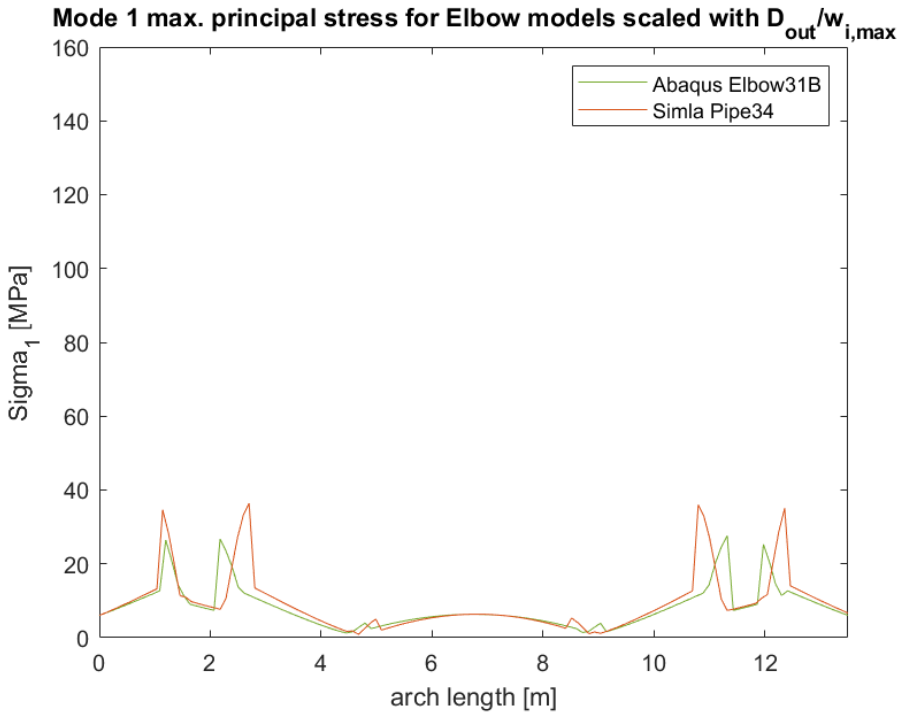

Figure 15: Maximum principal unit stress of mode one for the two Elbow models in Simla and Abaqus. Plotted over accumulated arch length and scaled with respect to the outer diameter and maximum modal displacement.

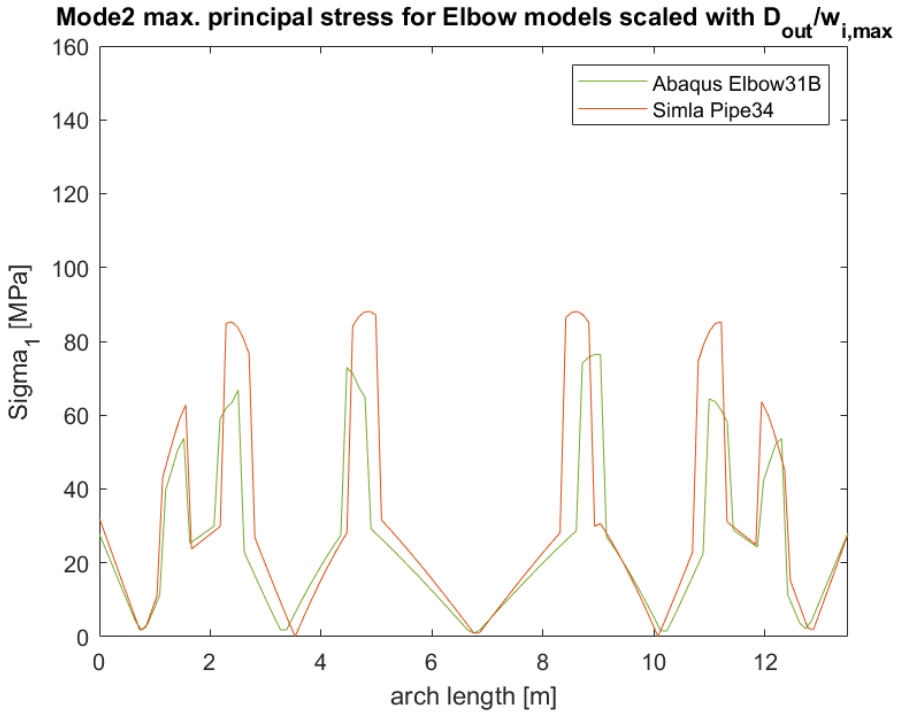

Figure 16: Maximum principal unit stress of mode two for the two Elbow models in Simla and Abaqus. Plotted over accumulated arch length and scaled with respect to the outer diameter and maximum modal displacement.

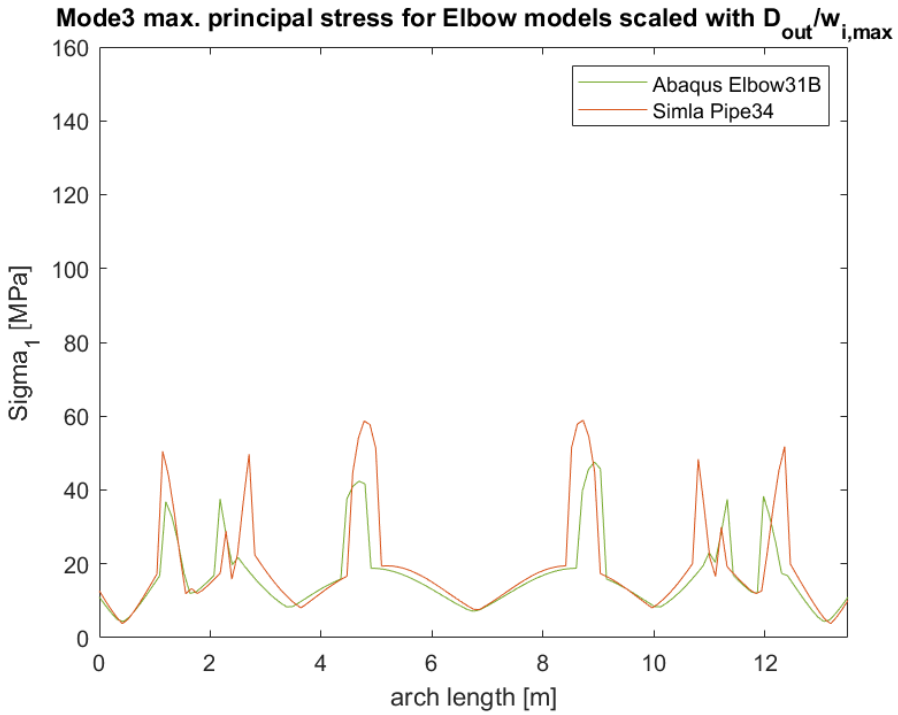

Figure 17: Maximum principal unit stress of mode three for the two Elbow models in Simla and Abaqus. Plotted over accumulated arch length and scaled with respect to the outer diameter and maximum modal displacement.

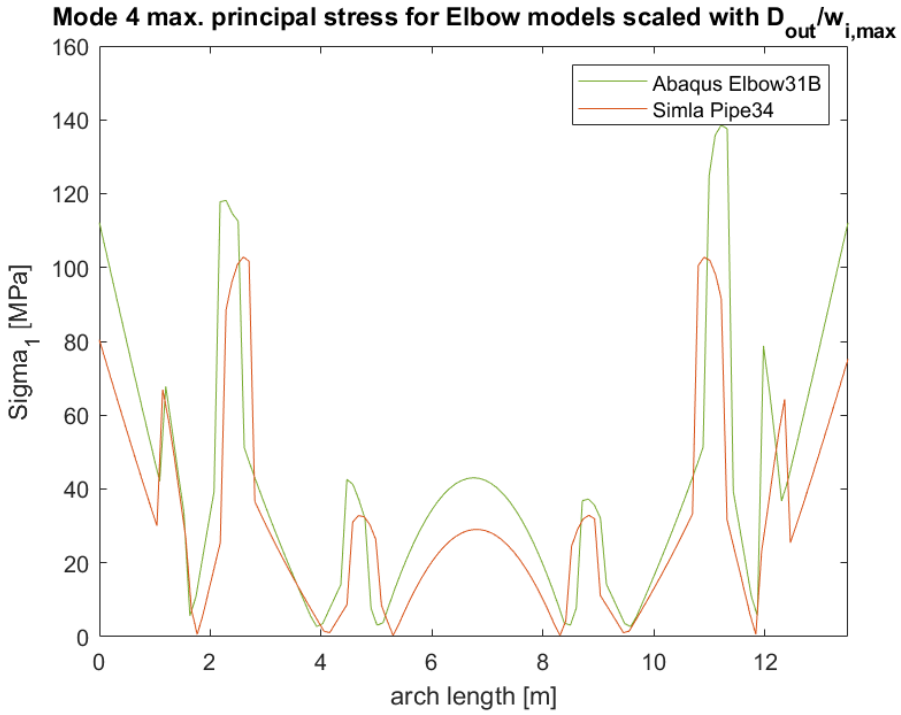

Figure 18: Maximum principal unit stress of mode four for the two Elbow models in Simla and Abaqus. Plotted over accumulated arch length and scaled with respect to the outer diameter and maximum modal displacement.

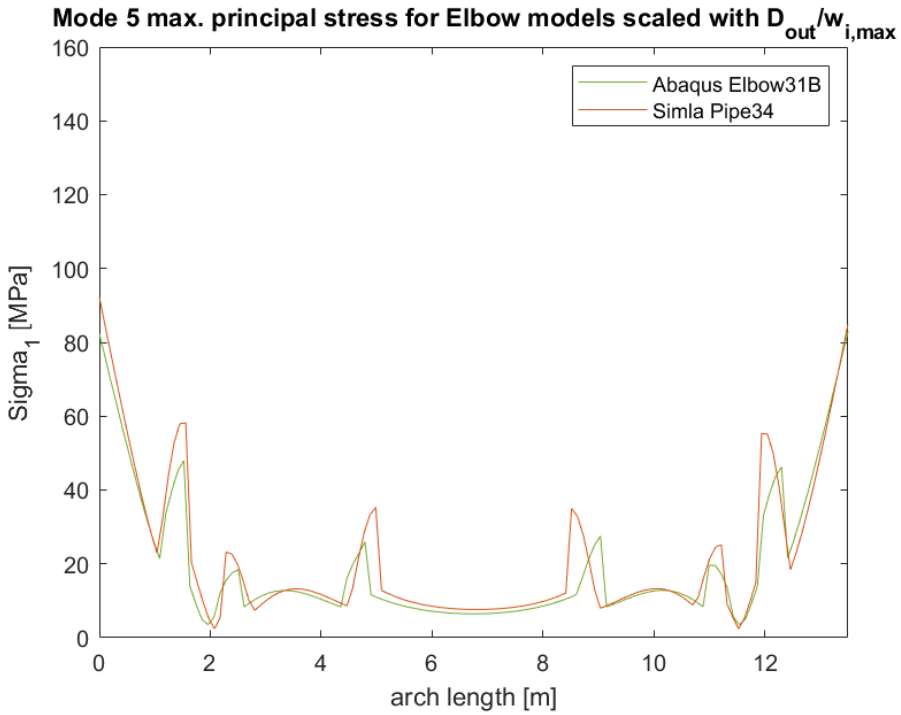

Figure 19: Maximum principal unit stress of mode five for the two Elbow models in Simla and Abaqus. Plotted over accumulated arch length and scaled with respect to the outer diameter and maximum modal displacement.

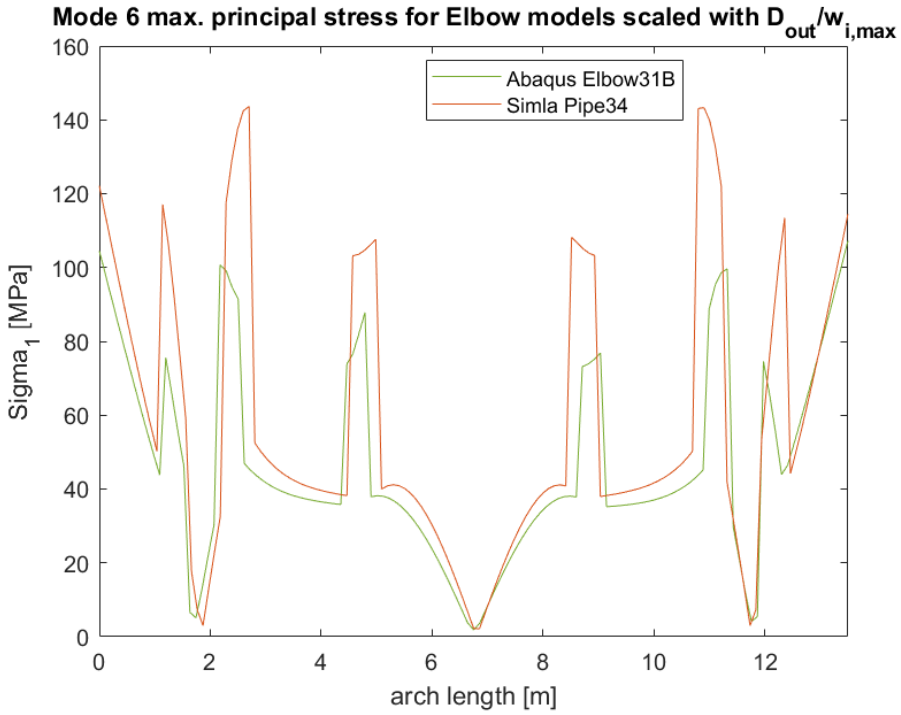

Figure 20: Maximum principal unit stress of mode six for the two Elbow models in Simla and Abaqus. Plotted over accumulated arch length and scaled with respect to the outer diameter and maximum modal displacement.

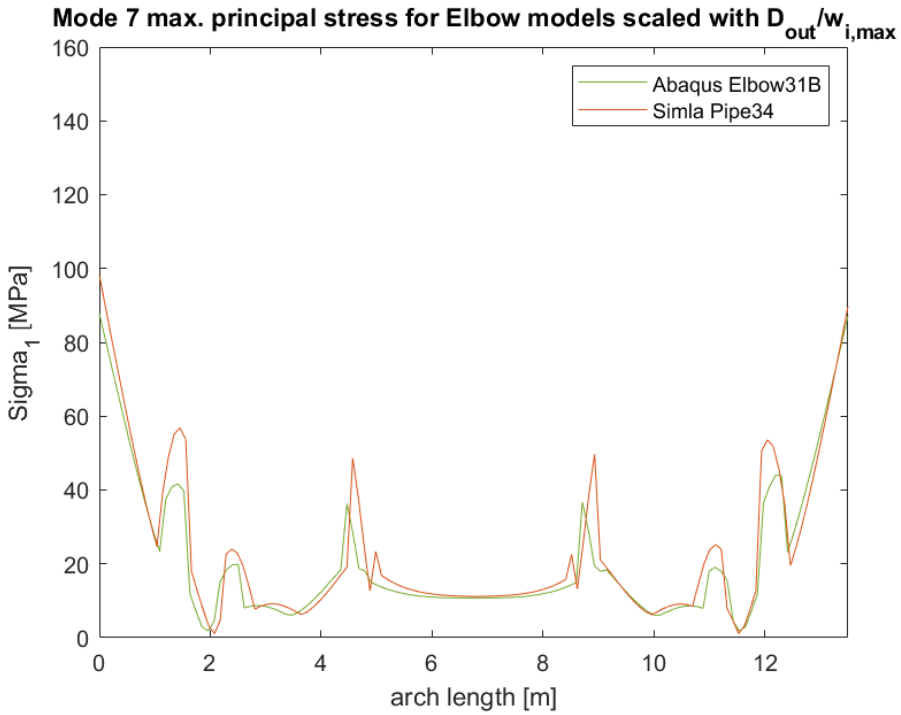

Figure 21: Maximum principal unit stress of mode seven for the two Elbow models in Simla and Abaqus. Plotted over accumulated arch length and scaled with respect to the outer diameter and maximum modal displacement.

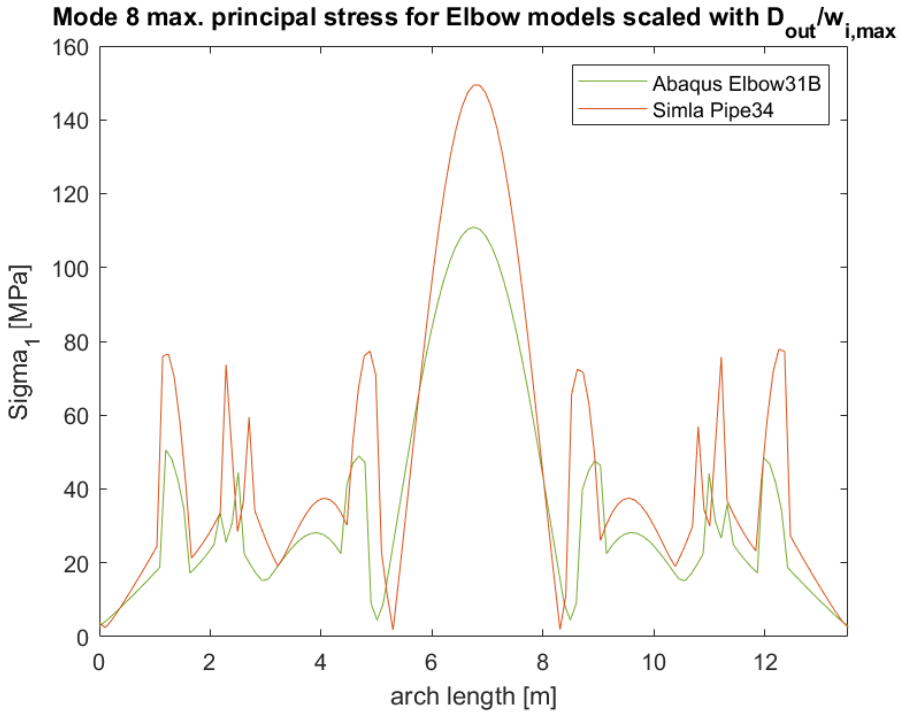

Figure 22: Maximum principal unit stress of mode eight for the two Elbow models in Simla and Abaqus. Plotted over accumulated arch length and scaled with respect to the outer diameter and maximum modal displacement.

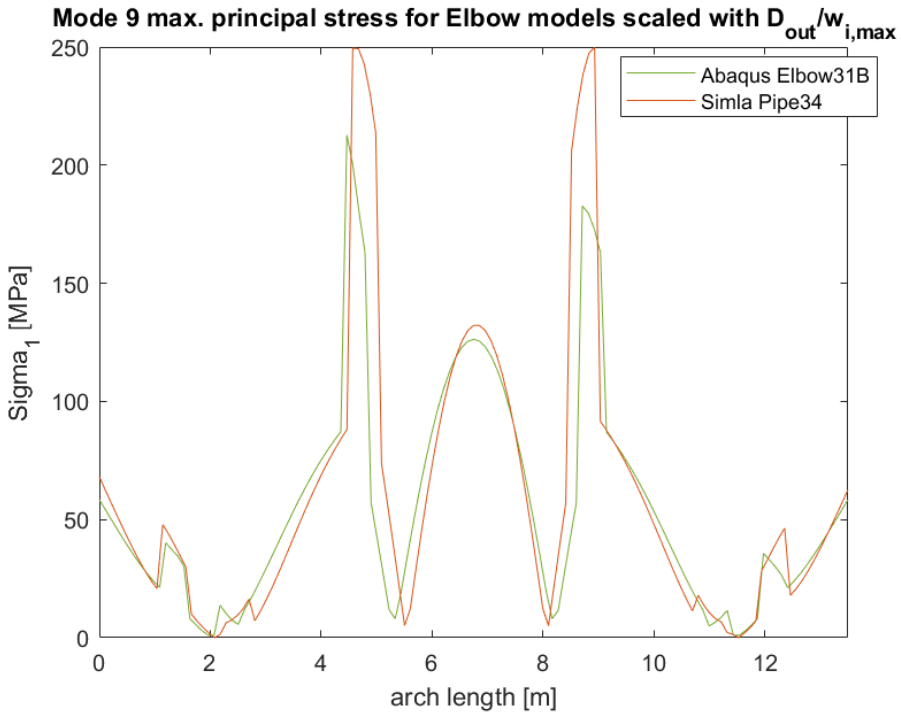

Figure 23: Maximum principal unit stress of mode nine for the two Elbow models in Simla and Abaqus. Plotted over accumulated arch length and scaled with respect to the outer diameter and maximum modal displacement.

Appendix B: Simla VIV motion details

Results from the VIV tool in Simla are listed below in more detail. They were obtained with the following parameters:
$CVI1 = 1.2$
$CV = 1.2$
$\hat{f}_{1I1} = 0.13$

Table 1: Oscillating frequencies, amplitude response and identified modes for the Pipe34 model in 10° flow at position of accelerometer five with $C_{\mathrm{Drag}} = 1.1$

	x-direction			y-direction			z-direction		
Uc	f_{osc}	A/D	mode	f_{osc}	A/D	mode	f_{osc}	A/D	mode
[m/s]	[Hz]	[-]	[-]	[Hz]	[-]	[-]	[Hz]	[-]	[-]
0.05	0.72	0.0005	1	0.72	0.0005	1	0.72	0.0005	1
0.1	1.59	0.0049	2	1.59	0.0049	2	1.59	0.0049	2
0.15	1.88	0.0882	2	0.37	0.0112	1	1.88	0.0118	2
0.2	1.91	0.160	2	0.49	0.0451	1	1.91	0.0224	2
0.25	1.93	0.200	2	0.77	0.467	1	1.93	0.0291	2
0.3	1.95	0.229	2	0.80	0.621	1	1.95	0.0377	2
0.35	1.97	0.250	2	0.83	0.669	1	1.97	0.0820	2
0.4	2.00	0.257	2	0.84	0.700	1	3.47	0.105	6
0.45	2.03	0.248	3	0.87	0.670	1	3.48	0.120	6
0.5	2.07	0.225	3	0.89	0.648	1	3.49	0.132	6
0.55	1.88	0.206	2	0.95	0.449	1	7.13	0.0432	9
0.6	3.95	0.127	7	1.97	0.495	2	7.20	0.0418	9
0.65	4.11	0.0265	7	2.05	0.679	3	7.25	0.0523	9
0.7	4.17	0.0309	7	2.08	0.778	3	7.31	0.0545	9
0.75	7.85	0.0518	9	2.12	0.836	3	7.85	0.0594	9
0.8	7.91	0.0581	9	2.15	0.861	3	7.91	0.0653	9
0.85	7.95	0.0608	9	2.17	0.899	3	7.95	0.0680	9
0.9	4.39	0.0374	7	2.20	0.948	3	7.53	0.0713	9
0.95	4.45	0.0356	7	2.23	0.951	3	7.59	0.0815	9
0.98	4.48	0.0402	7	2.24	0.979	3	7.63	0.0955	9

Table 2: Oscillating frequencies, amplitude response and identified modes for the Pipe34 model in 10° flow at position of accelerometer three with $C_{\mathrm{Drag}} = 1.1$

	x-direction			y-direction			z-direction		
Uc	f_{osc}	A/D	mode	f_{osc}	A/D	mode	f_{osc}	A/D	mode
[m/s]	[Hz]	[-]	[-]	[Hz]	[-]	[-]	[Hz]	[-]	[-]
0.05	0.72	0.0002	1	0.72	0.0002	1	0.72	0.0002	1
0.1	1.59	0.0012	2	1.59	0.0012	2	1.59	0.0012	2
0.15	1.88	0.0154	2	0.37	0.0016	1	1.88	0.0087	2
0.2	1.91	0.0274	2	0.51	0.0051	1	1.91	0.0170	2
0.25	1.93	0.0339	2	0.77	0.0409	1	1.93	0.0218	2
0.3	1.95	0.0372	2	0.80	0.0534	1	1.95	0.0287	2
0.35	1.97	0.0702	2	0.83	0.0610	1	1.97	0.0763	2
0.4	3.47	0.0859	6	0.84	0.0635	1	3.47	0.0984	6
0.45	3.48	0.0970	6	0.87	0.0673	1	3.48	0.114	6
0.5	3.49	0.105	6	0.89	0.0782	1	3.49	0.127	6
0.55	7.13	0.060	9	0.95	0.0525	1	7.13	0.0440	9
0.6	7.20	0.076	9	1.97	0.106	2	7.20	0.0476	9
0.65	7.25	0.080	9	2.05	0.135	3	7.25	0.0582	9
0.7	7.31	0.087	9	2.08	0.144	3	7.31	0.0636	9
0.75	7.85	0.093	9	2.12	0.154	3	7.85	0.0677	9
0.8	7.91	0.096	9	2.15	0.161	3	7.91	0.0736	9
0.85	7.95	0.105	9	2.17	0.146	3	7.95	0.0756	9
0.9	7.53	0.110	9	2.20	0.166	3	7.53	0.0745	9
0.95	7.59	0.117	9	2.23	0.188	3	7.59	0.0841	9
0.98	7.63	0.124	9	2.24	0.477	3	7.63	0.100	9

Table 3: Oscillating frequencies, amplitude response and identified modes for the Pipe34 model in 10° flow at position of accelerometer five with $C_{\mathrm{Drag}} = 1.2$

	x-direction			y-direction			z-direction		
Uc	f_{osc}	A/D	mode	f_{osc}	A/D	mode	f_{osc}	A/D	mode
[m/s]	[Hz]	[-]	[-]	[Hz]	[-]	[-]	[Hz]	[-]	[-]
0.05	0.72	0.0007	1	0.72	0.0007	1	0.72	0.0007	1
0.1	1.57	0.0049	2	1.57	0.0049	2	1.57	0.0049	2
0.15	1.88	0.0827	2	0.37	0.0111	1	1.88	0.0110	2
0.2	1.91	0.149	2	0.51	0.0464	1	1.91	0.0208	2
0.25	1.93	0.186	2	0.76	0.435	1	1.93	0.0271	2
0.3	1.95	0.212	2	0.80	0.578	1	1.95	0.0347	2
0.35	1.97	0.233	2	0.83	0.637	1	1.97	0.0793	2
0.4	2.00	0.242	2	0.84	0.661	1	3.47	0.100	6
0.45	2.04	0.228	3	0.87	0.635	1	3.48	0.116	6
0.5	2.08	0.222	3	0.91	0.616	1	3.49	0.126	6
0.55	1.85	0.191	2	0.93	0.526	1	7.56	0.0376	9
0.6	3.93	0.106	7	1.96	0.462	2	7.20	0.0401	9
0.65	7.75	0.0564	9	2.05	0.645	3	7.75	0.0435	9
0.7	4.16	0.0274	7	2.08	0.714	3	7.31	0.0500	9
0.75	7.85	0.0499	9	2.12	0.769	3	7.85	0.0553	9
0.8	7.91	0.0537	9	2.15	0.808	3	7.91	0.0615	9
0.85	4.33	0.0336	7	2.17	0.862	3	7.48	0.0629	9
0.9	4.39	0.0355	7	2.20	0.877	3	7.55	0.0631	9
0.95	4.45	0.0342	7	2.23	0.890	3	2.23	0.0819	3
0.98	4.49	0.0352	7	2.24	0.901	3	7.65	0.0870	9

Table 4: Oscillating frequencies, amplitude response and identified modes for the Pipe34 model in 10° flow at position of accelerometer three with $C_{\mathrm{Drag}} = 1.2$

	x-direction			y-direction			z-direction		
Uc	f_{osc}	A/D	mode	f_{osc}	A/D	mode	f_{osc}	A/D	mode
[m/s]	[Hz]	[-]	[-]	[Hz]	[-]	[-]	[Hz]	[-]	[-]
0.05	0.72	0.0002	1	0.72	0.0002	1	0.72	0.0002	1
0.1	1.57	0.0012	2	1.57	0.0012	2	1.57	0.0012	2
0.15	1.88	0.0145	2	0.37	0.0016	1	1.88	0.0082	2
0.2	1.91	0.0254	2	0.51	0.0052	1	1.91	0.0157	2
0.25	1.93	0.0313	2	0.76	0.0378	1	1.93	0.0204	2
0.3	1.95	0.0350	2	0.80	0.0497	1	1.95	0.0265	2
0.35	1.97	0.0718	2	0.83	0.0582	1	3.45	0.0744	6
0.4	3.47	0.0845	6	0.84	0.0616	1	3.47	0.0935	6
0.45	3.48	0.0959	6	0.87	0.0635	1	3.48	0.110	6
0.5	3.49	0.102	6	0.91	0.0755	1	3.49	0.121	6
0.55	7.56	0.0444	9	0.93	0.0557	1	7.56	0.0357	9
0.6	7.20	0.0712	9	1.96	0.0981	2	7.20	0.0448	9
0.65	7.75	0.0710	9	2.05	0.134	3	7.75	0.0458	9
0.7	7.31	0.0831	9	2.08	0.135	3	7.31	0.0581	9
0.75	7.85	0.0853	9	2.12	0.148	3	7.85	0.0608	9
0.8	7.91	0.0903	9	2.15	0.152	3	7.91	0.0673	9
0.85	7.48	0.103	9	2.17	0.145	3	7.48	0.0654	9
0.9	7.55	0.100	9	2.20	0.151	3	7.55	0.0675	9
0.95	7.61	0.116	9	2.23	0.229	3	7.61	0.0820	9
0.98	7.65	0.115	9	2.24	0.287	3	7.65	0.0881	9

Table 5: Oscillating frequencies, amplitude response and identified modes for the Pipe31 model in 10° flow at position of accelerometer five with $C_{\mathrm{Drag}} = 1.1$

	x-direction			y-direction			z-direction		
Uc	f_{osc}	A/D	mode	f_{osc}	A/D	mode	f_{osc}	A/D	mode
[m/s]	[Hz]	[-]	[-]	[Hz]	[-]	[-]	[Hz]	[-]	[-]
0.05	0.72	0.0004	1	0.72	0.0004	1	0.72	0.0004	1
0.1	1.93	0.0023	2	1.93	0.0023	2	1.93	0.0023	2
0.15	2.15	0.0262	2	0.39	0.0100	1	2.15	0.0027	2
0.2	2.27	0.115	3	0.51	0.0294	1	2.27	0.0147	3
0.25	2.29	0.164	3	0.79	0.302	1	2.29	0.0219	3
0.3	2.31	0.189	3	0.84	0.572	1	2.31	0.0298	3
0.35	2.33	0.210	3	0.87	0.639	1	2.33	0.0333	3
0.4	2.36	0.223	3	0.88	0.645	1	2.36	0.080	3
0.45	2.39	0.231	3	0.91	0.627	1	3.73	0.101	6
0.5	2.41	0.233	3	0.93	0.587	1	3.75	0.115	7
0.55	2.44	0.234	3	0.96	0.574	1	3.76	0.127	7
0.6	2.48	0.224	4	1.00	0.547	1	3.77	0.136	7
0.65	4.25	0.158	7	2.13	0.587	2	8.28	0.0524	9
0.7	4.35	0.0603	7	2.17	0.697	2	8.36	0.0453	9
0.75	4.40	0.0292	7	2.20	0.778	2	8.44	0.0501	9
0.8	4.45	0.0287	7	2.23	0.861	2	8.51	0.0525	9
0.85	4.49	0.0317	7	2.24	0.892	2	8.57	0.0543	9
0.9	4.53	0.0327	7	2.27	0.931	3	8.64	0.0565	9
0.95	4.59	0.0394	7	2.29	1.054	3	8.71	0.0644	9
0.98	4.63	0.0345	7	2.31	0.948	3	8.75	0.0621	9

Table 6: Oscillating frequencies, amplitude response and identified modes for the Pipe31 model in 10° flow at position of accelerometer three with $C_{\mathrm{Drag}} = 1.1$

	x-direction			y-direction			z-direction		
Uc	f_{osc}	A/D	mode	f_{osc}	A/D	mode	f_{osc}	A/D	mode
[m/s]	[Hz]	[-]	[-]	[Hz]	[-]	[-]	[Hz]	[-]	[-]
0.05	0.72	0.0001	1	0.72	0.0001	1	0.72	0.0001	1
0.1	1.93	0.0007	2	1.93	0.0007	2	1.93	0.0007	2
0.15	2.15	0.0060	2	0.39	0.0023	1	2.15	0.0018	2
0.2	2.27	0.0233	3	0.51	0.0054	1	2.27	0.0101	3
0.25	2.29	0.0326	3	0.79	0.0391	1	2.29	0.0153	3
0.3	2.31	0.0386	3	0.84	0.0707	1	2.31	0.0211	3
0.35	2.33	0.0421	3	0.87	0.0815	1	2.33	0.0237	3
0.4	2.36	0.0775	3	0.88	0.0883	1	2.36	0.0740	3
0.45	3.73	0.0959	6	0.91	0.0969	1	3.73	0.0931	6
0.5	3.75	0.105	7	3.35	0.0982	5	3.75	0.107	7
0.55	3.76	0.114	7	0.96	0.0926	1	3.76	0.120	7
0.6	3.77	0.119	7	1.00	0.0796	1	3.77	0.129	7
0.65	8.28	0.0644	9	2.13	0.143	2	8.28	0.0533	9
0.7	8.36	0.0693	9	2.17	0.165	2	8.36	0.0454	9
0.75	8.44	0.0807	9	2.20	0.175	2	8.44	0.0554	9
0.8	8.51	0.0824	9	2.23	0.185	2	8.51	0.0576	9
0.85	8.57	0.0892	9	2.24	0.188	2	8.57	0.0580	9
0.9	8.64	0.0924	9	2.27	0.171	3	8.64	0.0584	9
0.95	8.71	0.0965	9	2.29	0.209	3	8.71	0.0672	9
0.98	8.75	0.100	9	2.31	0.195	3	8.75	0.0656	9

Table 7: Oscillating frequencies, amplitude response and identified modes for the Pipe31 model in 10° flow at position of accelerometer five with $C_{\mathrm{Drag}} = 1.2$

	x-direction			y-direction			z-direction		
Uc	f_{osc}	A/D	mode	f_{osc}	A/D	mode	f_{osc}	A/D	mode
[m/s]	[Hz]	[-]	[-]	[Hz]	[-]	[-]	[Hz]	[-]	[-]
0.05	0.72	0.0004	1	0.72	0.0004	1	0.72	0.0004	1
0.1	1.92	0.0023	2	1.92	0.0023	2	1.92	0.0023	2
0.15	2.15	0.0257	2	0.39	0.0100	1	2.15	0.0028	2
0.2	2.27	0.108	3	0.51	0.0293	1	2.27	0.0137	3
0.25	2.29	0.152	3	0.77	0.287	1	2.29	0.0203	3
0.3	2.31	0.177	3	0.84	0.532	1	2.31	0.0269	3
0.35	2.33	0.196	3	0.87	0.610	1	2.33	0.0321	3
0.4	2.36	0.208	3	0.88	0.614	1	2.36	0.0828	3
0.45	2.39	0.216	3	0.91	0.593	1	3.73	0.0976	6
0.5	2.43	0.219	3	0.93	0.570	1	3.75	0.107	7
0.55	2.45	0.214	3	0.96	0.551	1	3.76	0.119	7
0.6	2.49	0.208	4	1.00	0.534	1	3.77	0.131	7
0.65	4.23	0.153	7	2.11	0.542	2	8.28	0.0441	9
0.7	4.32	0.0529	7	2.16	0.645	2	8.36	0.0408	9
0.75	4.39	0.0251	7	2.20	0.724	2	8.44	0.0490	9
0.8	4.44	0.0285	7	2.23	0.779	2	8.51	0.0468	9
0.85	4.49	0.0298	7	2.24	0.825	2	8.57	0.0545	9
0.9	4.53	0.0311	7	2.27	0.872	3	8.64	0.0554	9
0.95	4.59	0.0312	7	2.29	0.875	3	8.71	0.0497	9
0.98	4.67	0.0659	7	2.33	0.853	3	9.32	0.0557	9

Table 8: Oscillating frequencies, amplitude response and identified modes for the Pipe31 model in 10° flow at position of accelerometer three with $C_{\mathrm{Drag}} = 1.2$

	x-direction			y-direction			z-direction		
Uc	f_{osc}	A/D	mode	f_{osc}	A/D	mode	f_{osc}	A/D	mode
[m/s]	[Hz]	[-]	[-]	[Hz]	[-]	[-]	[Hz]	[-]	[-]
0.05	0.72	0.0001	1	0.72	0.0001	1	0.72	0.0001	1
0.1	1.92	0.0007	2	1.92	0.0007	2	1.92	0.0007	2
0.15	2.15	0.0059	2	0.39	0.0023	1	2.15	0.0018	2
0.2	2.27	0.0219	3	0.51	0.0055	1	2.27	0.0094	3
0.25	2.29	0.0303	3	0.77	0.0371	1	2.29	0.0143	3
0.3	2.31	0.0353	3	0.84	0.0653	1	2.31	0.0189	3
0.35	2.33	0.0396	3	0.87	0.0773	1	2.33	0.0235	3
0.4	2.36	0.0789	3	0.88	0.0840	1	3.72	0.0751	6
0.45	3.73	0.0909	6	0.91	0.0899	1	3.73	0.0900	6
0.5	3.75	0.0986	7	0.93	0.0884	1	3.75	0.101	7
0.55	3.76	0.109	7	0.96	0.0866	1	3.76	0.112	7
0.6	3.77	0.115	7	1.00	0.0688	1	3.77	0.125	7
0.65	8.28	0.0633	9	2.11	0.132	2	8.28	0.0454	9
0.7	8.36	0.0684	9	2.16	0.151	2	8.36	0.0451	9
0.75	8.44	0.0743	9	2.20	0.164	2	8.44	0.0523	9
0.8	8.51	0.0821	9	2.23	0.175	2	8.51	0.0499	9
0.85	8.57	0.0858	9	2.24	0.180	2	8.57	0.0586	9
0.9	8.64	0.0878	9	2.27	0.160	3	8.64	0.0552	9
0.95	8.71	0.0886	9	2.29	0.159	3	8.71	0.0550	9
0.98	9.32	0.0907	9	2.33	0.231	3	9.32	0.0655	9

Table 9: Oscillating frequencies, amplitude response and identified modes for the Pipe34 model in 45° flow at position of accelerometer seven with $C_{\mathrm{Drag}} = 1.1$

	x-direction			y-direction			z-direction		
Uc	f_{osc}	A/D	mode	f_{osc}	A/D	mode	f_{osc}	A/D	mode
[m/s]	[Hz]	[-]	[-]	[Hz]	[-]	[-]	[Hz]	[-]	[-]
0.05	0.72	0.0004	1	0.72	0.0004	1	0.72	0.0004	1
0.1	0.78	0.0013	1	0.78	0.0013	1	0.78	0.0013	1
0.15	0.82	0.0084	1	0.82	0.228	1	1.63	0.0019	2
0.2	1.90	0.0198	2	0.85	0.246	1	2.40	0.0224	4
0.25	1.92	0.1864	2	0.87	0.258	1	1.92	0.0061	2
0.3	1.93	0.1701	2	0.88	0.298	1	1.93	0.0127	2
0.35	0.88	0.0514	1	0.88	0.276	1	2.40	0.0252	4
0.4	1.97	0.1786	2	0.98	0.357	1	2.38	0.0201	4
0.45	1.13	0.0376	1	1.13	0.176	1	2.20	0.0222	3
0.5	1.33	0.0420	1	1.33	0.132	1	2.22	0.0341	3
0.55	1.50	0.0670	2	1.50	0.142	2	2.25	0.0475	3
0.6	1.77	0.192	2	1.77	0.146	2	2.25	0.0555	3
0.65	1.92	0.424	2	1.92	0.180	2	2.22	0.0590	3
0.7	1.95	0.577	2	1.95	0.237	2	1.95	0.0729	2
0.75	1.98	0.537	2	1.98	0.254	2	1.98	0.0845	2
0.8	1.97	0.664	2	1.97	0.236	2	1.57	0.130	2
0.85	2.00	0.622	2	2.00	0.266	2	2.17	0.230	3
0.9	2.05	0.565	3	6.33	0.273	8	2.27	0.432	3
0.95	2.48	0.118	4	2.48	0.112	4	2.48	1.048	4
0.98	2.50	0.0407	4	2.48	0.118	4	2.48	1.066	4

Table 10: Oscillating frequencies, amplitude response and identified modes for the Pipe34 model in 45° flow at position of accelerometer three with $C_{\mathrm{Drag}} = 1.1$

	x-direction			y-direction			z-direction		
Uc	f_{osc}	A/D	mode	f_{osc}	A/D	mode	f_{osc}	A/D	mode
[m/s]	[Hz]	[-]	[-]	[Hz]	[-]	[-]	[Hz]	[-]	[-]
0.05	0.71	0.0001	1	0.71	0.0001	1	0.71	0.0001	1
0.1	0.79	0.0007	1	0.79	0.0007	1	0.79	0.0007	1
0.15	0.81	0.0018	1	0.81	0.0178	1	1.63	0.0025	2
0.2	2.40	0.0128	4	0.84	0.0215	1	2.40	0.0136	4
0.25	1.92	0.0319	2	0.87	0.0546	1	1.92	0.0210	2
0.3	1.93	0.0373	2	3.28	0.0912	5	1.93	0.0317	2
0.35	3.32	0.0325	5	3.32	0.138	5	3.32	0.0363	5
0.4	1.97	0.0577	2	3.36	0.141	5	3.36	0.0624	5
0.45	3.43	0.0617	6	3.43	0.157	6	3.43	0.0811	6
0.5	3.45	0.0781	6	3.45	0.171	6	3.45	0.101	6
0.55	3.48	0.0909	6	3.48	0.187	6	3.48	0.124	6
0.6	3.51	0.105	6	3.51	0.204	6	3.51	0.125	6
0.65	1.92	0.131	2	3.55	0.237	6	3.55	0.146	6
0.7	1.95	0.164	2	3.59	0.248	6	3.59	0.213	6
0.75	1.99	0.135	2	3.61	0.232	7	3.61	0.173	7
0.8	1.96	0.190	2	3.92	0.251	7	1.96	0.189	2
0.85	1.99	0.250	2	3.99	0.249	7	1.99	0.226	2
0.9	2.27	0.291	3	2.25	0.241	3	2.27	0.331	3
0.95	2.48	0.594	4	2.48	0.119	4	2.48	0.702	4
0.98	2.49	0.590	4	2.49	0.160	4	2.49	0.721	4

Table 11: Oscillating frequencies, amplitude response and identified modes for the Pipe34 model in 45° flow at position of accelerometer seven with $C_{\mathrm{Drag}} = 1.2$

	x-direction			y-direction			z-direction		
Uc	f_{osc}	A/D	mode	f_{osc}	A/D	mode	f_{osc}	A/D	mode
[m/s]	[Hz]	[-]	[-]	[Hz]	[-]	[-]	[Hz]	[-]	[-]
0.05	0.70	0.0004	1	0.70	0.0004	1	0.70	0.0004	1
0.1	0.78	0.0014	1	0.78	0.0014	1	0.78	0.0014	1
0.15	0.82	0.0069	1	0.82	0.207	1	1.63	0.0023	2
0.2	1.90	0.0249	2	0.85	0.223	1	2.40	0.0219	4
0.25	1.92	0.173	2	0.87	0.233	1	1.92	0.0048	2
0.3	0.80	0.0474	1	0.80	0.199	1	2.12	0.0131	3
0.35	1.95	0.157	2	0.92	0.337	1	2.40	0.0152	4
0.4	1.97	0.140	2	0.98	0.285	1	2.17	0.0192	3
0.45	1.97	0.110	2	1.07	0.321	1	2.35	0.0152	4
0.5	1.32	0.0437	1	1.32	0.132	1	2.23	0.0358	3
0.55	1.48	0.0813	2	1.48	0.159	2	2.27	0.0642	3
0.6	1.75	0.175	2	1.75	0.142	2	2.25	0.0680	3
0.65	1.92	0.3978	2	1.92	0.184	2	1.92	0.0620	2
0.7	1.95	0.5586	2	1.95	0.234	2	1.95	0.0711	2
0.75	1.98	0.4955	2	1.98	0.250	2	1.98	0.0713	2
0.8	1.93	0.5358	2	1.93	0.272	2	1.93	0.122	2
0.85	2.00	0.5847	2	2.00	0.248	2	2.17	0.222	3
0.9	2.05	0.4928	3	6.35	0.246	8	2.25	0.400	3
0.95	2.47	0.0371	4	2.47	0.104	4	2.47	0.969	4
0.98	2.48	0.0334	4	2.48	0.110	4	2.48	0.977	4

Table 12: Oscillating frequencies, amplitude response and identified modes for the Pipe34 model in 45° flow at position of accelerometer three with $C_{\mathrm{Drag}} = 1.2$

	x-direction			y-direction			z-direction		
Uc	f_{osc}	A/D	mode	f_{osc}	A/D	mode	f_{osc}	A/D	mode
[m/s]	[Hz]	[-]	[-]	[Hz]	[-]	[-]	[Hz]	[-]	[-]
0.05	0.71	0.0001	1	0.71	0.0001	1	0.71	0.0001	1
0.1	0.79	0.0006	1	0.79	0.0006	1	0.79	0.0006	1
0.15	0.81	0.0015	1	0.81	0.0161	1	0.81	0.0018	1
0.2	2.41	0.0130	4	0.84	0.0191	1	2.41	0.0140	4
0.25	1.92	0.0308	2	3.21	0.0516	5	1.92	0.0209	2
0.3	3.28	0.0200	5	3.28	0.0898	5	3.28	0.0204	5
0.35	1.95	0.0422	2	3.31	0.117	5	3.31	0.0391	5
0.4	3.37	0.0537	5	3.37	0.137	5	3.37	0.0622	5
0.45	3.43	0.0642	6	3.43	0.136	6	3.43	0.0801	6
0.5	3.45	0.0760	6	3.45	0.156	6	3.45	0.0985	6
0.55	3.49	0.0944	6	3.49	0.174	6	3.49	0.123	6
0.6	3.52	0.0979	6	3.52	0.188	6	3.52	0.123	6
0.65	1.92	0.121	2	3.56	0.220	6	3.56	0.122	6
0.7	1.95	0.147	2	3.60	0.237	7	3.60	0.174	7
0.75	1.99	0.125	2	3.63	0.215	7	3.63	0.149	7
0.8	1.93	0.191	2	3.88	0.215	7	1.93	0.190	2
0.85	2.16	0.217	3	3.99	0.228	7	2.16	0.224	3
0.9	2.25	0.287	3	2.25	0.212	3	2.25	0.296	3
0.95	2.47	0.544	4	2.47	0.111	4	2.47	0.660	4
0.98	2.48	0.532	4	2.48	0.121	4	2.48	0.667	4

Table 13: Oscillating frequencies, amplitude response and identified modes for the Pipe31 model in 45° flow at position of accelerometer seven with $C_{\mathrm{Drag}} = 1.1$

	x-direction			y-direction			z-direction		
Uc	f_{osc}	A/D	mode	f_{osc}	A/D	mode	f_{osc}	A/D	mode
[m/s]	[Hz]	[-]	[-]	[Hz]	[-]	[-]	[Hz]	[-]	[-]
0.05	0.71	0.0003	1	0.71	0.0003	1	0.71	0.0003	1
0.1	0.83	0.0008	1	0.83	0.0008	1	0.83	0.0008	1
0.15	0.85	0.0026	1	0.85	0.223	1	2.57	0.0023	4
0.2	0.88	0.0077	1	0.88	0.248	1	1.77	0.0053	2
0.25	2.28	0.0389	3	0.63	0.200	1	2.62	0.0688	4
0.3	2.29	0.1187	3	0.79	0.188	1	2.67	0.0386	4
0.35	2.31	0.1421	3	0.93	0.351	1	2.51	0.0313	4
0.4	2.41	0.0581	3	0.99	0.273	1	2.27	0.0218	3
0.45	2.32	0.0553	3	1.16	0.136	1	2.30	0.0302	3
0.5	2.32	0.0825	3	1.17	0.137	1	2.33	0.0305	3
0.55	1.47	0.0426	1	1.47	0.142	1	2.37	0.0846	3
0.6	1.65	0.061	2	1.65	0.124	2	2.39	0.0635	3
0.65	1.62	0.067	2	6.17	0.164	8	7.23	0.0698	9
0.7	1.79	0.099	2	6.23	0.178	8	1.87	0.0955	2
0.75	2.09	0.121	2	6.28	0.132	8	2.09	0.102	2
0.8	2.23	0.547	2	2.23	0.254	2	2.33	0.0855	3
0.85	2.28	0.576	3	2.28	0.241	3	1.63	0.122	2
0.9	2.32	0.635	3	2.32	0.276	3	1.79	0.178	2
0.95	2.36	0.621	3	2.36	0.270	3	2.36	0.274	3
0.98	2.38	0.5969	3	0.01	0.629	1	2.61	0.913	4

Table 14: Oscillating frequencies, amplitude response and identified modes for the Pipe31 model in 45° flow at position of accelerometer three with $C_{\mathrm{Drag}} = 1.1$

	x-direction			y-direction			z-direction		
Uc	f_{osc}	A/D	mode	f_{osc}	A/D	mode	f_{osc}	A/D	mode
[m/s]	[Hz]	[-]	[-]	[Hz]	[-]	[-]	[Hz]	[-]	[-]
0.05	0.72	0.0001	1	0.72	0.0001	1	0.72	0.0001	1
0.1	0.83	0.0003	1	0.83	0.0003	1	0.83	0.0003	1
0.15	0.85	0.0012	1	0.85	0.0202	1	2.57	0.0012	4
0.2	0.88	0.0032	1	0.88	0.0246	1	2.47	0.0026	4
0.25	2.61	0.0362	4	2.19	0.0574	2	2.61	0.0405	4
0.3	2.68	0.0267	4	3.32	0.0903	5	2.68	0.0270	4
0.35	2.31	0.0410	3	3.36	0.129	5	2.31	0.0331	3
0.4	3.40	0.0293	5	3.40	0.158	5	3.40	0.0243	5
0.45	3.44	0.0281	5	3.44	0.165	5	3.44	0.0329	5
0.5	3.49	0.0474	5	3.49	0.174	5	3.49	0.0488	5
0.55	3.57	0.0701	6	3.84	0.178	7	3.57	0.0865	6
0.6	3.69	0.108	6	3.69	0.155	6	3.69	0.136	6
0.65	3.73	0.123	6	3.92	0.197	7	3.73	0.156	6
0.7	1.87	0.112	2	3.96	0.222	7	3.79	0.125	7
0.75	8.37	0.164	9	2.09	0.263	2	2.09	0.187	2
0.8	2.24	0.168	2	2.24	0.232	2	2.24	0.146	2
0.85	2.28	0.179	3	2.28	0.245	3	2.28	0.190	3
0.9	2.32	0.200	3	2.32	0.234	3	2.32	0.159	3
0.95	2.36	0.238	3	2.36	0.209	3	2.11	0.165	2
0.98	2.45	0.576	3	2.39	0.200	3	2.47	0.615	4

Table 15: Oscillating frequencies, amplitude response and identified modes for the Pipe31 model in 45° flow at position of accelerometer seven with $C_{\mathrm{Drag}} = 1.2$

	x-direction			y-direction			z-direction		
Uc	f_{osc}	A/D	mode	f_{osc}	A/D	mode	f_{osc}	A/D	mode
[m/s]	[Hz]	[-]	[-]	[Hz]	[-]	[-]	[Hz]	[-]	[-]
0.05	0.70	0.0002	1	0.70	0.0002	1	0.70	0.0002	1
0.1	0.83	0.0009	1	0.83	0.0009	1	0.83	0.0009	1
0.15	0.87	0.0024	1	0.87	0.202	1	2.57	0.0014	4
0.2	0.90	0.0072	1	0.90	0.225	1	2.43	0.0051	3
0.25	2.30	0.130	3	0.90	0.176	1	2.30	0.0033	3
0.3	0.80	0.015	1	0.80	0.151	1	2.67	0.0320	4
0.35	0.90	0.0242	1	0.90	0.244	1	2.23	0.0207	2
0.4	2.33	0.158	3	1.00	0.356	1	0.73	0.0170	1
0.45	2.27	0.0456	3	1.17	0.124	1	2.30	0.0188	3
0.5	2.37	0.0616	3	1.17	0.145	1	2.33	0.0264	3
0.55	1.47	0.0429	1	1.47	0.136	1	2.37	0.0366	3
0.6	1.63	0.0543	2	1.63	0.125	2	2.40	0.0472	3
0.65	1.63	0.0703	2	6.17	0.156	8	1.07	0.0595	1
0.7	1.80	0.0811	2	6.23	0.144	8	1.90	0.0822	2
0.75	2.33	0.409	3	2.33	0.143	3	2.33	0.127	3
0.8	2.23	0.456	2	2.23	0.218	2	2.23	0.0750	2
0.85	2.27	0.539	3	2.27	0.224	3	1.63	0.106	2
0.9	2.33	0.590	3	2.33	0.257	3	1.77	0.138	2
0.95	2.37	0.577	3	2.37	0.286	3	2.37	0.252	3
0.98	2.37	0.544	3	6.50	0.321	8	2.47	0.433	4

Table 16: Oscillating frequencies, amplitude response and identified modes for the Pipe31 model in 45° flow at position of accelerometer three with $C_{\mathrm{Drag}} = 1.2$

	x-direction			y-direction			z-direction		
Uc	f_{osc}	A/D	mode	f_{osc}	A/D	mode	f_{osc}	A/D	mode
[m/s]	[Hz]	[-]	[-]	[Hz]	[-]	[-]	[Hz]	[-]	[-]
0.05	0.72	0.0001	1	0.72	0.0001	1	0.72	0.0001	1
0.1	0.83	0.0003	1	0.83	0.0003	1	0.83	0.0003	1
0.15	0.85	0.0010	1	0.85	0.0185	1	2.57	0.0010	4
0.2	0.88	0.0032	1	0.88	0.0221	1	2.51	0.0038	4
0.25	2.28	0.0264	3	0.92	0.0515	1	2.28	0.0144	3
0.3	2.68	0.0228	4	3.32	0.0868	5	2.68	0.0232	4
0.35	3.36	0.0205	5	3.36	0.129	5	3.36	0.0173	5
0.4	2.32	0.0433	3	3.40	0.142	5	3.40	0.0298	5
0.45	3.44	0.0281	5	3.44	0.153	5	3.44	0.0342	5
0.5	3.49	0.0486	5	3.49	0.159	5	3.49	0.0507	5
0.55	3.67	0.0833	6	3.67	0.147	6	3.67	0.0962	6
0.6	3.71	0.114	6	3.71	0.150	6	3.71	0.137	6
0.65	3.75	0.115	7	3.92	0.171	7	3.75	0.125	7
0.7	1.89	0.105	2	3.97	0.215	7	3.77	0.118	7
0.75	2.32	0.193	3	3.79	0.249	7	3.79	0.182	7
0.8	2.23	0.162	2	2.23	0.218	2	2.23	0.178	2
0.85	2.28	0.151	3	2.28	0.210	3	2.28	0.180	3
0.9	2.32	0.186	3	2.32	0.233	3	2.32	0.164	3
0.95	2.36	0.217	3	2.36	0.214	3	2.11	0.152	2
0.98	2.45	0.304	3	2.39	0.214	3	2.45	0.305	3

Table 17: Oscillating frequencies, amplitude response and identified modes for the Pipe34 model in 90° flow at position of accelerometer seven with $C_{\mathrm{Drag}} = 1.1$

	x-direction			y-direction			z-direction		
Uc	f_{osc}	A/D	mode	f_{osc}	A/D	mode	f_{osc}	A/D	mode
[m/s]	[Hz]	[-]	[-]	[Hz]	[-]	[-]	[Hz]	[-]	[-]
0.05	0.13	0.0002	1	0.13	0.0002	1	0.13	0.0002	1
0.1	1.87	0.0046	2	1.87	0.0046	2	1.87	0.0046	2
0.15	0.43	0.0041	1	0.85	0.247	1	0.42	0.0121	1
0.2	0.55	0.0030	1	0.90	0.253	1	2.33	0.0315	4
0.25	1.53	0.0216	2	0.97	0.205	1	2.63	0.0218	4
0.3	0.82	0.0349	1	1.03	0.031	1	0.93	0.0259	1
0.35	1.05	0.0358	1	1.07	0.044	1	1.03	0.0353	1
0.4	1.73	0.0591	2	1.13	0.050	1	1.10	0.0628	1
0.45	1.72	0.159	2	5.95	0.099	8	1.07	0.0505	1
0.5	1.67	0.309	2	6.08	0.113	8	1.18	0.0796	1
0.55	1.85	0.801	2	6.10	0.153	8	2.07	0.121	3
0.6	1.88	0.985	2	6.18	0.134	8	2.05	0.197	3
0.65	1.92	1.013	2	6.23	0.167	8	2.27	0.512	3
0.7	1.95	1.023	2	2.45	0.149	4	2.45	1.012	4
0.75	1.97	1.058	2	0.02	0.185	1	2.48	1.082	4
0.79	1.97	1.023	2	0.02	0.308	1	2.50	1.107	4

Table 18: Oscillating frequencies, amplitude response and identified modes for the Pipe34 model in 90° flow at position of accelerometer three with $C_{\mathrm{Drag}} = 1.1$

	x-direction			y-direction			z-direction		
Uc	f_{osc}	A/D	mode	f_{osc}	A/D	mode	f_{osc}	A/D	mode
[m/s]	[Hz]	[-]	[-]	[Hz]	[-]	[-]	[Hz]	[-]	[-]
0.05	0.13	0.0001	1	0.13	0.0001	1	0.13	0.0001	1
0.1	1.09	0.0023	1	1.09	0.0023	1	1.09	0.0023	1
0.15	0.41	0.0049	1	0.85	0.0200	1	2.11	0.0059	3
0.2	2.33	0.0130	4	0.91	0.0263	1	2.33	0.0170	4
0.25	2.64	0.0116	4	3.21	0.0895	5	2.64	0.0129	4
0.3	0.93	0.0196	1	3.29	0.132	5	0.93	0.0221	1
0.35	3.24	0.0284	5	3.35	0.162	5	3.24	0.0399	5
0.4	3.37	0.0606	5	3.40	0.188	5	3.37	0.0821	5
0.45	1.72	0.0568	2	3.45	0.200	6	3.45	0.0636	6
0.5	1.67	0.0933	2	3.51	0.198	6	1.67	0.0655	2
0.55	1.84	0.158	2	3.91	0.215	7	1.84	0.125	2
0.6	1.89	0.249	2	3.95	0.220	7	1.89	0.200	2
0.65	1.92	0.401	2	3.84	0.233	7	2.28	0.414	4
0.7	2.45	0.654	4	3.89	0.273	7	2.45	0.753	4
0.75	2.48	0.712	4	2.48	0.234	4	2.48	0.811	4
0.79	2.51	0.734	4	2.51	0.321	4	2.51	0.840	4

Table 19: Oscillating frequencies, amplitude response and identified modes for the Pipe34 model in 90° flow at position of accelerometer seven with $C_{\mathrm{Drag}} = 1.2$

	x-direction			y-direction			z-direction		
Uc	f_{osc}	A/D	mode	f_{osc}	A/D	mode	f_{osc}	A/D	mode
[m/s]	[Hz]	[-]	[-]	[Hz]	[-]	[-]	[Hz]	[-]	[-]
0.05	0.15	0.0002	1	0.15	0.0002	1	0.15	0.0002	1
0.1	1.87	0.0044	2	1.87	0.0044	2	1.87	0.0044	2
0.15	0.42	0.0033	1	0.85	0.226	1	0.42	0.0121	1
0.2	1.48	0.0061	2	0.92	0.228	1	2.33	0.0295	4
0.25	1.53	0.0229	2	1.00	0.203	1	2.65	0.0210	4
0.3	0.90	0.0349	1	1.05	0.030	1	0.97	0.0192	1
0.35	1.02	0.034	1	1.08	0.041	1	1.03	0.0382	1
0.4	1.73	0.055	2	1.17	0.049	1	1.10	0.0546	1
0.45	1.73	0.141	2	5.95	0.086	8	1.38	0.0555	2
0.5	1.67	0.289	2	6.07	0.105	8	1.18	0.0646	1
0.55	1.83	0.735	2	6.10	0.140	8	2.08	0.125	3
0.6	1.88	0.997	2	6.18	0.159	8	2.08	0.185	3
0.65	1.92	0.944	2	6.23	0.162	8	2.25	0.478	3
0.7	1.93	0.939	2	2.43	0.146	4	2.43	0.930	4
0.75	1.95	0.957	2	2.47	0.140	4	2.47	1.006	4
0.79	1.97	0.973	2	0.02	0.213	1	2.50	1.053	4

Table 20: Oscillating frequencies, amplitude response and identified modes for the Pipe34 model in 90° flow at position of accelerometer three with $C_{\mathrm{Drag}} = 1.2$

	x-direction			y-direction			z-direction		
Uc	f_{osc}	A/D	mode	f_{osc}	A/D	mode	f_{osc}	A/D	mode
[m/s]	[Hz]	[-]	[-]	[Hz]	[-]	[-]	[Hz]	[-]	[-]
0.05	0.13	0.0001	1	0.13	0.0001	1	0.13	0.0001	1
0.1	0.28	0.0022	1	0.28	0.0022	1	0.28	0.0022	1
0.15	0.41	0.0053	1	0.85	0.0183	1	0.41	0.0061	1
0.2	2.35	0.0122	4	2.85	0.0264	4	2.35	0.0160	4
0.25	2.64	0.0120	4	3.20	0.0803	5	2.64	0.0120	4
0.3	0.96	0.0193	1	3.29	0.129	5	0.96	0.0179	1
0.35	3.25	0.0287	5	3.35	0.149	5	3.25	0.0415	5
0.4	3.37	0.0564	5	3.40	0.169	5	3.37	0.0737	5
0.45	1.37	0.0501	2	3.45	0.182	6	1.43	0.0512	2
0.5	1.67	0.0885	2	3.52	0.188	6	1.67	0.0705	2
0.55	1.84	0.150	2	3.92	0.189	7	1.84	0.119	2
0.6	1.89	0.231	2	3.79	0.201	7	1.89	0.193	2
0.65	2.25	0.367	3	3.83	0.236	7	2.25	0.386	3
0.7	2.44	0.605	4	3.88	0.272	7	2.44	0.694	4
0.75	2.47	0.660	4	4.43	0.236	7	2.47	0.757	4
0.79	2.49	0.685	4	4.47	0.301	7	2.49	0.786	4

Table 21: Oscillating frequencies, amplitude response and identified modes for the Pipe31 model in 90° flow at position of accelerometer seven with $C_{\mathrm{Drag}} = 1.1$

	x-direction			y-direction			z-direction		
Uc	f_{osc}	A/D	mode	f_{osc}	A/D	mode	f_{osc}	A/D	mode
[m/s]	[Hz]	[-]	[-]	[Hz]	[-]	[-]	[Hz]	[-]	[-]
0.05	0.13	0.0002	1	0.13	0.0002	1	0.13	0.0002	1
0.1	0.27	0.0015	1	0.27	0.0015	1	0.27	0.0015	1
0.15	2.16	0.0061	2	0.89	0.246	1	0.41	0.0103	1
0.2	0.56	0.0043	1	0.95	0.256	1	2.41	0.0227	3
0.25	2.73	0.0156	4	1.03	0.225	1	2.75	0.0239	4
0.3	1.61	0.0248	2	1.09	0.225	1	0.92	0.0225	1
0.35	0.93	0.0515	1	1.23	0.197	1	1.05	0.0470	1
0.4	2.08	0.0373	2	1.28	0.161	1	1.16	0.0777	1
0.45	2.00	0.0410	2	1.37	0.176	1	1.21	0.0950	1
0.5	1.93	0.0568	2	6.15	0.167	8	2.40	0.0821	3
0.55	1.80	0.131	2	6.24	0.177	8	1.24	0.113	1
0.6	2.01	0.253	2	6.31	0.150	8	2.01	0.173	2
0.65	2.20	0.688	2	6.36	0.164	8	2.20	0.258	2
0.7	2.29	1.057	3	0.01	0.216	1	2.60	0.861	4
0.75	2.31	1.024	3	0.01	0.241	1	2.63	0.997	4
0.79	2.32	0.988	3	0.01	0.245	1	2.67	1.068	4

Table 22: Oscillating frequencies, amplitude response and identified modes for the Pipe31 model in 90° flow at position of accelerometer three with $C_{\mathrm{Drag}} = 1.1$

	x-direction			y-direction			z-direction		
Uc	f_{osc}	A/D	mode	f_{osc}	A/D	mode	f_{osc}	A/D	mode
[m/s]	[Hz]	[-]	[-]	[Hz]	[-]	[-]	[Hz]	[-]	[-]
0.05	0.13	0.0001	1	0.13	0.0001	1	0.13	0.0001	1
0.1	0.27	0.0026	1	0.27	0.0026	1	0.27	0.0026	1
0.15	0.41	0.0050	1	0.89	0.0232	1	0.41	0.0052	1
0.2	2.41	0.0104	3	0.95	0.0271	1	2.41	0.0117	3
0.25	2.75	0.0158	4	3.25	0.0857	5	2.75	0.0153	4
0.3	0.92	0.0158	1	3.35	0.133	5	0.87	0.0180	1
0.35	1.05	0.0246	1	3.40	0.164	5	1.05	0.0303	1
0.4	3.52	0.0438	5	3.44	0.185	5	3.52	0.0504	5
0.45	3.64	0.0592	6	3.49	0.197	5	3.64	0.0727	6
0.5	2.40	0.0517	3	3.55	0.210	5	2.40	0.0505	3
0.55	1.80	0.0589	2	3.60	0.195	6	1.80	0.0705	2
0.6	2.01	0.0751	2	3.67	0.195	6	2.01	0.106	2
0.65	2.20	0.196	2	3.79	0.189	7	2.20	0.176	2
0.7	2.60	0.661	4	4.29	0.193	7	2.60	0.626	4
0.75	2.63	0.722	4	2.63	0.243	4	2.63	0.716	4
0.79	2.67	0.761	4	2.67	0.200	4	2.67	0.769	4

Table 23: Oscillating frequencies, amplitude response and identified modes for the Pipe31 model in 90° flow at position of accelerometer seven with $C_{\mathrm{Drag}} = 1.2$

	x-direction			y-direction			z-direction		
Uc	f_{osc}	A/D	mode	f_{osc}	A/D	mode	f_{osc}	A/D	mode
[m/s]	[Hz]	[-]	[-]	[Hz]	[-]	[-]	[Hz]	[-]	[-]
0.05	0.13	0.0002	1	0.13	0.0002	1	0.13	0.0002	1
0.1	0.27	0.0012	1	0.27	0.0012	1	0.27	0.0012	1
0.15	2.17	0.0063	2	0.88	0.222	1	0.42	0.0100	1
0.2	0.55	0.0012	1	0.95	0.234	1	2.42	0.0220	3
0.25	2.75	0.0123	4	1.05	0.201	1	2.75	0.0232	4
0.3	1.62	0.0137	2	2.27	0.0158	3	0.93	0.0159	1
0.35	0.95	0.0425	1	1.23	0.0328	1	1.08	0.0410	1
0.4	2.08	0.0276	2	1.30	0.0419	1	1.15	0.0438	1
0.45	2.07	0.0427	2	1.40	0.0588	1	1.20	0.0514	1
0.5	1.88	0.0410	2	6.15	0.102	8	1.15	0.0750	1
0.55	1.80	0.133	2	6.23	0.117	8	1.27	0.0930	1
0.6	2.02	0.240	2	6.32	0.141	8	2.02	0.155	2
0.65	2.20	0.637	2	6.37	0.148	8	2.20	0.227	2
0.7	2.27	0.852	3	6.37	0.184	8	2.45	0.529	3
0.75	2.30	0.945	3	2.62	0.153	4	2.62	0.910	4
0.79	2.32	0.942	3	0.02	0.209	1	2.65	0.994	4

Table 24: Oscillating frequencies, amplitude response and identified modes for the Pipe31 model in 90° flow at position of accelerometer three with $C_{\mathrm{Drag}} = 1.2$

	x-direction			y-direction			z-direction		
Uc	f_{osc}	A/D	mode	f_{osc}	A/D	mode	f_{osc}	A/D	mode
[m/s]	[Hz]	[-]	[-]	[Hz]	[-]	[-]	[Hz]	[-]	[-]
0.05	0.13	0.0001	1	0.13	0.0001	1	0.13	0.0001	1
0.1	0.28	0.0018	1	0.28	0.0018	1	0.28	0.0018	1
0.15	0.41	0.0052	1	0.89	0.0215	1	0.41	0.0052	1
0.2	2.43	0.0102	3	0.95	0.0258	1	2.43	0.0112	3
0.25	2.76	0.0149	4	3.25	0.0834	5	2.76	0.0167	4
0.3	0.93	0.0125	1	3.67	0.0972	6	0.93	0.0134	1
0.35	1.03	0.0245	1	3.40	0.156	5	1.03	0.0295	1
0.4	3.52	0.0427	5	3.44	0.170	5	3.52	0.0503	5
0.45	3.65	0.0583	6	3.49	0.179	5	3.65	0.0712	6
0.5	2.40	0.0510	3	3.56	0.191	6	2.40	0.0474	3
0.55	1.81	0.0659	2	3.61	0.178	6	1.81	0.0702	2
0.6	2.03	0.0768	2	3.69	0.175	6	2.03	0.103	2
0.65	2.20	0.192	2	3.81	0.181	7	2.20	0.168	2
0.7	2.44	0.421	3	4.25	0.192	7	2.44	0.378	3
0.75	2.61	0.660	4	2.61	0.239	4	2.61	0.657	4
0.79	2.64	0.705	4	2.64	0.205	4	2.64	0.715	4

Appendix C: Response model calculations

C.1 10° flow direction

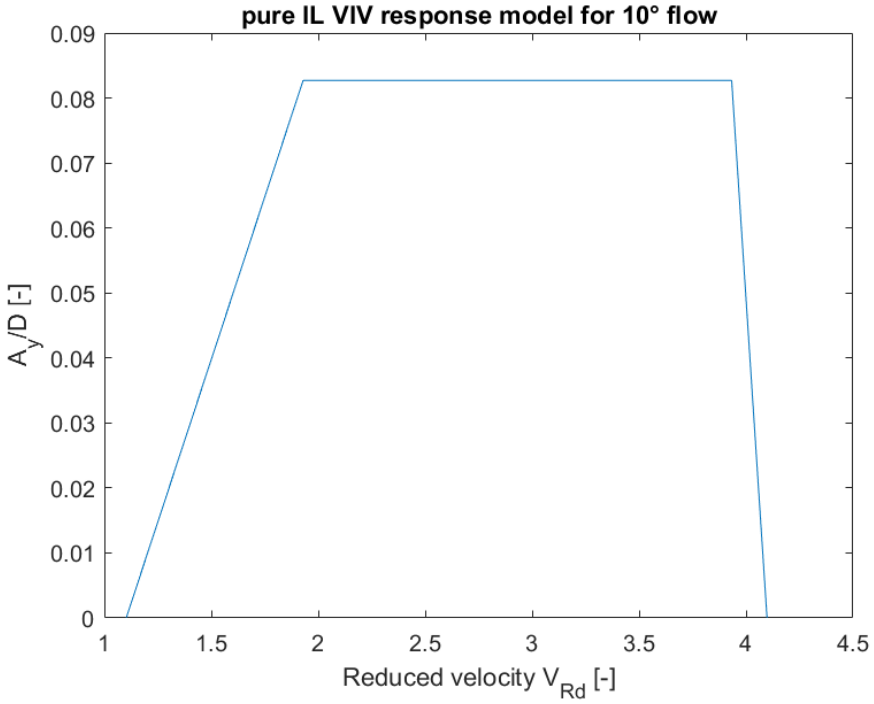

Figure 24: IL response model for the 10° flow direction

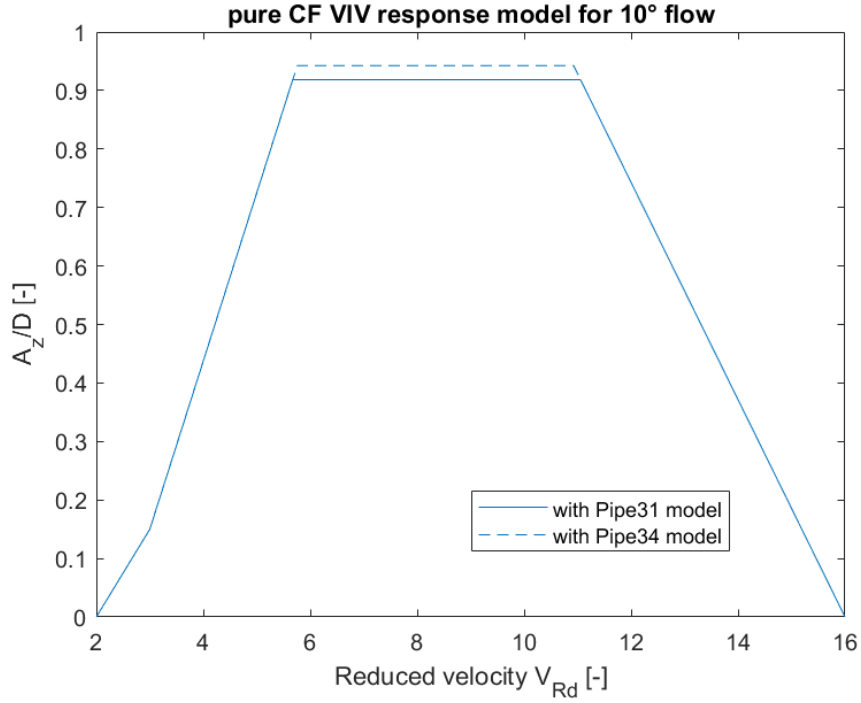

Figure 25: CF response model for the 10° flow direction

Table 25: IL unit response amplitudes for 10° flow with Pipe34 model

	mode 2		mode 4		mode 6		mode 9	
Uc	$V_{\mathrm{red}}(f_0)$	A/D	$V_{\mathrm{red}}(f_0)$	A/D	$V_{\mathrm{red}}(f_0)$	A/D	$V_{\mathrm{red}}(f_0)$	A/D
[m/s]	[-]	[-]	[-]	[-]	[-]	[-]	[-]	[-]
0.05	0.43	0	0.34	0	0.24	0	0.12	0
0.1	0.86	0	0.67	0	0.48	0	0.25	0
0.15	1.30	0.0296	1.01	0.00111	0.71	0	0.37	0
0.2	1.73	0.0728	1.35	0.0348	0.95	0	0.50	0
0.25	2.16	0.1160	1.69	0.0685	1.19	0.0190	0.62	0
0.3	2.59	0.1376	2.02	0.1022	1.43	0.0427	0.75	0
0.35	3.02	0.1238	2.36	0.1359	1.66	0.0665	0.87	0
0.4	3.46	0.1101	2.70	0.1343	1.90	0.0903	1.00	0
0.45	3.89	0.0964	3.03	0.1235	2.14	0.1141	1.12	0.0125
0.5	4.32	0	3.37	0.1128	2.38	0.1379	1.25	0.0250
0.55	4.75	0	3.71	0.1021	2.61	0.1368	1.37	0.0374
0.6	5.18	0	4.04	0.0859	2.85	0.1292	1.50	0.0499
0.65	5.62	0	4.38	0	3.09	0.1217	1.62	0.0624
0.7	6.05	0	4.72	0	3.33	0.1141	1.75	0.0749
0.75	6.48	0	5.06	0	3.57	0.1065	1.87	0.0874
0.8	6.91	0	5.39	0	3.80	0.0990	2.00	0.0999
0.85	7.34	0	5.73	0	4.04	0.0859	2.12	0.1124
0.9	7.78	0	6.07	0	4.28	0	2.25	0.1249
0.95	8.21	0	6.40	0	4.52	0	2.37	0.1374
0.98	8.47	0	6.61	0	4.66	0	2.45	0.1421

Table 26: CF unit response amplitudes for 10° flow with Pipe34 model

	mode 1		mode 3		mode 5		
Uc	$V_{\text{red}}(f_0)$	A/D	$V_{\text{red}}(f_0)$	A/D	$V_{\text{red}}(f_0)$	A/D	mode with max A/D
[m/s]	[-]	[-]	[-]	[-]	[-]	[-]	[-]
0.05	1.02	0	0.39	0	0.25	0	no CF mode
0.1	2.05	0.00701	0.79	0	0.50	0	mode 1
0.15	3.07	0.169	1.18	0	0.74	0	mode 1
0.2	4.09	0.463	1.57	0	0.99	0	mode 1
0.25	5.12	0.757	1.96	0	1.24	0	mode 1
0.3	6.14	0.919	2.36	0.0534	1.49	0	mode 1
0.35	7.16	0.919	2.75	0.112	1.73	0	mode 1
0.4	8.19	0.919	3.14	0.190	1.98	0	mode 1
0.45	9.21	0.919	3.53	0.302	2.23	0.034	mode 1
0.5	10.23	0.919	3.93	0.415	2.48	0.072	mode 1
0.55	11.26	0.880	4.32	0.528	2.73	0.109	mode 1
0.6	12.28	0.690	4.71	0.640	2.97	0.146	mode 1
0.65	13.30	0.500	5.10	0.753	3.22	0.212	mode 3
0.7	14.33	0.310	5.50	0.866	3.47	0.283	mode 3
0.75	15.35	0.120	5.89	0.919	3.72	0.355	mode 3
0.8	16.37	0	6.28	0.919	3.96	0.426	mode 3
0.85	17.40	0	6.68	0.919	4.21	0.497	mode 3
0.9	18.42	0	7.07	0.919	4.46	0.568	mode 3
0.95	19.44	0	7.46	0.919	4.71	0.639	mode 3
0.98	20.06	0	7.70	0.919	4.86	0.682	mode 3

Table 27: C_a-Correction and CF-induced IL modes for 10° flow with Pipe34 model

	mode 1			mode 3			
Uc	$C_{a,CF\text{-}RES}$	$f_{CF\text{-}RES}$	$2\times f_{CF\text{-}RES}$	$C_{a,CF\text{-}RES}$	$f_{CF\text{-}RES}$	$2\times f_{CF\text{-}RES}$	CF-IL candidate
[m/s]	[-]	[Hz]	[Hz]	[-]	[Hz]	[Hz]	[-]
0.05	1	0.808	1.62	1	2.105	4.21	-
0.1	1.42	0.771	1.54	1	2.105	4.21	2
0.15	4.93	0.587	1.17	1	2.105	4.21	2
0.2	3.91	0.626	1.25	1	2.105	4.21	2
0.25	2.88	0.676	1.35	1	2.105	4.21	2
0.3	1.86	0.738	1.48	4.204	1.600	3.20	2
0.35	0.84	0.823	1.65	5.251	1.500	3.00	2
0.4	-0.19	0.945	1.89	4.859	1.535	3.07	2
0.45	-0.50	1.00	1.99	4.466	1.573	3.15	2
0.5	1	0.81	1.62	4.073	1.614	3.23	2
0.55	1	0.808	1.62	3.681	1.658	3.32	2
0.6	1	0.808	1.62	3.288	1.706	3.41	2
0.65	1	0.808	1.62	2.895	1.759	3.52	6
0.7	1	0.808	1.62	2.503	1.817	3.63	6
0.75	1	0.808	1.62	2.110	1.880	3.76	6
0.8	1	0.808	1.62	1.717	1.951	3.90	6
0.85	1	0.808	1.62	1.325	2.031	4.06	6
0.9	1	0.808	1.62	0.932	2.121	4.24	6
0.95	1	0.808	1.62	0.539	2.225	4.45	6
0.98	1	0.808	1.62	0.304	2.295	4.59	6

C.2 90° flow direction

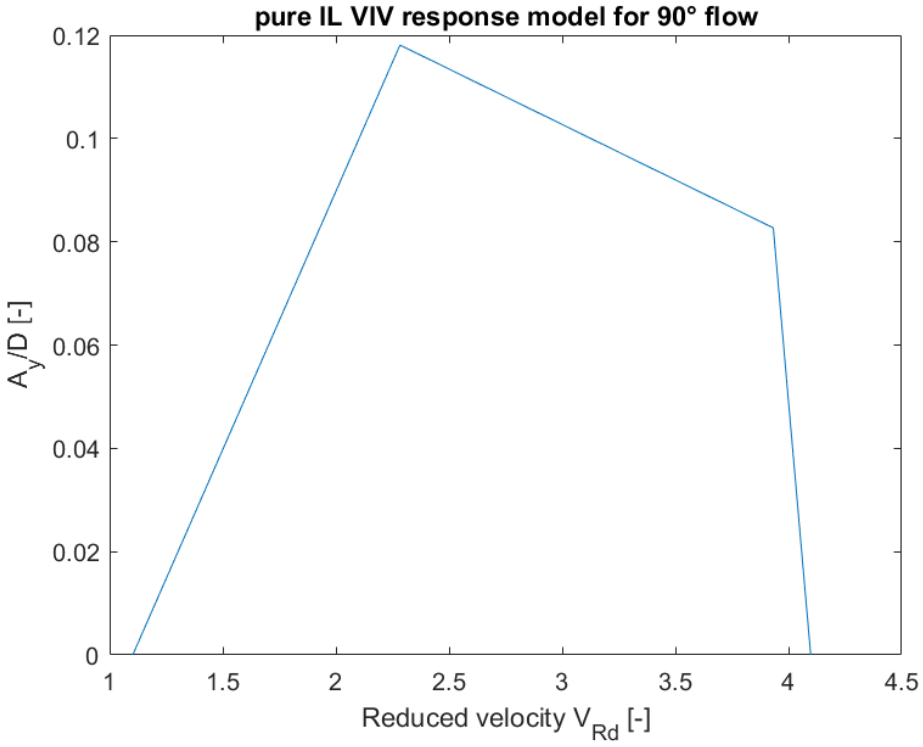

Figure 26: IL response model for the 90° flow direction

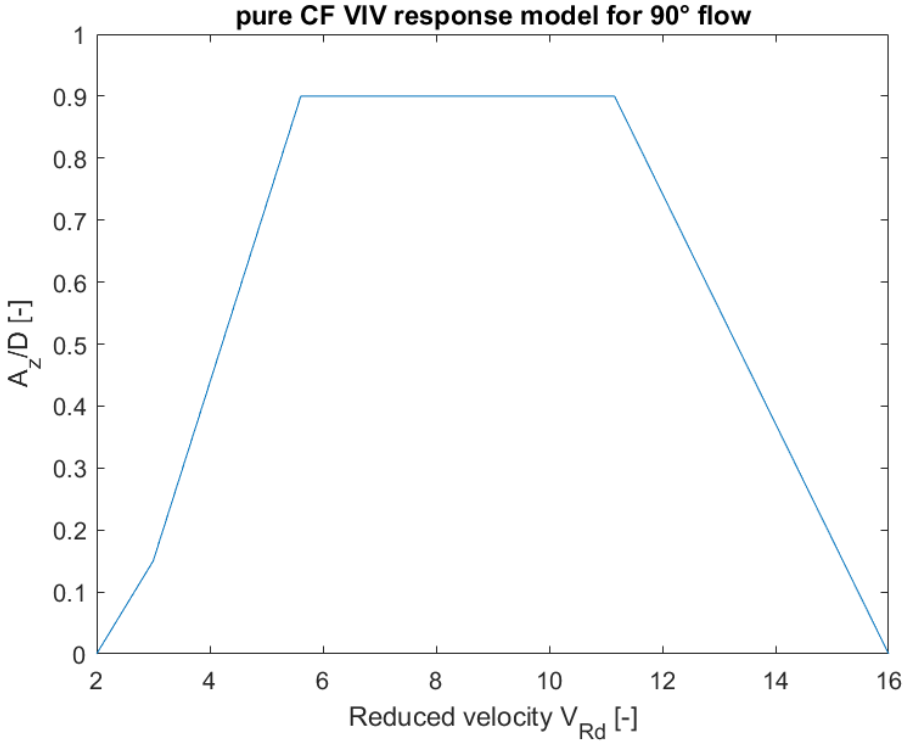

Figure 27: CF response model for the 90° flow direction

Table 28: IL unit response amplitudes for 90° flow with Pipe34 model

	mode 1		mode 3		mode 5		mode 7	
Uc	$V_{\mathrm{red}}(f_0)$	A/D	$V_{\mathrm{red}}(f_0)$	A/D	$V_{\mathrm{red}}(f_0)$	A/D	$V_{\mathrm{red}}(f_0)$	A/D
[m/s]	[-]	[-]	[-]	[-]	[-]	[-]	[-]	[-]
0.05	1.02	0	0.39	0	0.25	0	0.22	0
0.1	2.05	0.095	0.79	0	0.50	0	0.44	0
0.15	3.07	0.101	1.18	0.008	0.74	0	0.67	0
0.2	4.09	0.002	1.57	0.047	0.99	0	0.89	0
0.25	5.12	0	1.96	0.086	1.24	0.014	1.11	0.001
0.3	6.14	0	2.36	0.116	1.49	0.039	1.33	0.023
0.35	7.16	0	2.75	0.108	1.73	0.063	1.56	0.046
0.4	8.19	0	3.14	0.099	1.98	0.088	1.78	0.068
0.45	9.21	0	3.53	0.091	2.23	0.113	2.00	0.090
0.5	10.23	0	3.93	0.083	2.48	0.114	2.22	0.112
0.55	11.26	0	4.32	0	2.73	0.108	2.45	0.114
0.6	12.28	0	4.71	0	2.97	0.103	2.67	0.110
0.65	13.30	0	5.10	0	3.22	0.098	2.89	0.105
0.7	14.33	0	5.50	0	3.47	0.092	3.11	0.100
0.75	15.35	0	5.89	0	3.72	0.087	3.33	0.095
0.79	16.37	0	6.28	0	3.96	0.067	3.56	0.091

Table 29: CF unit response amplitudes for 90° flow with Pipe34 model

	mode 2		mode 4		mode 6		
Uc	$V_{\text{red}}(f_0)$	A/D	$V_{\text{red}}(f_0)$	A/D	$V_{\text{red}}(f_0)$	A/D	mode with max A/D
[m/s]	[-]	[-]	[-]	[-]	[-]	[-]	[-]
0.05	0.43	0	0.34	0	0.24	0	no CF mode
0.1	0.86	0	0.67	0	0.48	0	no CF mode
0.15	1.30	0	1.01	0	0.71	0	no CF mode
0.2	1.73	0	1.35	0	0.95	0	no CF mode
0.25	2.16	0.024	1.69	0	1.19	0	mode 2
0.3	2.59	0.089	2.02	0.0033	1.43	0	mode 2
0.35	3.02	0.156	2.36	0.054	1.67	0	mode 2
0.4	3.46	0.280	2.70	0.104	1.90	0	mode 2
0.45	3.89	0.404	3.03	0.159	2.14	0.0212	mode 2
0.5	4.32	0.528	3.37	0.255	2.38	0.057	mode 2
0.55	4.75	0.652	3.71	0.352	2.62	0.093	mode 2
0.6	5.18	0.776	4.04	0.449	2.85	0.128	mode 2
0.65	5.62	0.900	4.38	0.545	3.09	0.176	mode 2
0.7	6.05	0.900	4.72	0.642	3.33	0.244	mode 2
0.75	6.48	0.900	5.06	0.739	3.57	0.312	mode 2
0.79	6.91	0.900	5.39	0.836	3.81	0.380	mode 2

Table 30: C_a-Correction and CF-induced IL modes for 90° flow with Pipe34 model

	mode 2			
Uc	$C_{a,CF\text{-}RES}$	$f_{CF\text{-}RES}$	$2\times f_{CF\text{-}RES}$	CF-IL candidate
[m/s]	[-]	[Hz]	[Hz]	[-]
0.05	1	1.913	3.83	-
0.1	1	1.913	3.83	-
0.15	1	1.913	3.83	-
0.2	1	1.913	3.83	-
0.25	2.44	1.603	3.21	5
0.3	5.41	1.261	2.52	3
0.35	4.98	1.298	2.60	3
0.4	4.54	1.338	2.68	3
0.45	4.11	1.38	2.76	5
0.5	3.68	1.43	2.86	5
0.55	3.25	1.483	2.97	5
0.6	2.82	1.544	3.09	5
0.65	2.38	1.612	3.22	5
0.7	1.95	1.690	3.38	5
0.75	1.52	1.781	3.56	7
0.79	1.09	1.889	3.78	7

C.3 45° flow direction

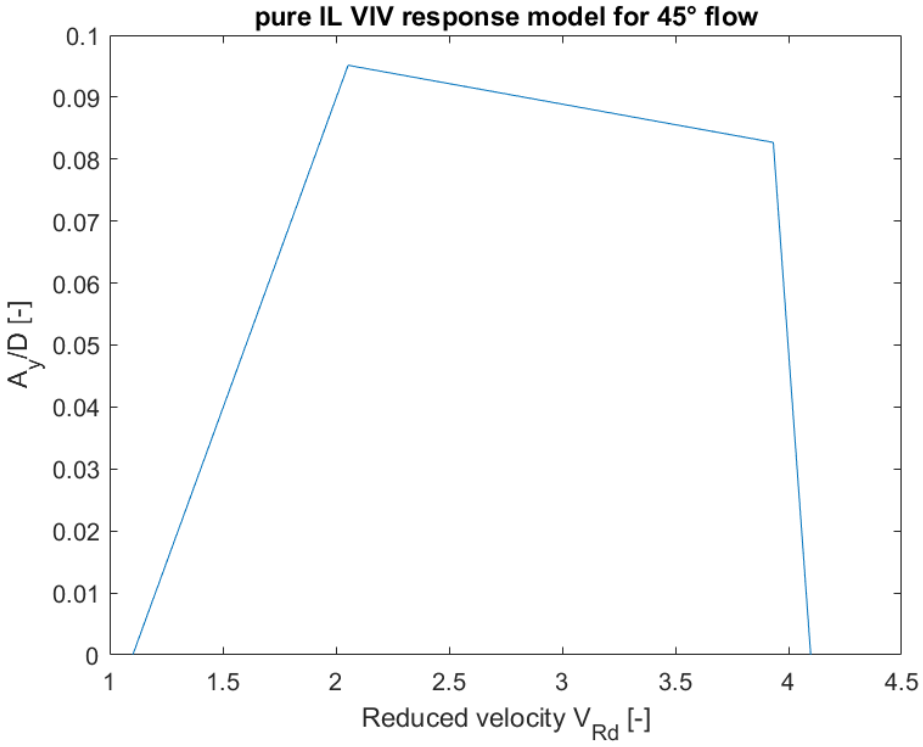

Figure 28: IL response model for the 45° flow direction

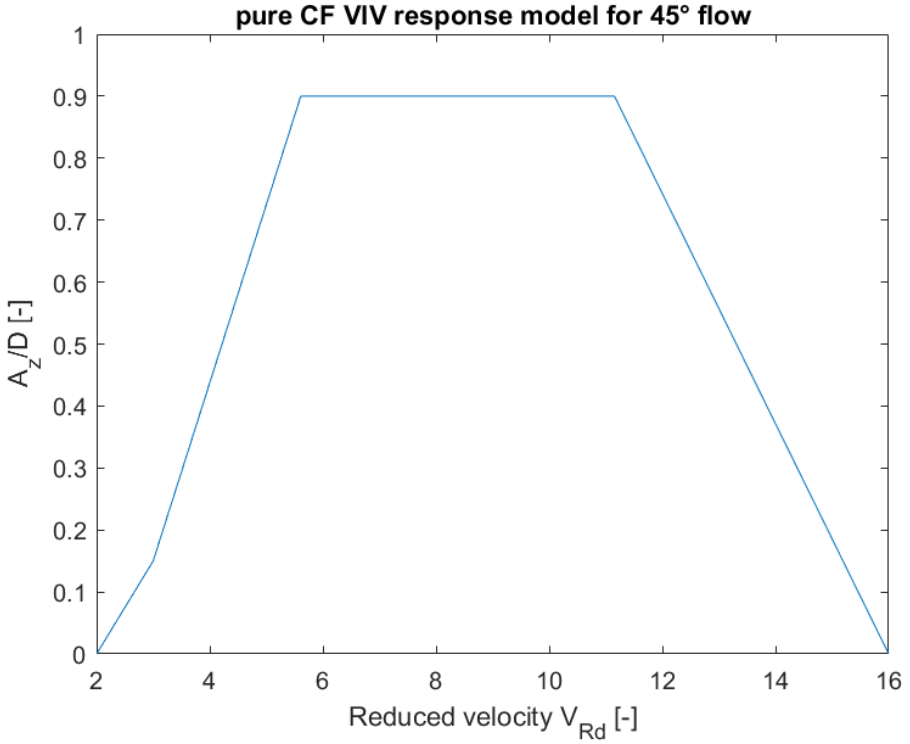

Figure 29: CF response model for the 45° flow direction

Table 31: IL unit response amplitudes for 45° flow with Pipe34 model

	mode 1		mode 2		mode 3		mode 5	
Uc	$V_{\mathrm{red}}(f_0)$	A/D	$V_{\mathrm{red}}(f_0)$	A/D	$V_{\mathrm{red}}(f_0)$	A/D	$V_{\mathrm{red}}(f_0)$	A/D
[m/s]	[-]	[-]	[-]	[-]	[-]	[-]	[-]	[-]
0.05	1.02	0	0.43	0	0.39	0	0.25	0
0.1	2.05	0.0947	0.86	0	0.79	0	0.50	0
0.15	3.07	0.0886	1.30	0.0196	1.18	0.0078	0.74	0
0.2	4.09	0.0022	1.73	0.0628	1.57	0.0471	0.99	0
0.25	5.12	0	2.16	0.0947	1.96	0.0863	1.24	0.0139
0.3	6.14	0	2.59	0.0918	2.36	0.0934	1.49	0.0386
0.35	7.16	0	3.02	0.0890	2.75	0.0908	1.73	0.0634
0.4	8.19	0	3.46	0.0861	3.14	0.0882	1.98	0.0882
0.45	9.21	0	3.89	0.0832	3.53	0.0856	2.23	0.0942
0.5	10.23	0	4.32	0	3.93	0.0830	2.48	0.0926
0.55	11.26	0	4.75	0	4.32	0	2.73	0.0909
0.6	12.28	0	5.18	0	4.71	0	2.97	0.0893
0.65	13.30	0	5.62	0	5.10	0	3.22	0.0876
0.7	14.33	0	6.05	0	5.50	0	3.47	0.0860
0.75	15.35	0	6.48	0	5.89	0	3.72	0.0844
0.8	16.37	0	6.91	0	6.28	0	3.96	0.0670
0.85	17.40	0	7.34	0	6.68	0	4.21	0
0.9	18.42	0	7.78	0	7.07	0	4.46	0
0.95	19.44	0	8.21	0	7.46	0	4.71	0
0.98	20.06	0	8.47	0	7.70	0	4.86	0

Table 32: CF unit response amplitudes for 45° flow with Pipe34 model

	mode 1		mode 2		mode 3		
Uc	$V_{\text{red}}(f_0)$	A/D	$V_{\text{red}}(f_0)$	A/D	$V_{\text{red}}(f_0)$	A/D	mode with max A/D
[m/s]	[-]	[-]	[-]	[-]	[-]	[-]	[-]
0.05	1.02	0	0.43	0	0.39	0	no CF mode
0.1	2.05	0.0070	0.86	0	0.79	0	mode 1
0.15	3.07	0.169	1.30	0	1.18	0	mode 1
0.2	4.09	0.463	1.73	0	1.57	0	mode 1
0.25	5.12	0.757	2.16	0.0240	1.96	0	mode 1
0.3	6.14	0.900	2.59	0.089	2.36	0.0534	mode 1
0.35	7.16	0.900	3.02	0.156	2.75	0.112	mode 1
0.4	8.19	0.900	3.46	0.280	3.14	0.190	mode 1
0.45	9.21	0.900	3.89	0.404	3.53	0.302	mode 1
0.5	10.23	0.900	4.32	0.528	3.93	0.415	mode 1
0.55	11.26	0.880	4.75	0.652	4.32	0.528	mode 1
0.6	12.28	0.690	5.18	0.776	4.71	0.640	mode 2
0.65	13.30	0.500	5.62	0.900	5.10	0.753	mode 2
0.7	14.33	0.310	6.05	0.900	5.50	0.866	mode 2
0.75	15.35	0.120	6.48	0.900	5.89	0.900	mode 2 and 3
0.8	16.37	0	6.91	0.900	6.28	0.900	mode 2 and 3
0.85	17.40	0	7.34	0.900	6.68	0.900	mode 2 and 3
0.9	18.42	0	7.78	0.900	7.07	0.900	mode 2 and 3
0.95	19.44	0	8.21	0.900	7.46	0.900	mode 2 and 3
0.98	20.06	0	8.47	0.900	7.70	0.900	mode 2 and 3

Table 33: C_a-Correction and CF-induced IL modes for 45° flow with Pipe34 model

	mode 1			mode 2		
Uc	$C_{a,CF\text{-}RES}$	$f_{CF\text{-}RES}$	$2\times f_{CF\text{-}RES}$	$C_{a,CF\text{-}RES}$	$f_{CF\text{-}RES}$	$2\times f_{CF\text{-}RES}$
[m/s]	[-]	[Hz]	[Hz]	[-]	[Hz]	[Hz]
0.05	1	0.81	1.62	1	1.91	3.83
0.1	1	0.76	1.52	1	1.91	3.83
0.15	4.93	0.55	1.10	1	1.91	3.83
0.2	3.91	0.59	1.19	1	1.91	3.83
0.25	2.88	0.65	1.30	2	1.60	3.21
0.3	1.86	0.72	1.44	5.41	1.26	2.52
0.35	0.84	0.83	1.66	4.98	1.30	2.60
0.4	-0.19	1.00	2.00	4.54	1.34	2.68
0.45	-0.50	1.08	2.16	4.11	1.38	2.76
0.5	1	0.81	1.62	3.68	1.43	2.86
0.55	1	0.81	1.62	3.25	1.48	2.97
0.6	1	0.81	1.62	2.82	1.54	3.09
0.65	1	0.81	1.62	2.38	1.61	3.22
0.7	1	0.81	1.62	1.95	1.69	3.38
0.75	1	0.81	1.62	1.52	1.78	3.56
0.8	1	0.81	1.62	1.09	1.89	3.78
0.85	1	0.81	1.62	0.66	2.02	4.04
0.9	1	0.81	1.62	0.22	2.18	4.36
0.95	1	0.81	1.62	-0.21	2.38	4.77
0.98	1	0.81	1.62	-0.47	2.54	5.08

Table 34: C_a-Correction and CF-induced IL modes for 45° flow with Pipe34 model

	mode 3			
Uc	$C_{a,CF\text{-}RES}$	$f_{CF\text{-}RES}$	$2\times f_{CF\text{-}RES}$	CF-IL candidate
[m/s]	[-]	[Hz]	[Hz]	[-]
0.05	1	2.10	4.21	-
0.1	1	2.10	4.21	2
0.15	1	2.10	4.21	1
0.2	1	2.10	4.21	1
0.25	1	2.10	4.21	1
0.3	4.20	1.51	3.02	2
0.35	5.25	1.40	2.80	2
0.4	4.86	1.44	2.88	2
0.45	4.47	1.48	2.96	3
0.5	4.07	1.52	3.05	2
0.55	3.68	1.57	3.15	2
0.6	3.29	1.63	3.25	2
0.65	2.90	1.69	3.37	5
0.7	2.50	1.75	3.50	5
0.75	2.11	1.83	3.65	6
0.8	1.72	1.91	3.82	7
0.85	1.32	2.01	4.02	7
0.9	0.93	2.13	4.25	7
0.95	0.54	2.26	4.53	7
0.98	0.30	2.36	4.72	8

Appendix D: Matlab routine for fatigue damage

Main body

```
clc; clear; clf;

D_out=0.0605; %m
D_inn=0.055; %m
R_out=D_out/2; %m
t=(D_out-D_inn)/2; %m
I_ring=pi*R_out^3*t; %m^4
J_x=2*I_ring; %m^4
W_ring=I_ring/R_out; %m^3
Time=linspace(0, 2000, 200000); %sec
Timesec=linspace(0, 2000, 150020); %sec
Time1=linspace(1,7501,7501); %sec (for one load case)
ncurr=20;

theta_i=pi/8*[1 2 3 4 5 6 7 8 9 10 11 12 13 14 15 16]; %rad
Uc=[0.05 0.1 0.15 0.20 0.25 0.30 0.35 0.4 0.45 0.5 0.55 0.6
    0.65 0.7 0.75 0.8 0.85 0.9 0.95 0.98]; %current speed in
    m/s
%f0=[0.837709304194545, 2.19914089174982, 2.28591606607719,
    2.62849624468059, 3.38003525448659, 3.72608396290345,
    3.76461284710912, 6.34128947642239, 7.16139273390445]; %
    Pipe31 model
f0=[0.807579589672381, 1.91303048870593, 2.10472461004975,
    2.45217339029321, 3.33582603189090, 3.47389120695643,
    3.71780380586922, 6.27390743330342, 6.61419043114963]; %
    Pipe34 model

%FFT input
dt=0.01;
fMaxM=1/dt;
fnyq=fMaxM/2;
Ndt=7501;
F=0:fMaxM/(Ndt-1):fMaxM;
%plot(F,abs(b))
%%
```

```
28 %calling data from DYNPLOT. For file extension A: C_Drag
       =1.1, for B: C_Drag=1.2
29 [Mx_05, Mx_10, Mx_15,Mx_20,Mx_25,Mx_30,Mx_35,Mx_40,Mx_45,
       Mx_50,...
30       Mx_55,Mx_60, Mx_65,Mx_70,Mx_75,Mx_80,Mx_85,Mx_90,Mx_95,
             Mx_98,...
31       My_05, My_10, My_15, My_20,My_25,My_30,My_35,My_40,My_45
             ,My_50,...
32       My_55,My_60, My_65,My_70,My_75,My_80,My_85,My_90,My_95,
             My_98,...
33       Mz_05, Mz_10, Mz_15,Mz_20,Mz_25,Mz_30,Mz_35,Mz_40,Mz_45,
             Mz_50,...
34       Mz_55,Mz_60, Mz_65,Mz_70,Mz_75,Mz_80,Mz_85,Mz_90,Mz_95,
             Mz_98]=calling_stress_data_EL1_A();
35
36 Mx=[Mx_05 Mx_10 Mx_15 Mx_20 Mx_25 Mx_30 Mx_35 Mx_40 Mx_45
       Mx_50 Mx_55 Mx_60,...
37       Mx_65 Mx_70 Mx_75 Mx_80 Mx_85 Mx_90 Mx_95 Mx_98];
38 My=[My_05 My_10 My_15,My_20,My_25,My_30,My_35,My_40,My_45,
       My_50,My_55,My_60,...
39       My_65,My_70,My_75,My_80,My_85,My_90,My_95,My_98];
40 Mz=[Mz_05 Mz_10  Mz_15,Mz_20,Mz_25,Mz_30,Mz_35,Mz_40,Mz_45,
       Mz_50,Mz_55,Mz_60,...
41       Mz_65,Mz_70,Mz_75,Mz_80,Mz_85,Mz_90,Mz_95,Mz_98];
42
43 Pos0=[1 10001 20001  30001  40001 50001  60001 70001 80001
       90001 100001 110001 120001 130001 140001 150001 160001
       170001 180001 190001];
44 Pos1=[10000 20000 30000 40000 50000 60000 70000 80000 90000
       100000 110000 120000 130000 140000 150000 160000 170000
       180000 190000 200000];
45
46 Pos0sec=[1     7502 15003 22504 30005 37506 45007 52508 60009
        67510 75011 82512 90013 97514 105015  112516 120017
       127518 135019 142520];
47 Pos1sec=[7501 15002 22503 30004 37505 45006 52507 60008
       67509 75010 82511 90012 97513 105014  112515 120016
       127517 135018 142519 150020];
48
```

```
49 %%
50 %preallocate sizes of arrays
51 MXX=zeros(10000,20);
52 MXXtot=zeros(200000,1);
53 sectionMX=zeros(7501,20);
54 sectionMX0=zeros(7501,20);
55 sectionMXtot=zeros(150020,1);
56 MaxMX=zeros(1,20);
57 FFTiX=zeros(7501,20);
58 FFTabsX=zeros(7501,20);
59 FFTMaxMX=zeros(1,20);
60 f_oscX=zeros(1,20);
61
62 MYY=zeros(10000,20);
63 MYYtot=zeros(200000,1);
64 sectionMY=zeros(7501,20);
65 sectionMY0=zeros(7501,20);
66 sectionMYtot=zeros(150020,1);
67 MaxMY=zeros(1,20);
68 FFTiY=zeros(7501,20);
69 FFTabsY=zeros(7501,20);
70 FFTMaxMY=zeros(1,20);
71 f_oscY=zeros(1,20);
72
73 MZZ=zeros(10000,20);
74 MZZtot=zeros(200000,1);
75 sectionMZ=zeros(7501,20);
76 sectionMZ0=zeros(7501,20);
77 sectionMZtot=zeros(150020,1);
78 MaxMZ=zeros(1,20);
79 FFTiZ=zeros(7501,20);
80 FFTabsZ=zeros(7501,20);
81 FFTMaxMZ=zeros(1,20);
82 f_oscZ=zeros(1,20);
83
84 sigma_xx_MY=zeros(7501,20,16);
85 sigma_xx_MZ=zeros(7501,20,16);
86 sigma_xxi=zeros(7501,20,16);
87 %%
```

```
88 for i=1:ncurr
89     %scale moments around x-axis (condition when initial
           curvature is applied)
90     MXX(:,i)=(Mx(:,i)-Mx(160,i));
91     MXXtot(Pos0(i):Pos1(i))=MXX(:,i);
92     MYY(:,i)=(My(:,i)-My(160,i));
93     MYYtot(Pos0(i):Pos1(i))=MYY(:,i);
94     MZZ(:,i)=(Mz(:,i)-Mz(160,i));
95     MZZtot(Pos0(i):Pos1(i))=MZZ(:,i);
96
97 %moments over 75 seconds (steady current condition)
98 sectionMX(:,i)=MXX(1000:8500,i); %select data over 75
       seconds
99 sectionMX0(:,i)=sectionMX(:,i)-mean(sectionMX(:,i)); %scale
       it around x-axis (zero mean)
100 sectionMXtot(Pos0sec(i):Pos1sec(i))=sectionMX0(:,i);
101 MaxMX(i)=max(sectionMX0(:,i)); %maximum moment due to VIV
       response
102 %FFT
103 FFTiX(:,i)=fft(sectionMX0(:,i));
104 FFTabsX(:,i)=abs(FFTiX(:,i));
105 [FFTMaxX, indexX] = max(FFTabsX(:,i));
106 f_oscX(i)= F(indexX);
107
108 sectionMY(:,i)=MYY(1000:8500,i); %select data over 75
       seconds
109 sectionMY0(:,i)=sectionMY(:,i)-mean(sectionMY(:,i)); %scale
       it around zero mean
110 sectionMYtot(Pos0sec(i):Pos1sec(i))=sectionMY0(:,i);
111 section_MY_nzm(Pos0sec(i):Pos1sec(i))=sectionMY(:,i);
112 MaxMY(i)=max(sectionMY0(:,i)); %maximum moment due to VIV
       response
113 %FFT
114 FFTiY(:,i)=fft(sectionMY0(:,i));
115 FFTabsY(:,i)=abs(FFTiY(:,i));
116 [FFTMaxY, indexY] = max(FFTabsY(:,i));
117 f_oscY(i) = F(indexY);
118
```

```
119 sectionMZ(:,i)=MZZ(1000:8500,i); %select data over 75
        seconds
120 sectionMZ0(:,i)=sectionMZ(:,i)-mean(sectionMZ(:,i)); %scale
        it around zero mean
121 sectionMZtot(Pos0sec(i):Pos1sec(i))=sectionMZ0(:,i);
122 MaxMZ(i)=max(sectionMZ0(:,i)); %maximum moment due to VIV
        response
123 %FFT
124 FFTiZ(:,i)=fft(sectionMZ0(:,i));
125 FFTabsZ(:,i)=abs(FFTiZ(:,i));
126 [FFTMaxZ, indexZ] = max(FFTabsZ(:,i));
127 f_oscZ(i) = F(indexZ);
128 end
129
130 %%
131 %Stresses from moments
132 %for 16 points around circumference
133 for i=1:16 %loop over points around circumference
134     %with moments scaled around zero mean
135     %flexural stresses
136     sigma_xx_MY(:,:,i)= sectionMY0(:,:)./I_ring.*R_out.*1E
            -6;
137     sigma_xx_MZ(:,:,i)= sectionMZ0(:,:)./I_ring.*R_out.*1E
            -6;
138     sigma_xxi(:,:,i)= - sigma_xx_MY(:,:,i).*sin(theta_i(i))
            + sigma_xx_MZ(:,:,i).*cos(theta_i(i)); %el. end 1
139 %     %unscaled:
140 %     sigma_xx_MY_nzm(:,:,i)= sectionMY(:,:)./I_ring.*R_out
        .*1E-6;
141 %     sigma_xx_MZ_nzm(:,:,i)= sectionMZ(:,:)./I_ring.*R_out
        .*1E-6;
142 %     sigma_xxi_nzm(:,:,i)=-sigma_xx_MY_nzm(:,:,i).*sin(
        theta_i(i))+sigma_xx_MZ_nzm(:,:,i).*cos(theta_i(i));
143 end
144
145 %torsion stress and max. flexural stress
146 tau_x=sectionMX0./J_x.*R_out.*1E-6;
147 sigma_princ_MY=max(sigma_xx_MY, [],3);
148 sigma_princ_MZ=max(sigma_xx_MZ, [],3);
```

```
149 [sigma_xx,index_xx]=max(sigma_xxi, [],3);
150
151 %point around circumference where sigma_xx is max:
152 theta_xx=rad2deg(theta_i(mode(index_xx,1)));
153 theta_xx_index=mode(index_xx,1);
154
155 %principal stresses and principal stress direction (2D
      section)
156 sigma1=(sigma_xx)./2+sqrt((sigma_xx./2).^2+tau_x.^2);
157 sigma2=(sigma_xx)./2-sqrt((sigma_xx./2).^2+tau_x.^2);
158 theta1rad=atan(2.*tau_x./(sigma_xx))./2;
159 theta1=rad2deg(theta1rad)+theta_xx;
160 theta1min=min(theta1);
161 theta1max=max(theta1);
162 theta1range=theta1max-theta1min;
163 for i=1:ncurr
164     theta_i_tot(Pos0sec(i):Pos1sec(i))=theta1(:,i);
165 end
166
167 % figure(4)
168 % plot(Timesec,deg2rad(theta_i_tot))
169 % set(gca,'YTick',0:pi/2:2*pi)
170 % set(gca,'YTickLabel',{'0','pi/2','pi','3*pi/2','2*pi'})
171 % title('Principal stress direction during VIV')
172 % ylabel('theta_{Sigma1} [rad]')
173 % xlabel('Time [sec]')
174
175 [Seq_sigma, ni75sec_sigma] = rainflow_and_Seq(sigma_xx,
      Time1); %flexural stress
176 [Seq_tau, ni75sec_tau] = rainflow_and_Seq(tau_x, Time1); %
      torsion stress
177 [Seq_1, ni75sec_1] = rainflow_and_Seq(sigma1, Time1); %first
      principal stress
178 %%
179 %fatigue damage
180 Tyear=365*24*60*60; %[s]
181 cp=1; %Probability of occurance
182 ni_sigma=ni75sec_sigma./75.*Tyear.*cp; %number of cycles per
      year
```

```
183 ni_tau=ni75sec_tau./75.*Tyear.*cp;
184 ni_1=ni75sec_1./75.*Tyear.*cp;
185 f_sigma_RF=ni75sec_sigma./75; %cycle-counting frequency
186 f_tau_RF=ni75sec_tau./75;
187
188 % %SN curve D with slope -1/5
189 m=5;
190 a2bar=10^15.606;
191
192 %SN curve applied on Seq
193 N_SN_sigma=a2bar.*Seq_sigma.^(-m);
194 N_SN_tau=a2bar.*Seq_tau.^(-m);
195 N_SN_1=a2bar.*Seq_1.^(-m);
196 Dminersum_sigma=ni_sigma./N_SN_sigma;
197 Dminersum_tau=ni_tau./N_SN_tau;
198 Dminersum=ni_1./N_SN_1;
```

Import time signals

```
1 function [Mx_05, Mx_10, Mx_15,Mx_20,Mx_25,Mx_30,Mx_35,Mx_40,
      Mx_45,Mx_50,...
2       Mx_55,Mx_60, Mx_65,Mx_70,Mx_75,Mx_80,Mx_85,Mx_90,Mx_95,
            Mx_98,...
3       My_05, My_10, My_15, My_20,My_25,My_30,My_35,My_40,My_45
            ,My_50,...
4       My_55,My_60, My_65,My_70,My_75,My_80,My_85,My_90,My_95,
            My_98,...
5       Mz_05, Mz_10, Mz_15,Mz_20,Mz_25,Mz_30,Mz_35,Mz_40,Mz_45,
            Mz_50,...
6       Mz_55,Mz_60, Mz_65,Mz_70,Mz_75,Mz_80,Mz_85,Mz_90,Mz_95,
            Mz_98]=calling_stress_data_EL1_A()
7
8 %calling variables from dynplot
9 %moments around x-axis
10 MX_05=importdata('EL1_MX_05A.txt',' ',8);
11 Mx_05=MX_05.data(501:10500,1);
12 MX_10=importdata('EL1_MX_10A.txt',' ',8);
13 Mx_10=MX_10.data(501:10500,1);
14 MX_15=importdata('EL1_MX_15A.txt',' ',8);
15 Mx_15=MX_15.data(501:10500,1);
```

```
16 MX_20=importdata('EL1_MX_20A.txt',' ',8);
17 Mx_20=MX_20.data(501:10500,1);
18 MX_25=importdata('EL1_MX_25A.txt',' ',8);
19 Mx_25=MX_25.data(501:10500,1);
20 MX_30=importdata('EL1_MX_30A.txt',' ',8);
21 Mx_30=MX_30.data(501:10500,1);
22 MX_35=importdata('EL1_MX_35A.txt',' ',8);
23 Mx_35=MX_35.data(501:10500,1);
24 MX_40=importdata('EL1_MX_40A.txt',' ',8);
25 Mx_40=MX_40.data(501:10500,1);
26 MX_45=importdata('EL1_MX_45A.txt',' ',8);
27 Mx_45=MX_45.data(501:10500,1);
28 MX_50=importdata('EL1_MX_50A.txt',' ',8);
29 Mx_50=MX_50.data(501:10500,1);
30 MX_55=importdata('EL1_MX_55A.txt',' ',8);
31 Mx_55=MX_55.data(501:10500,1);
32 MX_60=importdata('EL1_MX_60A.txt',' ',8);
33 Mx_60=MX_60.data(501:10500,1);
34 MX_65=importdata('EL1_MX_65A.txt',' ',8);
35 Mx_65=MX_65.data(501:10500,1);
36 MX_70=importdata('EL1_MX_70A.txt',' ',8);
37 Mx_70=MX_70.data(501:10500,1);
38 MX_75=importdata('EL1_MX_75A.txt',' ',8);
39 Mx_75=MX_75.data(501:10500,1);
40 MX_80=importdata('EL1_MX_80A.txt',' ',8);
41 Mx_80=MX_80.data(501:10500,1);
42 MX_85=importdata('EL1_MX_85A.txt',' ',8);
43 Mx_85=MX_85.data(501:10500,1);
44 MX_90=importdata('EL1_MX_90A.txt',' ',8);
45 Mx_90=MX_90.data(501:10500,1);
46 MX_95=importdata('EL1_MX_95A.txt',' ',8);
47 Mx_95=MX_95.data(501:10500,1);
48 MX_98=importdata('EL1_MX_98A.txt',' ',8);
49 Mx_98=MX_98.data(501:10500,1);
50
51 %moments around y-axis
52 MY_05=importdata('EL1_MY_05A.txt',' ',8);
53 My_05=MY_05.data(501:10500,1);
54 MY_10=importdata('EL1_MY_10A.txt',' ',8);
```

```
55 My_10=MY_10.data(501:10500,1);
56 MY_15=importdata('EL1_MY_15A.txt',' ',8);
57 My_15=MY_15.data(501:10500,1);
58 MY_20=importdata('EL1_MY_20A.txt',' ',8);
59 My_20=MY_20.data(501:10500,1);
60 MY_25=importdata('EL1_MY_25A.txt',' ',8);
61 My_25=MY_25.data(501:10500,1);
62 MY_30=importdata('EL1_MY_30A.txt',' ',8);
63 My_30=MY_30.data(501:10500,1);
64 MY_35=importdata('EL1_MY_35A.txt',' ',8);
65 My_35=MY_35.data(501:10500,1);
66 MY_40=importdata('EL1_MY_40A.txt',' ',8);
67 My_40=MY_40.data(501:10500,1);
68 MY_45=importdata('EL1_MY_45A.txt',' ',8);
69 My_45=MY_45.data(501:10500,1);
70 MY_50=importdata('EL1_MY_50A.txt',' ',8);
71 My_50=MY_50.data(501:10500,1);
72 MY_55=importdata('EL1_MY_55A.txt',' ',8);
73 My_55=MY_55.data(501:10500,1);
74 MY_60=importdata('EL1_MY_60A.txt',' ',8);
75 My_60=MY_60.data(501:10500,1);
76 MY_65=importdata('EL1_MY_65A.txt',' ',8);
77 My_65=MY_65.data(501:10500,1);
78 MY_70=importdata('EL1_MY_70A.txt',' ',8);
79 My_70=MY_70.data(501:10500,1);
80 MY_75=importdata('EL1_MY_75A.txt',' ',8);
81 My_75=MY_75.data(501:10500,1);
82 MY_80=importdata('EL1_MY_80A.txt',' ',8);
83 My_80=MY_80.data(501:10500,1);
84 MY_85=importdata('EL1_MY_85A.txt',' ',8);
85 My_85=MY_85.data(501:10500,1);
86 MY_90=importdata('EL1_MY_90A.txt',' ',8);
87 My_90=MY_90.data(501:10500,1);
88 MY_95=importdata('EL1_MY_95A.txt',' ',8);
89 My_95=MY_95.data(501:10500,1);
90 MY_98=importdata('EL1_MY_98A.txt',' ',8);
91 My_98=MY_98.data(501:10500,1);
92
93 %moments around z-axis
```

```
94 MZ_05=importdata('EL1_MZ_05A.txt',' ',8);
95 Mz_05=MZ_05.data(501:10500,1);
96 MZ_10=importdata('EL1_MZ_10A.txt',' ',8);
97 Mz_10=MZ_10.data(501:10500,1);
98 MZ_15=importdata('EL1_MZ_15A.txt',' ',8);
99 Mz_15=MZ_15.data(501:10500,1);
100 MZ_20=importdata('EL1_MZ_20A.txt',' ',8);
101 Mz_20=MZ_20.data(501:10500,1);
102 MZ_25=importdata('EL1_MZ_25A.txt',' ',8);
103 Mz_25=MZ_25.data(501:10500,1);
104 MZ_30=importdata('EL1_MZ_30A.txt',' ',8);
105 Mz_30=MZ_30.data(501:10500,1);
106 MZ_35=importdata('EL1_MZ_35A.txt',' ',8);
107 Mz_35=MZ_35.data(501:10500,1);
108 MZ_40=importdata('EL1_MZ_40A.txt',' ',8);
109 Mz_40=MZ_40.data(501:10500,1);
110 MZ_45=importdata('EL1_MZ_45A.txt',' ',8);
111 Mz_45=MZ_45.data(501:10500,1);
112 MZ_50=importdata('EL1_MZ_50A.txt',' ',8);
113 Mz_50=MZ_50.data(501:10500,1);
114 MZ_55=importdata('EL1_MZ_55A.txt',' ',8);
115 Mz_55=MZ_55.data(501:10500,1);
116 MZ_60=importdata('EL1_MZ_60A.txt',' ',8);
117 Mz_60=MZ_60.data(501:10500,1);
118 MZ_65=importdata('EL1_MZ_65A.txt',' ',8);
119 Mz_65=MZ_65.data(501:10500,1);
120 MZ_70=importdata('EL1_MZ_70A.txt',' ',8);
121 Mz_70=MZ_70.data(501:10500,1);
122 MZ_75=importdata('EL1_MZ_75A.txt',' ',8);
123 Mz_75=MZ_75.data(501:10500,1);
124 MZ_80=importdata('EL1_MZ_80A.txt',' ',8);
125 Mz_80=MZ_80.data(501:10500,1);
126 MZ_85=importdata('EL1_MZ_85A.txt',' ',8);
127 Mz_85=MZ_85.data(501:10500,1);
128 MZ_90=importdata('EL1_MZ_90A.txt',' ',8);
129 Mz_90=MZ_90.data(501:10500,1);
130 MZ_95=importdata('EL1_MZ_95A.txt',' ',8);
131 Mz_95=MZ_95.data(501:10500,1);
132 MZ_98=importdata('EL1_MZ_98A.txt',' ',8);
```

```
133 Mz_98=MZ_98.data(501:10500,1);
134 end
```

Rainflow counting and equivalent stress ranges

```
1  function [Seq, ni75sec]=rainflow_and_Seq(sigma1,Time1)
2
3  % %Rainflow counting
4  %c=cycle counts: count, range, mean, start, end
5  %hist=histogram,
6  %rmm=histogram bin edges,
7  %idx=linear indices of reversals
8  % periods1=c1(:,5)-c1(:,4); %sec
9  % fcyc1=1./periods1; %1/sec
10
11 % %SN curve data
12 m2=5;
13
14 %Uc=0.05
15 [c1,hist1,edges1,rmm1,idx1] = rainflow(sigma1(:,1),Time1);
16 n0_1=sum(hist1,2); %number of cycles for each stress range
17 S0_1=edges1(2:length(edges1)); %stress ranges
18 num=0;
19 N1=0;
20 for i=1:length(S0_1)
21 num=num+(n0_1(i).*S0_1(i).^m2);
22 N1=N1+n0_1(i);
23 end
24 Seq_1=(num./N1).^(1/m2);
25 %Uc=0.10
26 [c2,hist2,edges2,rmm2,idx2] = rainflow(sigma1(:,2),Time1);
27 n0_2=sum(hist2,2); %number of cycles for each stress range
28 S0_2=edges2(2:length(edges2)); %stress ranges
29 num=0;
30 N2=0;
31 for i=1:length(S0_2)
32 num=num+(n0_2(i).*S0_2(i).^m2);
33 N2=N2+n0_2(i);
34 end
35 Seq_2=(num./N2).^(1/m2);
```

```
%Uc=0.15
[c3,hist3,edges3,rmm3,idx3] = rainflow(sigma1(:,3),Time1);
n0_3=sum(hist3,2); %number of cycles for each stress range
S0_3=edges3(2:length(edges3)); %stress ranges
num=0;
N3=0;
for i=1:length(S0_3)
num=num+(n0_3(i).*S0_3(i).^m2);
N3=N3+n0_3(i);
end
Seq_3=(num./N3).^(1/m2);
%Uc=0.20
[c4,hist4,edges4,rmm4,idx4] = rainflow(sigma1(:,4),Time1);
n0_4=sum(hist4,2); %number of cycles for each stress range
S0_4=edges4(2:length(edges4)); %stress ranges
num=0;
N4=0;
for i=1:length(S0_4)
num=num+(n0_4(i).*S0_4(i).^m2);
N4=N4+n0_4(i);
end
Seq_4=(num./N4).^(1/m2);
%Uc=0.25
[c5,hist5,edges5,rmm5,idx5] = rainflow(sigma1(:,5),Time1);
n0_5=sum(hist5,2); %number of cycles for each stress range
S0_5=edges5(2:length(edges5)); %stress ranges
num=0;
N5=0;
for i=1:length(S0_5)
num=num+(n0_5(i).*S0_5(i).^m2);
N5=N5+n0_5(i);
end
Seq_5=(num./N5).^(1/m2);
%Uc=0.30
[c6,hist6,edges6,rmm6,idx6] = rainflow(sigma1(:,6),Time1);
n0_6=sum(hist6,2); %number of cycles for each stress range
S0_6=edges6(2:length(edges6)); %stress ranges
num=0;
N6=0;
```

```
for i=1:length(S0_6)
num=num+(n0_6(i).*S0_6(i).^m2);
N6=N6+n0_6(i);
end
Seq_6=(num./N6).^(1/m2);
%Uc=0.35
[c7,hist7,edges7,rmm7,idx7] = rainflow(sigma1(:,7),Time1);
n0_7=sum(hist7,2); %number of cycles for each stress range
S0_7=edges7(2:length(edges7)); %stress ranges
num=0;
N7=0;
for i=1:length(S0_7)
num=num+(n0_7(i).*S0_7(i).^m2);
N7=N7+n0_7(i);
end
Seq_7=(num./N7).^(1/m2);
%Uc=0.40
[c8,hist8,edges8,rmm8,idx8] = rainflow(sigma1(:,8),Time1);
n0_8=sum(hist8,2); %number of cycles for each stress range
S0_8=edges8(2:length(edges8)); %stress ranges
num=0;
N8=0;
for i=1:length(S0_8)
num=num+(n0_8(i).*S0_8(i).^m2);
N8=N8+n0_8(i);
end
Seq_8=(num./N8).^(1/m2);
%Uc=0.45
[c9,hist9,edges9,rmm9,idx9] = rainflow(sigma1(:,9),Time1);
n0_9=sum(hist9,2); %number of cycles for each stress range
S0_9=edges9(2:length(edges9)); %stress ranges
num=0;
N9=0;
for i=1:length(S0_9)
num=num+(n0_9(i).*S0_9(i).^m2);
N9=N9+n0_9(i);
end
Seq_9=(num./N9).^(1/m2);
%Uc=0.50
```

```
114 [c10,hist10,edges10,rmm10,idx10] = rainflow(sigma1(:,10),
        Time1);
115 n0_10=sum(hist10,2); %number of cycles for each stress range
116 S0_10=edges10(2:length(edges10)); %stress ranges
117 num=0;
118 N10=0;
119 for i=1:length(S0_10)
120 num=num+(n0_10(i).*S0_10(i).^m2);
121 N10=N10+n0_10(i);
122 end
123 Seq_10=(num./N10).^(1/m2);
124 %Uc=0.55
125 [c11,hist11,edges11,rmm11,idx11] = rainflow(sigma1(:,11),
        Time1);
126 n0_11=sum(hist11,2); %number of cycles for each stress range
127 S0_11=edges11(2:length(edges11)); %stress ranges
128 num=0;
129 N11=0;
130 for i=1:length(S0_11)
131 num=num+(n0_11(i).*S0_11(i).^m2);
132 N11=N11+n0_11(i);
133 end
134 Seq_11=(num./N11).^(1/m2);
135 %Uc=0.60
136 [c12,hist12,edges12,rmm12,idx12] = rainflow(sigma1(:,12),
        Time1);
137 n0_12=sum(hist12,2); %number of cycles for each stress range
138 S0_12=edges12(2:length(edges12)); %stress ranges
139 num=0;
140 N12=0;
141 for i=1:length(S0_12)
142 num=num+(n0_12(i).*S0_12(i).^m2);
143 N12=N12+n0_12(i);
144 end
145 Seq_12=(num./N12).^(1/m2);
146 %Uc=0.65
147 [c13,hist13,edges13,rmm13,idx13] = rainflow(sigma1(:,13),
        Time1);
148 n0_13=sum(hist13,2); %number of cycles for each stress range
```

```
149 S0_13=edges13(2:length(edges13)); %stress ranges
150 num=0;
151 N13=0;
152 for i=1:length(S0_13)
153 num=num+(n0_13(i).*S0_13(i).^m2);
154 N13=N13+n0_13(i);
155 end
156 Seq_13=(num./N13).^(1/m2);
157 %Uc=0.70
158 [c14,hist14,edges14,rmm14,idx14] = rainflow(sigma1(:,14),
      Time1);
159 n0_14=sum(hist14,2); %number of cycles for each stress range
160 S0_14=edges14(2:length(edges14)); %stress ranges
161 num=0;
162 N14=0;
163 for i=1:length(S0_14)
164 num=num+(n0_14(i).*S0_14(i).^m2);
165 N14=N14+n0_14(i);
166 end
167 Seq_14=(num./N14).^(1/m2);
168 %Uc=0.75
169 [c15,hist15,edges15,rmm15,idx15] = rainflow(sigma1(:,15),
      Time1);
170 n0_15=sum(hist15,2); %number of cycles for each stress range
171 S0_15=edges15(2:length(edges15)); %stress ranges
172 num=0;
173 N15=0;
174 for i=1:length(S0_15)
175 num=num+(n0_15(i).*S0_15(i).^m2);
176 N15=N15+n0_15(i);
177 end
178 Seq_15=(num./N15).^(1/m2);
179 %Uc=0.80
180 [c16,hist16,edges16,rmm16,idx16] = rainflow(sigma1(:,16),
      Time1);
181 n0_16=sum(hist16,2); %number of cycles for each stress range
182 S0_16=edges16(2:length(edges16)); %stress ranges
183 num=0;
184 N16=0;
```

```
for i=1:length(S0_16)
num=num+(n0_16(i).*S0_16(i).^m2);
N16=N16+n0_16(i);
end
Seq_16=(num./N16).^(1/m2);
%Uc=0.85
[c17,hist17,edges17,rmm17,idx17] = rainflow(sigma1(:,17),
    Time1);
n0_17=sum(hist17,2); %number of cycles for each stress range
S0_17=edges17(2:length(edges17)); %stress ranges
num=0;
N17=0;
for i=1:length(S0_17)
num=num+(n0_17(i).*S0_17(i).^m2);
N17=N17+n0_17(i);
end
Seq_17=(num./N17).^(1/m2);
%Uc=0.90
[c18,hist18,edges18,rmm18,idx18] = rainflow(sigma1(:,18),
    Time1);
n0_18=sum(hist18,2); %number of cycles for each stress range
S0_18=edges18(2:length(edges18)); %stress ranges
num=0;
N18=0;
for i=1:length(S0_18)
num=num+(n0_18(i).*S0_18(i).^m2);
N18=N18+n0_18(i);
end
Seq_18=(num./N18).^(1/m2);
%Uc=0.95
[c19,hist19,edges19,rmm19,idx19] = rainflow(sigma1(:,19),
    Time1);
n0_19=sum(hist19,2); %number of cycles for each stress range
S0_19=edges19(2:length(edges19)); %stress ranges
num=0;
N19=0;
for i=1:length(S0_19)
num=num+(n0_19(i).*S0_19(i).^m2);
N19=N19+n0_19(i);
```

```
221 end
222 Seq_19=(num./N19).^(1/m2);
223 %Uc=0.98
224 [c20,hist20,edges20,rmm20,idx20] = rainflow(sigma1(:,20),
      Time1);
225 n0_20=sum(hist20,2); %number of cycles for each stress range
226 S0_20=edges20(2:length(edges20)); %stress ranges
227 num=0;
228 N20=0;
229 for i=1:length(S0_20)
230 num=num+(n0_20(i).*S0_20(i).^m2);
231 N20=N20+n0_20(i);
232 end
233 Seq_20=(num./N20).^(1/m2);
234
235 Seq=[Seq_1 Seq_2 Seq_3 Seq_4 Seq_5 Seq_6 Seq_7 Seq_8 Seq_9
      Seq_10 Seq_11 ...
236     Seq_12 Seq_13 Seq_14 Seq_15 Seq_16 Seq_17 Seq_18 Seq_19
          Seq_20];
237 ni75sec=[N1 N2 N3 N4 N5 N6 N7 N8 N9 N10 N11 N12 N13 N14 N15
      N16 N17 N18 N19 N20];
238 end
```

Linda Sieber

VIV fatigue of rigid spool for subsea template by a time domain model

NTNU
Norwegian University of
Science and Technology

CHALMERS
UNIVERSITY OF TECHNOLOGY